

ALMA MATER STUDIORUM
UNIVERSITÀ DI BOLOGNA

DOTTORATO DI RICERCA IN
ASTROFISICA

Ciclo XXXIII

Tesi di Dottorato

**On detecting the cosmic web and its
magnetic field**

Presentata da:
Nicola Locatelli

Supervisore:
Prof. Franco Vazza

Coordinatore di Dottorato:
Prof. Francesco Rosario
Ferraro

Co-supervisore:
Prof. Daniele Dallacasa
Dr. Gianni Bernardi

Esame finale anno 2021

Settore Concorsuale: 02/C1 - Astronomia, Astrofisica, Fisica della Terra e
dei Pianeti

Settore Scientifico Disciplinare: FIS/05 - Astronomia e Astrofisica

Studia e fatti onore [...]

Giorgio Paglia, 20 Nov. 1944

Abstract

Magnetic fields are known to permeate space over a remarkable range of scales, from meter-large bodies up to \sim Mpc wide clusters of galaxies. It is still debated whether their origin is either "primordial", involving their early formation in the homogeneous universe, or "astrophysical", i.e. from feed-back into the inter-galactic space by the first dense and highly magnetised structures formed (e.g. stars, galaxies, AGN). Observing galaxy cluster outskirts and filaments of the cosmic web have been proposed as keys to test the above scenarios, as the current strength and morphology of their evolved magnetic field is believed to correlate with the initial conditions in the most rarefied environments. In this thesis, we push different and complementary observational techniques of radio-astronomy (namely direct imaging, Faraday rotation and fast radio burst studies) on dedicated data from new generation instruments, in combination with state-of-the-art cosmological simulations, in order to constrain the properties of the magnetic fields at \sim Mpc scale at low redshift. This work provides relevant advances into observational constraints of magnetic fields in cluster outskirts (e.g. $0.4 \mu\text{G} < B_{\text{Mpc}} < 10 \mu\text{G}$ in the outskirts of the galaxy cluster A2249) and intra-cluster filaments ($B_{\text{Mpc}} < 0.25 - 0.75 \mu\text{G}$). We explore the feasibility and possible systematics of Faraday rotation studies with new and next generation instrumentation (JVLA, SKA) and provide new perspectives to best exploit their use. We also constrain the population properties of transient phenomena known as fast radio bursts (FRBs), which can be used as background sources for the study of the large scale structures. Our findings hint to either an evolving luminosity function of FRBs or to the presence of un-diagnosed selection effect in the current available samples. Finally, we plan (and implement) the refurbishment of an old radio telescope, the Northern Cross in Medicina, for dedicated FRB search. We characterise the instrument sensitivity at the frequency of 408 MHz and use it to estimate detection rates with respect to different possible and complementary set-up, e.g. a follow-up mode of known FRBs and a wide-area survey.

Contents

1	Introduction	11
1.1	What is the Cosmic Web? What is it alike?	11
1.2	Why is it important to characterize it?	13
1.2.1	The "missing baryon" problem	13
1.2.2	The warm-hot inter-galactic medium (WHIM)	16
1.2.3	Baryon profile distribution around massive halos	17
1.3	The magnetised cosmic web	18
1.3.1	Is the Universe magnetised?	18
1.3.2	Is the cosmic web magnetised?	19
1.3.3	Why is it important to access the LSS magnetic field?	23
1.3.4	How do we probe the Cosmic Web magnetic field?	26
2	Synchrotron diffuse emission	29
2.1	Radio imaging of the IGM	29
2.2	The Cornetto Relic in A2249	34
2.2.1	Radio relics into context	35
2.2.2	General properties of Abell 2249	36
2.2.3	Radio observations	36
2.2.4	X-ray: XMM observation	38
2.2.5	Results	41
2.2.6	Modelling of physical properties	45
2.2.7	Section summary	48
2.3	Constraints on the cosmic web magnetic field	49
2.3.1	Context of the experiment	49
2.3.2	Method	54
2.3.3	Results	62
2.3.4	Discussion	64
2.3.5	Section summary	75

3	Faraday Rotation	79
3.1	The Faraday effect as a probe of the IGMF	79
3.2	Inter-cluster filaments with Faraday rotation	83
3.2.1	Faraday rotation in galaxy clusters	83
3.2.2	Predictions of magnetic fields in filaments	85
3.2.3	Simulations of extragalactic magnetic fields	88
3.2.4	Filament selection and properties	89
3.2.5	Mock Rotation Measure observations	90
3.2.6	Non-parametric tests of RM distributions	92
3.2.7	Detectability of intra-cluster filaments using RM	92
3.2.8	Properties of most likely detectable filaments	98
3.2.9	Alternative models of magnetic fields in filaments	99
3.2.10	Section summary	103
3.3	The Pandora's cluster: Abell 2744	106
3.3.1	Abell 2744	106
3.3.2	Forecasts and strategy	109
3.3.3	VLA L-band data	112
3.3.4	Data calibration	114
3.3.5	Full-Stokes wide-field imaging	115
3.3.6	Preliminary RM results and discussion	121
4	Fast Radio Bursts	125
4.1	Fast Radio Bursts as a probe of the IGM	125
4.2	FRBs' cosmological distribution: the V/V_{\max} test	129
4.2.1	Context of the experiment	130
4.2.2	$\langle V/V_{\max} \rangle$ value estimation	133
4.2.3	Data samples	136
4.2.4	Method	137
4.2.5	$\langle V/V_{\max} \rangle$ of the FRB samples	142
4.2.6	Comparison with simulated populations	143
4.2.7	Results	145
4.2.8	Discussion	147
4.2.9	Section summary	150
4.3	The Northern Cross FRB project at 408 MHz	151
4.3.1	Context of the experiment	151
4.3.2	Instrument description	153
4.3.3	Test observations	155
4.3.4	FRB survey design	158
4.3.5	Section summary	167

<i>CONTENTS</i>	9
5 Conclusions	169
6 Bibliography	173

Chapter 1

Introduction

1.1 What is the Cosmic Web? What is it alike?

The evolution of small scale fluctuations of an isotropic and homogeneous density field under the contrasting actions of gravity, space time expansion and a cosmological constant has brought the Universe to be observed at its largest scales as a nonlinear pattern in the displacement of its brightest occurrence: the galaxies. Groups and clusters of galaxies are the most prominent patterns in the galaxy distributions. They are connected by other elongated ensembles of aligned galaxies which we call filaments and sheets. Vast void regions, emptied of matter, fill the volumes in between the large scale network (see Fig. 1.1 for a portion of the observed infrared (IR)/optical galaxy distribution). The cosmic structures normally encompass large contributes of matter other than galaxies, such as diffuse hot gas and dark matter.

Despite the large angular scales outlined by the cosmic structures and the wide area that they cover across the sky, it is just very recently that we have been able to witness the cosmic web pattern: only forty-four years ago it became first evident that the gathering of galaxies in groups, clusters and super-clusters in the local Universe was not consistent with being generated by projection effects of a random distribution in space ([de Vaucouleurs, 1976](#)).

It became soon evident that the densest condensations of matter were joined by "chains" of galaxies (which could be either straight or slightly curved) and that the plains joining different filaments were also populated by galaxies ([Einasto et al., 1980](#)) forming proper sheets delimiting the already known cosmological voids ([Einasto et al., 1975](#)).

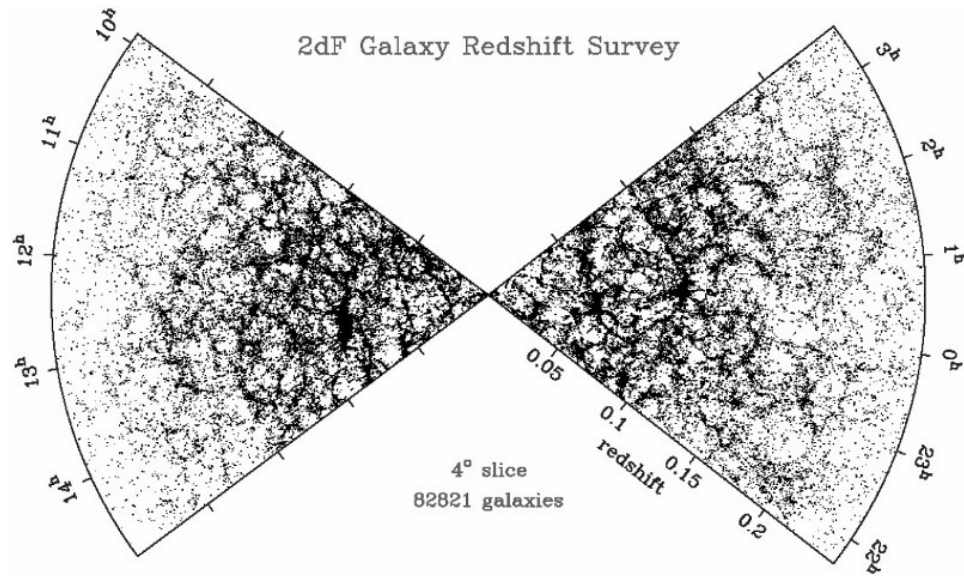


Figure 1.1: Colless et al. (2001): 2dF Galaxy Redshift Survey.

The actual name of "Cosmic Web" has been introduced by Bond et al. (1996), who also resolved the tension between the competing bottom-up and top-down theories about the large scale structure (LSS) formation by providing the numerical proof that the final state of the web was actually already present in embryonic form in the over-density pattern of the initial fluctuations, and was later on sharpened by the nonlinear growth of the structures themselves.

Numerical methods and simulations in particular constituted a fundamental tool to understand the cosmic web since its discovery (Klypin and Shandarin, 1983) due to the non-linearity of its evolution and became always more detailed, capable and prominent in the study of its global properties as well as of its features as seen by different probes, namely different wavelengths. Cosmological parameters implemented into simulations together with numerical recipes for the description of physical processes spread over a large set of scales constitute nowadays the benchmark upon which theories are probed by observations. The various elements of the Cosmic Web are expected to dominate the matter distribution in different over-density δ_n (with respect to the cosmic average value $\langle n \rangle \simeq 10^{-6} \text{ cm}^{-3}$) and correlation length L environments: $\delta_n \sim 10^{-2} - 10^0$ and $L > 10 \text{ Mpc}$ (megaparsec) for voids,

$\delta_n \sim 10^0 - 10^2, L \sim 1 - 10$ Mpc for filaments, $\delta_n \sim 10^2 - 10^3, L \sim 1$ Mpc for cluster halos and $\delta_n \geq 10^3, L \leq 0.1$ Mpc for galaxy halos.

1.2 Why is it important to characterize it?

1.2.1 The "missing baryon" problem

Large-scale and high-resolution hydrodynamic simulations of cosmological volumes assuming standard cold dark matter model with a cosmological constant Λ (Λ CDM, where "cold" indicates the non-relativistic speed of the non-/weakly interacting "dark" matter) help to predict the distribution of "baryons"¹ at both present and moderate redshift.

Initial conditions for the simulations are provided by different probes at different redshifts on the cosmological parameters describing the energy density content of what composes our Universe. One (relevant) example is the cosmological parameter describing the baryon energy density $\Omega_b h^2$ (where $h = H_0/100 \text{ km s}^{-1} \text{ Mpc}^{-1}$ and H_0 is the Hubble constant) with respect to the total matter content (i.e. including dark matter) Ω_m . Equivalently the fraction f_b of baryons, defined as $f_b \equiv \Omega_b/\Omega_m$, can be used. While both Ω_b and Ω_m evolve as $(1+z)^3$, f_b is independent from the redshift².

The independent probes constraining the Ω_b (or f_b) parameter in particular, are namely the observations of the Lyman α ($\text{Ly}\alpha$) forest at $z = 2$, the observed light element ratios attributed to standard nucleosynthesis (Cen and Ostriker, 1999) and the Cosmic Microwave Background (CMB) radiation maps. The $\text{Ly}\alpha$ forest is the set of the many lines corresponding to the $n = 2 \rightarrow n = 1$ atomic transition of the hydrogen neutral atom that show up as absorption features in the optical spectra of distant quasars, each red-shifted from the rest wavelength of 912\AA according to the position of the intervening neutral hydrogen cloud that generates it along the line-of-sight (LoS) from the quasar to the observer (Lynds, 1971; Weinberg et al., 2003, for a review). By computing the amount of neutral hydrogen at $z = 2$, Ω_b has been constrained to $\Omega_b \geq 0.017h^{-2} = 0.035$ for $h = 0.70$

¹According to the Standard Model of physics, baryons are composite particles made of three quarks, which most stable and common configurations are protons (Up-Up-Down quarks) and neutrons (Up-Down-Down quarks). Strictly speaking electrons are elementary particles called leptons, not baryons, but a convention in astronomy is to group them together under the same category.

²For completeness Ω_b is also slightly decreasing with time as in the cores of the stars some of the rest mass of the baryons is converted by nuclear fusion into photons and neutrinos. However this effect is negligible.

(Rauch et al., 1997; Weinberg et al., 1997). Furthermore, the cosmological models that involve Ω_b together with the standard theory for the growth of structure reproduce also other observed features of the Ly α forest such as column density and equivalent width distributions (Cen et al., 1994; Hernquist et al., 1996), their redshift dependence (Miralda-Escudé et al., 1996) and spatial correlations.

Independent on Ly α observations and before the accurate measurement of CMB anisotropies, the observed light-element abundance ratios from extragalactic HII regions combined with standard nucleosynthesis provided another test of expected baryon density $\Omega_b h^2 = 0.019 \pm 0.001$ and showed to be consistent with the Ly α measurement (Burles and Tytler, 1998a,b; Cyburt et al., 2016, for an updated review). However, with the advent of CMB measurements, the cosmological parameters have been estimated with much higher precision and today the argument has been reversed in favour of estimates of the primordial abundance ratios of the light elements. The most recent expected value for Ω_b comes from the CMB anisotropy map made by the *Planck* satellite (Planck Collaboration et al., 2016b) $\Omega_b h^2 = 0.02225 \pm 0.00023$ (68% confidence limit).

The above measurements provided information on the baryon content of the Universe at high redshift ($z \geq 2$). The same picture at low redshift, however, has been found to lack of a significant amount of ordinary matter (Fukugita et al., 1998). Surveys of galaxies collected only up to $\sim 10\%$ of the baryons in gravitationally collapsed objects such as galaxies, groups, and clusters. This long-standing issue has been known since two decades as the "missing baryon problem" (Cen and Ostriker, 1999).

Meanwhile, the list and abundance of metals has been incremented towards lower redshift through the detection of other absorption lines in addition to the Ly α such as the OVI line in the far ultraviolet, the OVII and CV lines in the soft X-ray band (see Nicastro et al., 2017; Shull et al., 2012, for reviews of the baryon budget). The largest reservoirs of baryonic matter is believed to be (and has been partially already found) the plasma phase of ordinary matter filling the space between the galaxies, called the intergalactic medium (IGM), present in different environments and thermodynamic states: halos of galaxies; the circum-galactic medium (CGM); the diffuse medium residing within (intra-cluster medium, ICM) and outside (warm-hot intergalactic medium, WHIM) the virial radius of clusters of galaxies. The latter medium, the WHIM, distributed over the largest scales, is particularly relevant and deserves a more detailed description, since it is believed to account for the remaining 80% – 90% of cosmological baryons outside collapsed structures in the local Universe.

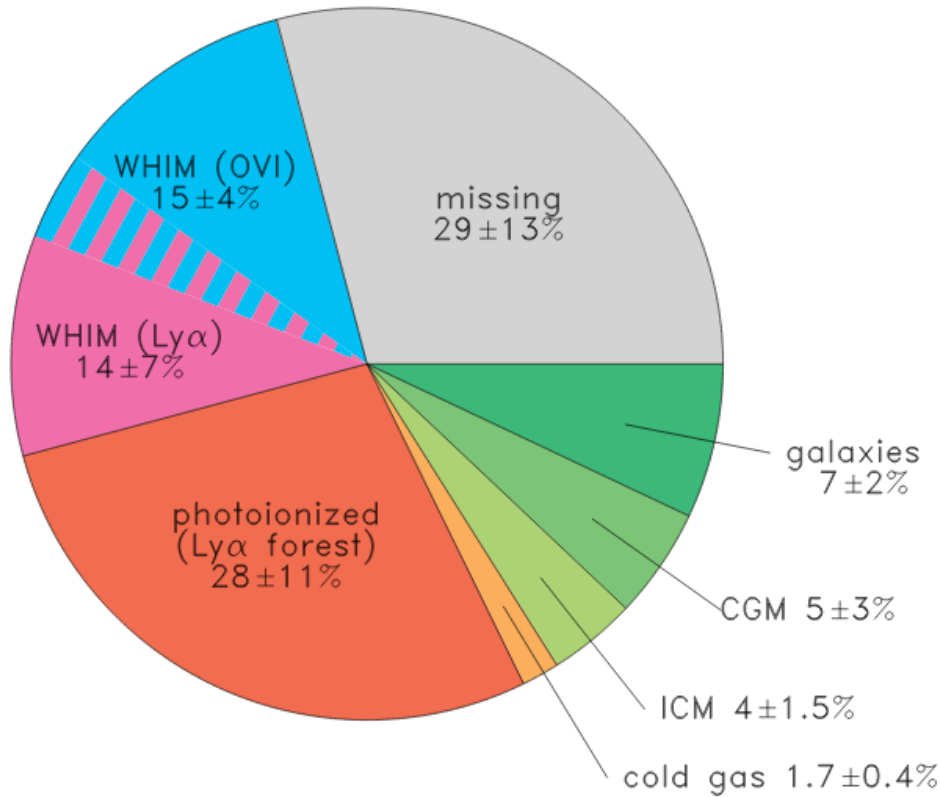


Figure 1.2: Shull et al. (2012): summary of current measurements of the low-redshift baryon census. Slices of the pie-chart show baryons in collapsed form (galaxies, groups, clusters), in the circumgalactic medium (CGM) and intra-cluster medium (ICM) and in cold gas (HI and HeI). Reservoirs include diffuse photoionized $\text{Ly}\alpha$ forest and WHIM (see § 1.2.2) traced by OVI (oxygen VI) and broad $\text{Ly}\alpha$ absorbers. Blended colors ($\text{Ly}\alpha$ and OVI) have combined total of $25 \pm 8\%$, accounting for double-counting of WHIM at $10^5 - 10^6$ K with detectable metal ions. The collapsed phases (galaxies, CGM, ICM, cold neutral gas) total $18 \pm 4\%$. Formally, $29 \pm 13\%$ of the baryons remain unaccounted for.

Finding the “missing” baryons and their thermodynamic and spatial distribution is very important as they hold the boundary conditions of accretion onto, and feedback within, galactic halos.

1.2.2 The warm-hot inter-galactic medium (WHIM)

According to hydrodynamical simulations, during the continuous process of structure formation, in particular after $z = 2$, baryons in the IGM condense into a filamentary web encompassing electron densities $n_e \simeq 10^{-6} - 10^{-4} \text{ cm}^{-3}$. Stationary shock waves of cosmological scale ($\geq \text{Mpc}$) form at the accreting boundaries of the collapsing structures, heating the in-falling gas up to temperatures of $T \simeq 10^5 - 10^7 \text{ K}$, building up the largest constituent of the IGM hydrogen at present, ionized for the most part (Cen and Ostriker, 1999; Davé et al., 2001). This shock-heated medium, enriched of metals by AGN activity and outflows, can be observed into three distinct phases depending on its temperature:

- $T \sim 10^{5-5.7} \text{ K}$: constituting the warm part of the WHIM, this gas is partially ionized, with a mass fraction of neutral atomic hydrogen $f_{HI} > 10^{-6}$, can be observed through OVI and CV absorption lines. This phase has been detected (Shull et al., 2012). It has been estimated to contain a 15% fraction of the baryons which had not been previously included in the observed budget. This brought the total observed fraction to $\sim 60\%$ leaving a smaller -still large, however- $\sim 30 - 40\%$ fraction of missing baryons to be searched for;
- $T \sim 10^{5.7-6.3} \text{ K}$: the WHIM gets further ionised, with $f_{HI} > 10^{-6-7}$ and can be observed through OVII lines. This diffuse phase in particular is expected to include the vast majority of the missing baryons (30 – 40%), and the detection through OVII absorption lines has been claimed in recent years (Nicastro et al., 2018);
- $T \sim 10^{6.3-7} \text{ K}$: this hot WHIM phase is found at the outskirts of galaxy clusters and large groups. It is basically in plasma phase (i.e. fully ionised) and constitutes the coldest end of the hotter intra-cluster medium, with $T > 10^7 \text{ K}$ commonly observed as diffuse Bremsstrahlung emission in the X-ray band at the core of clusters. Eckert et al. (2015) reported X-ray observations of the plasma at 10^7 K distributed into radial structures around the cluster Abell 2744. The diffuse hot gas

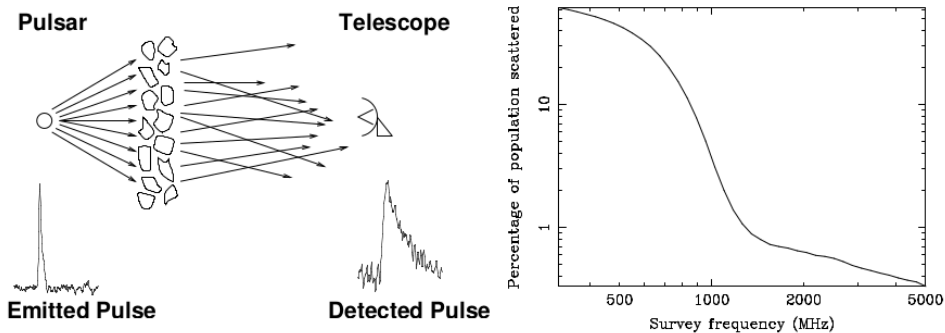


Figure 1.3: Lorimer (2008): Dispersion smearing acting on the signal produced by a transient radio source (e.g. a pulsar) while travelling through an ionized medium to the observer.

structures are coherent over scales of 8 Mpc and coincide with overdensities of galaxies and dark matter, with baryonic mass accounting for 5 – 10% of their total mass.

1.2.3 Baryon profile distribution around massive halos

Direct measurements of the the majority of the missing baryons through absorption lines and continuum thermal emission are still affected by large uncertainties (Shull et al., 2012; Nicastro et al., 2018, e.g.) or limited by constraints on the high densities and temperatures required (Eckert et al., 2015). In addition to these observables, every diffuse ionized baryon along a LoS would contribute equally to delaying the arrival time of any radio signal, as a function of its frequency, coming from extragalactic distance. This is a well known and studied effect in plasma physics, called signal dispersion (a sketch of the physical process and signal profile is provided in Fig. 1.3). Unfortunately, the arrival time of radio waves from stationary sources is degenerate with frequency, since they are continuously emitting, defying the same definition of any arrival time. It is however possible to measure arrival times from transient radio sources, such as pulsars. The dispersion of their (periodic) pulses is indeed widely used to inform about the baryon content (free-electrons) of the inter-stellar medium (ISM) of the Milky Way (Cordes and Lazio, 2002; Yao et al., 2017). If we do not consider the Magellanic Clouds, pulsars are known and observed only within our galaxy and cannot be used to probe further distances, thus preventing a similar method to be

used for informing about the IGM.

Luckily enough, this used to be true only until recent years, that is before the discovery of a new class of extragalactic transient radio sources, known as Fast Radio Bursts (FRBs) (Lorimer et al., 2007). As transient sources their signal is dispersed across the observed frequency band, and as extragalactic, what disperse it is the integrated free electron density along the LoS, namely the IGM, in addition to contributions from plasma local to the (unknown) emitting source, host galaxy, and the Milky Way ISM (Ioka, 2003; Inoue, 2004; McQuinn, 2014). By building a large sample (hundreds) of dispersion measurements from arcminute-localized FRBs located at $z > 0.5$ it is in principle possible to constrain the baryonic mass profile at twice the virial radius surrounding different matter halos down to halo masses of $10^{12} M_{\odot}$ (M_{\odot} is the solar mass), thus in environments not accessible from and complementary to the other probes (McQuinn, 2014).

For a deepened dissertation on FRBs as probes of the IGM we refer the reader to the following § 4.1.

1.3 The magnetised cosmic web

1.3.1 Is the Universe magnetised?

There is a rather clear understanding of the LSS formation from the small inhomogeneities observed in the CMB radiation at $z \simeq 1100$ and their amplification through gravitational collapse resulting from the energy density balances between light, matter, curvature and a cosmological constant, up to the local Universe at $z = 0$, but how did magnetic fields in galaxies and clusters of galaxies form and evolve? are they also present in the LSS web or not at all or up to which extent? Key processes for structure formation are gas dynamics and gravitational collapse, together with differential gas rotation and turbulence. The latter elements are known to be key processes for the amplification and sustain of magnetic fields observed in galaxies and galaxy clusters (Widrow et al., 2012).

As a matter of fact, magnetic fields in astrophysical systems are observed at all physical scales. The smallest astronomical objects known to hold a magnetic field are asteroids (Kivelson et al., 1993; Vallee, 1998; Weiss et al., 2012, and references therein), planets and their satellites (Kivelson et al., 2004; Kivelson, 2015, for a review). Main sequence stars also commonly hold magnetic fields of \sim G order with smaller features such as sunspots and solar prominences reaching up to 100 – 1000 G (= 0.1 T).

At larger scales, the average total magnetic field in the Milky Way is

$\simeq 6\mu\text{G}$ in the region around the Solar System, increasing to $20 - 40\mu\text{G}$ in the region of the Galactic center. Dense clouds of atomic (HI) and cold molecular (H_2) hydrogen are observed in large radio filamentary structures near the Galactic center. They host fields of up to several mG strength (Heiles and Crutcher, 2005; Wielebinski and Beck, 2005; Beck, 2007) while outside, the field at $\sim 10 - 100$ kpc scale is mostly parallel to the plane of the Galactic disk. The diffuse and polarized radio emission from the Milky Way as observed with radio telescopes and with the WMAP satellite, as well as Faraday rotation measures (RM) from polarized background sources, both within and outside the Galaxy (e.g. from pulsars and extragalactic radio sources) have been also extensively analyzed to obtain a three-dimensional structure modeling the Milky Way's magnetic field (Sun et al., 2008; Jansson and Farrar, 2012; Van Eck et al., 2011). These same surveys revealed many structures in the magnetized interstellar medium at the small (i.e. parsec) scales (Reich, 2006). The 3D large-scale structure follows the spiral arms determined from the star (optical) distribution, similar to what observed in other galaxies. Furthermore large-scale field reversals in the disk are observed, as well as star-forming regions giving rise to several distortions in the field morphology (Beck and Wielebinski, 2013, for a review). The scale height of the Galactic halo magnetic field has been recently estimated to 2.0 ± 0.3 kpc (Sobey et al., 2019).

As far as extragalactic magnetic fields are concerned, they have been observed in galaxies other than the Milky Way since late '70s (Segalovitz, 1976; Tosa and Fujimoto, 1978) and their intensity and morphology has been extensively presented in many review papers (we refer the reader to Kronberg, 1994; Widrow, 2002; Beck, 2012) and reproduced by magneto-hydrodynamical (MHD) simulations (Pakmor et al., 2014; Rieder and Teyssier, 2016, 2017). The presence of magnetic fields in other galaxies has been also probed with respect to time, finding evidences in galaxies up to $z = 2$ (Kronberg et al., 1992; Athreya et al., 1998; Kronberg et al., 2008; Mao et al., 2017). These observations also test how the origin and amplification determined from magnetic field intensity and morphology are consistent between galaxies in the local Universe and at higher redshift.

1.3.2 Is the cosmic web magnetised?

Galaxy clusters and the intergalactic medium are well known to be permeated by magnetic fields coherent over Mpc-scales. The astrophysical objects that have been found to entail magnetic fields over such large scales are mostly observed in the radio bands within or around massive galaxy clus-

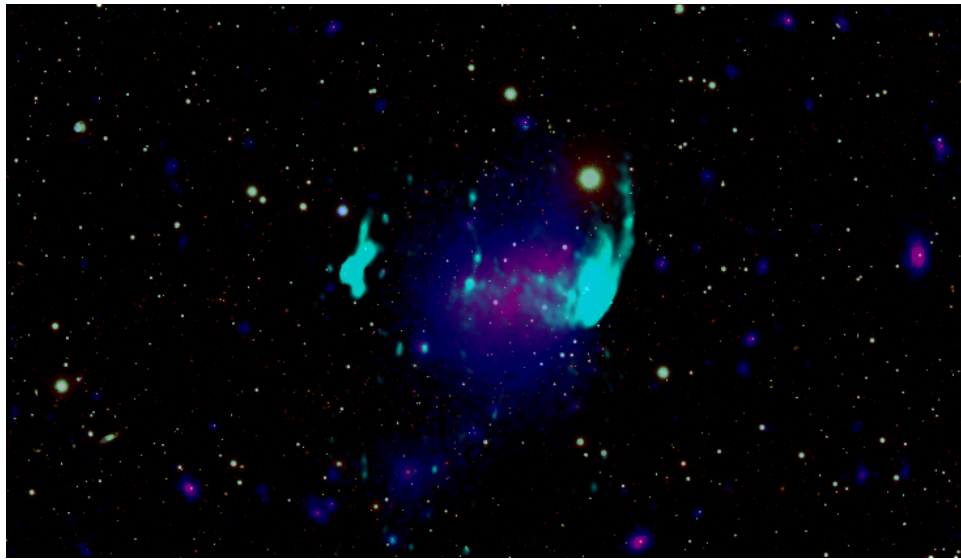


Figure 1.4: Multi-frequency overlaid image of the galaxy cluster RXCJ1314.4-2515: optical (BRz colors), X-ray (blue-red), and radio (green). The radio emission highlights the presence of magnetic fields and relativistic particles across the cluster volume. Courtesy of Chiara Stuardi

ters and have been classified in different fashions depending on location, morphology, spectrum, degree of polarization and luminosity. Namely they are giant radio halos, mini-halos and radio relics (we refer the reader to [van Weeren et al., 2019](#), for a recent review with emphasis on radio observations and properties). An example of the phenomenology of magnetic fields in galaxy clusters is provided in Fig. 1.4. The X-ray thermal emission of the galaxy cluster RXCJ1314.4-2515 observed by the XMM-Newton satellite instrument is overlaid to the optical image of the sky background crowded by galaxies. The green patches indicate radio emission detected at ~ 1 GHz with the Jansky Very Large Array (JVLA) radio interferometer. Diffuse continuum radio flux ascribed to synchrotron emission always highlights the presence of magnetic fields and relativistic particles. Through studies of the Faraday rotation effect, quantified through the rotation measure (RM, we refer the reader to Chapter § 3 of this work for definitions and details on the Faraday rotation effect in radio astronomy), it has been found that those clusters holding a cooling time of the gas much shorter than the Hubble time (called *relaxed* or *cool core* clusters), also hold central magnetic field intensities of $\sim 10 \mu\text{G}$, whereas clusters showing a disturbed morphology, turbulent motions and significant bulk kinetic energy of their components, mainly due to recent past merging events (for this called *disturbed* or *merging* clusters), have smaller amplitude magnetic fields of $\sim \mu\text{G}$ ([Taylor et al., 2001](#); [Carilli and Taylor, 2002](#); [Giacintucci et al., 2009](#); [Kale et al., 2015](#); [Govoni et al., 2017](#)). The fields in the central regions of these clusters are turbulent, with coherence lengths of 10 kpc and spatial scales in the range 5-500 kpc ([Feretti et al., 2012](#)).

One existent method to overcome the sensitivity limitations of direct imaging at radio wavelengths is to recover information on the magnetic field along the line of sight thanks to the Faraday effect which induces on the polarized light from background sources (see further section § 3.2 for details on the method). However the sparse grid of available background radio sources, limited by the instrument sensitivities, nowadays still prevents to reach firm conclusions on the radial trend of the magnetic field in galaxy clusters. Future radio facilities at $\sim\text{GHz}$ frequencies such as MeerKAT and SKA-MID are expected to be game-changers with this respect, as we will show later on in § 3.2. Despite the current limitations, a correlation between the central electron density and mean central magnetic field strength, has recently been confirmed using data for 9 clusters ([Govoni et al., 2017](#)). However the mean central magnetic field does not seem to be correlated to the other cluster properties, such as temperature. Also the magnetic field profile, minimum, maximum and relevant scales and its power spectrum in

galaxy clusters are still poorly known (van Weeren et al., 2019). For a more theoretical review about magnetic field amplification mechanisms in clusters we refer the reader to Vazza et al. (2017) and Donnert et al. (2018).

Volume-averaged (i.e. not location- or object-specific) limits on magnetic fields over cosmological scales have also been obtained using different methods, so that, in general the strength is $\leq nG$ (Blasi et al., 1999; Kahniashvili et al., 2010; Böhringer et al., 2016). However, due to the different model assumptions comparing these values with magnetic field strengths observed in single cosmological objects (e.g. galaxy clusters) is non trivial and has to be taken with caution.

In addition, very recent and innovative works used both archival and new radio polarization data to estimate the all-sky contribution of the intervening IGM again exploiting the Faraday rotation effect, but on a clever statistical argument: they computed the RM difference in pairs of extragalactic polarized sources located adjacent to each other on the plane of the sky (Vernstrom et al., 2019; O’Sullivan et al., 2020). This difference includes several and same contributions from diverse media along the LoS for all pairs (e.g. ISM, Milky Way halo, local environment of the source, etc.), apart from a putative IGM contribution that acts only in case that the extragalactic radio sources included in the pair are not physically related to each other. By comparing the root-mean-square RM difference ΔRM_{rms} separately over a set of physically related pair of sources (namely the radio lobes of a radio galaxy) and over a set of random pair of unrelated background sources, the average RM scatter caused by the magnetised and ionised IGM has been extracted and upper limits on the IGM magnetic field strength have been set to $\leq 40nG$ (Vernstrom et al., 2019) and $\leq 4nG$ (O’Sullivan et al., 2020) respectively using data from the NVSS (Condon et al., 1998) at 1.4 GHz and the the LOw Frequency ARray (LOFAR) at 144 MHz.

Finally, in cosmic voids, lower limits to magnetic fields have been suggested to amount down to $\sim 10^{15}$ G, arguing that outflows from isolated dwarf galaxies, observed to be magnetised both in voids and denser environments, can bring and diffuse magnetic fields into voids (Beck et al., 2013). Another argument able to sets lower limit on the intergalactic magnetic field (IGMF) comes from the highest energies. In fact blazars produce gamma rays with energies ≥ 1 TeV that interact with the diffuse extragalactic background light (EBL) before propagating to cosmological distances ($\leq 10-100$ Mpc) (Aharonian et al., 2007; Franceschini et al., 2008). The interactions of \geq TeV gamma rays with the EBL leads to the production of electron-positron pairs in the intergalactic space that in turns emit a secondary cascade of lower-energy ($\sim GeV$) gamma rays through inverse Compton scat-

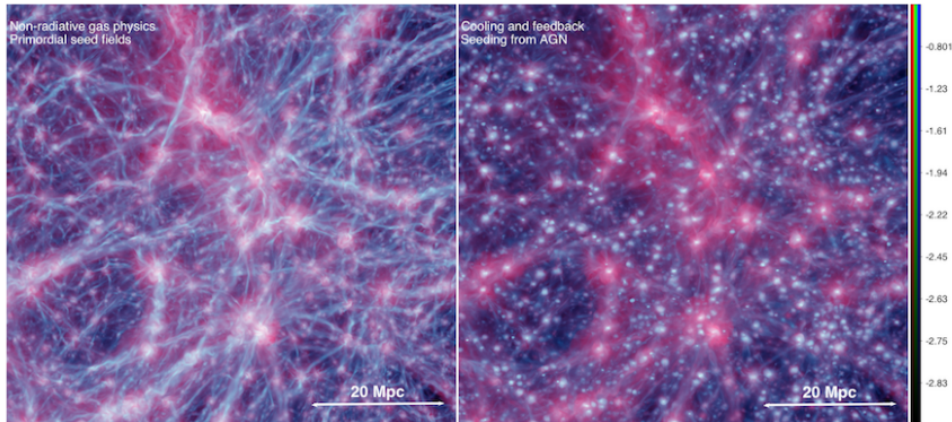


Figure 1.5: [Vazza et al. \(2017\)](#): Volume rendering of the average temperature (red colors) and average magnetic field strength (green+blue) along the line of sight, for a primordial magnetogenesis scenario with initial magnetic field $B_0 = 1$ nG (left) or a cooling feedback model where magnetic fields have been injected by AGN (right). For both quantities the mass-weighted average along the line of sight are shown. Magnetic field strengths ranges from $10^{-4} \mu\text{G}$ to $1 \mu\text{G}$ in both panels.

tering with the CMB photons. The flux and spectrum of this reprocessed emission thus depends on the intensity of the IGMF, that acts by deflecting the pairs off the LoS and thus diluting the intrinsic emission over a large solid angle. The non-detection of this secondary emission from blazars inferred from observations carried by the Fermi/Large Area Telescope, can thus be translated into lower limits on the intergalactic magnetic field of $B \geq 10^{-15} - 10^{-16} \text{G}$ ([Neronov and Vovk, 2010](#); [Tavecchio et al., 2010](#)).

1.3.3 Why is it important to access the LSS magnetic field?

We outlined in the previous paragraphs what we know to date about the magnetic fields coherently distributed over the largest cosmological structures. The effort to study magnetic fields has been driving the development and improving performances of MHD simulations over the last two decades. Cosmological magnetic fields have been tightly connected to particle acceleration and have been demonstrated to produce effects on turbulence, large-scale plasma motions, convection, cloud collapse, viscous dissipation, heat and momentum transport processes by inhibiting heat conduction, spa-

tial mixing of gas, and propagation of cosmic rays (Vazza et al., 2017). All these are key elements and processes that shape the large scale structure formation and evolution.

Despite the recognition of the role played by large scale magnetic fields, and their present observations, their origin remains largely uncertain. The question on their origin is a rather fundamental one in particular. The pre-existence of much weaker seed fields is an hypothesis being commonly accepted but yet to be proven. These weak fields may then be amplified by turbulence/dynamo and/or shock/compression arising during structure formation and merger events. As the result of turbulent motions for instance, different magnetic field scales have been shown to be able to survive (e.g. Kahniashvili et al., 2013). However, the origin of seed fields remains an open question. The CMB measurement provided upper limits to the intensity of magnetic fields but hasn't constituted a proof for their existence: are these seed fields in place already at its epoch and just too weak to be detected or they have formed later on? With this respect, may the seed fields be produced locally in early stars and/or (proto)galaxies and then injected in the interstellar and intergalactic medium (Rees, 2006)? They could also arise during galaxy formation, at later epochs of the Universe, being powered by magnetized winds and jets expanding into the IGM from the galaxies. These questions are as important as they are tough to be answered, since observations of magnetic fields are today performed especially in the peaks of the over-density distribution, while they are scarce and of difficult interpretation in more rarefied environments.

The eventual discovery of primordial magnetic fields will imply interesting physics that may involve the generation of currents during the early phases of the Universe such as inflation, phase transitions and baryogenesis (Harrison, 1973; Kahniashvili et al., 2010, 2011; Widrow et al., 2012; Durrer and Neronov, 2013; Kahniashvili et al., 2016; Subramanian, 2016). Physical processes have been proposed to act in the early phases of the Universe. A small and incomplete sample includes the ‘‘Biermann-battery’’ mechanism (Kulsrud et al., 1997) and aperiodic plasma fluctuations in the inter-galactic plasma (Schlickeiser, 2012). In addition, resistive mechanisms (Miniati and Bell, 2011) or ionization fronts around the first stars (Langer et al., 2005) might provide further amplification to the primordial fields already in-place. This general class of magneto-genesis models is commonly referred to as *primordial* models. The persistence of primordial magnetic field structures in voids today depends on the particular magnetization mechanism at play: they may be characterized by large (Zel'dovich, 1970; Turner and Widrow, 1988) or small (\leq Mpc, Chernin 1967) coherence lengths. Their observation

could possibly also inform on the generation of primordial helicity (Semikoz and Sokoloff, 2005; Campanelli, 2009; Kahniashvili et al., 2016). To provide an idea of the room for improvements of the current knowledge, the uncertainty in primordial magnetic fields at present, allows their intensity within the range $\sim 10^{-34} - 10^{-10}$ G.

If magnetic fields, instead, were triggered and released by processes involved within the formation of stars and/or galaxies, they might have affected their thermodynamic state acting on the transport of heat and entropy, heavy nuclei and cosmic rays in the cosmic structures simultaneously forming (Planelles et al., 2016). We will generally dub this second class of models as *astrophysical*. Any magnetization process connected to galaxy formation is found to be poorly efficient in small overdensity environments. This is due to the dilution following the Universe expansion of the injected fields, as well as the reduction in the number of sources in regions of lower density (Widrow et al., 2012). Fig. 1.5 shows two examples of the simulated IGMF intensity and spatial distribution at $z = 0$ for the two classes of magnetic field initial conditions taken from Vazza et al. (2017).

The largest scale magnetic field observed today are believed to result from the amplification of the postulated seed fields outlined above. The amplification at all scales is driven by the field's flux-freezing³ within the plasma which is adiabatically expanding (Marinacci et al., 2015), thus following the structures growth as

$$B = B_0 \left(\frac{n}{\langle n \rangle} \right)^{\frac{2}{3}} \quad (1.1)$$

where B_0 is the seed magnetic field intensity and $n/\langle n \rangle$ is the local overdensity of the plasma with respect to the (comoving) critical value $\langle n \rangle$. However at large over-densities, namely the ICM, magnetic field has been found to keep memory of the past turbulent activity of the cluster rather than the original conditions (Beresnyak and Miniati, 2016). This independence from initial conditions in galaxy clusters and more generally in turbulent plasma is due to the small scale dynamo acting in addition to the adiabatic compression of the field lines. The small scale dynamo is an MHD process of magnetic field amplification driven by turbulence and shear motions in the plasma (Ryu et al., 2008). The exponential growth of the magnetic intensity under small scale dynamo action enables its detection through synchrotron

³the term *flux-freezing* indicates that the flux $\psi = \int_S \mathbf{B} d\mathbf{S}$ of the magnetic field through a closed surface \mathbf{S} is constant over time. It directly follows from Ohm's law $\mathbf{J} = \sigma(\mathbf{E} + \mathbf{v} \times \mathbf{B})$ in absence of currents $\mathbf{J} = 0$. \mathbf{B} is then proportional to a surface and thus $B \propto n^{2/3}$, where n is the average density of the plasma.

emitting electrons but in turn rapidly erases information on the initial value B_0 . Turbulence can be set into the ICM by merging events and stationary accretion of matter onto the cluster. Not only the amount of turbulence is expected to be larger in the ICM with respect to the IGM, but also simulations indicate the turbulence to be sub-sonic in the former, opposed to a transonic or mildly-supersonic regime in the latter case (Ryu et al., 2008), although actual conditions depends also on individual object history and other poorly known plasma conditions (such as the age of the system, the nature of the turbulent forcing, the magnetic Reynolds number, Federrath et al. (2014); Beresnyak and Miniati (2016)). This trend in combination with a suppression of the small scale dynamo in highly supersonic flows (Haugen and Brandenburg, 2004) points to the large scale magnetic field outside galaxy clusters (i.e. filaments and voids) as elite places where today’s magnetic field still carries information on the initial conditions, namely B_0 . We note that from eq. 1.1 it appears not only the linearity between the observed magnetic field B and the initial value B_0 , but also the importance of the characterization of the density environment n . Observing the large scale magnetic field in under-dense environments such as filaments and voids today has the remarkable value of informing us on the seed field intensity and coherence length and thus probe the different magnetogenesis scenarios.

1.3.4 How do we probe the Cosmic Web magnetic field?

We outlined the scope and importance of understanding the initial magnetization conditions through probing today’s IGMF in filaments/voids. We have seen that for the smallest overdensity environment lower and upper limits based on clever arguments exists (see § 1.3.2), however IGMF into voids offer little chance to be directly measured due to the sparsity/absence of galaxies and the very low density of the plasma which they encompass. Higher chances may be obtained from the filamentary environment in the Cosmic Web. Higher densities reaching up to cluster values at their outskirts and a larger number of galaxies embedded in the hot plasma (see § 1.2.2) offer challenging but easier targets (with respect to voids) to different techniques which are commonly used in galaxy cluster observation and characterization. These techniques include direct X-ray and radio continuum imaging of the hot and magnetised plasma, magnetic field tomography of foreground structures through the Faraday rotation effect which B induces on linearly polarized light from background sources. Most recently a new possibility came from the combination of the Faraday effect with, the signal dispersion of radio waves from extragalactic transient sources. (Vazza

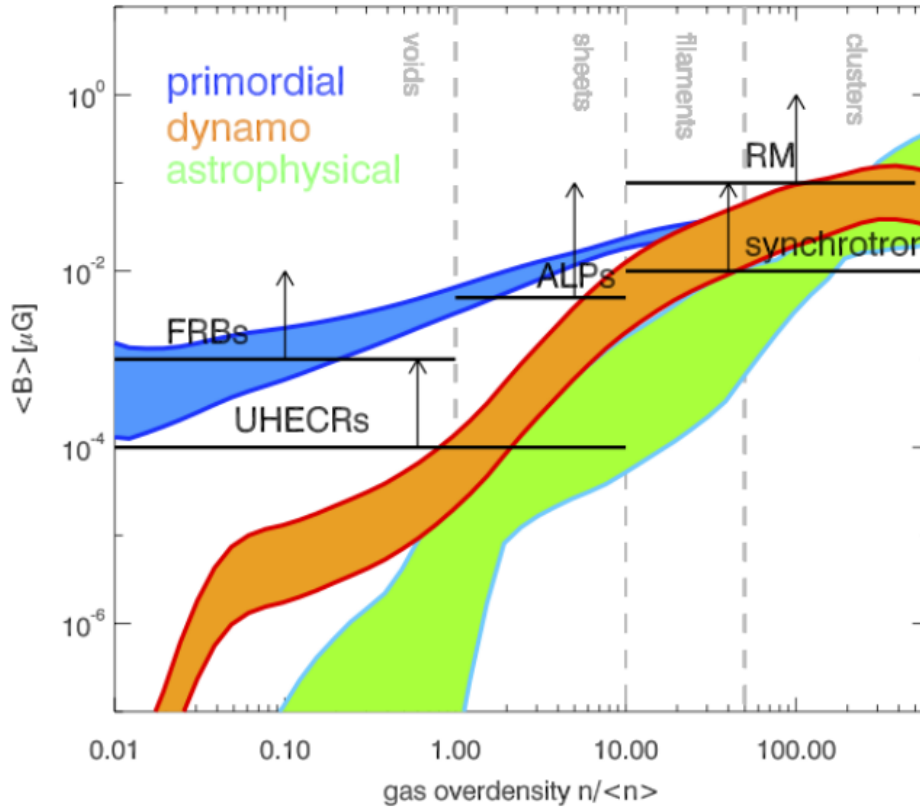


Figure 1.6: Overview of the distribution of extragalactic magnetic fields predicted by the simulations in [Vazza et al. \(2017\)](#) and of the approximate observational limits which can probe them.

[et al., 2017](#), we report their plot in Fig. 1.6) outlined the strengths of the different methods in constraining the magnetic field amplitude in different overdensity environments at the largest scales, from voids up to clusters. In this work we make use of these three methods at various level of details and development to study the magnetized Cosmic Web, and the structure of the Chapters closely follows this method's division. We refer the reader to the begin of each section for more details on all the useful definitions and concepts of the different methods.

Chapter 2

Synchrotron diffuse emission

2.1 Radio imaging of the IGM

The most straightforward way to think of finding, discovering, detecting a general target is usually by means of its direct observation by obtaining an image of it. With this respect, the WHIM makes no exception and the most promising windows to detect it in emission are certainly the X-ray and radio bands (see [Nicastro, 2016](#), and references therein). While the X-ray band would hopefully provide evidence for the volume-filling fraction of the hottest and densest phases of the WHIM (see an example in [Fig. 2.1](#)), the radio domain is expected to encompass the emission from the (small) fraction of relativistic electrons of the WHIM that might be accelerated by quasi-stationary strong accretion shocks, forming at the boundaries of the gravitationally collapsed LSS ([Ryu and Kang, 2003](#); [Pfrommer et al., 2006](#)). Indeed, several current and future large ground-based and satellite facilities are being built and deployed also for this very purpose, such as the *Athena* X-ray Observatory¹ and the already operative radio telescopes LOFAR, MWA, ASKAP, MeerKAT as well as the the next-generation Square Kilometer Array (SKA)².

From cosmological simulations the radio emission is expected to have a steep spectrum $S_\nu \propto \nu^{-\alpha}$ with $\alpha = 1.1 \pm 0.1$ (α is the *spectral index*), making the low frequencies more suited to the goal. In addition, the emission is expected to produce a very faint $\leq \mu\text{Jy arcsec}^{-2}$ signal at 100 MHz over large ($\sim \text{deg}$) scales ([Keshet et al., 2004](#); [Brown, 2011](#); [Vazza et al., 2015b](#); [Brown et al., 2017](#); [Vernstrom et al., 2017](#); [Vacca et al., 2018](#)). Simulations

¹<http://www.the-athena-x-ray-observatory.eu>

²<https://www.skatelescope.org/>

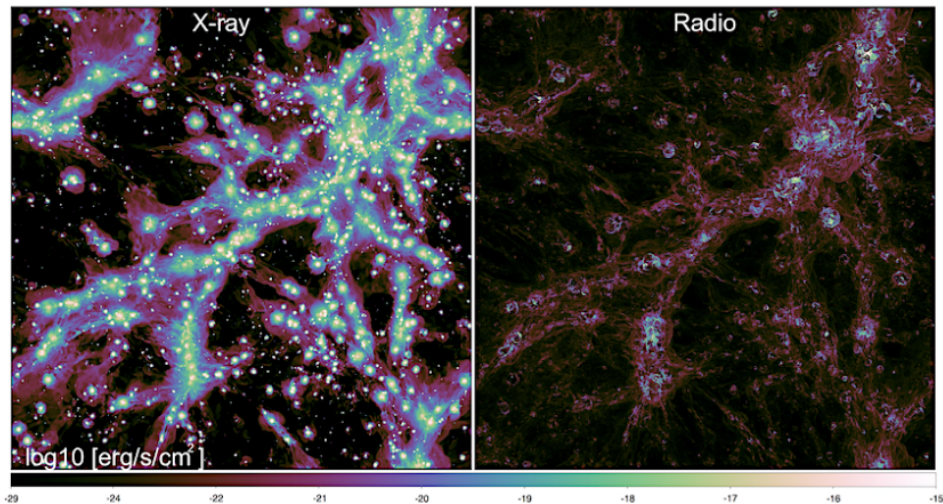


Figure 2.1: [Vazza et al. \(2019\)](#): Projected X-ray emission (0.8-1.2 keV) and mock radio emission (260 MHz) from the cosmic web, for a simulated 100^3 Mpc^3 volume at $z = 0.05$.

also suggested the best targets for a first evidence to consist in close and interacting pairs of massive galaxy clusters ([Vazza et al., 2019](#)). In fact, diffuse radio emission from very close pairs has already been imaged using LOFAR ([Akamatsu et al. 2017](#), for a tentative detection and [Govoni et al. 2019](#); [Botteon et al. 2020b](#) for direct imaging of X-ray plus radio bridges, also presented in Fig. 2.2). In these cases, the galaxy clusters involved are very close to each other and thought to be in a pre-merger phase where their ICM is maximally compressed and heated at the interface between them, at the intersection of their virial radii. Despite the dense and hot environment still characteristic of the ICM and the possible presence of further amplification mechanisms required from their special conditions ([Brunetti and Vazza, 2020](#)), they represent clear cases of methods and targets that can hopefully be inspected with deeper observations.

Within this context we present in Sec. 2.3 a first attempt to observe with LOFAR (144 MHz) the radio emission from the WHIM in between best-candidate pairs of galaxy clusters characterized by large separations ($\sim 10 \text{ Mpc}$). Despite being too distant between each other to involve current merging activity they have been selected to hold a high chance to be physically connected by an inter-cluster filament. Even the no-detection

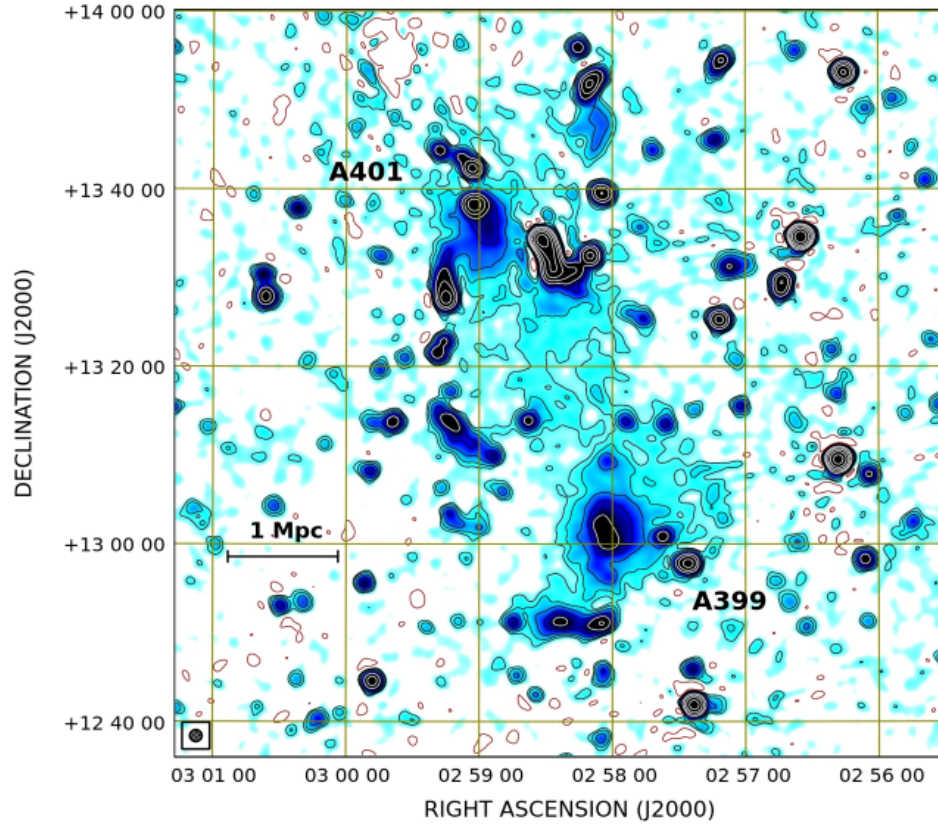


Figure 2.2: Govoni et al. (2019): LOFAR image of a radio bridge connecting the galaxy clusters A399 and A401. The $80''$ resolution image has an rms sensitivity of 1 mJy beam^{-1} . Contour levels increase by a factor of 2 starting at 3 mJy beam^{-1} . Red contours show -3 mJy beam^{-1} .

of any clear evidence for radio emission related to the (putative) shocked WHIM can provide useful information on the maximum level of compression and magnetisation of the inter-cluster medium. In fact, with the help of a novel method developed to compare observations with the direct outcome of realistic and physically motivated cosmological simulations we will translate a no-detection into constraints on the magnetic field $B_{\text{WHIM}} < 250 \text{ nG}$ (comoving, mass-weighted, at $z = 0$. See Sec. 2.3.4).

At present, one additional way to constrain properties of the large-scale IGM is to observe the ICM at the peripheries of galaxy clusters where accretion shocks from filaments might be present (Bagchi et al., 2006; Giovannini et al., 2010; Farnsworth et al., 2013), or, to observe the peripheries of merging galaxy clusters displaying a disturbed X-ray morphology. In this latter case, the shock waves generated by the merger are launched into the ICM and they are able to compress both the gas (Akamatsu and Kawahara, 2013; Akamatsu et al., 2017) and the magnetic fields (Govoni et al., 2019). Such shock waves, despite having generally smaller Mach numbers than stationary accretion shocks in filaments, thanks to the higher densities and stronger magnetic field of the ICM, they efficiently power arc-shaped segments of radio diffuse emission over the cluster-scale known as radio relics (see below Fig. 2.3 and Sec. 2.2.1 for additional details or refer to van Weeren et al., 2019, for a recent review). Despite they are still characteristic of the ICM, they provide valuable information on the medium up the shock front and light up the details of particle acceleration, gas distribution and magnetic fields at the interface between the ICM and the WHIM.

Within this context, in the following Sec. 2.2 we present the discovery at low frequency of a new and peculiar radio relic (published in Locatelli et al., 2020b), found at the periphery of the disturbed galaxy cluster A2249. In addition to constraining the magnetic field value at A2249's periphery to be $B > 0.4 \mu\text{G}$, we find that the relic displays the lowest average surface brightness reported to date among its class. This last feature, not only makes the new relic peculiar, but it may provide the evidence for a sub-class of radio relics for which the faint emission can be accounted for without the need for a supra-thermal population of seed electrons already in place before the shock passage, frequently invoked for brighter radio relics (Vazza et al., 2016; Botteon et al., 2020a).

In this Chapter, we model the synchrotron emission simulated/observed either at the periphery of or in between galaxy clusters as produced by relativistic electrons accelerated from the thermal IGM plasma by the Dif-

fusive Shock Acceleration (DSA) mechanism (Bell, 1978a,b; Blandford and Ostriker, 1978; Hoeft and Brüggén, 2007). In particular we will adopt the formalism of Hoeft and Brüggén (2007), hereafter HB07. The authors in their work adapt the Fermi-I-like mechanism of DSA to the case of shocks launched in the ICM environment, to derive the energy distribution of relativistic electrons $n_e(E)$ resulting in the downstream region after the shock passage, extracted from the thermal pool of the ICM. Such distribution is only dependent on: a) the thermodynamic properties of the plasma which is assumed to be ideal and governed by a polytropic equation with adiabatic index $\gamma = 5/3$; b) from the shock strength, parametrized by the Mach number $\mathcal{M} \equiv v_u/c_u$ where v_u and c_u are the shock and sound speeds respectively in the upstream medium (i.e. before the shock). The population of relativistic electrons modeled in such way relies on the assumption of a final continuous energy distribution between the thermal Maxwell-Boltzmann and the (freshly accelerated) relativistic regimes so that $n_E^{\text{th}}(E_{\text{min}}) = n_E^{\text{DSA}}(E_{\text{min}})$ and thus the energy of the coldest accelerated electron (E_{min} , at which resides the bulk of the electrons accelerated by weak shocks) is a fixed multiple of the thermal energy. The total relativistic energy density Φ_e in the downstream region can thus be fully described in terms of a fraction ξ_e of the kinetic energy density Φ_k of the shock. Hence, the fraction ξ_e , referred to as the *electron acceleration efficiency*, is a free parameter which can be constrained (together with the magnetic field strength) by the power-law index of the relativistic energy distribution of the electrons.

The details linking the relativistic component of an arbitrary energy distribution of charges to the synchrotron plus Inverse Compton losses are very well known since decades (Rybicki and Lightman, 1986), especially for power-law distributions such as the one produced by DSA. The spectral and intensity features of the observed emission can thus be directly used to constrain ξ_e together with the magnetic field B responsible for the emission. In particular we refer to the spectral index α (and normalization) of the observed radio emission. We note here that the formalism developed by HB07 models the gas flow in the downstream region as steady and laminar to avoid the formation of turbulence, whose dissipation is not included in the model. The total emission is computed by summing up all contributions of acceleration and losses within the plasma from the shock front to the distance where the electron spectrum is too cool and its radio emission becomes negligible. While considering the above essential formulation of DSA for shocks in the IGM as our benchmark model powering the synchrotron radio emission analysed in this Chapter, we refer the reader to the original work (HB07) for further details on the theory and its analytic treatment.

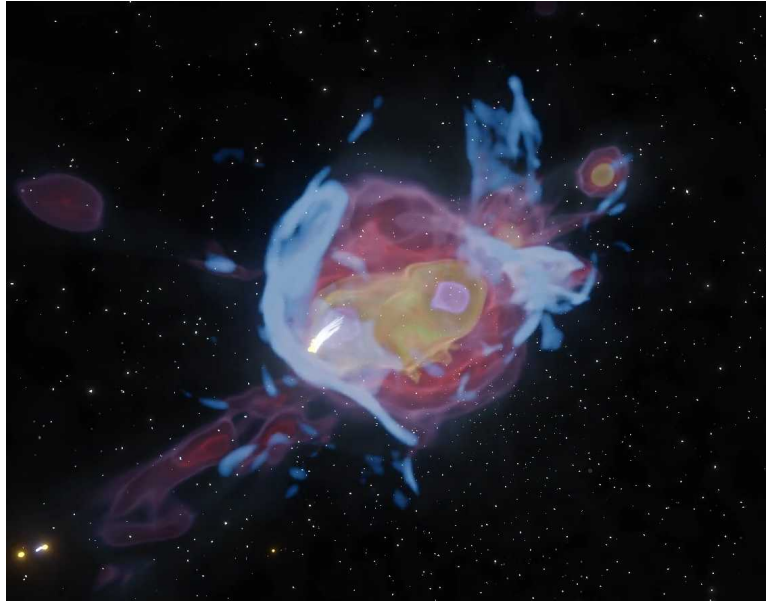


Figure 2.3: Slice from the artwork-rendered cosmological simulation (winner of the NRAO 2020 Image Contest) of radio relics arising from a galaxy cluster merger (the simulation is from Wittor et al., 2020). The X-ray emission from the hot plasma is shown red/yellow colors, while the blue patches highlight the radio diffuse emission forming the \sim Mpc-wide arc-shaped structures known as radio relics. The full video is publicly available at <https://vimeo.com/464248944/3fc17a5b8b>.

2.2 Magnetic fields at cluster outskirts: the ”Cornetto” radio relic in Abell 2249 (Locatelli et al., 2020b)

Abstract The origin of radio relics is usually explained via DSA or re-acceleration of electrons at/from merger shocks in galaxy clusters. The case of acceleration is challenged by the predicted low efficiency of low-Mach number merger shocks, unable to explain the power observed in most radio relics. In this Section we present the discovery of a new giant radio relic around the galaxy cluster Abell 2249 ($z = 0.0838$) using LOFAR. It is special since it has the lowest surface brightness of all known radio relics. We study its radio and X-ray properties combining LOFAR data with uGMRT, JVLA and XMM. This object has a total power of $L_{1.4\text{GHz}} = 4.1 \pm 0.8 \times 10^{23}$ W Hz $^{-1}$ and integrated spectral index $\alpha = 1.15 \pm 0.23$. We infer for this radio relic a lower bound on the magnetisation of $B \geq 0.4 \mu\text{G}$, a shock

Mach number of $\mathcal{M} \approx 3.79$, and a low acceleration efficiency consistent with DSA. This result suggests that a missing population of relics may become visible thanks to the unprecedented sensitivity of the new generation of radio telescopes operating at low frequencies.

2.2.1 Radio relics into context

Radio relics are elongated, arc-shaped diffuse synchrotron sources extended over \sim Mpc, usually found at the periphery of clusters of galaxies with on-going mergers, showing a steep spectrum ($\alpha > 1$, where $S_\nu \propto \nu^{-\alpha}$) with local steepening from the outer region towards the cluster centre (e.g. [van Weeren et al., 2019](#), for a review). Radio relics are strongly polarized at high frequencies, with a polarization fraction around 20 – 30% at 1.4 GHz and \sim 70% at 5 GHz ([van Weeren et al., 2010](#); [Kierdorf et al., 2017](#); [Loi et al., 2017](#)). Several radio relics have also been found to trace the position of shock waves, as detected as discontinuities in the X-ray brightness profiles of the intra-cluster medium (ICM) ([Akamatsu and Kawahara, 2013](#); [Botteon et al., 2018](#)). Merger shock waves are believed to be generated when clusters of galaxies collide, and then propagate along the direction of the merger. Shocks are more easily seen edge-on as projection boosts their surface brightness, and the same observational bias should also apply to radio relics. The kinetic energy dissipated at shocks should be related to the powering of the radio emission, via Diffusive Shock Acceleration (DSA, [Bell 1978a](#); [Jones and Ellison 1991](#)), as originally proposed by [Ensslin et al. \(1998\)](#). However, the Mach numbers that are independently inferred from discontinuities observed in X-rays are generally too weak ($\mathcal{M} \sim 2$) to account for the required electron acceleration efficiency by DSA in relics (e.g. [Botteon et al., 2020a](#), hereafter B+20). Moreover, shock waves in the intracluster medium should also accelerate protons that would create γ -ray emission in the collision with the thermal protons of the ICM. The level of the emission clearly depends on the magnetic field, CRs and ICM energy densities, however these γ -rays have not been detected ([Ackermann et al., 2016](#)) even for the more massive objects, which translates into limits on the maximum acceleration efficiency of protons in structure formation shocks ($< 10^{-3}$, [Vazza et al. 2016](#)). This conundrum can be by-passed when invoking a pre-existing population of mildly non-thermal electrons that get re-accelerated by the shocks ([Pinzke et al., 2013](#); [Kang and Ryu, 2015](#); [Markevitch et al., 2005](#)). In a few cases, Active Galactic Nuclei (AGN) could have supplied the relativistic electrons in the upstream region of the shock that creates the relic ([Bonafede et al., 2014](#); [van Weeren et al., 2017](#); [Stuardi et al., 2019](#)). Both acceleration and

reacceleration processes operate in the ICM and should contribute to the population of radio relics. We will adopt a flat- Λ CDM cosmology with $H_0 = 69.6 \text{ km s}^{-1} \text{ Mpc}^{-1}$ and $\Omega_M = 0.286$ throughout this Section.

2.2.2 General properties of Abell 2249

In this work we present the discovery of a giant radio relic found at the periphery of the galaxy cluster Abell 2249 (hereafter A2249; RA 257.44080, DEC 34.45566). It has been studied in detail at various wavelengths by a number of authors: the cluster mean redshift is $z = 0.0838$ (Laganá et al., 2019; Lopes et al., 2018; Bulbul et al., 2016); the velocity dispersion of its constituent galaxies is between $\sigma_{\text{vel}} = 894 \pm 50$ (Lopes et al., 2018) and $976 \pm 38 \text{ km s}^{-1}$ (Oh et al., 2018). Laganá et al. 2019 provided detailed XMM-Newton maps of temperature (peaking in the 4-7 keV energy band), pseudo-pressure, pseudo-entropy and metallicity in the central region, within the first $\sim 400 \text{ kpc}$ from the cluster centre. They classified A2249 as a non-cool-core (NCC) disturbed cluster. Moreover, a Dressler & Shectman three-dimensional test of the galaxy redshifts provides further evidence that the cluster is disturbed (Lopes et al., 2018). The radius and mass of the cluster are respectively $R_{500} = 1.1^{+0.3}_{-0.1} \text{ Mpc}$, $M_{500} = 3.73^{+0.18}_{-0.19} \times 10^{14} M_{\odot}$, derived from Planck data (Planck Collaboration et al., 2016a). At larger radii $R_{200} = 2.2 \pm 0.1 \text{ Mpc}$ and $M_{200} = 12.7 \pm 1.5 \times 10^{14} M_{\odot}$ (Lopes et al., 2018; Oh et al., 2018).

2.2.3 Radio observations

The low frequency observations of the A2249 field was carried out with LOFAR. The LOFAR HBA (120 – 168MHz) observation was carried out during Cycle 9 (Proposal Id:LC9_020). The centre of the pointing was not at the cluster centre, but at coordinates 17:01:13 +33:20:15 (RA, DEC), at a distance of 2.1 degrees. The on-source time is 8 hr with two scans of 10 min each on the flux calibrator 3C295. A first calibration and imaging run was performed using the LOFAR data reduction pipeline (v2.2³) involving both direction-independent (de Gasperin et al., 2019) and -dependent calibration of the data (Shimwell et al., 2017). Exploiting the sky models derived from the pipeline, we subtracted from the uv-data all sources outside a $1.9^{\circ} \times 1.9^{\circ}$ region centred on the relic. This was done using the PYthon Blob Detector and Source Finder (pybdsf; Mohan and Rafferty 2015). The resulting data was then self-calibrated (phase only) through nine iteration steps and then imaged using WSClean v2.4 (Offringa et al., 2014).

³<https://github.com/mhardcastle/ddf-pipeline>

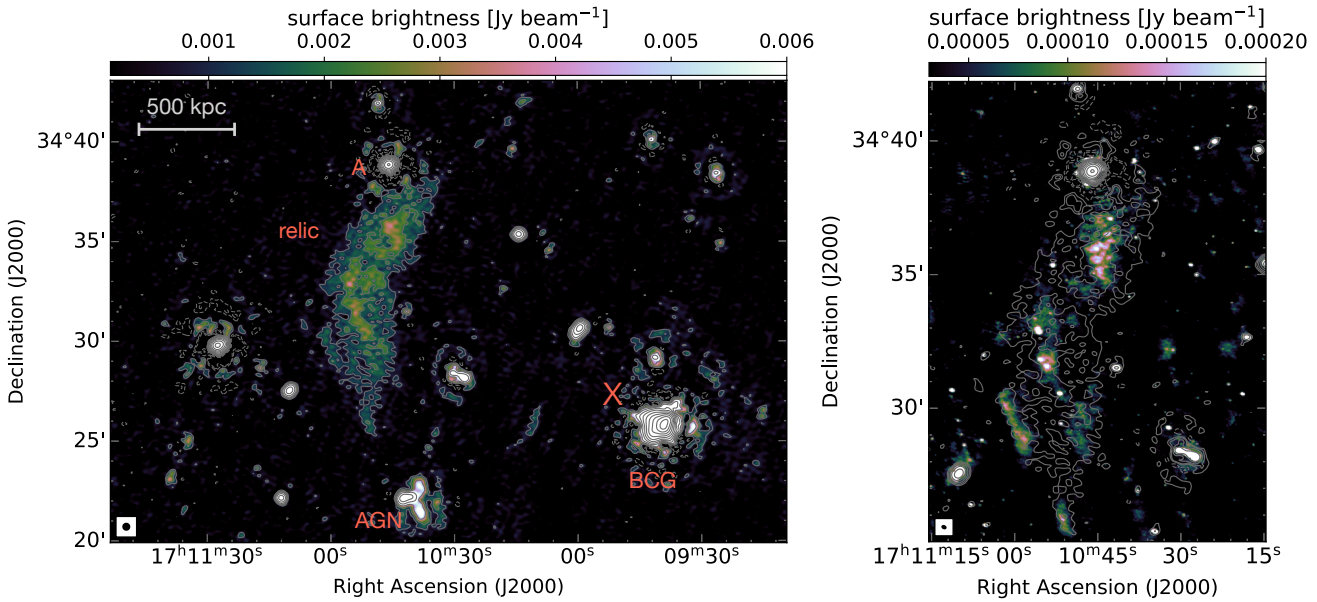


Figure 2.4: *Left*: LOFAR low resolution ($20''$) image of Abell 2249, showing a spectacular large-scale radio relic. The red cross marks the cluster center. Contour levels are drawn at $[1, 2, 4, 8, \dots] \times 3\sigma_{\text{rms}}$ and are from the LOFAR image. Negative $-3\sigma_{\text{rms}}$ contours are shown with dotted lines *Right*: uGMRT high resolution ($8'' \times 6''$) image of the relic, overlaid with LOFAR contours, revealing filamentary substructures.

We produced images at $6''$ and $20''$ (Fig. 2.4, left panel) resolution using a Briggs weighting scheme with robust -0.5 . The image at higher (lower) resolution has a rms noise floor of $230(350) \mu\text{Jybeam}^{-1}$. We determined and applied a correction factor (van Weeren et al., 2016; Hardcastle et al., 2016, see also) to match the LOFAR HBA flux densities of point-like sources with the ones derived from the TIFR GMRT Sky Survey (TGSS; Intema et al. 2017). We assume flux density uncertainties of 20%, similar to the LOFAR Two-meter Sky Survey images (Shimwell et al., 2019).

We also observed the cluster with the upgraded Giant Meter Radio Telescope (uGMRT), in Band-4 covering a frequency range of 550-950 MHz (proposal DDT-C100). The data were flagged and calibrated using CASA. We then ran several rounds of direction-dependent self-calibration using the LOFAR DDF-pipeline (see above). The image reaches a noise level of $16 \mu\text{Jybeam}^{-1}$ at 700 MHz.

We have also analysed two short snapshot observations at 1.46 GHz from the VLA archive. About 8 min (four 2-min scans well spaced in time) and 25 min (single scan) in C and D configuration were available (project codes AS220 and AG294, respectively). We obtained a combined image of the intersecting part of the bands after standard calibration of the two individual datasets. The pointing was set on the brightest central galaxy (BCG), which is about $15'$ off the relic position. This highly affected the local sensitivity. The combined C+D image (Fig. 2.5) allowed a resolution of about $30''$ and presents a number of separate patches of diffuse emission with peaks just above the local 3σ in the region of the relic (highlighted by the green circles in Fig. 2.5), with roughly the same morphology of the uGMRT image. The image clearly shows signal to noise degradation with increasing distance from the BCG, due to the relatively small primary beam size of the archival VLA observations. The Cornetto relic is located at the boundaries of the PB, however, flux enhancement is also evident when comparing it with regions at different azimuthal angles but same distance from the phase center (not shown).

2.2.4 X-ray: XMM observation

A2249 (also known under the name PSZ2 G057.61+34.93) has been observed as part of the XMM Heritage Cluster Project⁴ (The CHEX-MATE Collab-

⁴<http://xmm-heritage.oas.inaf.it>

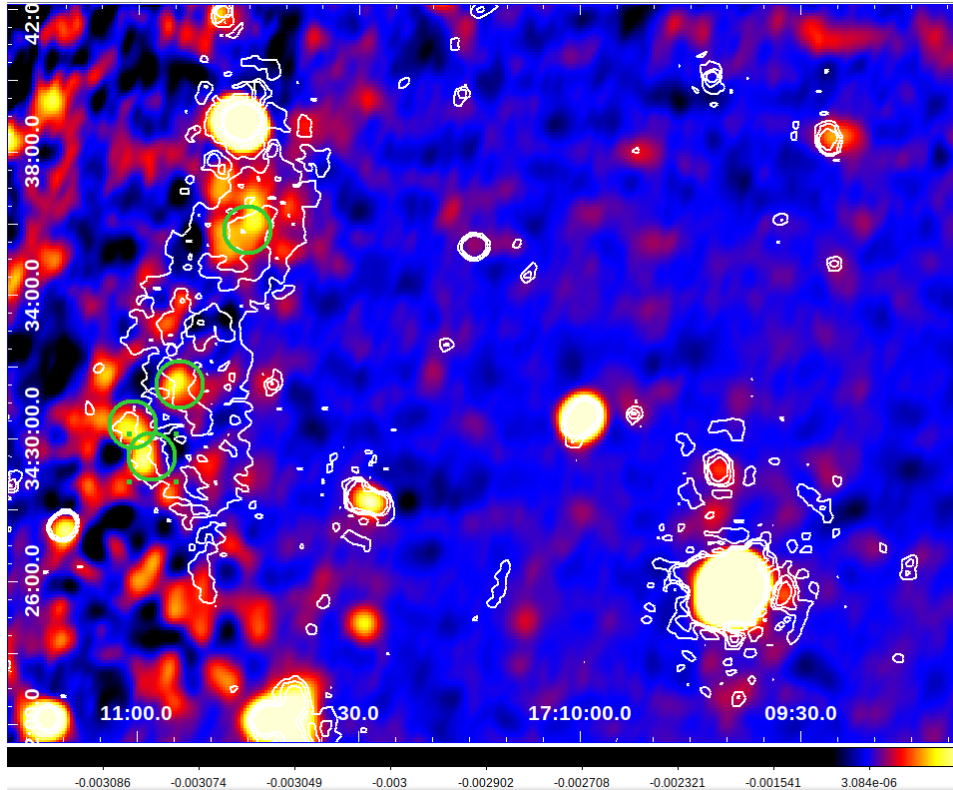


Figure 2.5: VLA (C+D configuration) archival observation ($300''$) image of Abell 2249. White contour levels are drawn at $[1, 2, 4, 8, \dots] \times 3\sigma_{\text{rms}}$ and are from the LOFAR image. The green circles highlight emission above $3\sigma_{\text{rms}}$ of the local VLA rms background level (σ_{rms} is evaluated at the same radial distance from the phase center to account for PB corrections).

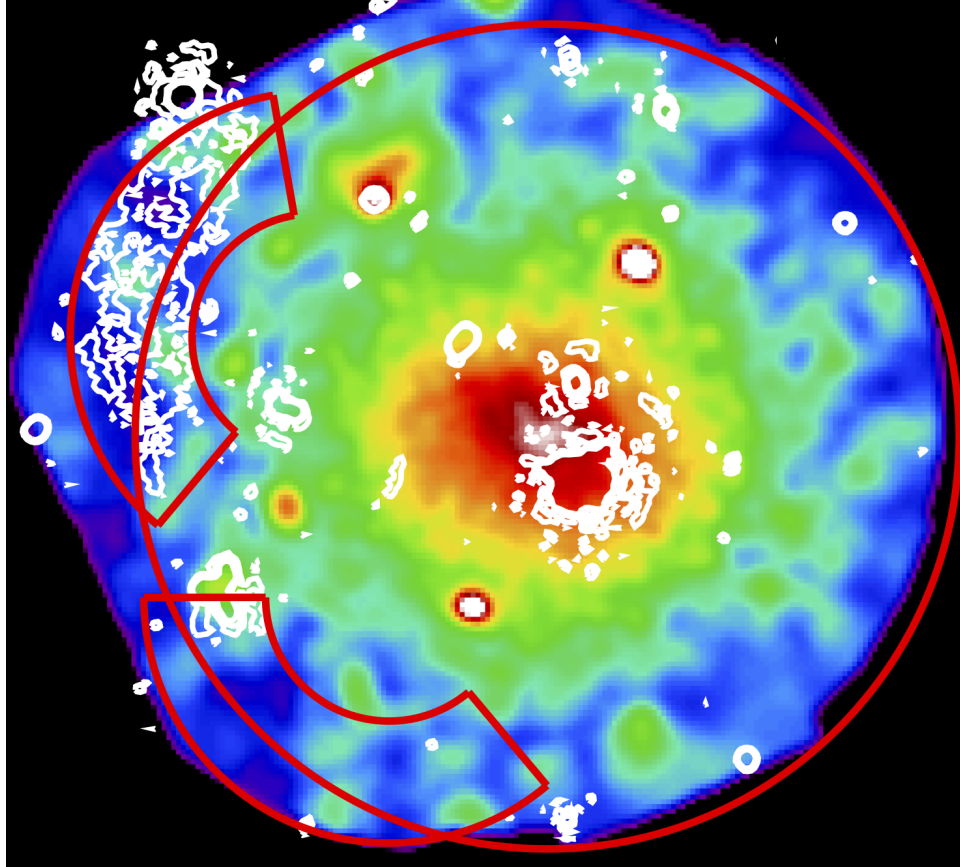


Figure 2.6: Background subtracted, exposure corrected and adaptively smoothed XMM image in the 0.7-1.2 keV band of A2249. The 144 MHz contours at $3, 6, 10\sigma$ of the low resolution ($20''$) LOFAR radio emission are overlaid in white. A circle of radius $14'$ is drawn to guide the eye for the two sectors used in the spectral analysis described in the text: one encompassing the relic radio emission and one test region of the same extension at the same radial distance from the cluster centre.

F_ν mJy	L_ν W Hz ⁻¹	$F_{700\text{ MHz}}$ mJy	α	$\Delta\Omega$ arcmin ²	R_{proj} Mpc	LAS arcmin	LLS Mpc
370 ± 70	$5.9 \pm 1.2 \times 10^{24}$	60 ± 12	1.15 ± 0.23	28.46	1.40	13.2	1.3

Table 2.1: Properties of the Cornetto relic in Abell 2249 ($z = 0.0838$) extracted from the LOFAR image at 144 MHz (if not stated otherwise): flux density F_ν ; luminosity L_ν ; flux density at 700 MHz (uGMRT) $F_{700\text{ MHz}}$; spectral index between 144 and 700 MHz α , solid angle $\Delta\Omega$; projected radial distance from cluster center R_{proj} ; largest angular scale LAS; largest linear scale LLS.

oration et al., 2020), a large and unbiased sample of 118 clusters, detected with a high signal-to-noise ratio in the Second Planck SZ Catalogue. We reduced the data with SAS v 16.1. The observation with OBSID 0827010501 has a total clean exposure time of 20.4 ks with MOS1, 20.7 with MOS2 and 16.1 with pn after filtering for soft proton flares (81% of the total time for MOS and 93% for the pn). We estimated the amount of residual soft protons following the procedure described in Cova et al. (2019) and found it to be negligible. For a full description of data reduction, image production and spectral extraction we refer to Ghirardini et al. (2019). In Fig. 2.6 we show the XMM image in the 0.7-1.2 keV band with the overlay of the radio contours at 144 MHz with 20'' resolution and the regions used for the spectral analysis. Given that the emission of the cluster is filling the entire field of view of XMM for the estimate of the sky background components in a similar way to Snowden et al. (2008) we used a spectrum from the ROSAT All-Sky Survey extracted from an annulus between 0.5 and 1 degree from the source. We fixed the Galactic N_{H} to $2.38 \times 10^{20} \text{ cm}^{-2}$ at HI LAB value (Kalberla et al., 2005) given the negligible difference with the value ($2.5 \times 10^{22} \text{ cm}^{-2}$) which estimates the possible contribution of molecular hydrogen (Willingale et al., 2013).

2.2.5 Results

Morphology The extended diffuse emission at 144 MHz (Fig. 2.4) is arc-shaped and oriented perpendicular to the radial direction from the cluster centre, in the North-East-East sector of A2249, spanning an angular radial range [11.0; 17.0]' from the cluster centre. The relic width is maximal at its the mean azimuthal direction and is minimal at the azimuthal ends of the diffuse emission, giving the radio relic a shape very similar to a crescent moon or the popular Italian sweet bun named "cornetto". The brightest

part of the relic at 144 MHz is found at an angular radial distance of $\simeq 14.7'$, that is a linear distance of 1.40 Mpc at the redshift of A2249. The relic's largest angular scale (LAS) is $\simeq 13.2'$, corresponding to a physical size of 1.3 Mpc at the redshift of the cluster. The northern end of the diffuse emission coincides with a bright unresolved radio source (A, Fig. 2.4 left panel), of $400 \text{ mJy beam}^{-1}$ at 144 MHz. The BCG of A2249 is visible in the south-west direction. Deconvolution artefacts remained around the bright sources A and BCG. The relic also shows elongated patches of emission of a few arcminutes, in analogy with the filamentary structures described in other radio relics (Owen et al., 2014; Pearce et al., 2017; Rajpurohit et al., 2018), whose origin is still unclear. The image at 700 MHz also shows diffuse emission at the relic position above 3σ , with a similar morphology as at lower frequency (Fig. 2.4 right panel).

Radio spectrum & luminosity The flux density and luminosity of the Cornetto relic at 144 MHz are $F_{144 \text{ MHz}} = 370 \pm 70 \text{ mJy}$ and $L_{144 \text{ MHz}} = 5.9 \pm 1.2 \times 10^{24} \text{ W Hz}^{-1}$, respectively. The integrated spectral index, calculated from the ratio of the total flux densities at 144 and 700 MHz in the relic region (determined at 144 MHz) is $\alpha = 1.15 \pm 0.23$. The observed quantities are summarized in Tab. 2.1.

Assuming $\alpha = 1.15$ to be constant we extrapolated the luminosity at 1.4 GHz to be $L_{1.4 \text{ GHz}} = 4.1 \pm 0.8 \times 10^{23} \text{ W Hz}^{-1}$. The Cornetto relic (red star, Fig. 2.7) is found to lie below the observed scaling relation between the radio power at 1.4 GHz and the largest linear size (LLS) of a sample of known radio relics presented in Nuza et al. (2017), extracted from the NRAO VLA Sky Survey (NVSS, Condon et al. 1998). From archival VLA images we find three different regions across the relic with matching 3σ contours between 144 MHz and 1.4 GHz. We computed the integrated power for these three regions and plotted them in Fig. 2.7 (red circles). The correlation in Fig. 2.7 has already been shown to be determined largely by the NVSS sensitivity (Nuza et al., 2017). The LOFAR observations presented here seem to open the window to a population of faint and diffuse relics that have not been seen to date.

X-ray properties at the position of the relic We extracted XMM MOS and pn spectra from an angular sector which covers the relic radio emission as shown in Fig. 2.6. The region extends beyond R_{500} and therefore the thermal emission is below the background. The temperature obtained is prone to large systematic errors and we therefore rely on the value obtained

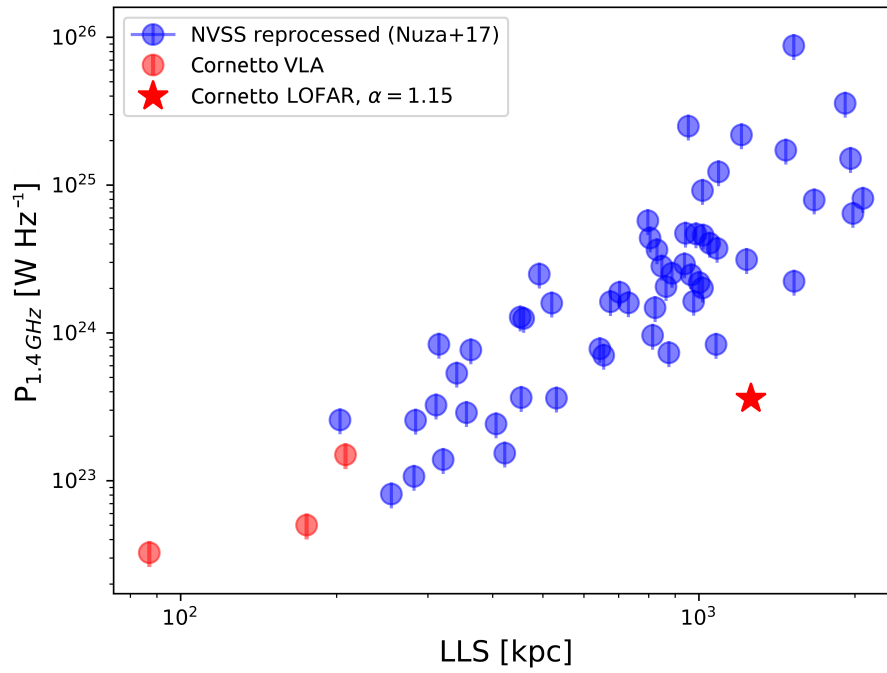


Figure 2.7: The luminosity at 1.4 GHz is plotted against the LLS for the radio relics detected in the NVSS (Nuza et al., 2017). The red star shows the power of the Cornetto relic extrapolated to 1.4 GHz. The red circles correspond to fluxes extracted from the green regions in Fig. 2.5.

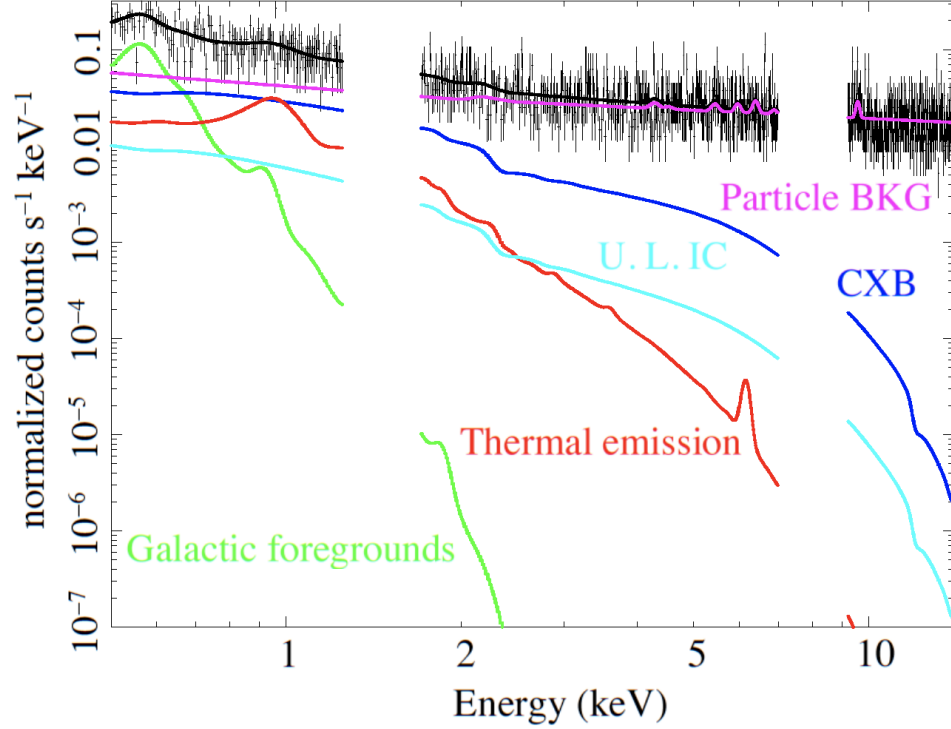


Figure 2.8: XMM pn spectrum extracted from the region of the relic radio emission. The magenta line shows the instrumental background, the green one the galactic foregrounds, the blue one the Cosmic X-ray Background, the red line the ICM thermal emission and the cyan one the 90% upper limit on the IC power law.

within the full annulus of $kT = 3.0 \pm 1.3$ keV together with an electron density $n_e = 6.4 \pm 1.5 \times 10^{-4} \text{ cm}^{-3}$. Assuming that temperature we modeled the expected IC emission as a power law with fixed photon index of 2.15 as derived from the radio spectral index and extrapolated a 90% upper limit of $1.0 \times 10^{-13} \text{ erg cm}^{-2} \text{ s}^{-1}$ in the 20-80 keV range. The X-ray spectrum in the relic region and its modeling is shown in Fig. 2.8. It is equivalent to the spectrum extracted from a region at the same radial distance from the cluster but avoiding the relic emission (see Fig. 2.6), confirming that any IC emission is clearly covered by the cluster thermal emission plus particle background.

2.2.6 Modelling of physical properties

Based on our observations we study the origin of the relic in A2249 and infer limits on its magnetic field.

Diffusive Shock Acceleration Assuming DSA, the power emitted by the Cornetto relic can be related to its shock properties (e.g. HB07; B+20):

$$L_{\nu, \text{obs}} = C \cdot \frac{A}{\text{Mpc}^2} \cdot \frac{n_{e,d}}{10^{-4} \text{ cm}^{-3}} \cdot \xi_e \cdot \frac{T_{e,d}^{3/2}}{\nu^{\alpha/2}} \frac{B^{1+\frac{\alpha}{2}}}{B^2 + B_{\text{CMB}}^2(z)}, \quad (2.1)$$

where A is the surface area of the shock spherical slab, calculated as $\sim LLS^2$ (we assumed the spherical slab to be as deep along the LoS as extended in the sky); $n_{e,d}$ is the downstream electron density; ξ_e is the (yet unknown) fixed fraction of the kinetic energy flux Φ_e/Φ_k injected at the shock front into suprathermal electrons; $T_{e,d}$ is the downstream electron temperature and B_{CMB} is the equivalent field of the Cosmic Microwave Background evaluated at the redshift of A2249. The normalisation C is $6.4 \times 10^{34} \frac{\text{erg}}{\text{sHz}}$ when $T_{e,d}$ in units of $[7 \text{ keV } k_B^{-1}]$, ν in units of 1.4 GHz and B in $[\mu\text{G}]$.

Considering the values in Tab. 2.1, an integrated spectral index $\alpha = 1.15$ (holding a Mach number $\mathcal{M} = \sqrt{(\alpha+1)/(\alpha-1)} = 3.79$) and the quantities derived from the XMM-Newton observations $k_B T_e \simeq 3.0 \pm 1.3 \text{ keV}$ and $n_{e,d} = 6.4 \pm 1.5 \times 10^{-4} \text{ cm}^{-3}$, we can constrain the (B, ξ_e) parameter space to reproduce $F_{144\text{MHz}}$ (DSA curves in Fig. 2.9). For completeness, we also consider the formulation of the model as found in B+20, which enforces the relativistic invariance in the HB07 model, which is particularly relevant for weak shocks. We obtain a magnetic field of $B = 1.2 \mu\text{G}$ for $\xi_e = 10^{-3}$ and $B = 6.0 \mu\text{G}$ for $\xi_e = 10^{-4}$. The values for ξ_e agree with models for DSA from shocks with Mach numbers $\mathcal{M} = 3.5 - 4.0$ (Kang and Ryu, 2015). Larger efficiencies are hard to reconcile with DSA and (in other objects) are used to argue for the existence of a pre-existing electron population that may have been re-accelerated by an earlier episode of shock acceleration. Re-acceleration has been invoked for most radio relics (all observed at frequencies $> 600 \text{ MHz}$) for which an underlying shock wave has been detected in X-rays at their location, with the exception is the radio relic in the El Gordo galaxy cluster (B+20). Instead, the efficiency required to power the Cornetto relic can be explained by DSA electrons from the thermal pool, by \sim a few μG magnetic field.

Equipartition Synchrotron radiation provides information on both the electron’s energy distribution and the magnetic field strength, B , in the medium. A simplistic assumption to disentangle the contribution of relativistic cosmic-rays (CRs) from magnetic fields is to assume equipartition between their energy densities in the plasma $\epsilon_{CR} = \epsilon_B$ (e.g. [Brunetti et al., 1997](#); [Beck and Krause, 2005](#)). In this case, the total energy density of magnetic fields and of CRs $\epsilon_B + \epsilon_{CR}$ also approaches a minimum value. Classical equipartition formulae use parameters of the spectral energy distribution of electrons not affected by energy losses. In the case of radio relics instead, the spectrum of downstream emitting electrons results from the combination injection, transport and energy losses. We thus derive equipartition conditions assuming that the magnetic field in radio relics gets the same energy density of downstream particles:

$$\frac{1}{2}\rho_u \frac{v_u^3}{v_d} \xi_e (1 + k) = \frac{B^2}{8\pi} \quad (2.2)$$

where k is the ratio of energy budget between p and e , ρ and v are the gas density and shock velocity computed for the media respectively upstream ($_u$) and downstream ($_d$) of the shock front. The jump conditions have been derived from the shock Mach number $\mathcal{M} = 3.79$. With this approach ξ_e is directly comparable with the values derived from DSA.

The results for B , k and ξ_e are degenerate, however the equipartition assumption alone constraints the parameter space between the curves for $k = 0$ (indicating a plasma where the energy budget is only given by e) and $B \ll 10\mu\text{G}$ resulting from $\xi_e(1 + k) \ll 1$. Combined with equipartition argument the efficiency selects the value of k .

Inverse Compton scattering Based on the observed radio flux and assuming a power-law distribution of relativistic electrons, we can estimate the hard X-ray emission from Inverse Compton (IC) scatter from the same electron population responsible for the observed radio emission (e.g. [Govoni and Feretti, 2004](#)). Then we can compare this to recent upper limits obtained using XMM-Newton observations in the 0.1-12 keV band. We quote the flux estimates extrapolated in the 20-80 keV band for ease of comparison with previous estimates (e.g. [Cova et al., 2019](#)). The IC flux 90% upper limit $F_{IC} \leq 1 \cdot 10^{-13} \text{ erg cm}^{-2} \text{ s}^{-1}$ extrapolated in the 20 – 80keV band sets a lower limit on $B > 0.4\mu\text{G}$. A magnetic field strength of $B_{\text{low}} = 0.6 \mu\text{G}$ (as suggested above assuming $\xi_e = 10^{-3}$) or lower would result into IC emission larger than the $F_{IC} \approx 3.17 \cdot 10^{-14} \text{ erg cm}^{-2} \text{ s}^{-1}$ upper limit derived for A523

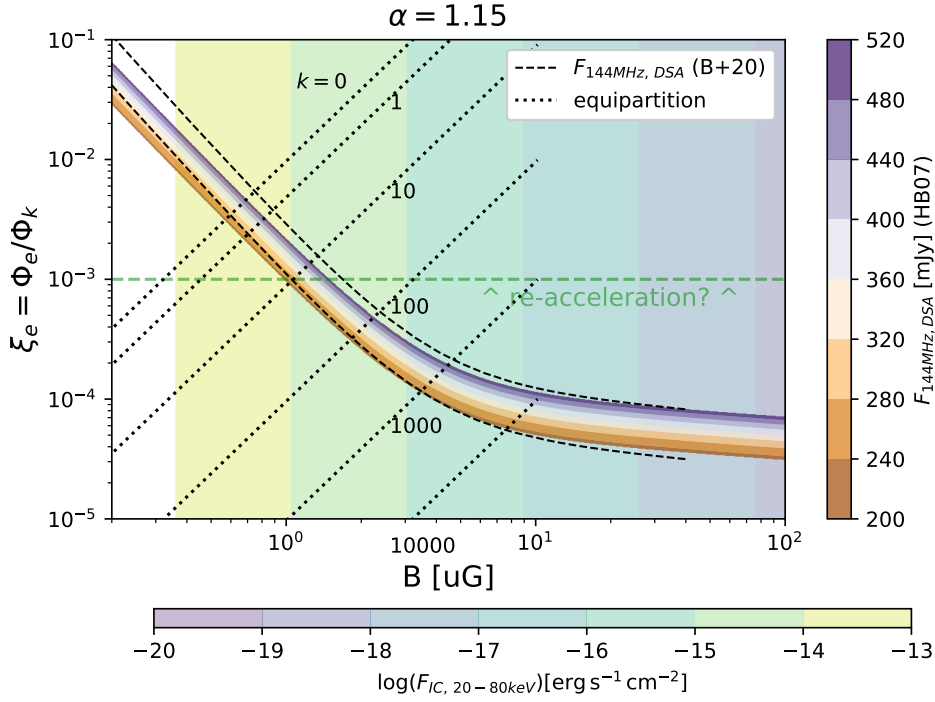


Figure 2.9: The (B, ξ_e) parameter space assuming $\alpha = 1.15$. The curves show the points that reproduce the $F_{144\text{MHz}}$ within 2σ uncertainty assuming DSA using HB07 (orange-white-purple) or B+20 (dashed black) formalism. The green-violet shaded background shows the inverse Compton fluxes expected in the 20 – 80keV band. The dotted lines show the values obtained assuming equipartition for different values of k .

by [Cova et al. \(2019\)](#). For comparison, $\alpha = 1.15$ and $B = 6.0 \mu\text{G}$ (implying $\xi_e = 10^{-4}$ for DSA) produces $F_{\text{IC}} \approx 5 \cdot 10^{-15} \text{ erg cm}^{-2} \text{ s}^{-1}$, i.e. about one order of magnitudes below present- day upper limits. The lower limit from IC combined with the limit $B \ll 10 \mu\text{G}$ from energy arguments implies efficiencies $\xi_e \in [5 \cdot 10^{-5} - 10^{-2}]$. Larger values would violate equipartition.

2.2.7 Section summary

In this Section we presented the discovery of extended, diffuse radio relic in A2249, found at low frequencies (120-168 MHz) with LOFAR. We have also observed the new relic (called Cornetto relic) at 700 MHz with the uGMRT and found patches of emission in coincidence of the brightest parts of the relic also in VLA archival data at 1.4 GHz. The magnetic field at the relic is estimated to be $B > 0.4 \mu\text{G}$, depending on model assumptions and the electron acceleration efficiency $\xi_e \leq 10^{-2}$ of the putative merger shock. The limits have been set from the absence of Inverse Compton emission in the [0.1 – 12] keV energy band.

The Cornetto relic is among the largest relics discovered to-date (13.2', corresponding to 1.26 Mpc) as well as the faintest one with such extent, once extrapolated at 1.4 GHz, lying at about a factor ~ 10 below the observed scaling relation between the radio power at 1.4 GHz and the LLS of radio relics.

Its low luminosity is well explained by DSA for the inferred plasma and shock parameters, unlike most other radio relics that require a higher electron acceleration efficiency and invoke past acceleration events acting on the seed electron population already present in the ICM thermal pool.

This discovery, only made possible by the unprecedented sensitivity of LOFAR to large angular scales at low frequencies, may hint to a population of low-power, faint and diffuse radio relics, for which re-acceleration has not taken place (or not yet) or is inefficient with respect to standard DSA. This can be explored by the new generation low-frequency arrays (e.g. LOFAR, SKA-low).

2.3 Upper limits to the magnetic field into cosmological filaments from LOFAR

Abstract Strong accretion shocks are expected to illuminate the warm-hot inter-galactic medium encompassed by the filaments of the cosmic web, through synchrotron radio emission. Given their high sensitivity, low-frequency (large) radio facilities may already be able to detect signatures of this extended radio emission from the region in between close pairs of massive galaxy clusters. In this work we exploit the non-detection of such diffuse emission by deep observations of two pairs of relatively close ($\simeq 10$ Mpc) and massive ($M_{500} \geq 10^{14} M_{\odot}$) galaxy clusters using the LOw-Frequency ARray (LOFAR). By combining the results from the two putative inter-cluster filaments, we derive new independent constraints on the median strength of inter-galactic magnetic fields: $B_{\text{Mpc}} < 2.5 \times 10^2$ nG (95% CL) assuming that strong shocks $\mathcal{M} > 4$ accelerate relativistic electrons with an efficiency $\xi_e = 0.01$. Based on cosmological simulations and assuming a primordial origin of the B-fields, these estimates can be used to limit the amplitude of primordial seed magnetic fields: $B_0 \leq 10$ nG. We advise the observation of similar cluster pairs as a powerful tool to set tight constraints on the amplitude of extragalactic magnetic fields.

2.3.1 Context of the experiment

On the largest scales of the Universe (≥ 10 Mpc), galaxy groups and clusters are connected by elongated distributions of galaxies called filaments and sheets which are believed to be also permeated by diffuse gas, and possibly by magnetic fields. Until now, a straightforward and direct detection of inter-galactic medium (IGM) and magnetic field (IGMF) has been prevented by the very low density of the plasma ($n_{\text{IGM}} \leq 10^{-4} \text{ cm}^{-3}$) and its relatively low temperature ($T_{\text{IGM}} \leq 10^7$ K). However, increasing evidence (Nicastro et al., 2018; Macquart et al., 2020) is recently confirming the long-lived expectations for the warm-hot gas phase of the IGM (WHIM, with $T_{\text{WHIM}} \sim 10^5 - 10^7$, $n_{\text{WHIM}} \sim 10^{-5} - 10^{-4}$) to contain up to half of the baryon content at low redshift (Cen and Ostriker, 1999; Davé et al., 2001).

Accretion shocks are believed to reside along and within the filaments of the cosmic web as well as at the outskirts of galaxy clusters. These shocks are expected to amplify magnetic fields and to accelerate particles up to relativistic energies (Ryu et al., 2008). Their presence might then enable the detection of the WHIM through its synchrotron emission signature at radio wavelengths, and, indeed, the direct observation of the tip of the ice-

berg of this diffuse emission has already been discovered at radio frequencies (Govoni et al., 2019; Botteon et al., 2020b). In these few cases the plasma conditions are still hotter and denser than what expected for the typical WHIM and the detected emission lays within the clusters virial radii. Further investigation in this direction will be supported in the near future by the upcoming radio facilities (ngVLA, MeerKAT, SKA-mid) and especially at very low frequencies (LOFAR, MWA, SKA-low). In fact, the low frequency emission should be brighter up to further out the clusters virial radii thanks to the expected spectral behaviour as $S_\nu \propto \nu^{-1}$ with respect to frequency ν (Vazza et al., 2015b). A way to overcome sensitivity limitations is to quantify the Faraday effect induced by magneto-ionized plasma along the line of sight to a polarized background radio source and build a tomography of the WHIM by means of a grid of background sources (see Akahori et al. 2014; Vacca et al. 2016). A thorough exploitation of this method currently suffers from the lack of large and dense grids of polarized sources, however it is expected to provide important results thanks to the upcoming radio facilities (Locatelli et al., 2018). Complementary, recent upper limits on the IGMF intensity and scale have been derived from the cross-correlation of diffuse radio synchrotron emission with the underlying galaxy distribution (Vernstrom et al., 2017; Brown et al., 2017) or by cross-correlating the difference in rotation measures of physically related pairs of extended radio galaxies, compared with the one derived from randomly paired and close lobes (Vernstrom et al., 2019; O’Sullivan et al., 2020; Stuardi et al., 2020).

Why is it important to assess the IGMF properties in the cosmic web at late times? The magnetic fields in galaxies and galaxy clusters, commonly observed today, arise from strong amplification from efficient MHD small-scale mechanisms (Ryu et al., 2008) which are responsible of a fast saturation of the fields, thus erasing information on their initial conditions, and in turn of their origin (Beresnyak and Miniati, 2016). Instead, in the WHIM environment, the amplification of primordial magnetic fields is found in simulations to be mainly driven by the field compression as its lines freeze into the plasma plus the contribution of small scale shocks. These mechanisms do not bring the field to saturation and provide a tool of assessing the history and original conditions of the field by means of the level of magnetisation observed today (Vazza et al., 2014, 2015b; Donnert et al., 2018). For the above reasons it is crucial to constrain the magnetic field in the WHIM in order to determine the original scenario for the large scale magnetic field origin and evolution in the Universe.

Cosmological MHD simulations predict the intensity of the IGMF at low redshift to range within 1 and 100 nG (Dolag et al., 1999; Brüggén et al.,

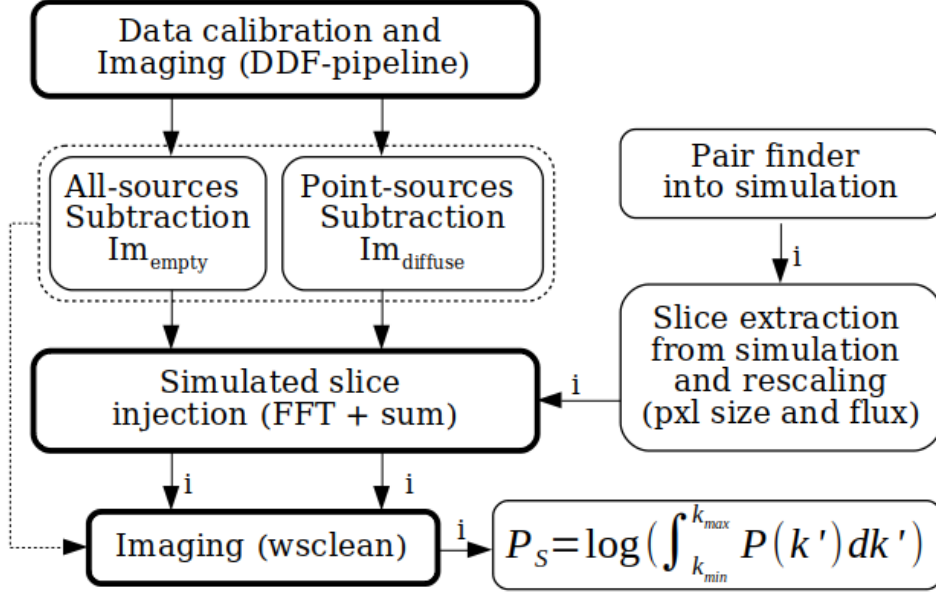


Figure 2.10: Diagram of the method outlined in Sec. 2.3.2. Thick boxes highlight the most computationally expensive steps. Links labelled with the letter "i" are computed iteratively over the simulated pairs.

2005; Vazza et al., 2017). In this paper we introduce a novel method for a robust inference of an upper limit on the initial B_0 and current B values of the IGMF within the large-scale filaments of the cosmic web. The method explores the amount of diffuse emission detected at 144 MHz with LOFAR along the direction connecting pairs of galaxy clusters. We outline the method used to explore the upper limits on the IGMF into cosmological filaments in the following Sec. 2.3.2; we show its results in Sec. 2.3.3 and discuss their assumptions and implications in Sec. 2.3.4; we draw our conclusions in Sec. 2.3.5. We note that throughout this section we assumed a Λ CDM cosmological model, with baryonic and dark matter and dark energy density parameters $\Omega_{\text{BM}} = 0.0455$, $\Omega_{\text{DM}} = 0.2265$, $\Omega_{\Lambda} = 0.728$ respectively and a Hubble constant $H_0 = 70.2 \text{ km s}^{-1} \text{ Mpc}^{-1}$.

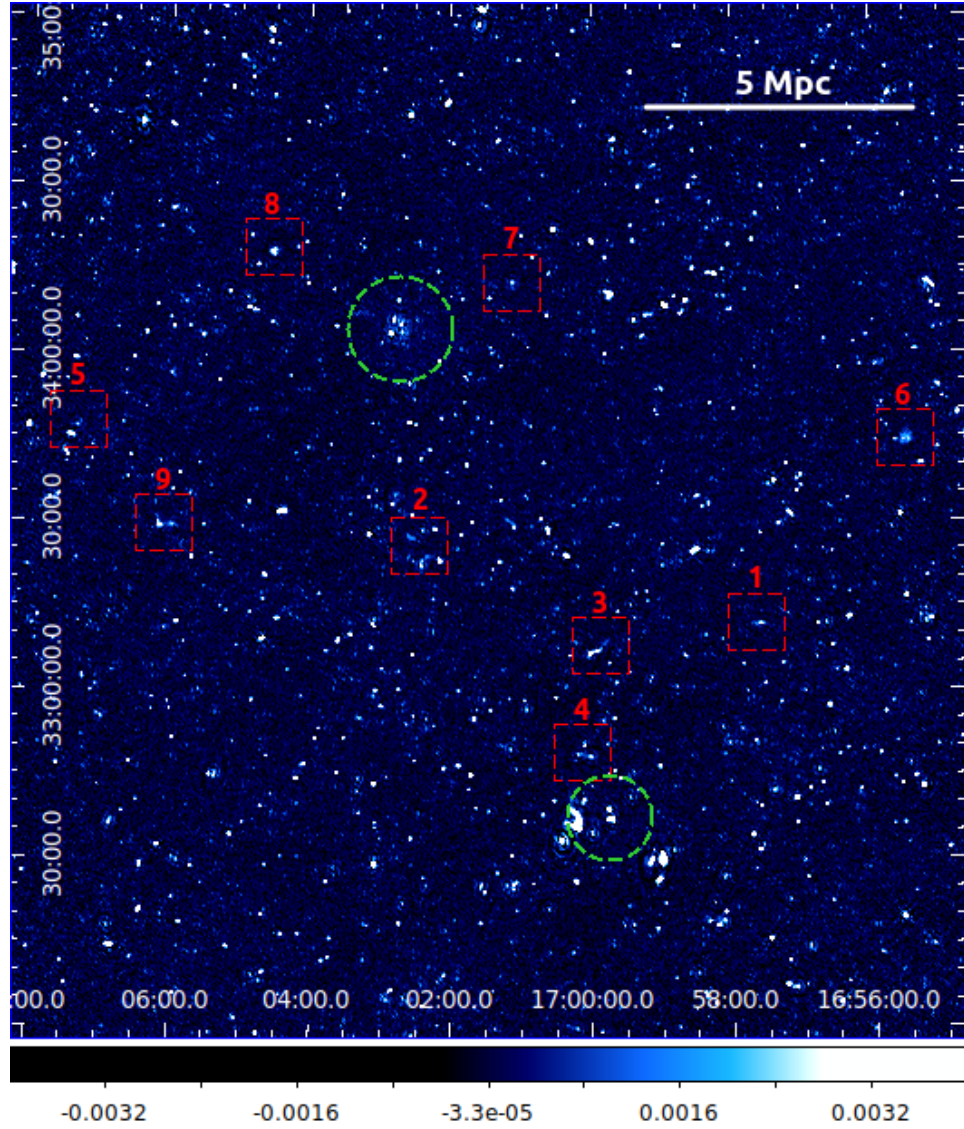


Figure 2.11: LOFAR low-resolution ($20''$) image at 144 MHz of the cluster pair RXC-J1659-J1702. The dashed circles are centered on the clusters and have corresponding radius R_{500} . The red dashed boxes have been zoomed in Fig. 2.19. We indicated the 5 Mpc unit at the redshift of the pairs $z = 0.10$. The color bar is in units of Jy beam^{-1} .

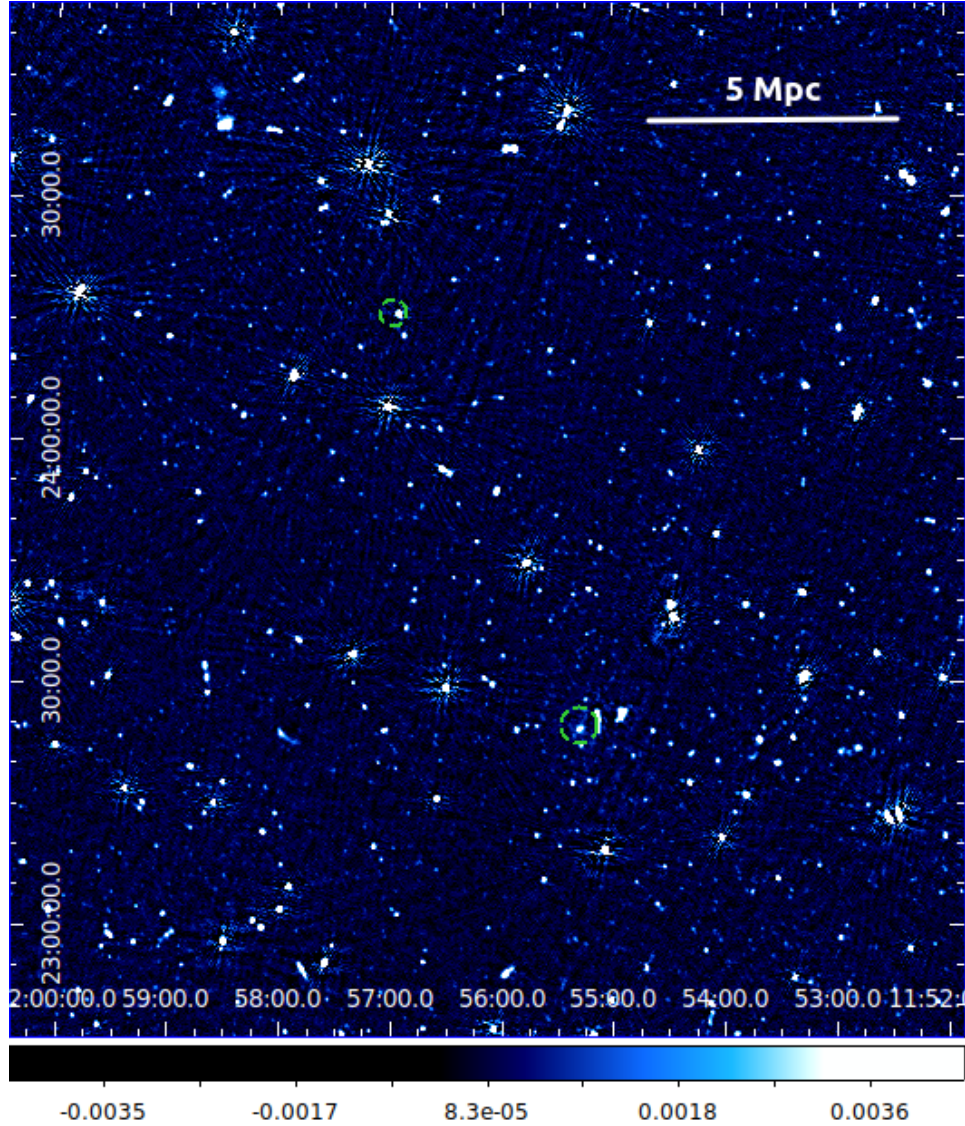


Figure 2.12: LOFAR low-resolution ($20''$) image at 144 MHz of the cluster pairs RXC_J1155-J1156. The dashed circles are centered on the clusters and have corresponding radius R_{500} . We indicated the 5 Mpc unit at the redshift of the pairs $z = 0.14$. The color bar is in units of Jy beam^{-1} .

2.3.2 Method

In order to look for large scale emission from the cosmic web, we observed pairs of galaxy clusters and the putative inter-cluster filaments connecting them. The cluster pairs were selected from the MCXC Meta-Catalog of X-Ray Detected Clusters of Galaxies⁵ (Piffaretti et al., 2011) by applying cuts in declination ($\delta \geq 10$ deg), redshift ($z \leq 0.3$) and maximum angular separation ($\theta \leq 5$ deg). These values are tailored to the proposed LOFAR observations. The two most promising pairs that, according to cosmological simulations, maximise the probability of a physical connection between the clusters in terms of total mass and separation (real and projected), were proposed and observed at the LOFAR during Cycle 9 (Proposal Id:LC9_020). The most important properties of the two observed pairs of clusters are given in Tab.2.2.

In a nutshell, after calibrating, imaging and removing contaminating sources from the LOFAR data, we quantify the confidence of having observed (or not) diffuse emission from the inter-cluster filaments by injecting simulated diffuse emission produced by large scale (\geq Mpc) accretion shocks, into the original radio visibility data (uvw) for a large ($\mathcal{O}(100)$) subset of simulated filaments/cluster pairs and by imaging them as done for the real observations.

In this section we provide further details on the analysis performed on the actual observations, the simulated data set prepared for the injection and the injection procedure (also sketched by the diagram in Fig. 2.10).

LOFAR radio observations We observed the two cluster pairs RXCJ1659.7+3236-RXCJ1702.7+3403 (hereafter RXC_J1659-J1702) and RXCJ1155.3+2324-RXCJ1156.9+2415 (hereafter RXC_J1155-J1156) using LOFAR. The fields containing these two targets were co-observed together with two pointings of the LOFAR Two-meter Sky Survey (LoTSS; Shimwell et al., 2017) taking advantage of the multi-beam capabilities of the instrument. The observing setup of our observations thus follows that of LoTSS, namely 8 hr on-source time book-ended by two 10 min scans on the flux density calibrator in the frequency range 120-168 MHz using LOFAR in HBA_DUAL_INNER mode (see Shimwell et al., 2017, for details). A first calibration and imaging run was performed adopting the pipelines developed to analyze LoTSS pointings (Shimwell et al., 2017, 2019), aiming to correct both for direction-independent and direction-dependent effects exploiting PREFACTOR (Williams

⁵<http://heasarc.gsfc.nasa.gov/W3Browse/all/mcxc.html>

et al., 2016; van Weeren et al., 2016; de Gasperin et al., 2019), KILLMS (Tasse, 2014a,b; Smirnov and Tasse, 2015), and DDFACET (Tasse et al., 2018). In particular, we made use the improved version of the direction-dependent data reduction pipeline (v2.2⁶, the same used for the second LoTSS data release DR2, Shimwell et al. in preparation) to produce images of the full LOFAR field-of-view at the central frequency of 144 MHz at high (6'') and low resolution (20'', shown in Fig. 2.11 and 2.12) using a Briggs weighting scheme (robust=-0.5). We refer the reader to Tasse et al. (submitted) for a thorough description of the steps performed by the pipeline. Using sky models derived from the pipeline, we subtracted the sources out of the uv-data in two different ways: either we subtracted all sources (by means of their clean components) found in the high and low resolution maps or we subtracted all sources detected in the high resolution image. The model components were determined during the high and low resolution images deconvolution making use of the PYthon Blob Detector and Source Finder (PYBDSF; Mohan and Rafferty 2015). The subtraction of the model components was performed in the visibility domain, adapting the model components by the direction-independent antenna gains obtained from the calibration. We then produced dirty images from the subtracted data. The images include the residual contribution to the surface brightness resulting from model approximation plus artefacts associated with imperfect model and solutions (Im_{empty}) plus patches of faint extended emission in the case in which only sources from the high resolution model were subtracted ($\text{Im}_{\text{diffuse}}$). The subtracted (dirty-)images Im_{empty} at low resolution (20'') have a rms noise floor of ~ 160 and $240 \mu\text{Jybeam}^{-1}$ for the two fields, respectively. The noise difference is consistent with the amount of flagged (i.e. discarded) data in the two observations.

Cosmological simulations We extracted the simulated inter-cluster filaments from the suite of simulations of the cosmic web properties described in Vazza et al. (2019) performed with the cosmological MHD code ENZO⁷ (Bryan et al., 2014). They consist in a comoving 100^3Mpc^3 box with a uniform grid of 2400^3 cells (and 2400^3 dark matter particles) with linear (comoving) resolution of 41.6 kpc per cell and dark matter mass $m_{dm} = 8.62 \times 10^6 M_{\odot}$ per dark matter particle. Magnetic fields have been initialized at $z = 45$ as a uniform background of $B_0 = 0.1 \text{nG}$ and evolved at run-time using the MHD method of Dedner (Dedner et al., 2002). We

⁶<https://github.com/mhardcastle/ddf-pipeline>

⁷www.enzo-project.org

Cluster name	R.A. [h,m,s]	Dec. [°,′,″]	z	L_X [erg/s]	M_{500} [M_\odot]	R_{500} [Mpc]	d_{2D} [°]	L_{fila} [Mpc]
RXCJ1155.3+2324	11 55 18	+23 24 27	0.142	$6.04 \cdot 10^{44}$	$5.60 \cdot 10^{14}$	1.19	0.93	8.25
RXCJ1156.9+2415	11 56 58	+24 15 29	0.139	$1.50 \cdot 10^{44}$	$2.40 \cdot 10^{14}$	0.90	0.93	8.25
RXCJ1659.7+3236	16 59 44	+32 36 49	0.101	$1.12 \cdot 10^{44}$	$2.04 \cdot 10^{14}$	0.87	1.57	10.13
RXCJ1702.7+3403	17 02 42	+34 03 43	0.095	$4.04 \cdot 10^{44}$	$4.49 \cdot 10^{14}$	1.01	1.57	10.13

Table 2.2: Main parameters of the two pairs of galaxy clusters observed in this work, based on the MCXC Meta-Catalog of X-Ray Detected Clusters of Galaxies (Piffaretti et al., 2011). In the last two columns, we provide the angular separation of the two cluster centres and the 3-dimensional length of the filament (considering the cluster to cluster distance).

note that a uniform initial magnetic field here would correspond to a scale-invariant spectrum in the models used for Cosmic Microwave Background (CMB) analysis (Aghanim et al., 2019; Paoletti and Finelli, 2019). We also note that the run was non-radiative and did not include any treatment for star formation or feedback from AGN. To a first approximation, these processes are not very relevant for the radio and X-ray properties of the peripheral regions of galaxy clusters and filaments (Vazza et al., 2017), which are our main focus.

Synchrotron emission model for cosmic shocks We produced synthetic maps of synchrotron radio emission assuming that diffusive shock acceleration (DSA, e.g. Kang et al. 2012 and references therein) accelerates a small fraction of thermal electrons swept by structure formation shocks up to relativistic energies, as in Vazza et al. (2019). We computed the radio emission from electrons in the downstream cooling region of shocks using the model of Hoeft and Brügggen (2007) and based on the shocks identified in post-processing in the simulation. The total acceleration efficiency at shocks, $\xi_e(\mathcal{M})$ (with \mathcal{M} the Mach number) is assumed to be the combination of two variables: the kinetic energy flux dissipated onto the acceleration of cosmic rays, $\psi(\mathcal{M})$, and the fraction going into electron acceleration, ξ'_e , giving $\xi_e(\mathcal{M}) = \xi'_e \cdot \psi(\mathcal{M})$. Following Hoeft and Brügggen (2007), the radio emission in the downstream of each shock is directly linked to the power-law energy distributions $N_\gamma \propto \gamma^{-p}$ of electrons accelerated by the shock front during a cooling time, through the integrated radio spectrum of $I(\nu) \propto \nu^{-s}$, where $s = (p - 1)/2 + 1/2$, with $p = 2(\mathcal{M}^2 + 1)/(\mathcal{M}^2 - 1)$ (Kardashev, 1962). With this approach and for the range of $\mathcal{M} \gg 5$ shocks usually

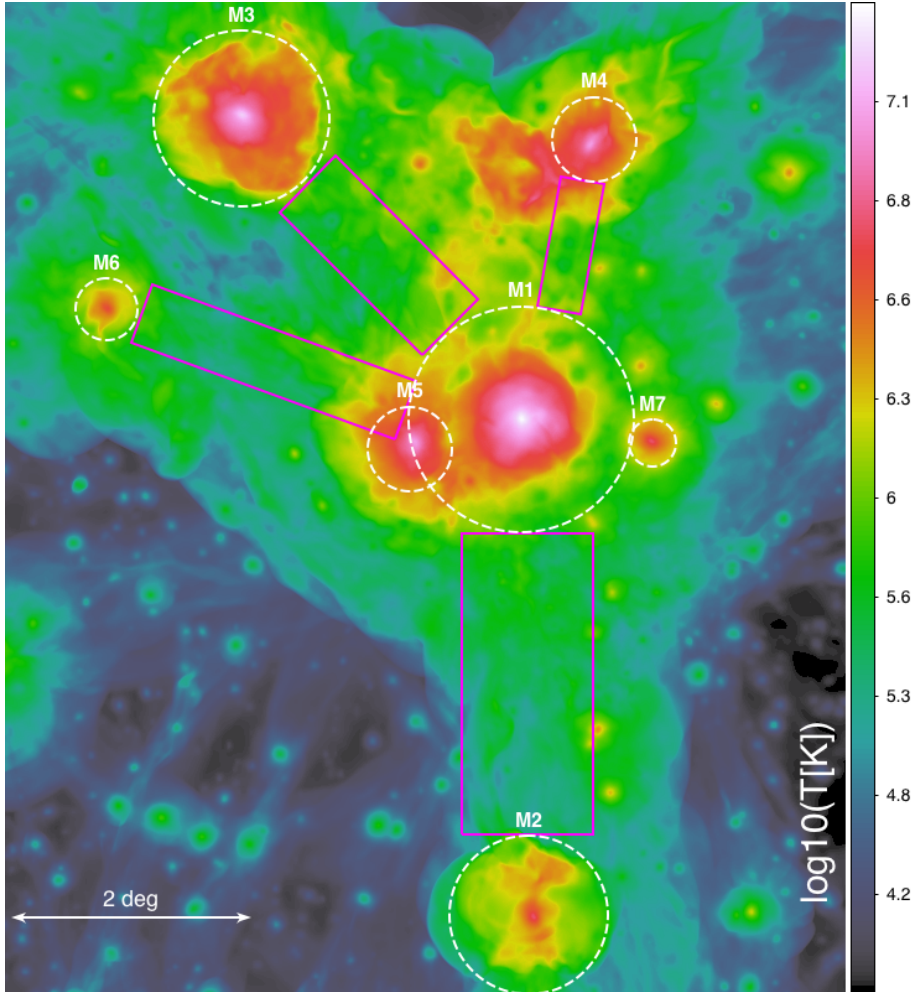


Figure 2.13: Example of mean gas temperature from the ENZO simulation. Circles mark the projected virial region of clusters, magenta rectangles mark filaments. The cluster field is placed at $z = 0.1$.

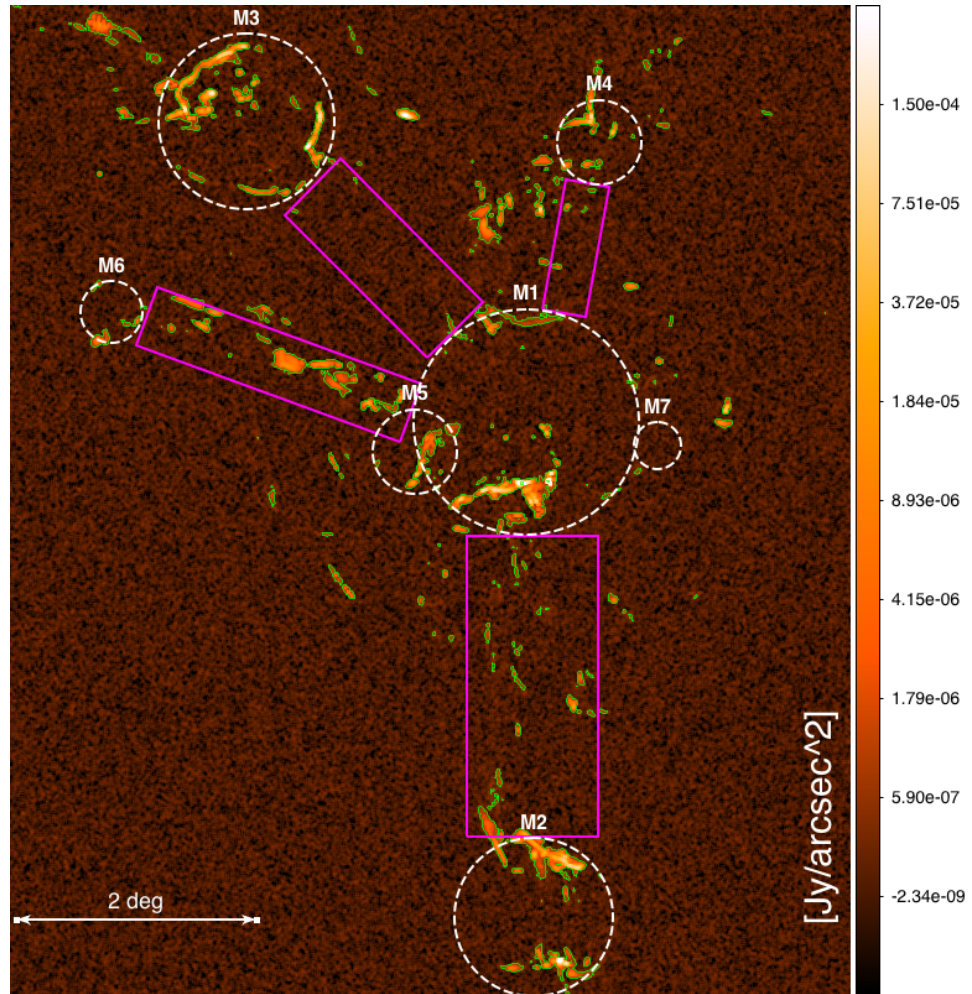


Figure 2.14: Mock LOFAR-HBA observation ($\nu = 140$ MHz, $25''$ resolution, $250 \mu\text{Jy beam}^{-1}$ noised added) for the ENZO simulation presented in Fig. 2.13. Circles mark the projected virial region of clusters, magenta rectangles mark filaments. The detectable emission ($\geq 3\sigma$) is marked with green contours.

found within and around simulated filaments, as well as for the $\leq \mu\text{G}$ magnetic fields in filaments (e.g. [Vazza et al., 2017](#)), the radio emission thus scales as $I(\nu) \propto \xi_e B^2 \nu^{-2}$. The baseline model used in this work assumes $\xi_e = 10^{-2}$, which is in line with DSA expectations for the maximal acceleration efficiency of relativistic electrons by strong shocks (e.g. [Hoeft and Brügggen, 2007](#); [Kang et al., 2012](#); [Bykov et al., 2019b](#)), also is also compatible with the modelling of supernova remnants (e.g. [Uchiyama et al., 2007](#); [Bykov et al., 2019a](#)). However, we shall notice that in typically weak ($\mathcal{M} \leq 4$) shocks leading to radio relics in galaxy clusters (e.g. [van Weeren et al., 2019](#)), the acceleration efficiencies implied by the observed relic radio fluxes can be much larger ($\xi_e \sim 0.1 - 1$, see e.g. [Stuardi et al. 2019](#) and [Botteon et al. 2020a](#)), thus making our maximal value of $\xi_e = 10^{-2}$ a conservative one. We notice however that very recent particle-in-cell (PIC) simulations (albeit in 1D and with some limiting assumptions) have derived a $\sim 5\%$ electron acceleration efficiency by strong shocks ([Xu et al., 2020](#)). For the remainder of the paper, the reader must thus bear in mind that our limits on B_{Mpc} must be accordingly rescaled if a different value of ξ_e is adopted.

[Fig. 2.13](#) gives an example of filaments connecting a massive cluster to other groups in its surrounding, in an ENZO cosmological simulation. A small but significant fraction of radio emission from shocks running on filaments connecting some of the pairs (e.g. M1-M2, M1-M4 and M1-M6 in [Fig. 2.13](#)) is above the detection threshold in LOFAR-HBA for our baseline model (see [Fig. 2.14](#)). In all cases, the detectable emission comes from relatively small and localised patches, extended a few $\sim 10'$ at most, with irregular shapes. Detecting the radio signal from cosmic filaments is indeed made challenging by the fact that the detectable fraction is just the tip of the iceberg of the wider "radio cosmic web", which makes a morphological classification of the emission often ambiguous. Indeed advanced Deep Learning techniques have been proposed for the detection of the cosmic web in next radio surveys ([Gheller et al., 2018](#)). In the following section we use this model to constrain the amplitude of the $\xi_e B^2$ combination based on our real LOFAR observations.

Generation of a mock catalog of inter-cluster filaments We selected simulated pairs holding individual cluster masses $M_{500} > 10^{13} M_\odot$ and linear (comoving) and projected angular distance of clusters in the pair within 20% deviation from the values of the observed pair (see the last and second-last columns in [Tab. 2.2](#)). We obtained 125 simulated cluster pairs selected for

RXC_J1659-J1702 and 103 pairs for RXC_J1155-J1156. The cluster pairs selected above mirror the separation selection criteria of our observations but include less massive clusters that may not involve a physical connection within one pair. We thus analysed in addition a sub-sample of high-mass clusters ($M_{500} > 3 \times 10^{13} M_{\odot}$) for which a physical connection and the presence of an inter-cluster filament was verified either manually and through a high temperature cut $T_{\text{WHIM}} > 10^5$ K of the WHIM within the inter-cluster filament. We refer to this sub-sample as *best*.

For a given simulated cluster pair, a box has been drawn and extracted along the direction connecting the pair. The box, including full information from the simulation ($\sim 30k$ cells on average), has been rescaled to match the angular scale and comoving transverse distance indicated by the pixel size and redshifts of the observed clusters, and the intensity of synchrotron emission has been scaled to match its luminosity distance by preserving the total power (see the lower left panel in Fig. 2.15 for an example).

The flux density has been also multiplied by a constant factor $f_B \equiv [B_0/(0.1 \text{ nG})]^2$. Under the assumption that the amplification of the magnetic field into the simulated filaments is affected by negligible small scale dynamo (Ryu et al., 2008), the amplification is thus mainly driven by the adiabatic compression of the magnetic field lines following from flux freezing⁸ into the plasma condensing during structure formation (Vazza et al., 2017). The magnetic field B at the end of the simulation is then scalable with respect to the initial B_0 . In turn, the synchrotron emission $S_{\nu} \propto B^2$ is also scalable with respect to B_0 as $S_{\nu} \propto B_0^2$. Since the synchrotron emission also depends on the amount of relativistic electrons, parametrised in the HB07 model by the electron acceleration efficiency ξ_e , we can test an arbitrary set of simulations just by multiplying the synchrotron emission obtained from the benchmark model ($B_0 = 0.1 \text{ nG}$) by an arbitrary factor $f_B \propto [B_0/(0.1 \text{ nG})]^2$.

Injection of model radio emission into real LOFAR images The rescaled simulated image of each mock pair of galaxy clusters was injected into the source-subtracted Measurement Set (MS), following the procedure sketched in Fig.2.10. In detail, each rescaled image was first Fourier-transformed, then written into the MS and finally added to the visibilities of the source-subtracted sky using WSCLEAN (Offringa et al., 2014). The writing process of the visibility into the MS guarantees that the added model is sampled by exactly the same angular scales as the observation recorded into

⁸the magnetic flux through a closed loop C enclosing the surface S is simply $\Phi_B = \int_S \mathbf{B} \cdot d\mathbf{S}$, valid for ideal plasma conditions

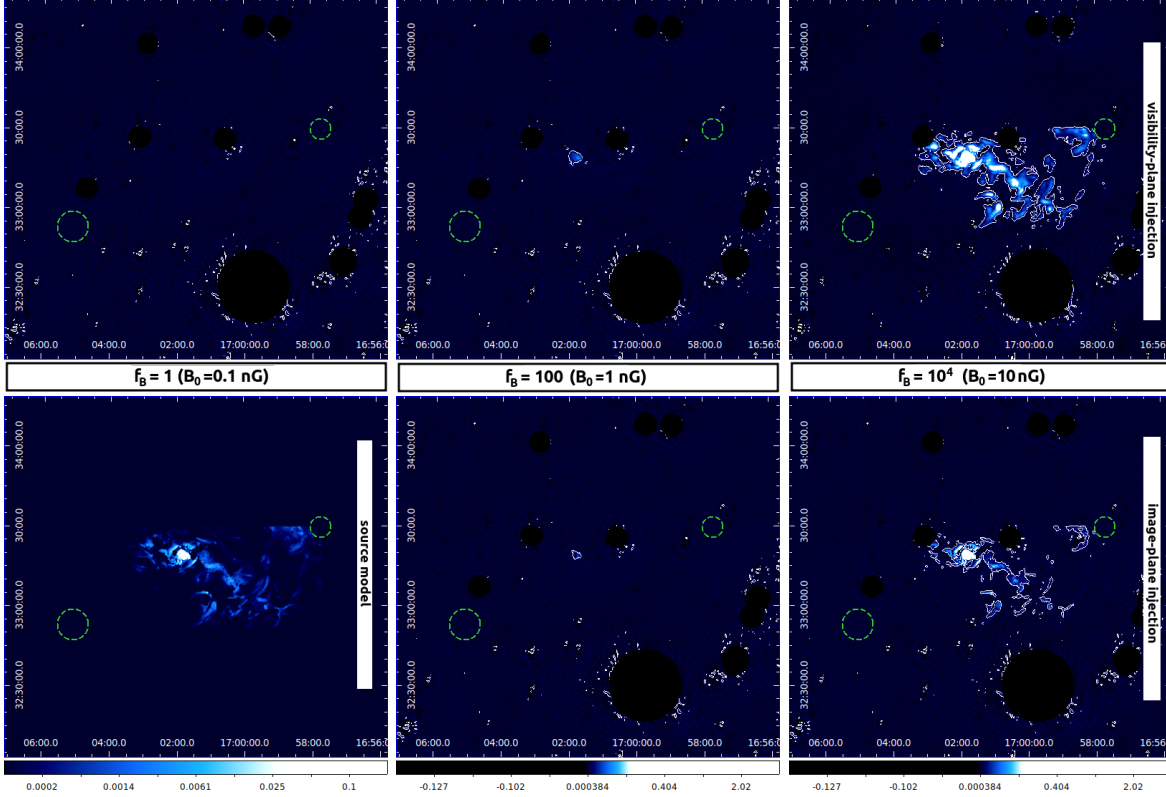


Figure 2.15: Example of source injection: the model of diffuse emission between a pair of simulated galaxy clusters (masked within their R_{200} , indicated by the green dashed circles) found in the simulation with $B_0 = 0.1$ nG (lower left panel) is multiplied by a factor $f_B = 1, 10^2, 10^4$ imaged and masked after being injected into the source-subtracted sky visibilities (upper left, upper central and upper right panels respectively), or it is injected through the image-plane (lower central and lower right panels for $f_B = 10^2, 10^4$ respectively). The image with $f_B = 1$ in the upper left panel, due to the very low brightness of the model with $B_0 = 0.1$ nG, results to be equal to the source-subtracted sky image Im_{empty} , in which the only features are the residuals from the source subtraction process which fall outside the masks. The white contours have been set to 5 times the rms value in Im_{empty} .

the same MS. We note that such injection does not take into account direction dependent effects that may act on the MS radio data. With the same software, the resulting data-set was imaged and deconvolved with a $20''$ uv-taper and synthesized beam, and Briggs weighting scheme (Briggs, 1995) with `robust=-0.25` and 2000 minor cycles (see Fig. 2.15 for output examples). For realistic values of the normalisation parameter f_B , the detectable emission is fragmented into small and sparse patches, associated with shocks internal to filaments. Therefore, we resort to statistical methods to assess the likelihood of each mock image to be compatible with our observed LOFAR fields. We computed the integral of the image power spectrum $P_S \equiv \log_{10} \left(\int_{k_{\min}}^{k_{\max}} P(k') dk' \right)$ where $P(k')$ is the power spectrum and k_{\min} and k_{\max} are determined by the image and beam size respectively (see Fig. 2.21 for an example). The sky model subtraction can leave bright residual artefacts depending on the goodness of the model used. These residuals can be as bright as $\sim 0.1 \text{ Jy beam}^{-1}$ around point-like sources and they may dominate the integral of the image power spectrum P_S . A zero-padding mask was manually generated for each pair of clusters in order to exclude those artefact from the computation of P_S in all images.

2.3.3 Results

From the cumulative probability distributions of the statistic P_S resulting from all the source injections, we can access how likely is for a model to provide an expected value smaller than the one recovered from the observations. From the image Im_{empty} , a $2.5 \text{ deg} \times 2.5 \text{ deg}$ square centered at the midpoint of the cluster pair, in which all the sources (point-like plus extended) have been subtracted, we compute $\tilde{P}_S \equiv P_S(\text{Im}_{\text{empty}})$. \tilde{P}_S corresponds to the total power in Im_{empty} distributed over all scales from twice the beam size (k_{\min}) up to half the image size (k_{\max}). All images resulting from injection thus have P_S equal or larger than the one computed for Im_{empty} (red dotted lines in Fig. 2.16). The statistic P_S resulting from the image in which diffuse emission was not subtracted $\text{Im}_{\text{diffuse}}$ are indicated by the blue dashed vertical lines in Fig. 2.16. Total of 3.1, 5.7 mJy of diffuse emission were found in $\text{Im}_{\text{diffuse}}$ in excess of Im_{empty} for RXC_J1659-J1702 and RXC_J1155-J1156 respectively. We outlined the probabilities for the different models in Tab. 2.3. The table reports also results from injection performed in the image plane (instead that in the uvw -plane) found in general to produce different probabilities of non-detection with respect to injection through the uvw -plane. We discuss this alternative method in Sec. 2.3.4.

The overall probability of a magnetic field model is simply the product of

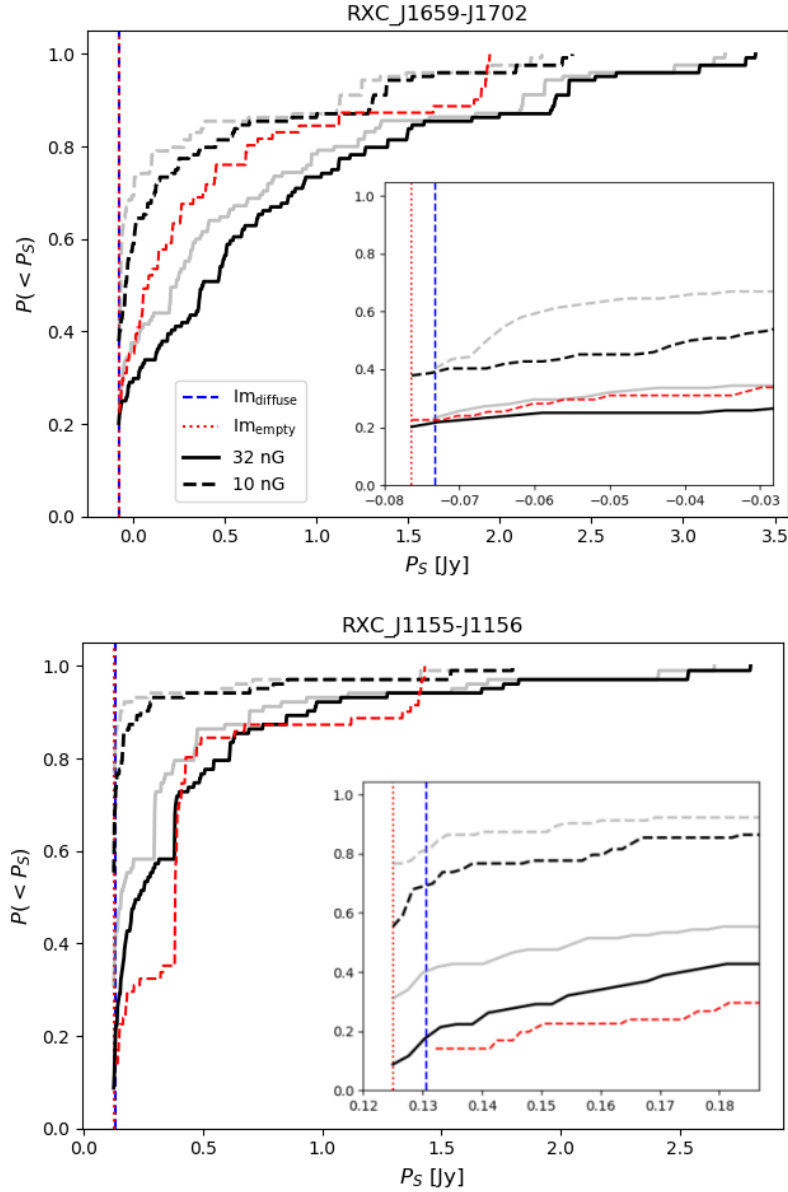


Figure 2.16: Probability distributions of finding statistics P_S smaller than the values set by the cluster pair RXC_J1659-J1702 (upper panel) and RXC_J1155-J1156 (lower panel) for scenarios with B_0 as labelled. The vertical lines show the P_S values computed without any injection from Im_{empty} (red dotted), $Im_{diffuse}$ (blue dashed). Black and grey lines show results for source injection performed respectively in the visibility and image domains. The insets show a zoom on the bins where $P(< P_S) \equiv P(< \tilde{P}_S)$.

the probabilities (of the model to produce lower statistics) of the two cluster pairs, since the experiments have been run independently on each pair. We compute these probabilities in the "all" bottom lines in Tab. 2.3. A model is more likely to be discarded, when its probability of having a smaller P_S than in our LOFAR observations is very small (or very high alternatively).

Our main results can be so summarised:

- the primordial scenario with a seed magnetic field of $B_0 \simeq 30$ nG has a small probability $P(< P_S) \simeq 0.05$ of explaining the small power excess in our observation of the RXC_J1659-J1702 and RXC_J1155-J1156 pairs, we then reject it with a confidence level (CL) of $> 95\%$.
- the models with a seed magnetic fields $B_0 < 30$ nG yield non-negligible (≥ 0.1) probabilities to produce a statistic equal to (o smaller than) the one observed.
- by tightening the constraint on individual cluster masses and on the presence of a inter-cluster filament connecting the clusters, the model with $B_0 = 10$ nG can be rejected as well with $CL > 95\%$.
- If any of the patches of diffuse emission observed is produced by shocks in the WHIM, then the $B_0 = 0.1$ nG model is highly disfavoured, as it is basically unable to produce any detectable emission (i.e the probability in Tab.2.3 of this model to produce less diffuse emission than what found in I_{empty} are always ≈ 1 ; we note that they have not been plotted in Fig. 2.16). Although we do not reject this scenario, we consider it implausible (see Sec. 2.3.4).

2.3.4 Discussion

From the original simulation holding $B_0 = 0.1$ nG, we extract the probability distribution functions (PDF) of the magnetic field values B_{Mpc} across the mock filaments selected according to the properties of the observed cluster pairs. We plot the resulting PDF($\log B_{\text{Mpc}}$) in Fig. 2.17. Given the expected lack of dynamo amplification in the WHIM, the magnetic field distributions PDF($\log B_{\text{Mpc}}$) corresponding to the other B_0 models can easily be rescaled linearly with the input seed field. We find a skewed distribution encompassing $B_{\text{Mpc}} = 1.0 - 7.4$ nG values (90% confidence range) with median $B_{\text{Mpc}} = 2.5$ nG (equivalent to $\log(B_{\text{Mpc}}/\text{nG}) = -8.6$) for the full sample. We note that the value of the magnetic field that produces the simulated

name	f_B	B_0 [nG]	uvw -plane		image-plane	
			Im_{empty}	$\text{Im}_{\text{diffuse}}$	Im_{empty}	$\text{Im}_{\text{diffuse}}$
RXC_J1659-J1702	1	0.1	1	1	1	1
	10^2	1	0.98	0.98	0.86	1
	10^4	10	0.38	0.39	0.40	0.40
	*best		0.23	0.23	0.24	0.24
	10^5	30	0.20	0.22	0.23	0.23
RXC_J1155-J1156	1	0.1	1	1	1	1
	10^2	1	0.77	0.96	0.85	0.97
	10^4	10	0.55	0.69	0.77	0.81
	*best		0.14	0.14	0.18	0.18
		10^5	30	0.09	0.18	0.31
all	1	0.1	1	1	1	1
	10^2	1	0.75	0.94	0.73	0.97
	10^4	10	0.21	0.21	0.31	0.32
	*best		0.03	0.03	0.04	0.04
		10^5	30	0.02	0.04	0.07

Table 2.3: Probabilities of obtaining a statistic P_S lower than the one observed in Im_{empty} and $\text{Im}_{\text{diffuse}}$, computed from source injection performed in the uvw -plane and in the image-plane. We highlight with bold face the values used to derive the limits on B and B_0 in this work.

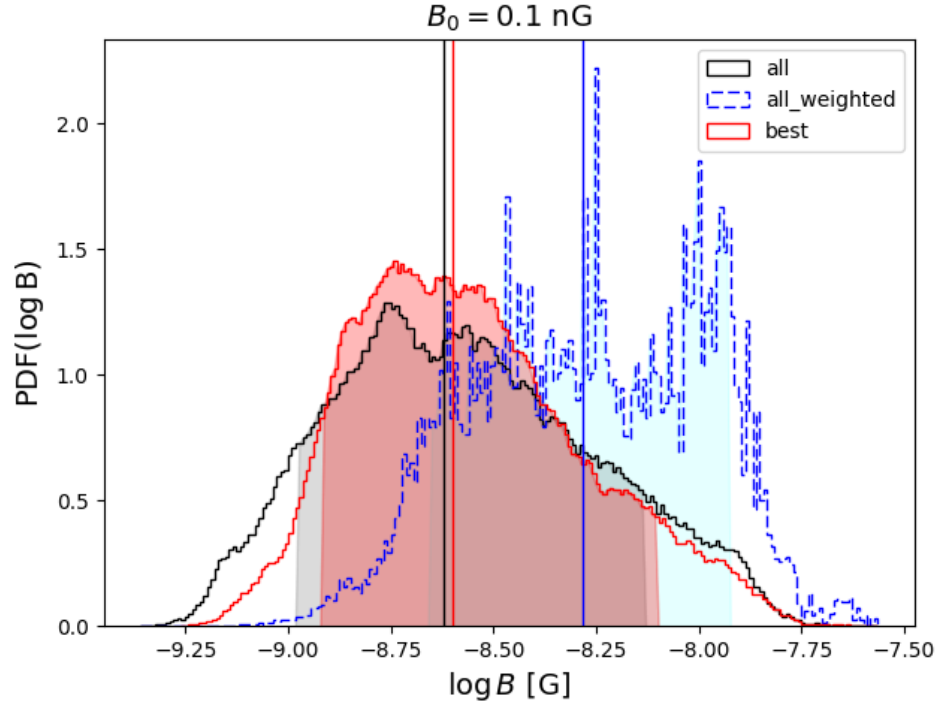


Figure 2.17: PDFs of the $\log B_{\text{Mpc}}$ field across all the simulated filaments in the $B_0 = 0.1 \text{ nG}$ model, for all the pairs in the mock sample (black line) and for the *best* sub-sample (red line). The dashed blue lines show the $\log B_{\text{Mpc}}$ distribution from all pairs weighted over the pixels emissivity. The filled hatched areas encompass the 10 – 90 percentile ranges. The vertical solid lines show the median of the distributions.

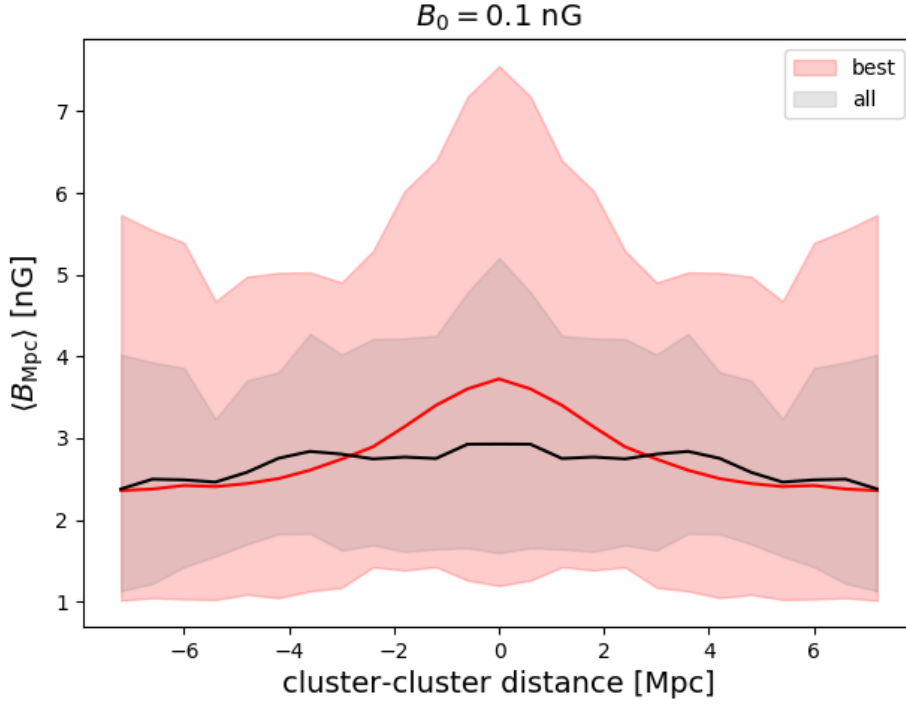


Figure 2.18: Average profile of mass-weighted magnetic field strength for all inter-cluster filaments extracted to resemble the two cluster pairs studied in this work and for the *best* sub-sample, resulting from the $B_0 = 0.1$ nG model. The solid lines give the median value of the two samples (with 235 and 142 objects, respectively) while the filled areas encompass the 10 – 90th percentiles of the distributions.

synchrotron emission lays in the high part of the B_{Mpc} distribution, as can be seen from the emission-weighted B_{Mpc} distribution in Fig. 2.17. We also give in Fig. 2.18 the average profiles of mass-weighted magnetic field strength for all simulated filaments extracted with the procedure above, for the two cluster pairs. On average, the profile of magnetic field is very uniform across 10 – 20 Mpc, with an average magnetic field along the line of sight for these objects of $\sim 2 - 3$ nG and a tail of rare and massive filaments that can reach ~ 10 nG.

To interpret the results provided in Fig. 2.16 and Tab. 2.3, we postulate three different assumptions that exploit the different type of source-

subtraction performed in the analysis, and that can be used to derive different priors from our data (vertical lines in Fig. 2.16):

- I : none of the residual diffuse emission after the point-like source subtraction (Im_{empty}) is produced by the shocked cosmic web;
- II : all of the residual diffuse emission in excess of Im_{empty} (i.e. $\text{Im}_{\text{diffuse}}$) is produced by the shocked cosmic web;
- III : at least some of the excess diffuse emission present in $\text{Im}_{\text{diffuse}}$ comes from the cosmic web.

Provided that we can fix the ξ_e acceleration efficiency at strong shocks ($\xi_e \approx 10^{-2}$), the assumption that none of the observed emission comes from cosmological shocks (I), produces in principle tighter constraints on B_{Mpc} (and B_0), since $P(P_S(\text{Im}_{\text{empty}})) \leq P(P_S(\text{Im}_{\text{diffuse}}))$ always. In practice, the constraints are just slightly tighter due to the small amount of diffuse emission found into $\text{Im}_{\text{diffuse}}$ with respect to Im_{empty} . Thus, under the first hypothesis that we did not observe the cosmic web emission, by scaling the B_{Mpc} distribution to match the $B_0 = 30$ nG model (i.e. a factor $\times 300$) we infer an upper limit to the current median IGMF into filaments of $B < 0.8 \mu\text{G}$ with 95% confidence (the same confidence level that applies to the rejection of $B_0 \geq 30$ nG models of the primordial magnetic field scenario). By considering the *best* sub-sample of cluster pairs with higher masses and connected by an inter-cluster filament we can further improve the constraints on B by rejecting with a $\text{CL} > 95\%$ also the $B_0 = 10$ nG model. Equivalently, this limit also sets $B_{\text{Mpc}} < 0.25 \mu\text{G}$ with the same CL. In principle we can not exclude that the observed pairs do not hold an inter-cluster filament, however this probability has been addressed in several works and amounts to $\leq 20\%$ for the mass range and separation of these two pairs of clusters (Colberg et al., 2005; Locatelli et al., 2018).

The assumption that the excess diffuse emission present in $\text{Im}_{\text{diffuse}}$ with respect to Im_{empty} is entirely due to shocked plasma of the WHIM (hypothesis II) can be readily tested by looking in detail at the diffuse emission patches which have been detected. In Fig. 2.19 we present close-up clippings of the diffuse patches found close to the pair RXC_J1659-J1702, taken from the low resolution LOFAR images (before source-subtraction). They are meant to help in assessing the nature of some of the diffuse emission, indicated by the dashed red circles in the panels of Fig. 2.19. We also marked with green X symbols the position of sources already known from

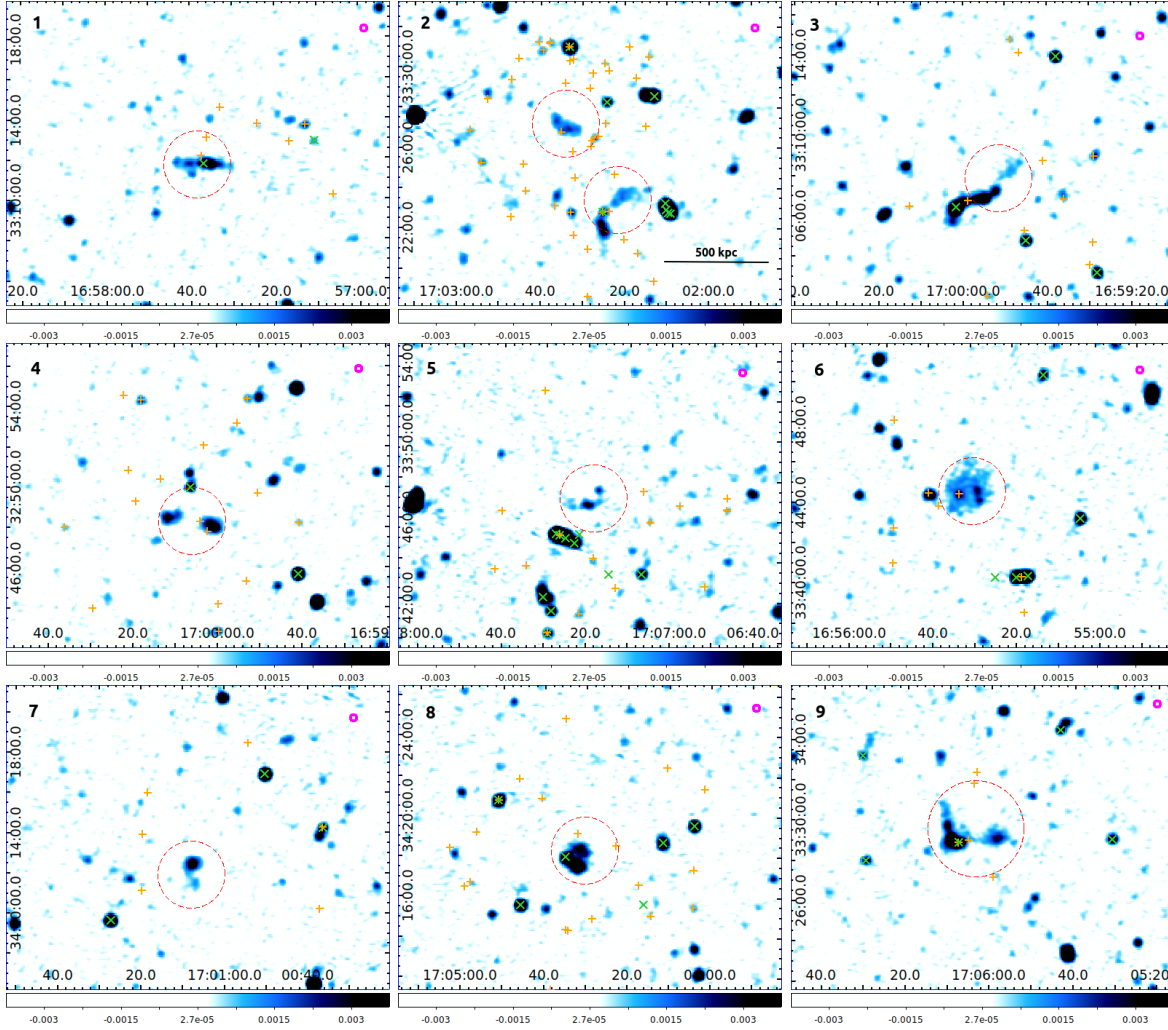


Figure 2.19: Zoom-in low resolution sky images ($20''$, see the magenta solid circles) centered over the patches of diffuse emission found in $\text{Im}_{\text{diffuse}}$ of RXC-J1659-J1702 as indicated by the dashed red circles. Green X symbols show the position of FIRST sources. Orange crosses show the position of SDSS galaxies with known spectroscopic redshift. Panels are numbered from 1 to 9 going from left to right and top to bottom. $1'' = 1.84$ kpc at $z = 0.10$, we marked the 500 kpc scale in panel 2 for comparison. color bars are in Jy beam^{-1} .

the VLA Faint Images of the Radio Sky at Twenty-centimeters (FIRST) survey (Becker et al., 1995). Most of the diffuse emission is plausibly linked to the lobes of radio-galaxies already detected at higher frequencies. Panel 7 (panels are numbered from 1 to 9 from left to right, top to bottom) shows what look like either a radio lobe or an artefact linked to a low-frequency point source. Panels 2, 5 and 6 instead show diffuse emission which is neither obviously not-linked to radio galaxies, nor to deconvolution artefacts. However, looking at their coordinates, sources 5 and 6 are found to be distant from the axis connecting the clusters, albeit within the imaged portion of the sky around the pair (see also Fig. 2.11). This makes their physical connection to the putative inter-cluster filament unlikely, even if the shocked cosmic web is expected to fill the space in between clusters in a non-trivial way, as shown in Fig. 2.14. Furthermore, the point-like source embedded into the diffuse emission in panel 6 is also found to be at a different redshift with respect to the cluster pair. For the above reasons, these patches can hardly be used in the comparison with the simulated inter-cluster filaments. The diffuse patches in panel 2 instead embed optical galaxies with redshift $z = 0.087, 0.093$, consistent with the cluster pair $z = 0.095 - 0.101$, however they are likely dying faint radio lobes, with no FIRST counterpart. Since there is no easy way to cross check all the different patches, we still computed the statistics for the most conservative scenario by assuming that the level of observed diffuse emission in excess of Im_{empty} is entirely due to the cosmic web. In this case, the level of confidence associated to the rejection of the same models loosens. However, the models rejected by casting hypothesis II are the same ones resulting from hypothesis I, though with slightly lower or even equal CL. (e.g. for the $B_0 = 30$ nG model the CL for its rejection decreases from 98% to 96% and all lower B_0 models remain unchanged. Furthermore, since hypothesis II has been falsified already by the examples described above and shown in Fig. 2.19, hypothesis I is strengthened in favor of hypothesis II and we thus refer to the former in order to draw our conclusions.

For completeness, a third additional and interesting way is instead the complementary hypothesis to the first one: we assume that at least some of the diffuse emission in excess of Im_{empty} comes from the cosmic web. The associated probabilities is then trivially $P(> P_S) = 1 - P(< P_S)$. In this case we are not interested in the level of diffuse emission in $\text{Im}_{\text{diffuse}}$, since we want to produce at least the one in Im_{empty} . Though disfavored, this scenario can not be discarded a priori since this would imply checking (e.g. through cross-correlations) all the different patches of diffuse emission in $\text{Im}_{\text{diffuse}}$ and proving that all of them are not connected to the emission from the

Cosmic Web, it is then instructive to inspect its implications. Under the assumption that we did see the cosmic web emission at least in part, then the $B_0 = 0.1$ nG model is ruled out with high confidence $\geq 99\%$ since it is not able to produce any observable emission brighter than the noise level of our LOFAR observation. In this scenario, $B_0 > 0.1$ nG can be set as a lower limit to the primordial magnetic field intensity and in turn $B > 2$ nG as the median value for the magnetic field into filaments today.

We have assumed that the normalisation f_B acting on the flux density is equivalent to a normalization of the final magnetic field strength B_{Mpc} as $f_B^{1/2}$ under the assumption of constant electron acceleration efficiency $\xi_e \sim 10^{-2}$. We note that changing the magnetic field changes the Lorentz force acting on the electrons and thus the characteristic frequency of their emission $\nu_s \propto B_{\text{Mpc}}\gamma^2$, where γ is the Lorentz factor of the electrons. However, since we always consider images at 144 MHz a change of B_{Mpc} turns into a change in the Lorentz factor of the electron population responsible for the 144 MHz emission, rather than a change in frequency. In addition, electrons with different γ hold different cooling times $\Delta t_{\text{cool}} \simeq 24.6/(B^2\gamma)\text{yr}$. We thus want to check that the re-normalization of B_0 within models considered still produces electron populations consistent with the observation of their emission. In Fig. 2.20 we plot the expected dependencies of the Lorentz factor from the magnetic field strength in producing particles emitting at 144 MHz (red solid line) and population cooling over different timescales (black lines). For all the re-normalized model considered, the Lorentz factor γ ranges between 8×10^3 and 1.5×10^4 , whereas the cooling time is always larger than 5 Gyr, and larger than the Hubble time for any $B_{\text{Mpc}} \leq 0.5 \mu\text{G}$. Electrons with $\gamma \sim 10^{3-4}$ are less energetic than the ones responsible for the 144 MHz emission in the benchmark model ($B_0 = 0.1$ nG). Hence, they can easily be produced by DSA and they do not age too fast so that we can still observe their emission. With this respect we note that the stronger shock population responsible for the DSA in the cosmic web follows the LSS formation and thus peaks at late times (i.e. $z < 1$, corresponding to a lookback time of ≤ 7 Gyr), thus preventing the cooling of the particles before our observation even for the model with largest $B_{\text{Mpc}} = 750$ nG ($B_0 = 30$ nG).

While checking that the source injection procedure (presented in Sec. 2.3.2 and sketched in Fig. 2.10) is actually needed in order to derive robust limits on B_{Mpc} and B_0 we also demonstrate that the method is essential to interpret observations in details by means of the outcome of simulations when dealing with radio data. With this respect, we produced the same statistic

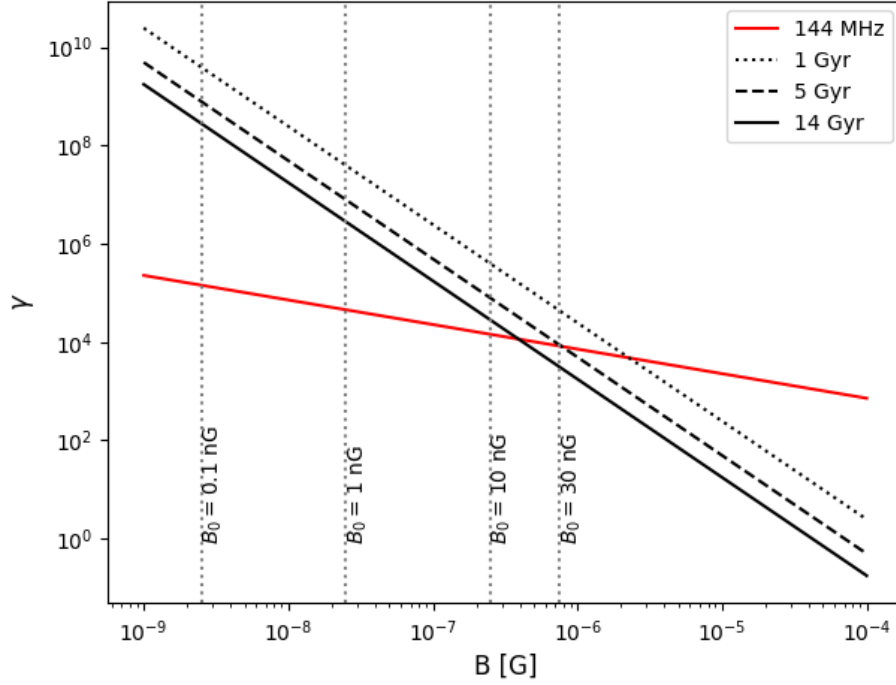


Figure 2.20: Lorentz factor γ of the electrons mainly responsible for the 144 MHz emission as function of the magnetic field strength (red line). The vertical dotted lines show the median values of B_{Mpc} retrieved for the simulations starting with B_0 as labelled. The black lines show the set of parameters for electrons losing their energy in different timescales, as labelled. In all models considered electrons have γ within the range $[8 \times 10^3; 1.5 \times 10^4]$ and cooling time is longer than 5 Gyr.

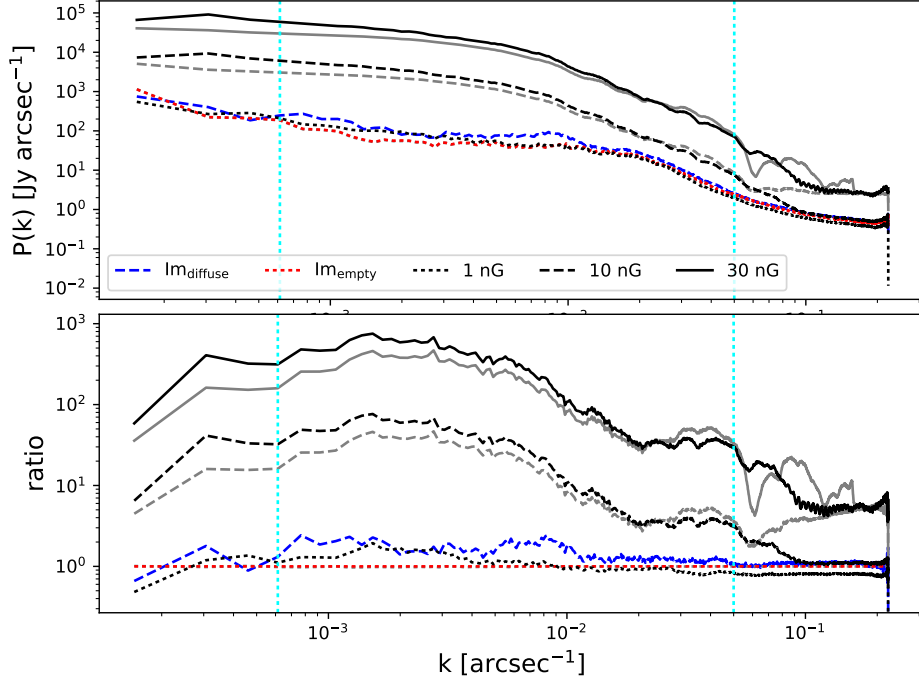


Figure 2.21: Power spectrum of the brightness of the injected filament shown in Fig. 2.15 for different B_0 models, as labelled. The vertical cyan dotted lines show the integration scale limits used to compute P_S . They correspond respectively to about half the largest scale in the image $k^{-1} = 2173'' \sim 483$ pixels and $k^{-1} = 40''$ (corresponding to twice the synthesized beam FWHM scale). Black lines show $P(k)$ resulting from the source injection into uvw visibilities whereas grey lines show the result from the image-plane addition of the simulated image onto Im_{empty} . The lower panel shows the same power spectra as in the upper panel, divided by the Im_{empty} line.

P_S for the simulations directly added to the residual image I_{empty} in terms of simple image sum, rather than following the central FFT + write + sum procedure involving visibilities. This procedure is much simpler and faster (shortening the computing time of a factor ~ 600). In Fig. 2.21 we plot the power spectra resulting from the injection in the RXC_J1659-J1702 field of one source as example (images of the same source are shown in Fig. 2.15) in order to inspect differences between the injection through the uvw - (black lines) and image-plane (grey lines), for the different B_0 models. As can be seen by comparing the black and gray lines, when the injection is performed within the image-plane the level of simulated emission at large scales is generally underestimated. As a consequence the models are consistent with the data with different probability up to $\pm 30\% P(< P_S)$ (see the values in Tab. 2.3). We interpret the difference in the results as due to the lack of model convolution with the instrument's Point Spread Function (PSF). In addition, the lack of convolution of the emission with a visibility weighting scheme able to maximise the evidence for extended diffuse emission into the data may also play a similar role. As far as an upper cut on the scales of the emission (corresponding to a lower bound on the baseline length in radio interferometers) is taken into account, and detailed power spectrum information does not constitute the largest budget of uncertainty in one analysis (in our case is the scatter in the properties of the -unknown- inter-cluster WHIM), the image sum is a much faster approach than the source injection through the uvw -plane, however it shall be used with caution as results are biased by a different sampling of the scales. The strength of the bias depends either on the sampling (window) function and the source power spectrum.

As a final caveat, our analysis assumes that for strong shocks in and around filaments, the acceleration efficiency of electrons is the one suggested by DSA, i.e. $\xi_e \sim 10^{-2}$. This assumes, in turn, that despite the rather low particle density and magnetisation, shocks can form and produce particle acceleration similar to what already observed for the outer regions of galaxy clusters in form of gaint radio relics (see van Weeren et al., 2019, for a review). Moreover, our analysis assumes that the acceleration of electrons at shocks can proceed independently on the obliquity between the upstream magnetic field and the shock normal. However, recent numerical works by Banfi et al. (2020) have shown that shocks surrounding the cosmic web are more often quasi-perpendicular than random chance, as an effect to the peculiar gas velocity flow following the formation of filaments. In this case, the vast majority of shocks in filaments are quasi-perpendicular and thus likely to be suitable for efficient electron acceleration (Xu et al., 2020). Furthermore, Masters et al. (2017) recently reported a significant electron

acceleration by the strong quasi-parallel shock while crossing the Saturn bow shock by the Cassini space mission, i.e. in plasma conditions similar to the ICM. The acceleration seems to occur in the portion of the shock where upstream cosmic-ray streaming instabilities generate perpendicular small-scale magnetic field components, leading to particle acceleration.

2.3.5 Section summary

In this work, for the first time, we attempted to combine dedicated LOFAR-HBA observations of inter-cluster filaments and numerical simulations of the magnetic cosmic web, in order to derive upper limits on the magnetisation of the WHIM.

While our LOFAR observations do detect patches of diffuse emission of unclear origin their morphology does not allow us to firmly associate the origin of the most prominent ones to the cosmic web. However, the presence of a faint diffuse large scale excess in comparison with numerical models allows us to derive inferences on the average magnetisation of such filaments, and possibly on the allowed initial amplitude of primordial seed magnetic fields. As a main outcome of our work (following from assuming that our observations constitute *non-detections* of diffuse emission from the cosmic web and fixing $\xi_e = 0.01$ for strong shocks), we derive an upper limit for the median magnetic field strength in filaments connecting massive galaxy clusters: $B_{\text{Mpc}} < 0.2 - 0.6 \mu\text{G}$, depending on whether future measurements will prove or exclude the presence of the WHIM between the observed cluster pairs. Based on the dynamical evolution of magnetic fields given by present simulations (which is mostly dominated by simple compression of magnetic field lines), this also implies an upper limit of $B_0 < 10 - 30 \text{ nG}$ on the amplitude of primordial seed fields.

As a mutually exclusive interpretation of our data, if some of the detected emission may partially come from the shocked WHIM, this would imply a median magnetic field of order of $B_{\text{Mpc}} \geq \text{nG}$ (see e.g. Fig. 2.17). This would be an important outcome as it would also possibly indicate primordial magnetic fields with intensity $B_0 \geq 0.1 \text{ nG}$.

Given the uncertainties connected to our method and the limited statistics of "detections" in our sample, we propend for the first interpretation of our result.

To put our new limits in comparison with other recent works (Hackstein et al. 2016; Pshirkov et al. 2016; Vernstrom et al. 2017; Brown et al. 2017; Vernstrom et al. 2019; O’Sullivan et al. 2020; Natwariya 2020, and Paoletti and Finelli 2019 for joint BICEP2/Keck - Planck 2018 updated results),

we show them in Fig. 2.22 separating the limits inferred for the IGMF or the magnetic field intensity of the IGMF (red arrows), the fields limits of the WHIM derived in this work (green arrows) and for the primordial magnetic field intensity B_0 (blue arrows). We note that our limits are still in agreement with the recent limits $0.134 < B_0/\text{nG} < 0.316$ set by the level of excess diffuse emission observed by ARCADE2 and EDGES 21cm line experiments (Natwariya, 2020). Furthermore, an apparent tension seems to arise between our lower limit to B_{Mpc} into filaments and the one derived from other probes such as the level of anisotropy in the arrival direction of charged ultra-high-energy cosmic rays used to limit the average amplitude of magnetic fields in voids to $\leq 1\text{nG}$ (Hackstein et al., 2016), or from the non-detection of a trend of rotation measures from distant radio sources with respect to redshifts (Pshirkov et al., 2016). Although computed over similar linear scales $\geq \text{Mpc}$ and globally refer to the IGM, they can still hardly be directly compared since referred to different IGM environments (e.g. voids, filaments, averaged). Interestingly a recent work has suggested that primordial magnetic fields with amplitude $\sim 0.1 \text{ nG}$ would possibly alleviate the existing tension between cosmological and standard candle-based estimates of H_0 (Jedamzik and Pogosian, 2020).

While it is hard to derive conclusive limits from these data, as no robust detection (although tentative) of the diffuse emission from the cosmic web can be claimed, this first attempt stresses the potential of low-frequency radio observations in constraining extragalactic magnetic fields, and its relevance to the study of cosmic magnetogenesis. With the analysis and the values obtained in this work, we can forecast to produce tighter constraint than the ones posed by CMB experiments by covering a $\sim \times 10$ larger sample of cluster pairs similar to the ones analysed here even in the case of other non-detections.

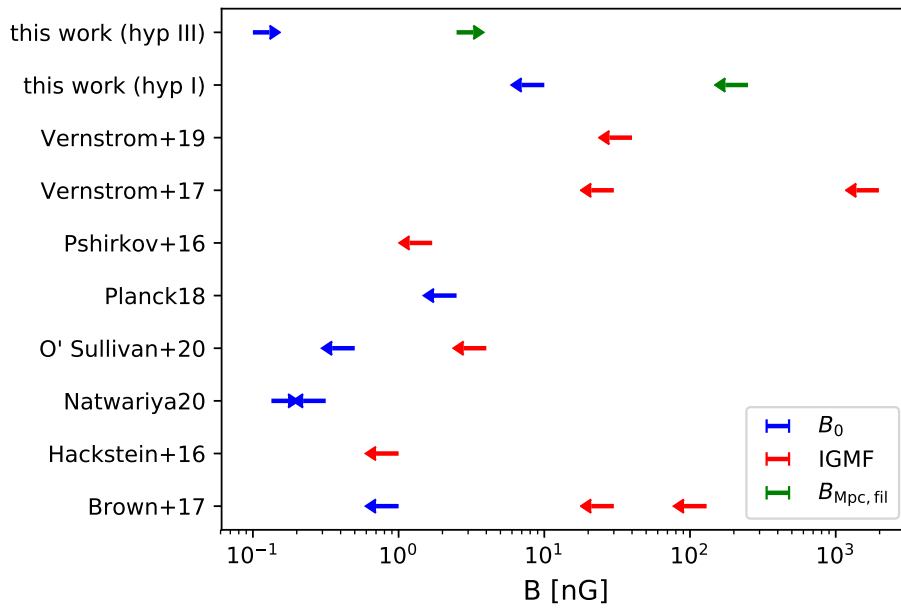


Figure 2.22: Summary of the current upper and lower limits to the volume-averaged IGMF (red arrows), B in the filaments' WHIM (green arrows) and B_0 (blue arrows).

Chapter 3

Faraday Rotation

3.1 The Faraday effect as a probe of the IGMF

The Faraday rotation effect is a powerful probe to detect magnetic fields embedded into an ionised gas. This set up is generally met across the IGM, usually assumed as an ideal plasma permeated by the IGMF. The Faraday rotation effect was first discovered in 1845 by Michael Faraday and it provided the very first evidence of the fundamental relation between electromagnetic phenomena and light, subsequently successfully theorized by James Clerk Maxwell a few years later. It consists in the rotation of the polarization angle ψ of linearly polarized light of wavelength λ passing through a dielectric material in the presence of a magnetic field. The polarization angle ψ rotates proportionally to the square of the wavelength λ^2 of the incoming light. The constant of proportionality is called *rotation measure* (RM), such that:

$$\psi - \psi_0 = RM\lambda^2 \quad (3.1)$$

where ψ_0 is the angle of the polarization plane of the light at $\lambda = 0$, or equivalently the polarization angle before the light passes through the magnetised dielectric ($RM = 0$, see Eq. 3.4 below). In practice, since $\lambda = 0$ is non-physical, ψ_0 can be approximated to the polarization angle at energy large enough so that $RM\lambda^2$ becomes negligible. For instance, for low RM values such the ones expected in the filament of the cosmic web $RM \sim 1 - 10 \text{ rad m}^{-2}$ this condition is met at lower energies (i.e. lower frequencies) with respect to the larger RMs arising from the ICM $RM \sim 10 - 100 \text{ rad m}^{-2}$ (Govoni et al., 2006, 2010; Bonafede et al., 2013). By measuring the polarization angles ψ_1 and ψ_2 at different wavelengths

$\lambda_1 \neq \lambda_2$ one can compute the quantity

$$\Delta\psi \equiv \psi_2 - \psi_1 = \psi_0 + RM\lambda_2^2 - (\psi_0 + RM\lambda_1^2) = RM\Delta\lambda^2 \quad (3.2)$$

where we defined $\Delta\lambda^2 \equiv \lambda_2^2 - \lambda_1^2$. The rotation measure is then obtained from observable quantities as

$$RM \left[\frac{\text{rad}}{\text{m}^2} \right] = \frac{\Delta\psi}{\Delta\lambda^2} \quad (3.3)$$

The RM factor was experimentally found to be proportional to: a) the amount of free electrons into the dielectric material (or equivalently the ionization fraction of a gas); b) the magnetic field strength in the direction parallel to the direction of propagation of the light B_{\parallel} ; c) the distance travelled through the magneto ionized medium $\int dl'$. The constant of proportionality can be directly derived from Maxwell equations and it relates it to the microphysics as

$$RM = \frac{e^3}{2\pi m_e^2 c^4} \int_L n_e(l) B_{\parallel}(l) dl \quad (3.4)$$

and by inserting the universal constant values, a more convenient form for astrophysical use can be considered:

$$RM = 0.81 \left[\frac{\text{rad}}{\text{m}^2} \right] \int_{\text{source}}^{\text{observer}} \frac{n_e(l)}{\text{cm}^{-3}} \frac{B_{\parallel}(l)}{\mu\text{G}} \frac{dl}{\text{pc}}. \quad (3.5)$$

The RM thus carries the combined information on the magnetic field weighted by the free electron content along the path between the source of linearly polarised light and the observer. Astronomers would not benefit from this effect if the sky was empty of sources of linearly polarised light. Luckily enough, synchrotron radiation powered by electrons holding a power-law energy distribution with index s generally retains, at the source, a few percent of linear polarization with respect to the total intensity, that is about

$$p[\%] = \frac{s+1}{s+7/3} \quad (3.6)$$

([Rybicki and Lightman, 1986](#)). Moreover, synchrotron emission is the mechanism that produces light for most radio galaxies detected above a few \sim mJy in the form of powerful radio jets and lobes of relativistic particles ejected from AGN. Deeper surveys may instead start to scratch the brightest end of the population of the so-called star-forming radio galaxies. In this

case, the sum of the synchrotron emission released over all the supernova events into the early-type galaxies' lifespan is detected at \sim GHz frequencies below ~ 0.1 mJy (Seymour et al., 2008). Considering that the LSS of the cosmic web develops only at late times with respect to the age of the Universe, that is about $z \leq 0.1$, whereas the distribution of radio galaxies and AGN peaks at higher redshift (Peacock, 1985; Willott et al., 2001), deep observations at radio wavelengths can provide us with a relatively dense grid of background sources of linearly polarized light. The denser the grid, the better will be the tomography of the magnetic field of the foreground LSS. We note that the existence of synchrotron radio sources is not the only (nor the main) reason to make the radio band the optimal one for measuring the Faraday effect in astronomy: the dependence of RM from $\Delta\lambda^2$ in fact greatly favours large wavelengths (i.e. low frequencies) with respect to short ones (i.e. high frequencies) when measuring small RMs, such as the values expected to arise from the relatively small densities ($n_e \leq 10^{-4} \text{ cm}^{-3}$) and weak magnetic field strengths ($B \simeq 0.1 \mu\text{G}$) of the cosmic web. If extended along a ~ 1 Mpc region along the LoS, such values would imply a rotation of the polarization angle with $RM \simeq 8 \text{ rad m}^{-2}$.

Evidence for the substantial magnetisation in the periphery of galaxy clusters has been presented already through the Faraday rotation effect. For instance, Bonafede et al. (2013) detected an excess in the RM computed along one sector of the Coma cluster, where also a radio relic is present. The observed RM requires significant amplification in excess to the $B \propto n_e^{2/3}$ drop due to the decreasing gas density, in the frozen-field approximation (Murgia et al., 2004; Bonafede, 2010). This result was found to be compatible with an enhancement of gas density and magnetic fields due the interaction of the cluster atmosphere with an infalling filamentary accretion, over \sim Mpc scales, which has also been suggested by radio continuum data (Brown and Rudnick, 2011).

O'Sullivan et al. (2019), using data from the LOFAR Two Metre Sky Survey (LoTSS), by studying the Faraday rotation measure (RM) and depolarisation of the RM signal through several LoS across the giant (LLS= 3.38 Mpc) radio galaxy J1235+5317 ($z = 0.34$), found a mean RM difference between the lobes of $2.5 \pm 0.1 \text{ rad m}^{-2}$, together with an RM variations at small scales of $\sim 0.1 \text{ rad m}^{-2}$. In addition to this, they checked for the presence of foreground LSS filaments based on optical spectroscopic source catalogues in the local universe and found an excess of filaments intersecting the LoS to one of the two radio lobes with respect to the other. By associating the entire RM difference between the lobes to the LSS filaments

excess allowed the authors to infer a gas density-weighted IGMF strength of $0.3\mu\text{G}$.

Similarly [Stuardi et al. \(2020\)](#) studied the polarization properties at low (LOFAR) frequencies of a large sample of radio galaxies (lobes) selected with a lower cut on their physical size and under-dense local environment. This features make the catalogue suited to probe the weak intergalactic magnetic field characterised by small RMs ([Akahori and Ryu, 2015](#)), to which LOFAR is very sensitive ($< 1 \text{ rad m}^{-2}$). Their analysis showed that indeed the lobes expand into a low-density local environment ($n_e < 10^{-5} \text{ cm}^{-3}$), permeated by weak ($< 0.1\mu\text{G}$) magnetic fields with fluctuations on scales of $3 - 25 \text{ kpc}$.

Last but not least, the correlation of RM from radio galaxy lobes can be profitably exploited to constrain the IGMF strength ([Vernstrom et al., 2019](#)), as we already discussed in the Introduction (see Sec. 1.3.2).

Dense RM grids are available today down to the $\sim \text{deg}^2$ scale ([Brown et al., 2003](#); [Anderson et al., 2020](#); [Riseley et al., 2020](#)). In order to probe single LSSs the angular scale must be reduced while keeping the surface density of sources large enough ([Vacca et al., 2016](#); [Akahori, 2018](#)) and complementary proxies for the LSS presence and characterization are needed in order to disentangle the $n_e B_{\parallel}$ product in Eq. 3.4. Deep observations with current instruments are crucial to this aim ([Akahori et al., 2014](#)). Within this context, in this Chapter we present studies on the feasibility and issues of accessing the RM contribution of the cosmic web from both a theoretical and observational point of view.

In Sec 3.2, by means of cosmological MHD simulations, we model the likelihood of distinguishing filament RM signal from a random grid of radio background sources detected around massive galaxy clusters, as function of their number and signal to noise, assuming realistic/nominal instrumental set-up for current/future experiments. We demonstrate that predictions and detection chances are highly dependent on the RM scatter intrinsic to the source population which may be due to either the near-source or the foreground environment (see also [Vacca et al. 2016](#)), as well as to the physical processes that seed and amplify magnetic fields. The work is aimed to design future experiments with a proper strategy able to minimize systematic errors.

In Sec. 3.3 we develop such strategies over the interferometric observation of a best-candidate LSS target, found around the massive galaxy cluster Abell 2744. Although the experiment benefits from a large amount of data and a thorough and motivated strategy, it can not be yet addressed as conclusive due to the presence of large systematics. However, our work becomes paramount to clearly address what further steps and developments

shall be undertaken in the near future to access similar important scientific goals.

3.2 The Challenge of Detecting intra-cluster Filaments with Faraday Rotation (Locatelli et al., 2018)

Abstract The detection of filaments in the cosmic web will be crucial to distinguish between the possible magnetogenesis scenarios and future large polarization surveys will be able to shed light on their magnetization level. In this Section, we use numerical simulations of galaxy clusters to investigate their possible detection. We compute the Faraday Rotation signal in intra-cluster filaments and compare it to its environment. We find that the expected big improvement in sensitivity with the SKA-MID will in principle allow the detection of a large fraction of filaments surrounding galaxy clusters. However, the contamination of the intrinsic Faraday Rotation of background polarized sources will represent a big drawback to the number of objects that can be significantly detected. We discuss possible strategies to minimize this effect and increase the chances of detection of the cosmic web with the large statistics expected from future surveys.

3.2.1 Faraday rotation in galaxy clusters

Magnetic fields in the Universe are observed to permeate a very wide range of spatial scales, from planetary ($\sim 10^6\text{m}$) to galactic ($\sim\text{kpc}$), up to galaxy cluster scales ($\sim\text{Mpc}$). However, at the largest scales, their value is constrained only in the regions where the plasma density and temperature allow their observation, i.e. in the ICM (e.g. Feretti et al. (2012) and references therein for a review). The amplification of magnetic fields in cosmic structures might have proceeded in a bottom-up small-scale turbulent dynamo (e.g. Ryu et al., 2008). Under such conditions, the dynamo should have erased most traces of the initial magnetization seeds, bringing the magnetic energy density close to equipartition with the plasma kinetic energy in galaxy clusters. This scenario well explains the observed magnetic fields in galaxy clusters, i.e. for densities and temperatures of $n \geq 10^{-4} [\text{cm}^{-3}]$ and $T \sim 1 - 10 \text{ keV}$, respectively, as supported by numerical simulations (e.g. Dolag et al., 1999; Vazza et al., 2017; Donnert et al., 2018).

On the other hand, the magnetization in the intergalactic medium (IGM) outside the virial radius of galaxy clusters ($n < 10^{-4} \text{ cm}^{-3}$ and temperature $\sim 10^5 - 10^7 \text{ K}$), is instead still largely unconstrained, despite that this gas phase should contain a large fraction ($\sim 50 - 60\%$) of the baryonic mass of the Universe. Measuring the magnetic field intensity and morphology in the IGM is crucial to constrain the primordial origin of extragalactic fields, out of which present day magnetic structures might have evolved (e.g. [Widrow et al., 2012](#)). Unluckily, direct observations of magnetic fields in the IGM are made challenging by the very high sensitivity required for the imaging (at most wavelengths).

Among the techniques nowadays available to study extragalactic magnetic fields there are several promising algorithms which apply to the rotation measure (RM) of linearly polarized signals emitted by radio galaxies. In particular, RM Synthesis ([Brentjens and de Bruyn, 2005](#)) is a powerful tool to extract valuable information from both magnetized layers and emitting sources along the line-of-sight (LOS). Attempts to constrain extragalactic magnetic fields on statistical bases have set upper limits at the level of $0.3 - 7 \mu\text{G}$ ([Xu et al., 2006](#); [Oppermann et al., 2015](#))¹. Very recently, the possible detection of the RM contribution by filaments overlapping the polarised emission by a giant radio galaxy has been presented by [O’Sullivan et al. \(2019\)](#) using LOFAR observations.

The application of RM Synthesis to galaxy cluster outskirts and filaments is limited by the low statistics of strong and diffuse background sources. In particular, diffuse sources would be of great interest since they probe several LoSs through the magnetized plasma. While the JVLA may already provide a detection threshold in polarization which is low enough to detect the "tip of the iceberg" of faint background sources as well as of the diffuse emission from shocks around filaments and clusters, a larger statistics of faint ($\leq 10 - 100 \mu\text{Jy}$) sources is expected from future radio facilities.

In particular, planned large radio polarisation surveys (e.g. with ASKAP, MeerKAT and the SKA-MID) will enable the use of hundreds of sources in the background of massive galaxy clusters for background RM studies ([Govoni et al., 2013](#); [Akahori et al., 2014](#); [Johnston-Hollitt et al., 2015](#); [Govoni et al., 2015](#); [Bonafede et al., 2015](#); [Loi et al., 2019b,a](#)). Moreover, statistical methods based on Bayesian inference are also being developed to allow a robust removal of the various galactic and extragalactic foreground contri-

¹Upper limits in the same range have been reported by statistical studies of cross-correlation between radio surveys and galaxy catalogs by [Vernstrom et al. \(2017\)](#) and [Brown et al. \(2017\)](#).

bution to the observed RM (Vacca et al., 2016). The deployment of large systematic polarization surveys will also enable the use of Fast Radio Burst as powerful lighthouse to study cosmic magnetic fields via RM analysis (Akahori et al., 2016; Vazza et al., 2018a; Akahori et al., 2018).

To date, only a few hints of the hottest ($\sim 10^5 - 10^7$ K) phase of the IGM, called the Warm Hot Intergalactic Medium (WHIM, see Nicastro (2016) for a recent review), have been detected by X-ray observations of cluster outskirts (e.g. Eckert et al., 2015, for A2744). Complementary to this, also microwave observations of the Sunyaev-Zeldovich (SZ) effect from single objects (e.g. Planck Collaboration et al., 2013; Bonjean et al., 2018) or via stacking (e.g. de Graaff et al., 2019) proved to be effective in detecting gas in filaments connecting closely interacting clusters.

Present or future available X-ray and SZ data provide a straightforward estimate of the gas density. Since the RM induced by a magnetized medium on polarized light depends linearly on the product of the magnetic field along the LoS (B_{\parallel}) and the density of the free electrons in the medium, RM observations can provide a powerful estimate of B_{\parallel} if robust estimates of the thermal electron density are available.

Here, we use numerical simulations to address for the first time the possibility of detecting at least the high-RM end of the magnetised cosmic web, by focusing on the observations of intra-cluster filaments connected to massive galaxy clusters via the Faraday Rotation effect. Despite the unavoidable uncertainties related to the correlation of density and magnetic field fluctuations in the WHIM of intra-cluster filaments, which affect the interpretation of RM data, this approach has the advantage of being independent of the distribution of relativistic electrons on such a large scale, which introduces instead other uncertainties (mostly connected to the unknown particle acceleration efficiency in such rarefied environments) in the quest for large-scale synchrotron emission from the cosmic web (e.g. Brown, 2011; Vazza et al., 2015b; Vernstrom et al., 2017; Brown et al., 2017)

3.2.2 Predictions of magnetic fields in filaments

The plasma conditions of the WHIM of typical cosmic filaments are predicted to be supersonic ($\mathcal{M} \sim 1 - 10$), with gas accretion mostly leading to predominantly compressive turbulence (Ryu et al., 2008). In particular, under the assumption of a small-scale dynamo amplification of weak seed magnetic fields and assuming a turbulent forcing time of $\sim 10 t_{\text{eddy}}$ (where $t_{\text{eddy}} \sim l_{\text{eddy}}/\sigma_v$ is the eddy turnover time for an eddy with linear size l_{eddy} and a velocity dispersion σ_v), Ryu et al. (2008) predicted a magnetic field

strength of

$$B_{\text{rms}} \simeq (8\pi \epsilon_{\text{turb}} \phi)^{1/2} \quad (3.7)$$

where ϵ_{turb} is the turbulent kinetic energy density and ϕ is a factor that accounts for the growth of magnetic energy under the typical local conditions. [Ryu et al. \(2008\)](#) estimated $\phi \sim 0.3 - 0.4$ and based on the gas conditions in their simulated filaments they concluded that that $B_{\text{rms}} \sim 10 - 10^2$ nG for the most massive and hot ($\geq 10^7$ K) filaments.

Based on the above picture, [Cho and Ryu \(2009\)](#) suggested the following formula for the RM dispersion across different lines of sight crossing a filament's volume:

$$\sigma_{\text{RM}} \sim 5 \text{ rad/m}^2 \frac{n_e}{10^{-4} \text{cm}^{-3}} \left(\frac{L_{\text{fila}}}{5 \text{ Mpc}} \right)^{1/2} \left(\frac{l_{\text{eddy}}}{0.3 \text{ Mpc}} \right)^{1/2} \frac{B_{\text{rms}}}{100 \text{ nG}} \quad (3.8)$$

where n_e is the thermal electron number density, L_{fila} is the filament thickness and l_{eddy} is the integral scale of the magnetic field power spectrum. It shall be remarked that in the above picture the typical magnetic field strength, B_{rms} , and the typical RM dispersion are reached *regardless* of the seed magnetic field, because in this scenario the final magnetisation is dominated by the dissipation of kinetic into magnetic energy, in a process in which any dependence on the initial seed field is soon lost.

While in the above case the scales and the strength of the amplified field B_{rms} are linked together, direct numerical simulations of magnetic field growth in filaments have disputed the above picture, which was derived assuming an entirely solenoidal forcing of turbulence in the IGM, forced for ~ 10 dynamical times ([Ryu et al., 2008](#)). Fully MHD cosmological simulations have indeed recently investigated the presence of small-scale magnetic dynamo amplification in cosmic filaments, reporting little-to-no evidence for volume-filling dynamo amplification (e.g. [Brüggen et al., 2005](#); [Vazza et al., 2014](#); [Marinacci et al., 2015](#); [Vazza et al., 2017](#)), opposite to the case of galaxy clusters simulated with the same techniques, in which case a small-scale dynamo has been observed (e.g. [Dolag et al., 1999](#); [Vazza et al., 2017](#)). The physical reason is that there is only a fairly limited number of dynamical times for amplifying the field as the magnetic eddies are advected onto the neighboring clusters, with velocities of several $\sim 10^2$ km/s, and moreover the input turbulent energy is predominantly supersonic (e.g. [Vazza et al., 2014](#); [Gheller et al., 2016](#)). This suggests that in general the medium

in filaments is an environment disfavoring the onset of efficient dynamo amplification.

In the lack of small-scale dynamo amplification, the magnetic field amplitude is anchored to the amplitude of the seed field via compression:

$$B_{\text{fila,low}} \simeq B_0 \cdot \left(\frac{n_e}{\langle n \rangle} \right)^{\alpha_B} \quad (3.9)$$

where B_0 is the seed field, $\langle n \rangle$ is the cosmic mean (gas) density and $\alpha_B \approx 2/3$ for isotropic gas compression. Cosmic filaments are only mildly non-linear objects of the cosmic web, and their average density is $n_e \sim 5 - 10 \langle n \rangle$ (e.g. Colberg et al., 2005; Dolag et al., 2006), hence their average magnetic field is only $\sim 3 - 5$ times larger than the original B_0 seed field. However, recent MHD simulations of cosmic filaments showed that the axial gas density profile of filaments is stratified at least over one decade (Gheller et al., 2015), as well as that the gas density fluctuations within filaments can extend up to $\sim 2 - 3$ decades in range, due to presence of substructures (Gheller et al., 2016). Hence while Eq. 3.9 gives a lower limit on the average magnetic fields in filaments for a given primordial magnetic seed, the internal distribution of magnetic field fluctuations can be as large as $B_{\text{fila,high}} \sim 10^2 - 10^3 B_0$ in simulations (Gheller et al., 2016). If this also happens in the real Universe, we should expect that the distribution of RMs from filaments can stretch over $\sim 4 - 5$ orders of magnitude, since density and magnetic field fluctuations are well correlated in the compressive regime (at scales $\geq 100\text{kpc}$), which would likely bias detections of RM towards the highest value of the distribution.

A scenario complementary to the "primordial" one is the one in which the seeding of magnetic fields in large-scale structures is entirely due to the "pollution" of magnetic fields by AGN and galactic activities (e.g. Donnert et al., 2009; Xu et al., 2009). In this case, little correlation should be expected between density and magnetic field fluctuations, yet the range of magnetic field values in filaments (and hence of RMs) is expected to be much more extended than in a primordial scenario, owing to the dilution of ejected magnetic fields away from sources, as well as by the expected drop in the number density of sources moving into the less dense Universe (e.g. Marinacci et al., 2015; Vazza et al., 2017).

3.2.3 Simulations of extragalactic magnetic fields

We simulated the formation of massive galaxy clusters using a customised version of the cosmological grid code ENZO (Bryan et al., 2014). We used the Dedner formulation of MHD equations (Wang and Abel, 2009) and used adaptive mesh refinement (AMR) to increase the dynamical resolution (e.g. Xu et al., 2009).

In this work, we mostly focus on *non-radiative* cosmological simulations that include only the effects of cosmic expansion, gravity and (magneto)hydrodynamics. However, in Sec .3.2.9 we also include for completeness simulations with cooling and feedback by AGN.

Each cluster forms in a volume of $(260 \text{ Mpc})^3$ (comoving), and is simulated starting from a root grid 256^3 cells and using 256^3 dark matter particles. The initial density perturbation field is taken from a suite of existing cluster simulations (e.g. Vazza et al., 2010, and other works derived from this). The innermost $\sim 25 \text{ Mpc}^3$ volume, centred on where each cluster forms, has been further refined 5 times (2^5) using AMR. Mesh refinements are initiated wherever the cell gas density is $\geq 1\%$ higher than its surroundings. This give us a maximum spatial resolution of $\Delta x_{\text{max}} \approx 31 \text{ kpc}$. The mass resolution for dark matter particle in the high resolution region is $m_{\text{DM}} = 9.1 \cdot 10^{10} M_{\odot}$ for all clusters.

The assumed cosmology in this Section is a Λ CDM model with: $H_0 = 72 \text{ km s}^{-1} \text{ Mpc}^{-1}$, $\Omega_{\text{M}} = 0.258$, $\Omega_{\text{b}} = 0.0441$ and $\Omega_{\Lambda} = 0.742$.

In this work we focus on three massive ($M_{100} \sim 10^{15} M_{\odot}$) simulated galaxy clusters, drawn from a larger sample: a) cluster "e1", with a virial mass of $M_{100} = 1.12 \cdot 10^{15} M_{\odot}$ and a virial radius of 2.67 Mpc, which was interested by a major merger at $z \approx 0.1$; b) cluster "e14", with a virial mass of $M_{100} = 1.00 \cdot 10^{15} M_{\odot}$ and a virial radius of 2.60 Mpc, which is in a fairly relaxed dynamical state by $z = 0$; c) cluster "e18b", with a virial mass of $M_{100} = 1.37 \cdot 10^{15} M_{\odot}$ and a virial radius of 2.80 Mpc, which was interested by a major merger at $z \approx 0.5$ and still is in a perturbed dynamical state at $z = 0$.

Our baseline model for the magnetic field in clusters is a simplistic "primordial" seeding scenario, in which we initialised the magnetic field to a uniform value B_0 across the entire computational domain, along each coordinate axis (Wittor et al., 2017; Vazza et al., 2018b). The initial magnetic seed field of 0.1 nG (comoving) is chosen to be below the upper limits from the analysis of the CMB (e.g. Subramanian, 2016), as well because with this initial magnetic field strength our simulations are able to produce a reasonable match to observed radio relic power (Wittor et al., 2017) as well as to

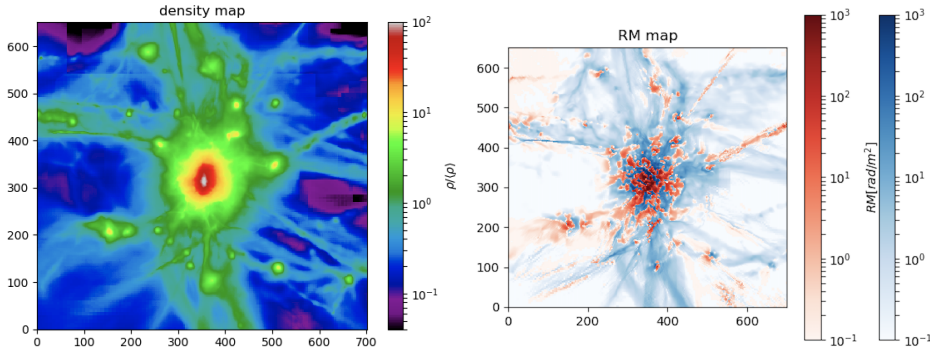


Figure 3.1: Projected gas density (left) and RM (right) for our cluster e18b at $z = 0$, for the non-radiative run with primordial magnetic fields. Each box has sides $22 \times 20 \text{ Mpc}^2$. X and Y coordinates show pixel number. Pixels have resolution of $\simeq 31 \text{ kpc}$.

In the RM map, we show with red colors pixels with $\text{RM} > 0$ and with blue colors the pixels with $\text{RM} < 0$.

the observed Faraday Rotation profile for the Coma cluster (Vazza et al., 2018b). An example of the projected gas density and RM for one of our simulated clusters is given in Fig.3.1, which shows the volume around each clusters that will be subject of our filament analysis. We notice already that the visible part of filaments connected to our objects is only a small fraction of the much more extended (and more rarefied) length of typical cosmic filaments, which is of several tens of Mpc in the cosmic volume (e.g. Gheller et al., 2015).

These simulations are non-radiative and there are no sources of thermal, kinetic or magnetic feedback. In order to bracket uncertainties, we will also test in Sec. 3.2.9 resimulations of the same clusters using an alternative scenario in which magnetic fields in the same objects have been seeded by past activity of AGN.

3.2.4 Filament selection and properties

Starting from the small sample presented above, we pre-selected filaments in each cluster and analyzed their projected properties along the three coordinate axis, in order to have preliminary set of 9 independent targets for our mock observation of RM in filaments.

For every 2-dimensional radial shell (with a fixed radial bin of $\Delta x = 31 \text{ kpc}$), and starting from R_{100} , we selected all the pixels with a projected

density in the range 66 – 98% of the density distribution, which efficiently tracks the gas which is in filaments but not clumped (by self-gravity and over-cooling) into dense substructures. Additionally, we limited our analysis to the $T \geq 10^6$ K projected temperature, in order to include only gas that can be potentially associated to soft X-ray emission. This procedure is designed to broadly mimic the selection based on X-ray or optical observations, which will become available in the next decade based on the combination of large surveys (e.g. Euclid, eRosita and more in the future, Athena).

The filaments were termed with the first three characters referring to the simulated cluster from which they were taken (e01, e14 or e18); a letter telling the axis along which the cluster was observed in order to retrieve different realizations (X, Y or Z); one or two letters telling the filament direction on the sky with respect to the cluster (N=North, S=South, E=East, W=West). Although automatic algorithms for the detection of cosmic filaments in 3-dimension have been developed also for our simulations (Gheller et al., 2015), here in the further analysis of data for simplicity we proceeded to the *visual* identification of single filaments around each cluster. The final dataset used for the following analysis consists of 29 filaments in total.

3.2.5 Mock Rotation Measure observations

Our predictions assume a uniform random distribution of polarised radio sources in the background of our clusters. For all 29 filaments in our sample, we extracted an increasing number ($N_S = \{5, 10, 15, 20, 25, 40, 65, 100\}$) of sources at random locations, and computed the statistical distribution of RM across the Faraday screen produced by each cluster and its environment (within a $\approx 25^3$ Mpc³ volume). For each run, we considered an equal number of sources in a "control field" (i.e. a field where there are no filaments or galaxy groups) as well as in a "filament" field (selected as above).

Beyond the effect of external RM from the cosmic web, for each mock observation we additionally included:

- A fixed contribution to RM from the Galactic foreground. We restricted ourselves to targets at high galactic latitude ($\geq 80^\circ$), for which the RM contribution is in general of $|RM_{\text{Gal}}| \leq 10$ rad/m² (Oppermann et al., 2015). In particular, we assumed here for simplicity a fixed +6.0 rad/m² contribution to each field, noticing that this contribution should in general be the easiest to disentangle in real observations, because the extent of the typical size of filaments around

galaxy clusters we consider here is $\leq 0.1 - 0.5^\circ$, i.e. much smaller than the typical angular scales of variations of the Galactic foreground. For example, based on Eq. 20 in [Anderson et al. \(2015\)](#), we can estimate a typical RM fluctuation of $\leq 0.5 \text{ rad/m}^2$ across 0.5° from the Galactic foreground.

- a residual contribution to the RM, RM_{res} , which includes an internal contribution to each background source RM_{src} ; a contribution from other extragalactic sources as intervening MgII absorbers RM_{MgII} ([Joshi and Chand, 2013](#)); a residual RM after Galactic foreground subtraction which can be present on scales smaller than the one used to fit the Galactic contribute $\text{RM}_{\text{MW, res}}$. This value has been estimated by [Schnitzeler \(2010\)](#) to be normally distributed with standard deviation $\sigma_{\text{res}} \leq 6 \text{ rad/m}^2$ and has been confirmed by [Banfield et al. \(2014, \$\sigma_{\text{ERS}}\$ in their work\)](#). We follow their procedure and put RM_{src} , RM_{MgII} and $\text{RM}_{\text{MW, res}}$ together in RM_{res} . However [Banfield et al. \(2014\)](#) note that the value is dependent on the background source population. At 1.4 GHz, the WISE-AGN population defined in [Jarrett et al. \(2011\)](#) biases the estimate of σ_{res} and shows a larger $\sigma_{\text{res}} = 12 \pm 0.2 \text{ rad/m}^2$. We thus consider the latter as a more conservative case, while we considered $\sigma_{\text{res}} = 6 \text{ rad/m}^2$ as a standard case based on literature works ([Schnitzeler, 2010](#); [Banfield et al., 2014](#)) that can be optimized e.g. using only star-forming nearby galaxies for background studies.

We thus randomly draw the RM_{res} value from a Gaussian distribution with standard deviation $\sigma_{\text{res}} = 12$ or 6 rad/m^2 , depending on the assumed background source population.

- The estimated error to RM $\delta_{\text{RM}} = \sqrt{3}/(\text{S/N}_P \Delta\lambda_{\text{max}}^2)$ ([Brentjens and de Bruyn, 2005](#); [Rudnick and Owen, 2014](#)) where S/N_P is the signal-to-noise ratio of the source in the polarized image and $\Delta\lambda_{\text{max}}^2$ is the difference between the largest and smallest observed λ^2 . Also for the latter we considered two possible different values: a) JVLA-like observations in which $\delta_{\text{RM}} = 8 \text{ rad/m}^2$ (assuming wide total bandwidth $\Delta\nu \simeq 1\text{GHz}$, L-band observations of background sources with $\text{S/N}_P > 3$); b) SKA-MID-like observations in which $\delta_{\text{RM}} = 1 \text{ rad/m}^2$ which corresponds to current estimates for SKA-MID performances (e.g. [Govoni et al., 2015](#)).

The simulated statistics are important to assess the crucial improvements in the significance of detections, as a function of the number of detected RMs (N_S) in the field and in filaments.

3.2.6 Non-parametric tests of RM distributions

We tested the null hypothesis that two random sets of RMs in filament and control field to belong to the same parent distribution. For each random run, the two sets of RMs are assembled by extracting N_S random values from the simulated distribution of RMs inside and outside the projected filamentary environment respectively, and added with noise, as defined in the previous section 3.2.4.

In detail, we performed the random extraction of 1000 trials for an increasing number of N_S sources, and computed the distribution of p-values from the Mann-Whitney (M-W) U test (Neuhäuser, 2011). We reject the null hypothesis whenever the p-value of the test is lower than or equal to $\alpha \equiv 0.05$, where α is the significance level. The Mann-Whitney U test has the advantage to test the equivalent null hypothesis that it is equally likely that a randomly selected value from one sample will be less than or larger than a randomly selected value from a second sample, which is precisely what we want to determine. This test does not require any assumption on the two compared distributions (non-parametric test).

Compared to the other more widely used non-parametric test: the Kolmogorov-Smirnov (K-S) D test, the M-W U test is known to be more reliable for small samples and therefore best suited for our analysis.

The number of rejected U tests (between the filament and control sets of N_S RM values each) over the 1000 tests randomly picked, is defined as the rejection fraction corresponding to the number N_S . High values of the rejection fraction (given in the following figures) will indicate high chance to detect a RM excess scatter in the filament set, with respect to the control field. Our fiducial rejection fraction threshold for calling a filament as detectable is set to 0.2. Though it gives a still low chance probability (1/5 of the times we test it against a control field), rejection fractions above this level are shown to actually improve with an increasing number of polarized background sources N_S . Lower rejection fractions are instead still dominated by systematics related either to the instrument or to the background source models.

3.2.7 Detectability of intra-cluster filaments using RM

We can now assess the chances of detecting the magnetic cosmic web connected to massive galaxy clusters under realistic observing conditions, by focusing on the challenge of significantly distinguish the excess RMs in filaments compared to control fields. In this mock observing procedure, we

assume to know the approximate location of filaments in the cluster neighborhood based on the X-ray or optical data (e.g. Eckert et al., 2015; Connor et al., 2018), and studying how many detected RMs will be necessary to statistically distinguish filaments from control fields, based on the outcome of the M-W test (averaged over 1000 independent realizations for each number of sources).

First, we show in Fig. 3.2 the rejection fraction of all the filaments in the sample for both a JVLA-like observation (upper panel) and a SKA-MID-like one (lower panel), as a function of N_S and in the ideal case in which there is no contamination from the residual RM on background sources ($\sigma_{\text{res}} = 0 \text{ rad/m}^2$). In this case, the key factor for the efficient detection of filaments compared to control fields is the sensitivity of the radio telescope. Even without the contamination from background and intervening sources, a JVLA-like observation will be able to significantly detect a handful of objects only by observing $N_S \geq 50$ sources. On the other hand, with the ~ 8 times increased sensitivity of the SKA-MID we observe a remarkable improvement in the simulated detection rate, with the majority of objects in the sample being fully (or marginally) detectable for a large number of sources. Even with ~ 10 sources per filament, a half of the objects in our sample should be statistically detectable against control fields.

However, the situation dramatically changes as soon as the additional contribution from the residual RM is included in the analysis.

In Fig. 3.3 we plot the rejection fraction of all the filaments in the sample for both a JVLA-like observation (left panels) and a SKA-MID-like one (right panels), as function of N_S .

For the magnetic field model considered here, it seems challenging for any JVLA-like observation to robustly distinguish the RM distributions of filament and control field sets, also with the unrealistically large number of $N_S = 100$ sources per single object. This is due to the low RM contribution of the Faraday screen (i.e. the magnetized plasma in the filament) when compared with the scatter of the assumed distribution of RM produced both internally and along the line of sight outside the filament (σ_{res}). Banfield et al. (2014) attribute the RM scatter along the line of sight as a contribution of both internal RM and intervening magnetized substructures and show that it can vary with the background source population. By considering the possibility of selecting only background sources with 6 rad/m^2 (Fig. 3.3, lower panels) our test show that a tentative detection of a few prominent filaments becomes possible for $N_S \geq 50$ sources.

Even in the most optimistic situation considered here, i.e. a survey

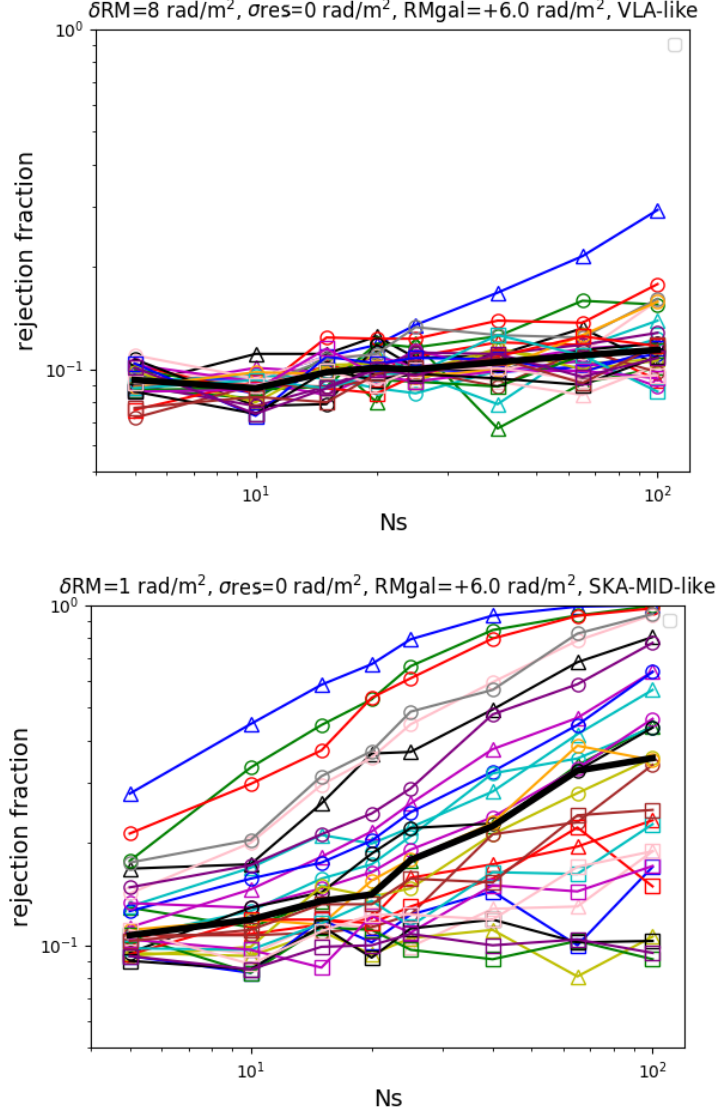


Figure 3.2: Fraction of rejected MW tests between target and control sample RM distributions (i.e. fraction of detections), for a given number N_S of available polarized background sources (i.e. RMs) in and around a filament. We assumed a primordial seeding scenario and set σ_{res} to 0 rad/m^2 for the residual RM on background sources. Different colors mark different filaments, whereas equal symbols point to the same mock central cluster. The solid black line show the median of the distribution. Upper panel: JVLA-like RM sensitivity $\delta_{\text{RM}} = 8 \text{ rad m}^{-2}$; Lower panel: SKA-MID-like sensitivity $\delta_{\text{RM}} = 1 \text{ rad m}^{-2}$. Color and mark codes of filaments are consistently kept through all the plots in this work.

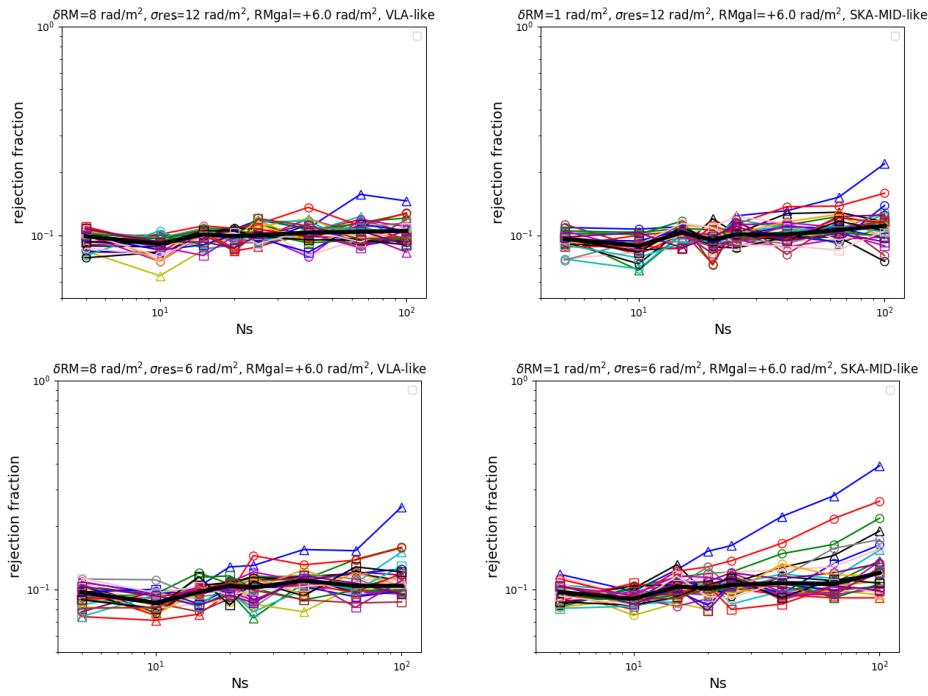


Figure 3.3: Rejection fraction for an increasing number of detected RM as in Fig. 3.2, but by assuming $\sigma_{\text{res}} = 12 \text{ rad/m}^2$ for the residual RM of sources (top panels), while the lower panels we assumed $\sigma_{\text{res}} = 6 \text{ rad/m}^2$.

with SKA-MID and a low contribution from residual RM on sources, the statistical detection of intra-cluster filaments will be feasible only for a small fraction of objects.

All our results can be summarized as follows:

- On average, with our procedure we estimate that galaxy clusters have 3.3 ± 0.9 projected filaments which can be identified by X-ray inspection. This result is consistent with the results by Colberg et al. (2005), who found that $\sim 80\%$ of clusters have 1 to 4 projected connections between them.
- Filaments selected in our procedure are on average $\sim 10 - 50$ times denser than the smooth environment around galaxy clusters, have a mean temperature of $T \sim 1 - 5 \cdot 10^7$ K and an average magnetic field of $B_{\text{rms}} \sim 10 - 50$ nG (see Sec. 3.2.8).
- The typical RM in filaments is in the range $\sim 0.2 - 2$ rad/m² for the primordial seeding scenario considered here, i.e. a factor $\sim 10^2$ larger than the average RM distribution in our control fields for the detectable ones, ~ 30 times larger for filaments in general. However, the distributions of RMs can reach up to ~ 10 rad/m² in a few % of the cells, and the chances of confirming the presence of magnetic fields in filaments rely on the detection of such rare fluctuations.
- The rejection fraction has been fitted with a power-law trend with respect to the number of detected sources N_S . Considering the 7 filaments with the highest rejection fraction in the most favorable case (i.e. extragalactic residual RM noise small or absent), Fig. 3.2, lower panel), the best fit gives $\text{rej. frac.} \propto N_S^{0.55 \pm 0.05}$ before saturation. To this end, just the filaments showing an improved rejection fraction above detection threshold even for small samples ($N_S = 5, 10, 15$) were considered. Including the other filaments would affect the trend with random low rejection rates.
- Limited to the most favorable objects and for low contribution from residual RM on the sources, the increased sensitivity that will be provided by SKA-MID compared to JVLA-like observations improves the rejection fractions distribution by a factor $\sim 3(1.5)$ at $N_S = 100(20)$, while the number of observations with a rejection fraction larger than 0.5 increases from 0(0) to 9(3) over 29 objects.
- The actual limiting factor for the detection of filaments is the extragalactic residual RM scatter σ_{res} , more than the number of detected

sources N_S throughout the field. Going from $\sigma_{\text{res}} = 0 \text{ rad/m}^2$ to $\sigma_{\text{res}} = 6(12) \text{ rad/m}^2$ the rejection fraction median drops down by a factor 3(3.3) even for the SKA-MID-like observation with 100 sources per set, and the observations with a rejection fraction larger than 0.5 falls from 31% to 0% even for this large N_S value.

Given the results above, how do we plan an observation able to retrieve a sufficient number of polarized background sources?

The current estimate for the surface density of polarized sources n_s at the highest resolution ($1.6''$) at 1.4 GHz is given by [Rudnick and Owen \(2014\)](#) who find $n_s = 45(P/30\mu\text{Jy})^{-0.6} \text{ deg}^2$, determined in the GOODS-N field down to a sensitivity of $14.5 \mu\text{Jy}$. Assuming a physical area A_{fil} and a distance z for the target, we can estimate the necessary sensitivity P_{rms} in a similar observation ($1.6''$ resolution at 1.4GHz) to sample a typical intra-cluster filament and detect a number N_s of polarized sources

$$P_{\text{rms}} \simeq 3\mu\text{Jy beam}^{-1} \left(\frac{A_{\text{fil}}}{25\text{Mpc}^2} \right)^{\frac{5}{3}} \left(\frac{N_s}{100} \right)^{-\frac{5}{3}} \left(\frac{z}{0.1} \right)^{-3.03} \quad (3.10)$$

where we assumed the following scaling between physical and angular size of an object with redshift z to be $1.857[\text{kpc}/''](z/0.01)^{0.91}$ (this relation is correct within a 7% relative error for the redshift range $0.01 \leq z \leq 0.3$). We remark that the estimate of P_{rms} given here is valid, strictly speaking, only for a $\simeq (1.5'')^2$ synthesized beam. Determining the sensitivity at lower resolutions this is not a trivial task. In fact, beam depolarization effects are introduced and they can be properly taken into account just by modeling the polarization structure of the background source populations.

The SKA-MID survey is planned to reach $0.09 \mu\text{Jy}$ in 1000 hrs at 1.4 GHz frequency and with a ~ 3 times finer resolution ($\simeq 0.5''$ [Bonafede et al. 2015](#)). A typical intra-cluster filament would thus cover $\simeq 0.55 \text{ deg}^2$ in the sky, which is approximately the putative SKA-MID field-of-view ($\simeq 0.49 \text{ deg}^2$). A JVLA observation with similar settings (1GHz total bandwidth centered at 1.4GHz, A-configuration array with resolution $1.5''$, 40% flagged data) would cover the target with a 4 pointings mosaic, requiring 68hrs of total observing time to reach the required sensitivity of $3\mu\text{Jy beam}^{-1}$ (17h per single pointing).

In summary, while a $\sim \times 8$ increase in RM sensitivity with the SKA-MID will in principle allow the detection of a ten-fold larger amount of filaments surrounding galaxy clusters, in practice the unavoidable disturbance by the

intrinsic RM noise of polarized sources will dramatically limit the number of objects for which detections of RM can be made statistically significant compared to control fields.

3.2.8 Properties of most likely detectable filaments

What features make a filament more likely to be detected compared to the others?

To address this question we computed the distribution of the projected gas density and mean magnetic field for the entire distribution of pixels in filaments or control fields, and contrasted this with the distribution from a subset of the 4 most detectable filaments (Fig.3.4), based on the previous Section.

Somewhat surprisingly, both the distribution of projected gas density and of projected magnetic field strength do not significantly differ when we compare lines of sight crossing detectable filaments with the rest of the population (while, of course, lines of sight crossing filaments are significantly denser and more magnetised than lines of sight crossing pixels in the control fields). However, the RM also depends on the distribution of scales in the magnetic field (as in Eq. 3.8).

We thus computed the power spectra of magnetic fields in different 3-dimensional sub-volumes in the field of our cluster e18b, motivated by recent simulations by our group, in which the signature of magnetic dynamo in the innermost cluster regions clearly stems in power spectra (Domínguez-Fernández et al., 2019). In particular we selected a cubic 4^3 Mpc^3 box coincident with a clearly detectable filament connected to the cluster (right of the cluster centre in Fig.1), a similar box coincident with an undetectable filament (left of the cluster centre), and a cubic volume on an empty "control field" located at the cluster virial radius of e18b. The 3-dimensional power spectra of magnetic field and of the density-weighted velocity field ($\rho^{1/2} \vec{v}^2$) were computed with a standard Fast Fourier Transform (FFT) algorithm, similar to our previous work (e.g. Vazza et al., 2014), and are shown in Fig. 3.5.

Regions containing filaments show a $\sim 5-10$ larger kinetic energy budget at all scales, while the magnetic field energy is even 10^3-10^4 larger than the control volume for $k \geq 10$ (≤ 400 kpc) scales. On such scales, the magnetic energy in the detectable filament is a few percent of the kinetic energy,

²We notice that the density weighting in the velocity spectra ensures that the magnetic and velocity spectra have the same units and can be quantitatively compared, as in Vazza et al. (2018b).

while it is $\leq 10^{-5}$ of the kinetic energy in the undetectable filament. The visual inspection further suggests that the sub-volume around the detectable filament contains more gas substructures, which are likely responsible for enhanced density fluctuations and for the mixing of magnetic field lines on small-scales. While the clumpiest part of this volume is excised from our RM analysis (see Sec.3.2.4), a higher degree of structures within the filament implies that the environment has surely been subject to a higher dynamical activity in the recent past, which significantly boosted the magnetic field beyond compression.

In summary, the most promising filament targets seem to be characterized by a higher level of substructures, associated with ongoing clump accretion, which enhances the tangling of magnetic field lines on ≤ 400 kpc scales, boosting the overall RM signal.

3.2.9 Alternative models of magnetic fields in filaments

In order to bracket uncertainties related to the (unknown) origin of extragalactic magnetic fields and on the details of gas physics, we first opposed our baseline "primordial" scenario to a second "astrophysical" scenario, in which we employed radiative simulations with a simple prescription for feedback from AGN. In such runs the gas loses energy at run-time assuming equilibrium cooling for a primordial chemical composition, and the launching of bipolar thermal jets from simulated AGN, which also deliver a fixed fraction ($\approx 1\%$) of the feedback energy into magnetic energy (see [Vazza et al. \(2017\)](#) for more details). In Fig. 3.6, we show the example of the RM for cluster e18b at $z = 0$, which well illustrates how in this second simulation the number of gas substructures is increased, while the level of RM in the diffuse WHIM is smaller compared to the primordial case, owing to the dilution of local sources of magnetisation outside of clusters. The right panel in the same Figure also shows the overall change in the distribution of RM in control fields and in filaments for the entire dataset in the two cases.

In the AGN seeding model we measure a tail of very high RM values ($\text{RM} > 20 \text{ rad/m}^2$) in the ICM and filaments, and lower RM values in the control field (which produces a larger contrast between them). Despite the high contrast, telling the two models apart based on the statistical analysis of observable RMs becomes more difficult (see Fig. 3.7) since virtually no filaments would be detectable in the AGN model, not even by considering no contamination from residual RM ($\sigma_{\text{res}} = 0 \text{ rad/m}^2$), and even for a SKA-MID-like observation (Fig. 3.7, right panel).

However, a possible way to investigate the AGN seeding scenario, in

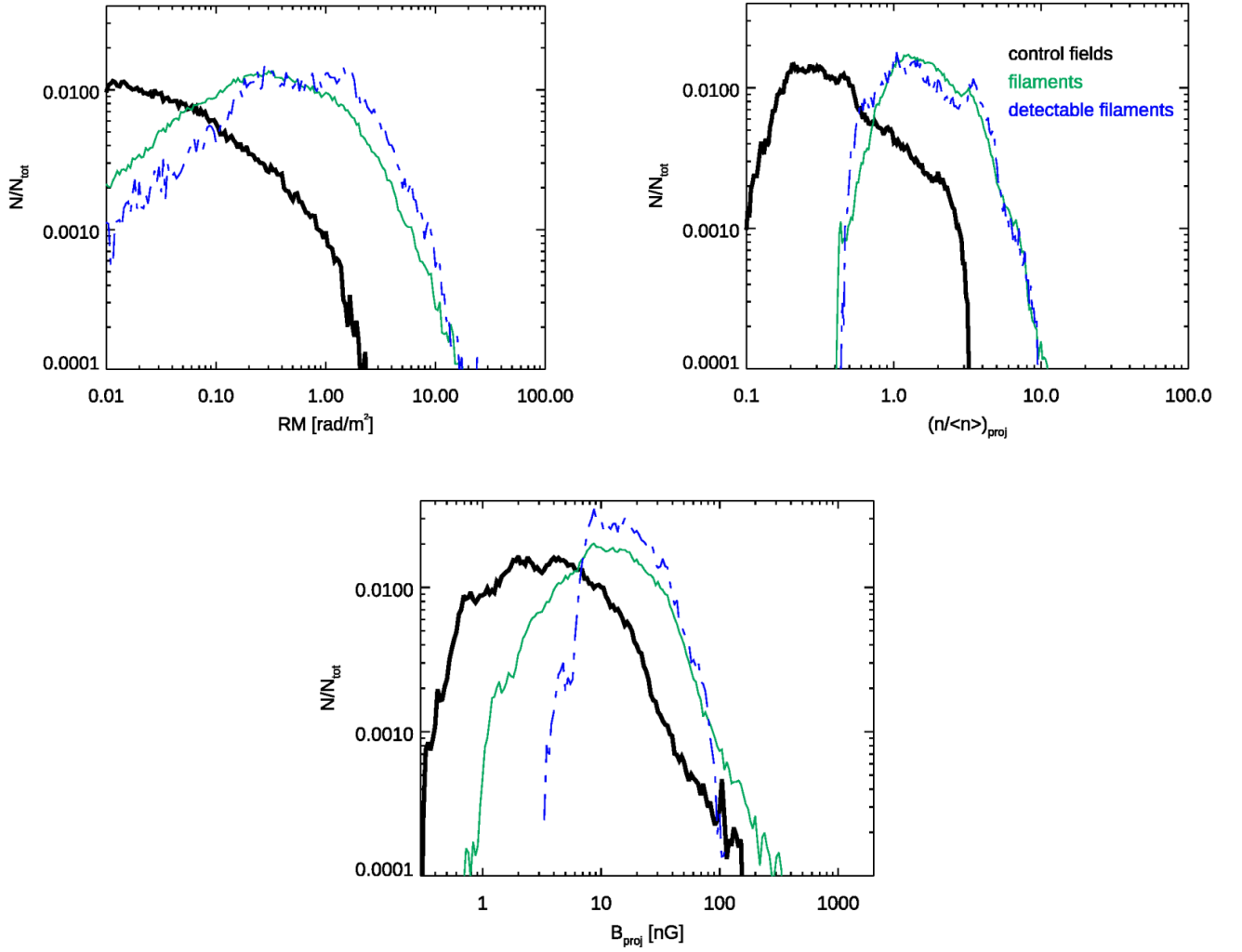


Figure 3.4: Distributions of RMs, projected mean gas density and mean magnetic field strength for all control fields and filaments considered in our datasets (primordial model, including all analyzed lines of sight). The additional dot-dashed lines show the distributions of the same fields limited to the 4 most detectable filaments in Fig. 3.3.

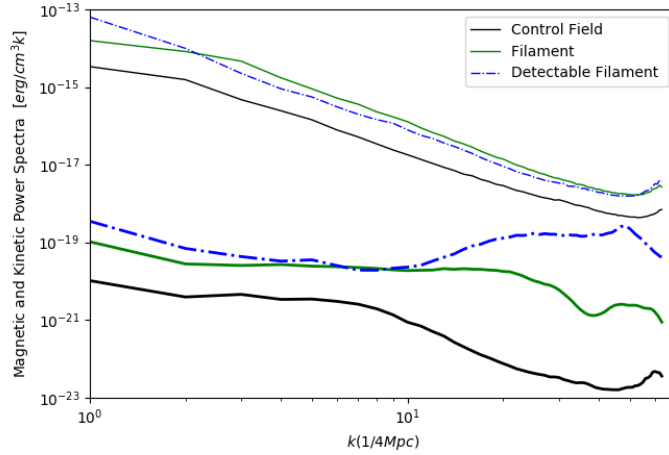


Figure 3.5: The upper thin lines show the 3-dimensional power spectra for the density weighted velocity field ($\rho^{1/2}v$) and the lower thick lines show the 3-dimensional magnetic power spectra in three sub-volumes of the cluster e18b.

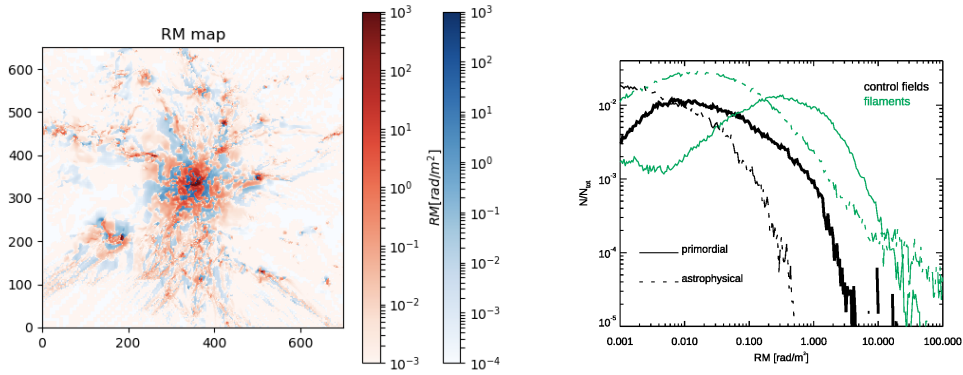


Figure 3.6: Left panel: RM distribution for our e18b cluster at $z = 0$, simulated with the cooling and feedback model, in which magnetic fields are injected by AGN activity. The box as the meaning of colors is as in Fig.1. Right panel: distribution of RMs for all filament and control fields, for the primordial and the astrophysical model.

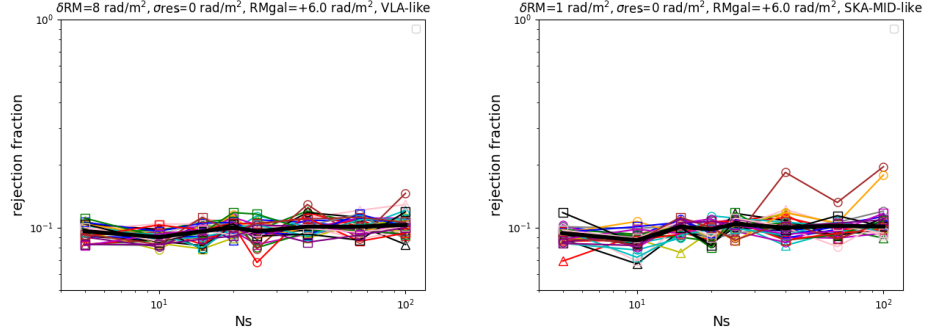


Figure 3.7: Same as Fig. 3.2 for the AGN seeding scenario.

the limit of a large number of background sources, would be to select only RM distributions in the close proximity of dense substructures within filaments (which are presently masked out in our analysis), where small scale fluctuations in RMs are expected to be more significant compared to the fluctuations of the Galactic foreground and to the residual scatter of RMs.

Second, we investigated a more optimistic primordial scenario, assuming a 10 times larger initial magnetic seed field ($B_{\text{init}}=1$ nG) compared to our baseline primordial model. This case is meant to bracket the possibility that magnetic fields in real filaments are stronger than what is captured by MHD method, which may be potentially affected by resolution effects as any finite-volume method (see however discussion in [Vazza et al. \(2014\)](#)). The assumed $B_{\text{init}}=1$ nG field is still below the most recent upper limit obtained by CMB analysis by [Planck Collaboration et al. \(2016b\)](#). For simplicity we obtained this model by upscaling the magnetic field and the RM in our baseline model by $\times 10$ in post-processing, which is motivated by the fact that magnetic fields in filaments are expected not to be in the saturated dynamo regime ([Ryu et al., 2008](#); [Marinacci et al., 2015](#)).

For this optimistic case, the chances of detecting the magneto-ionic filamentary medium are dramatically improved (see Fig. 3.8). For example, setting $\sigma_{\text{res}} = 6$ rad/m² makes JVLA-like observations of filaments to reach a rejection fraction larger than 0.5 in $\sim 34\%$ of the sample with $N_S = 100$ detected polarized sources, and $\sim 7\%$ with $N_S = 20$ sources. With the SKA-MID more than a half of our objects will be significantly detectable with $N_S = 100$ sources. Even for a small number of available polarized sources $N_S = 5$ about $\sim 10(17)\%$ of filaments have a chance of $\geq 1/5$ to be

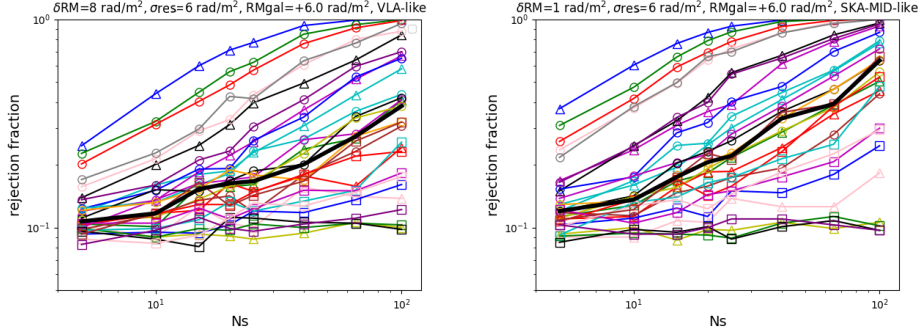


Figure 3.8: Same as Fig. 3.3 (lower panels) for the primordial seeding scenario with $B_{\text{init}} = 1$ nG.

distinguished from the control field in a JVLA(SKA-MID)-like observation.

We conclude that filaments still represent a key case to test hypothesis on the initial magnetization level at large scales ($\geq \text{Mpc}$) since the magnetic field normalization plays a key role in their detection rate.

3.2.10 Section summary

In this work, for the first time, we assessed the possibility of detecting the cosmic web around massive filaments with radio polarisation observations and under realistic observing conditions. Our investigation has been motivated by the expected increase in performances of new large radio facilities. In particular, the planned sensitivity of the SKA will produce a leap in our capability to measure non-thermal constituents of the cosmic web. While continuum surveys should lead to the discovery of hundreds of new extended radio sources in galaxy clusters (e.g. [Cassano et al., 2015](#); [Nuza et al., 2017](#)), the expected flurry of accurate polarization data from extended and point-like sources should finally enable the detection of the magnetized cosmic web around galaxy clusters, and to further study the topology and spatial distribution of magnetic fields on $\geq \text{Mpc}$ scales, also representing a powerful new tool to locate and study the WHIM component of "missing baryons".

Unlike other works in the past, here we considered the real exercise that future radio observations will have to face, i.e. the challenge of statistically comparing distributions of RMs in putative filaments and in nearby control fields, by taking into account realistic level of contamination from the

Galaxy, different populations of background sources, and also including a realistic RM sensitivity. To assess the detection rate, we used the statistical M-W estimator (Neuhäuser, 2011).

The results of our analysis show that pushing the instrumental RM sensitivity to ≤ 1 rad/m² is key to probe magnetic fields in filaments, due to the higher statistics of detectable polarised sources, which will allow us to distinguishing filaments from nearby control fields in a statistically robust way. However, our analysis shows that strong limitations to this search arise because of the spurious contributions to the RM on the polarized radio sources (e.g. Banfield et al., 2014; Lamee et al., 2016).

These spurious contributions can be never fully avoided, but minimized by selecting relatively nearby populations less affected by contributions to the RM along the LoS, or even populations showing smaller intrinsic RM scatter (e.g. WISE-Star radio sources (Banfield et al., 2014)) through cross-correlation with optical/infrared catalogs or self-consistently operating suitable cuts on their radio properties. In the scenario in which extragalactic fields have been mostly seeded by galaxies and AGN, we expect an extremely small detection rate of filaments around galaxy clusters via RM studies. Conversely, the systematic detection of RM from filaments (assuming the intrinsic contribution from sources can be opportunely minimized and the RM sensitivity is large enough) will provide an important hint for significant levels of volume-filling magnetic fields already in the early Universe (as a result of a primordial magnetogenesis), or to an anomalously large amplification efficiency of large-scale motions in the WHIM. Regardless of the magnetic seeding scenario, the filaments with the highest chances of detection via RM analysis in our sample are the ones with more gas substructures, which induce a higher level of compression and localized field amplification.

We caution that, since the target of our analysis are filaments in rich environment populated by hundreds or thousands of galaxies, making exact prediction on the role of magnetic seeding by galaxies remains challenging. The reliability on astrophysical seeding models depends on the still open issue of reaching a precise characterization of sub-grid star formation and AGN feedback, as well as the interplay between galaxies and the magnetized intergalactic medium around them.

However, our work strengthens the idea that the actual magnetization level of filaments (and in turn that of the entire Universe) will crucially affect the success of future large polarization surveys in their attempt of detecting

3.2. *INTER-CLUSTER FILAMENTS WITH FARADAY ROTATION*105

the Cosmic Web.

3.3 The Pandora’s cluster: Abell 2744

In order to discriminate between competing mechanisms for the origin of the observed extragalactic magnetic fields it is vital to detect magnetic fields outside of the virial radius of galaxy clusters (see Fig. 1.6). As already discussed in the introduction of this Chapter (Sec. 3.1 and 3.2.1), quantification of the Faraday rotation effect has already been proven to retain valuable information of the magnetic fields coherently distributed over large physical scales (Bonafede et al., 2013; Vernstrom et al., 2019; O’Sullivan et al., 2020; Stuardi et al., 2020).

In this Section we aim to inspect the RMs in the direction of a filament connected to the massive galaxy cluster Abell 2744, and to translate any excess with respect to a control sample composed by the RM from surrounding field sources, into a level of magnetisation of the WHIM. The feasibility of this study has been investigated and motivated by means of magneto-hydrodynamical cosmological simulations that we used to estimate the RM from filaments connected to a galaxy cluster with size similar to A2744.

3.3.1 Abell 2744

A2744 is a massive galaxy cluster containing a total mass of $1.8 \times 10^{15} M_{\odot}$ within a radius of 1.3 Mpc at redshift of $z = 0.306$. Eckert et al. (2015) combined X-ray and optical/near IR observations to detect the gas in five filaments around A2744, three of which are connected to the outer parts of the virial volume. The robust mass modelling of A2774 performed by Eckert et al. (2015) makes it a very promising candidate to study magnetic fields in filaments, since the location and the projected density of these gas structures are known with accuracy. Eq. 3.4 shows that n_e has to be characterized/assumed in order to break the degeneracy of the magnetic field on RM.

Several multi-wavelength datasets of A2744 are already available for a proper reconstruction of the plasma structure for the modeling of the magnetic field. In particular, Eckert et al. (2015) used XMM-Newton observations and weak-lensing to study a larger field of view containing cluster outskirts. A2744 has been imaged with CFHT/MegaCam (Braglia et al., 2009) in the i-band in 2009 providing data with higher quality with respect to the previous Subaru/SuprimeCam observation (Merten et al., 2011), over a $\sim 60' \times 60'$ field of view. More recently, the weak-lensing mass distribution was updated with newer Subaru/SuprimeCam data (Medezinski et al.,

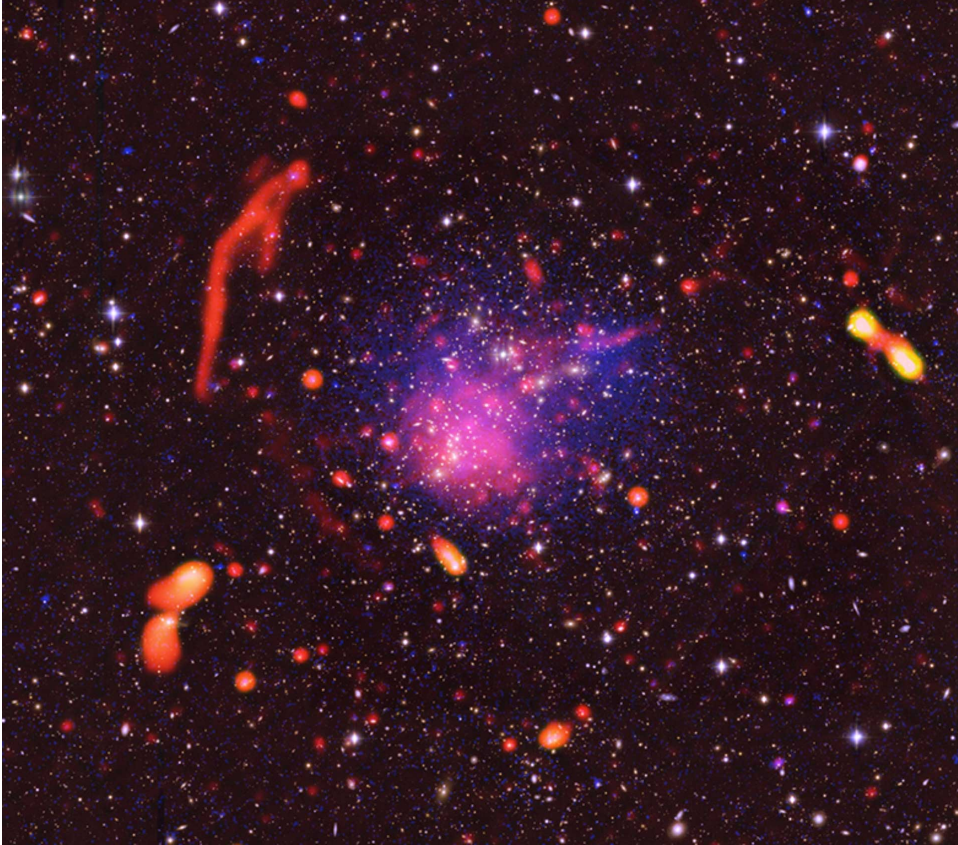


Figure 3.9: Multi-frequency overlaid image of the galaxy cluster Abell 2744: optical (BRz colors, [Medezinski et al. \(2016\)](#)), X-ray (blue), and radio (red, [Pearce et al. \(2017\)](#)). The radio emission highlights the presence of magnetic fields across the cluster volume.

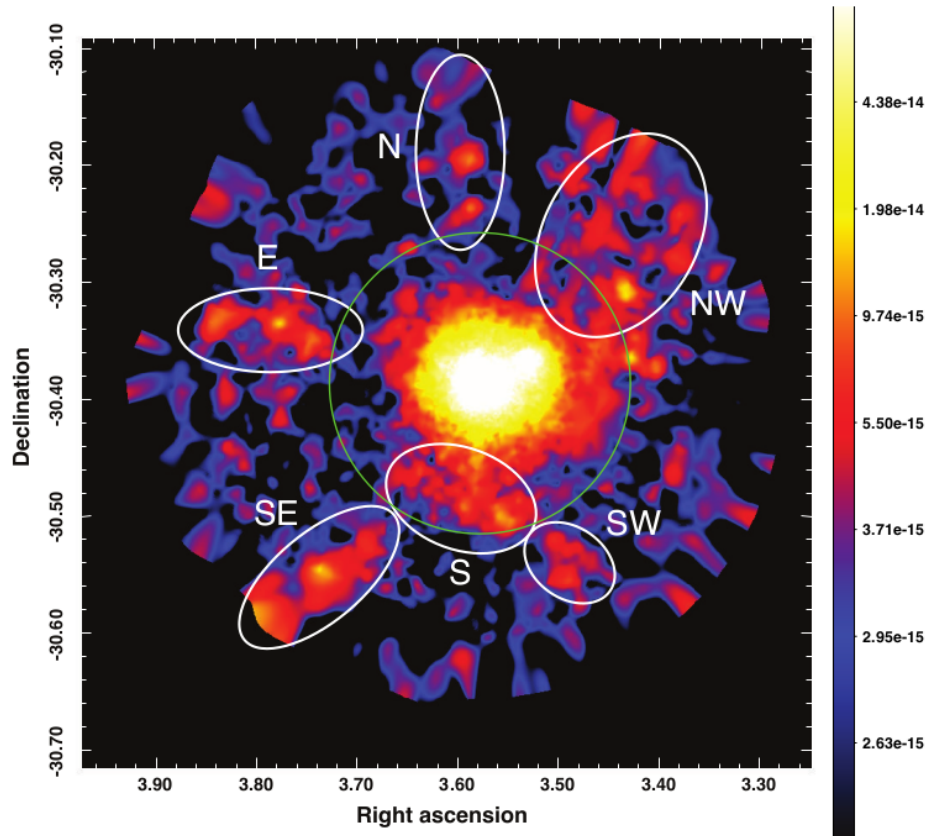


Figure 3.10: [Eckert et al. \(2015\)](#): 0.5-1.2 keV XMM map of the hot gas in and around the galaxy cluster Abell 2744. The surface-brightness is in units of $\text{erg cm}^{-2} \text{s}^{-1} \text{arcmin}^{-2}$. The locus at the virial radius of $\sim 2.1 h_{70}^{-1}$ Mpc is shown by the green circle. The white ellipses highlight the position of the diffuse structures.

2016). The cluster has also been observed using WFI at the MPE 2.2m telescope at La Silla Observatory, providing imaging in the B, V and R-bands over a $34' \times 34'$ field of view (taken between September 2000 and October 2011). We exploit their observations together with the XMM-Newton Xray Observatory providing extremely high quality data which already enabled Eckert et al. (2015) to detect large-scale filaments of gas connected to the cluster itself. Redshift information has been retrieved from the spectroscopic catalogue made by Owers et al. (2011) with the AAOmega MOS on the Anglo-Australian Telescope (AAT).

3.3.2 Forecasts and strategy

In the previous Section (3.2) we showed already several sample maps of RM from mock galaxy clusters and filaments. Gas and DM substructures are being accreted through large filaments connected to (central) virial volumes, and along these directions the RM is increased by a factor of $\sim 10 - 100$ compared to the RM in the cluster periphery. A further example is provided in Fig. 3.11, showing the simulated evolution of a $\sim 10^{15} M_{\odot}$ galaxy cluster with the ENZO grid code (Bryan et al., 2014), starting from a weak primordial magnetic field ($B_0 = 10^{-10}$ G comoving) later amplified by compression and turbulence.

In the range of gas parameters inferred for the filaments of A2744 (Eckert et al. 2015, $n \sim 10^{-4} \text{ cm}^{-3}$ and $T \sim 10^7$ K) the simulated RM is $\geq 10 \text{ rad m}^{-2}$ for about the half of the area covered by filaments. This may very likely constitute a lower limit on the true distribution of RM. In fact, the limited spatial resolution in the simulation (which limits the dynamo amplification) and also the analysis of the outer regions of the Coma cluster (however still inside the virial radius, Bonafede et al. 2013) showed excess magnetic field compared to theoretical expectations. On the other hand, we will gain crucial information even in the unlikely scenario in which no significant RM ($\leq 10 \text{ rad m}^{-2}$) would be detected.

We applied for dedicated JVLA observations with the goal of detecting the magnetic field in the filaments through the RM of sources located within/behind the filaments. The best strategy for our purposes was to observe the targets at $\sim \text{GHz}$ frequency (as demonstrated by Akahori et al., 2018) with high resolution. High resolution is required in order to avoid as much beam depolarization as possible. Beam depolarization is the decrease of the observed polarised signal as a result of the average over under-resolved cells where the linear polarization vector has different orientation. The above conditions can be met by using large interferometer arrays reaching $\sim \text{arc}$

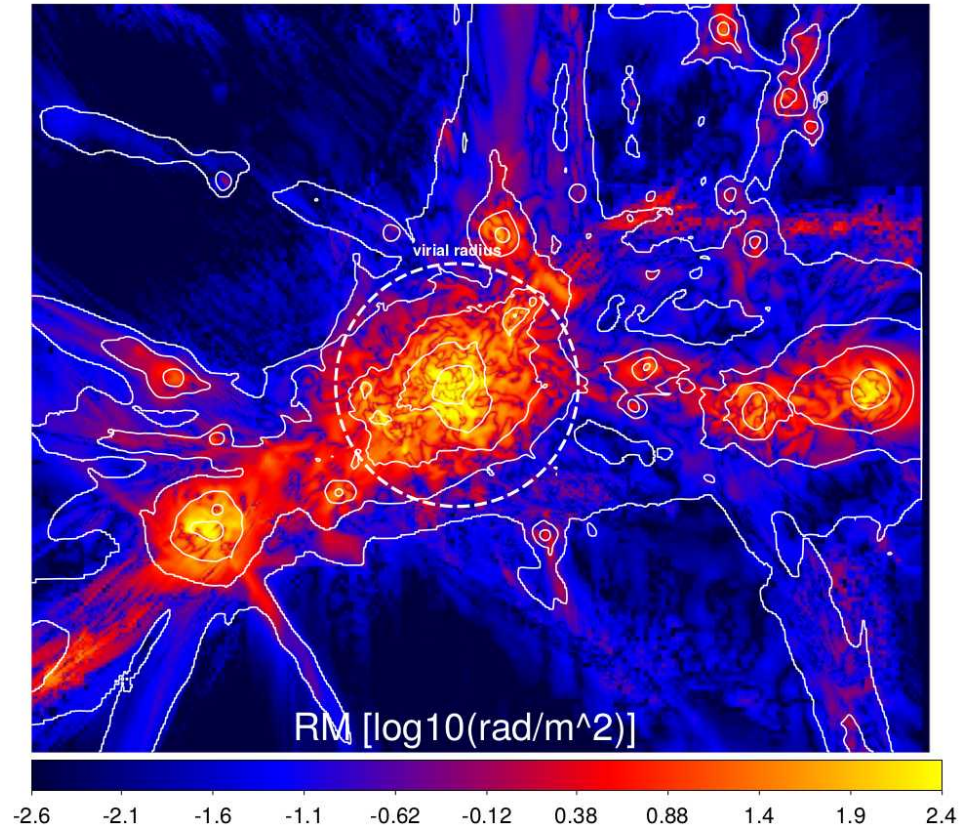


Figure 3.11: Map of RM for a simulated $\sim 10^{15}M_{\odot}$ cluster. The white contours trace the X-ray isocontours and the virial radius of the cluster is additionally shown in white.

second resolution, such as the Very Large Array (VLA) L band receiver in its most extended configuration (A). During 2017 we proposed and obtained such kind of VLA observations (proposal ID VLA_16B_190, P.I. Franco Vazza) centered on one of the X-ray diffuse structures (in the SE direction) observed from [Eckert et al. \(2015\)](#). In early 2019, with the same instrument and setup, two additional pointings with similar exposure were proposed and obtained (proposal ID VLA_19A-324, P.I. Nicola Locatelli), each centered on another extended structures around A2744 (E and NW filaments).

A crucial aspect of the observations is their long exposure, amounting to about 20 hours per target, aiming at reaching sufficient signal-to-noise ratio (S/N) also for faint sources. This requirement meets either the need for constructing the densest available grid of background sources, as the source density increases towards lower flux densities, and to exploit a strength of the RM synthesis method ([Brentjens and de Bruyn, 2005](#)): the accuracy $\delta\phi_p$ on the RM (i.e. the minimum $|\text{RM}|$ than can be measured) in fact is given by

$$\delta\phi_p = \frac{\sqrt{3}}{S/N_{U,Q}(\lambda_{\max}^2 - \lambda_{\min}^2)} \quad (3.11)$$

where λ_{\max} and λ_{\min} are the maximum and minimum observing wavelengths, so that the sensitivity to low RMs increases as the signal-to-noise ratio with which a source is detected in polarisation $S/N_{U,Q}$.

Archival observations of the target ([Pearce et al., 2017](#)) are available and can be used to estimate the number of sources that would be detectable in polarisation at a given sensitivity level. We need to detect at least 10-15 sources with $\text{RM} \geq 10 \text{ rad m}^{-2}$ in order to trace the magnetic field profile in the filaments. A control sample will be also needed to assess if an enhancement of RM is detected in the sources seen through the filament, and to estimate the Galactic contribution to the observed RM. A2744 is at Galactic latitude ($gb = -81.2 \text{ deg}$). Statistical reconstruction methods by [Oppermann et al. \(2012\)](#) indicate that the Galactic contribution is $\sim 6.3 \text{ rad m}^{-2}$ in the sky region of our target, although this values is obtained over a $\sim \text{deg}$ angular scale. Estimates of the turbulent ISM structure that builds the Galactic RM foreground $\sigma_{\text{RM,ISM}}$ over smaller scales can be obtained from the best-fit of the RM second-order transfer function (e.g. [Haverkorn et al., 2006](#)) computed by [Anderson et al. \(2015\)](#):

$$2\sigma_{\text{RM,ISM}}^2(\theta) \simeq 202 \times 10^{0.49 \log_{10} \theta} \text{ rad m}^{-2} \quad (3.12)$$

(eq.19-20 in their work) where θ is the angular scale in degrees and $\sigma_{\text{RM,ISM}}$ predicts the scatter induced by the ISM on the observed RM at that angular

scale. From their work we derive a $\sigma_{\text{ISM}} \sim 8 \text{ rad m}^{-2}$ over a $0.5 \text{ deg} (= 30')$ angular scale. This value can effectively affect our analysis since it is of the same order of the putative contribution from the LSS that we want to observe. However, we will be able to further investigate this issue and potentially break the ISM-WHIM degeneracy by computing the mean RM of the sources in the control regions, that is, from sources around the cluster but outside the filaments (in projection).

In addition to the Galactic foreground, another uncertainty $\sigma_{\text{RM,src}}$ arises from the intrinsic scatter of the magneto-ionised local environment of the background source population, as already demonstrated in the previous Sec. 3.2. The $\sigma_{\text{RM,src}}$ is expected to amount to a similar level than $\sigma_{\text{RM,ISM}}(0.5') \simeq 8 \text{ rad m}^{-2}$ (Schnitzeler, 2010). The sum of the above contribution may actually be dominant with respect to the LSS signal in general, however we recall that A2744 offers the first opportunity of X-ray selected filaments, in a LSS environment which bounds WHIM to ICM properties, and is thus characterised by larger densities and magnetic field strength than the average WHIM.

Assuming that sources will be polarised at the level of 5% (see Rudnick and Owen, 2014), and taking into account the decrease in sensitivity due to the primary beam response, our observations are meant to reach a noise rms of $2.5 \mu\text{Jy beam}^{-1}$ in order to observe the 20 brightest sources in polarisation with a signal to noise ≥ 3 .

3.3.3 VLA L-band data

Observations of the S-SE outskirts of A2744 were carried from 19 to 21 Jan 2017 during five different observational runs (proposal ID VLA_16B_190) collecting a total of 17.5 hrs including calibration rounds.

Observations of the E and NW outskirts of A2744 instead were carried with the same receiver and configuration but from 02 to 17 Jan 2019 during eight different observational runs (proposal ID VLA_19A_324) collecting about the same total time for each target, also including calibration time slots. The target coordinates (pointing centers) are reported in Tab. 3.1, where the observation times have also been outlined. Data were taken with the L-band receiver (1 – 2 GHz), in the A-configuration array, and have full Stokes information. The A-configuration gives the largest baselines and hence highest resolution ($\sim 1''$). High resolution is needed to limit beam depolarization and to determine small-scale RM fluctuations. The largest angular scale (LAS) achievable by the L-band receiver is $\text{LAS} \simeq 53''$. A2744 has also been selected due to its very low Galactic latitude, giving a prior

date	S-SE [h]	NW [h]	E [h]
07 Jan 2017	4		
08 Jan 2017	4		
19 Jan 2017	2		
20 Jan 2017	4		
21 Jan 2017	3		
02 Oct 2019		2.5	2.5
03 Oct 2019		2.5	2.5
04 Oct 2019		2.5	2.5
08 Oct 2019		2.5	2.5
13 Oct 2019		2.5	2.5
15 Oct 2019		2.5	2.5
16 Oct 2019		2.5	2.5
17 Oct 2019		2.5	2.5
total	17	17.5	17.5

Table 3.1: Outline VLA observations of A2744 outskirts. Target coordinates: S-SE (00h 14m 50.54s -30 deg 30’27’’); NW (00h 13m 50.00s -30 deg 15’49’’); E (00h 15m 06.50s -30 deg 20’07’’).

$RM_{\text{Gal}} = 6.3 \text{ rad m}^{-2}$ foreground level (Oppermann et al., 2015). The same low Galactic latitude however limits the target maximum elevation above the horizon at the VLA site to $\delta = 26^\circ$. This generates a UV coverage which produces a stretched synthesized beam at the maximum resolution ($1.5'' \times 3''$). We apply a $3''$ tapering to the visibilities and impose a fixed restoring beam of $3'' \times 3''$ during imaging, roughly corresponding to the resolution at the lowest frequency (1 GHz). This is required to correctly align the phases when producing images from different spectral channels having different synthesized beam sizes. The resulting point spread function (PSF) is sampled with a $0.4''$ angular cell size, corresponding to 1.830 kpc at the cluster’s redshift $z = 0.308$. Radio frequency interference (RFI) and bad raw data were flagged both manually and through the `rflag` routine of the CASA³ software. For each observation, a first direction-independent standard calibration was performed: the fluxes and bandpass behaviour were calibrated with models of the source 3C138 made available by the NRAO; the source J0011-2612 was used as phase calibrator. Further analysis of the S-SE field calibration are presented in the next Sec. 3.3.4.

³<https://casa.nrao.edu/casadocs>

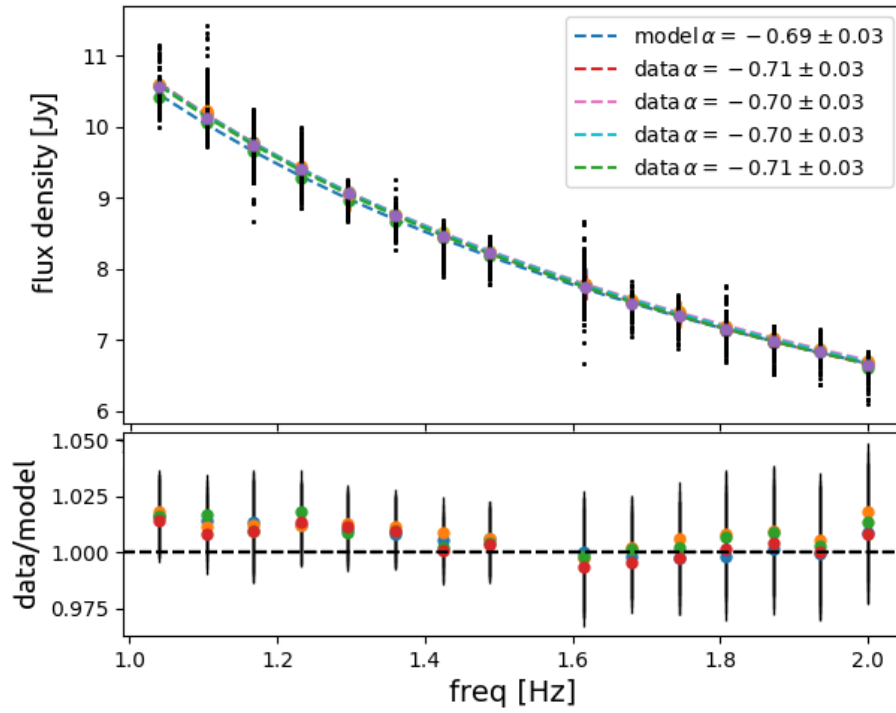


Figure 3.12: 3C138 spectrum computed from parallel-hand (RR and LL) visibility amplitudes. Errorbars are not visible in the upper panel, where black dots represent all visibilities averaged over time and sub-band. Standard deviation of visibility amplitudes are used as errorbars to the residuals in the lower panel. The power-laws fits the data of each observations independently. Flux density differs from the model of lower than 3%.

3.3.4 Data calibration

We present the initial direction-independent phase and flux calibration of the antenna correlations. Phase and amplitude, bandpass and polarization solutions for the antenna gains were computed and applied to the primary and polarization calibrator 3C138 and phase calibrator J0011-2612 as well as to the target.

The calibrated parallel hand antennae correlation amplitudes are plotted for all the sub-bands (64 MHz wide) in Fig. 3.12 for all 2017 observations. The obs-wise colored dots and errorbars in Fig. 3.12 show the mean and standard deviation values of each sub-band. The blue dashed line shows the

model of 3C138 derived from [Perley and Butler \(2013\)](#), involving a spectral index $\alpha = 0.69 \pm 0.03$ (with $S_\nu = \nu^{-\alpha}$). The residuals shown in the lower sub-panel of [Fig. 3.12](#) are within $< 3\%$ of the model flux at any frequency. We note that data at 1.6 GHz have been flagged due to the presence of intense RFIs across all nights.

In order to test the polarization calibration, we imaged the primary calibrator 3C138 in full-Stokes producing a spectral cube with channel width 16 MHz in the band 1-2 GHz using a standard gridded, Hogbom deconvolver and Briggs weighting scheme (robust=-0.25). Using a fixed restoring beam of $3''$ the source is unresolved in all channels.

In [Fig. 3.13](#) and [3.14](#) we show for each of the five observations the fractional Stokes parameters Q, U, and V, i.e. divided by Stokes I. At $3''$ resolution 3C138 is unresolved at 1 GHz, the peak surface brightness then equals the flux density of the calibrator.

In the upper panels we show the fractional polarization parameters, plus the linear polarization $L = \sqrt{Q^2 + U^2}$ in black and $|V|$ in green. In the bottom panels we computed the polarization angle $\psi = -0.5 \tan(U/Q)$. The blue dashed line shows the parallactic angle of 3C138 as derived by [Perley and Butler \(2013\)](#). [Perley and Butler \(2013\)](#) also derive a fractional polarization of 3C138 of {5.6, 7.5, 8.4, 9.0}% at {1.05, 1.45, 1.64, 1.95} GHz.

Despite the spectral ambiguities of the total intensity in the images of 3C138 that in turns reflect into the Q and U intensities, We note that both the source spectrum and the fractional polarization features remain consistent with the expectations: both the spectral index, the degree of polarization $P/I = 7.5\%$ at 1.45 GHz, its spectral trend, RM=0 and $\psi = -11$ deg are retrieved during all observations. We conclude that the target (on-axis) fractional polarization will be well-behaved.

3.3.5 Full-Stokes wide-field imaging

After a first round of imaging of the VLA data centered on the S-SE field presented above, a thorough inspection of the full-Stokes data cubes showed suspicious polarization behaviour, that is to say, a non-negligible Stokes V flux density of all point-like sources with a trend dependent on the sky position (thus hint of a direction-dependent effect), in addition to unexpected spectral features, such as very flat and even inverted spectra across (too) many of the same point-like sources. This motivated us to investigate the calibration and imaging of the data. Insight on calibration have been presented in the previous [Sec. 3.3.4](#). We concluded that on-axis parallel- and cross-hand calibration have been run successfully. This is consistent with the

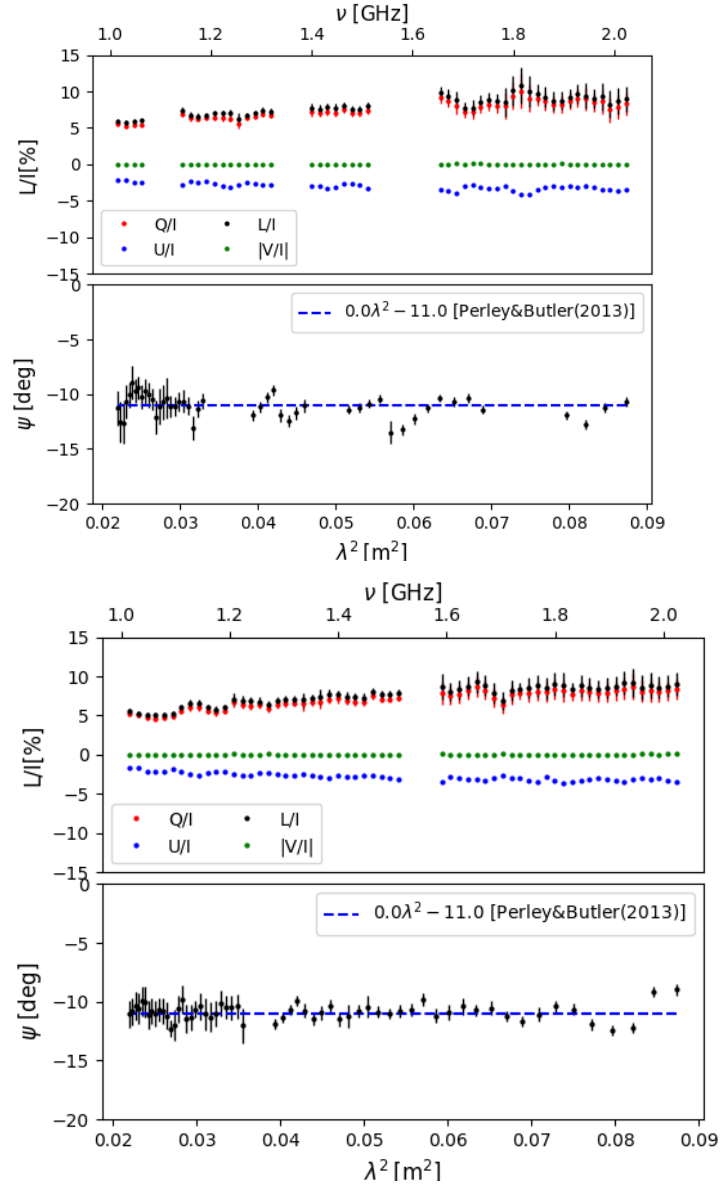


Figure 3.13: 3C138 fractional polarization properties (imaged at $3''$ resolution). Observations of 07 and 08 Jan 2017. $L^2 \equiv Q^2 + U^2$. ψ is the polarization angle computed as $-0.5 \arctan(U/Q)$ and converted in deg.

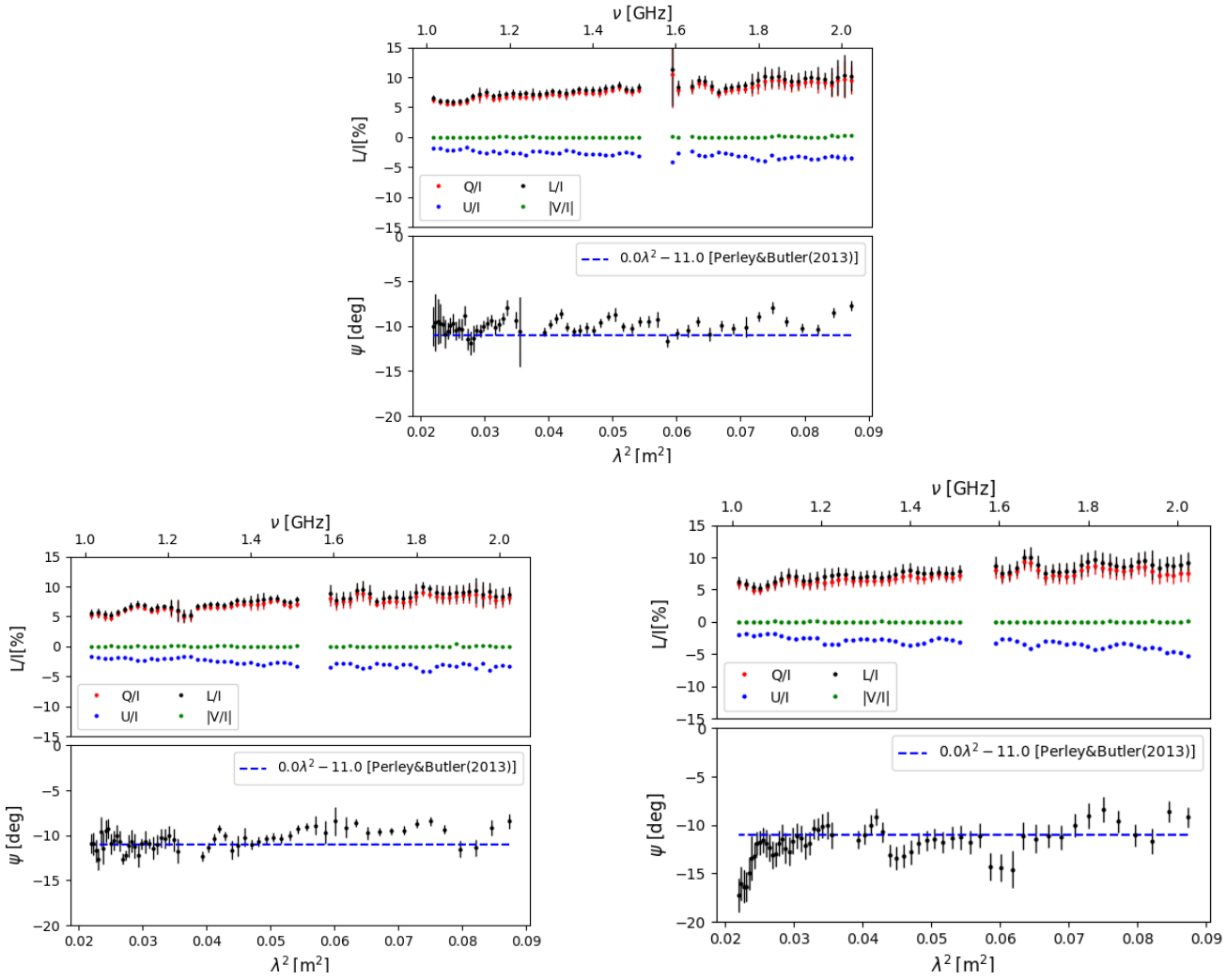


Figure 3.14: 3C138 fractional polarization properties Observations of from 19 to 21 Jan 2017.

direction-dependent nature of the systematic error. From the interferometer measurement equation, in fact, we know that direction- (i.e. baseline-) dependent features own to the image-plane and can not be corrected during standard antenna-dependent gain calibration, which concerns visibilities.

We recognized the arising Stokes V trend as an instrumental polarization leakage, first pointed out by [Bhatnagar et al. \(2008\)](#). This systematic error constitutes a major difficulty in imaging the polarization of VLA A-configuration data: instrumental polarization leakage from total to polarized intensity (and vice-versa) becomes non-negligible for faint sources, for which the true fractional polarization equals the instrumental contribution of a few percent of their total intensity. This effect must be thus solved out rather than just taken into account in the polarization interpretation and its managing has to be worked in the image-plane rather than in the uv-plane because, as we said, it is an intrinsically direction-dependent effect and it thus cannot be included in the calibration (i.e. direction-independent, or antenna-dependent) part of the measurement equation.

The way this issue it is dealt with is by using a gridded called AW-projection (AWP) during imaging ([Jagannathan et al., 2017](#)) that relies on a detailed characterization of the full-Stokes antennae illumination pattern (AIP). Since the AIP is dependent both on direction (i.e. the pixel), time, frequency and polarization, its characterization and computation during image gridding is computationally challenging. An R&D version of AWP algorithm is implemented and updated in CASA from version 5.5 on. We notice that CASA developers clearly warn that R&D algorithms are not considered as stable (see the documentation⁴⁵). The direction-dependency becomes particularly demanding: in fact the whole primary beam (PB) has to be considered, and this requires a large number of pixels when widely spaced array configurations are used. The L-band JVLA in configuration A needs $\sim 10^6$ pixels, over which an independent interpolation of the AIP value has to be computed. In addition, we notice that the AIP for the VLA L-band receiver has been produced by ray-tracing only for the total intensity. This means that the correction of the leakage between the polarizations can be described to first order only for parallel-hand visibility products (i.e. Stokes I and V), while for the cross-hand visibilities (i.e. Stokes Q and U) the correction is limited to the fact that if I is more accurate, then its leakage onto Q and U is smaller, however still present. The correction on Q and U

⁴<https://casa.nrao.edu/casadocs>

⁵<https://casa.nrao.edu/casadocs/casa-6.0/imaging/synthesis-imaging/wide-field-imaging-full-primary-beam>

is thus applicable today only to second-order, however it remains necessary. We refer the reader to Jagannathan et al. (2017) and references therein for insight on this issue.

Within this framework, I spent a three-months period (Sep-Dec 2019) at the Inter-university Institute for Data Intensive Astronomy (IDIA) in Cape Town (SA) to learn and test the AWP on our VLA data. IDIA exploits the Ilifu regional computing node⁶ based in Cape Town, for high performance computing dedicated to data-intensive astronomy, especially oriented to the SKA precursor MeerKAT telescope. The Ilifu facility is equipped with a SLURM architecture which supports GPU parallel processing and dynamic job/task scheduling to maximise exploitation of the computational resources⁷. In particular we submitted jobs using SLURM-batch (`sbatch`) scripts invoking python/MPICASA routines. The `sbatch` scripts set `--cpus-per-task=1` and `--ntasks-per-node=3` resources distributed over `--nodes=12` nodes, each exploiting a full `--mem=236GB` memory for a single image. This is a critically large amount of resources today.

After direction-independent calibration of all observations independently, data were re-grouped by sub-band into 16 sets from 1 to 2 GHz, with 64 MHz sub-bandwidth each. Each sub-band set was imaged into four channels of 16 MHz width each. Each channel was imaged separately asking for the computing resources outlined above. 10240^2 pixel full-Stokes images were created for each channel with $3''$ resolution, sampled by $0.4''$ sized pixels using Briggs weighting scheme with `robust` parameter 0.5 and deconvolved with `Hogbom` algorithm for maximum 50k minor iterations before a 5σ threshold over $10 \mu\text{Jy beam}^{-1}$ was reached. Through the `awproject` gridder (the CASA implementation of the AWP), the AIP was computed at every 30 deg rotation with respect to the sky and rotated at every 10 deg, using 512 w-planes. To produce each of the full-Stokes 16 MHz deconvolved channel images with the (very high amount of) resources allotted, about a week was required, that meant to spend about a month to produce images of the 4 channels over a 64 MHz sub-band using all observations (~ 17 hours exposure). This fact constituted (and still does) a bottleneck for the production of science-ready image products to analyse. We produced images of 24 channels distributed over 6 sub-bands conveniently chosen to cover about homogeneously the λ^2 space during progress, thus clustering more to the low-frequency half of the L wide-band.

In order to find faint sources, we also produced a single total intensity

⁶<http://www.ilifu.ac.za/il/home>

⁷see <https://docs.ilifu.ac.za/#/> for Ilifu-SLURM documentation

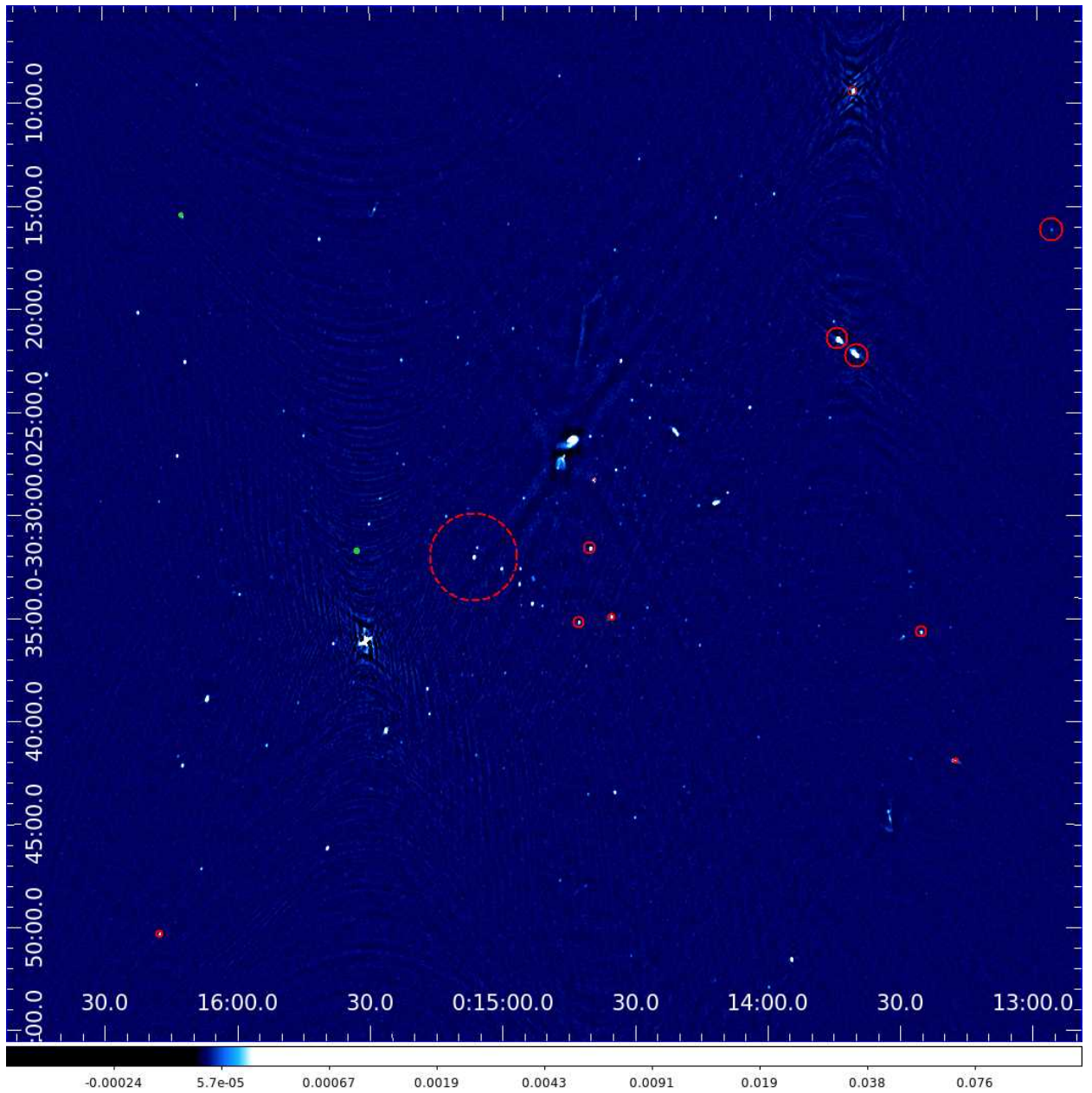


Figure 3.15: A2744 S-SE field image at $3''$ resolution. The RM of each source is derived using RM synthesis. It is represented as a circle with radius in arcseconds equal to the RM in rad m^{-2} (see Tab. 3.2 for the values). Red and green circles indicate positive and negative values respectively.

image using all observations (17.5 hours) and all the available (i.e. not flagged from RFI) bandwidth, by properly modeling the primary and synthesized beam chromaticity through a polynomial fit versus frequency of the model components found during deconvolution (i.e. `nterms=3` in the CASA `tCLEAN` task). The full-bandwidth full-observation image allows to reach a smaller rms noise level than the single channel images. Thanks to the larger S/N of the sources we thus managed to perform self-calibration of the antenna gains, increasing the S/N further. Since the full-data image production is mainly driven by faint source detection, we thus imaged only the Stokes I and used the `wproject` gridded for flat-sky approximation, without the need to correct for the AIP direction-dependent effect (and in turn to require large amount of computational resources). In Fig. 3.15 we show the deepest image (Stokes I) of the S-SE field of A2744, reaching an rms noise of $3.6 \mu\text{Jy beam}^{-1}$.

By using the PYthon Blob Detector and Source Finder (PyBDSF; Mohan and Rafferty 2015) on Fig. 3.15, we built a source catalogue holding a large source surface density of $\sim 400 \text{ deg}^{-2}$. In Fig. 3.16 we combined the Fig. 3.15 (red) with the X-ray smoothed map of A2744 as found by Eckert et al. (2015) (green), highlighting the LSS.

3.3.6 Preliminary RM results and discussion

From the PyBDSF source catalogue we were able to look for polarised emission in the direction of the sources even though they were not visible in the single channel images because of the larger noise level. We thus extracted full-Stokes information across the LoS to the sources and run the RM-synthesis algorithm `RM-tools`⁸ (Purcell et al., 2020). The algorithm provides valuable information on the source polarization properties. In particular we looked for the position of the peak in the Faraday spectrum that we assume as the source RM value (see Brentjens and de Bruyn, 2005, for definitions and details), its uncertainty as given by Eq. 3.11 and ψ_0 (see Eq. 3.1). In Tab. 3.2 we report the polarised sources with $S/N_{\text{Q,U}} > 3$ by their location and RM. In the same table we also include the value of the X-ray surface brightness in units of $10^{-7} \text{ photons keV}^{-1} \text{ cm}^{-2} \text{ s}^{-1}$ for the source positions covered by the XMM map. We considered a background noise of $5 \times 10^{-7} \text{ ph keV}^{-1} \text{ cm}^{-2} \text{ s}^{-1}$ derived as rms value computed in a region outside the relevant LSSs in the XMM map, at similar angular distance (with respect to the filaments) from the cluster center. In Fig. 3.15 and 3.16,

⁸available at <https://github.com/CIRADA-Tools/RM-Tools>

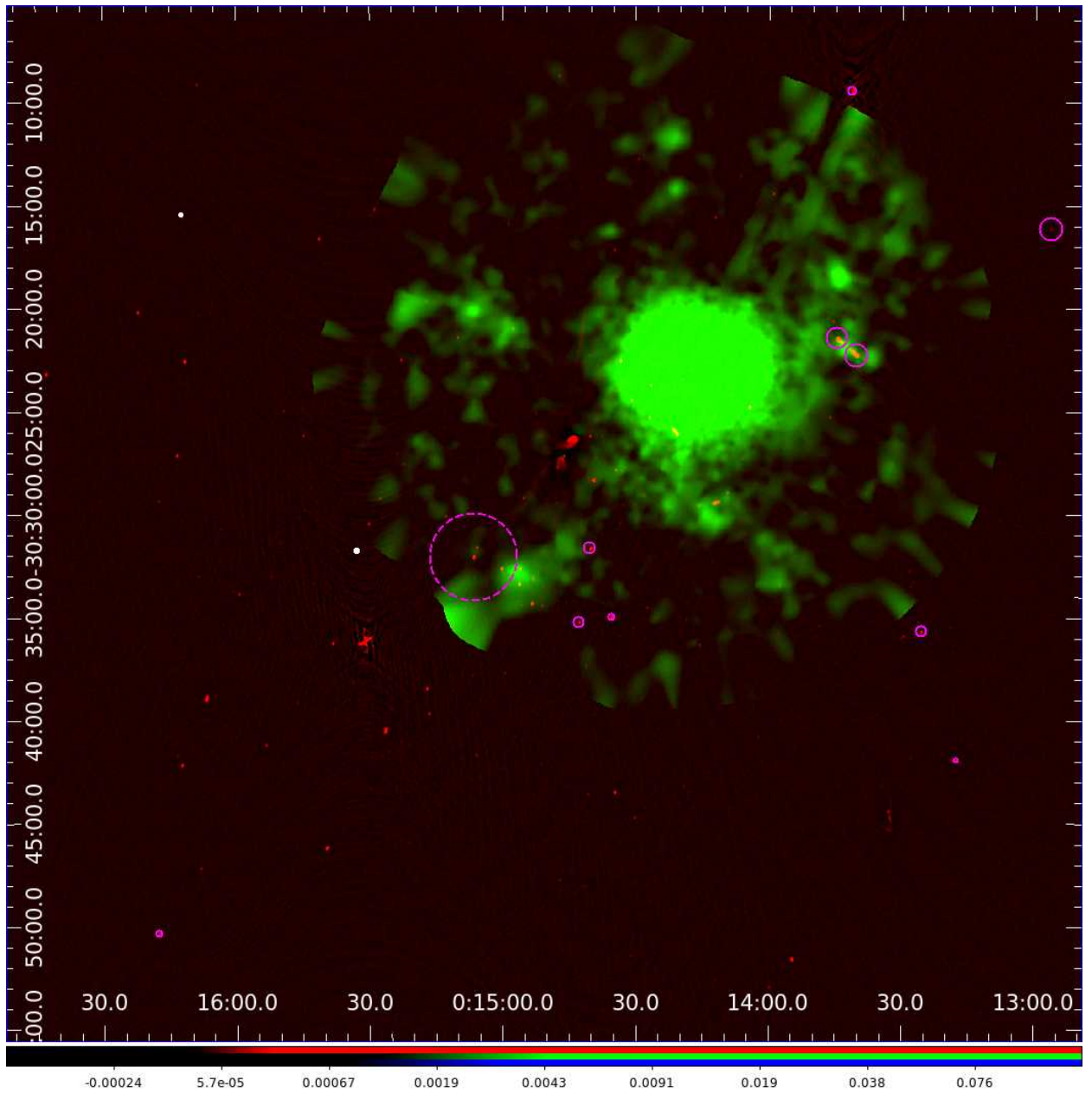


Figure 3.16: A2744 S-SE field multi-wavelength image. Green: XMM-Newton (Eckert et al., 2015); Red: VLA (see Fig. 3.15). As in Fig. 3.15, the RM of each source is represented as a circle with radius in arcseconds equal to the RM in rad m^{-2} . Magenta and white circles indicate positive and negative values respectively.

RA h m s	DEC deg ' ''	RM rad m ⁻²	F_X 10 ⁻⁷ ph keV ⁻¹ cm ⁻² s ⁻¹	Note
00 12 56.52	-30 16 08.04	+33 ± 7		
00 13 17.55	-30 41 55.65	+6 ± 4		
00 13 25.56	-30 35 42.00	+16 ± 8		
00 13 40.13	-30 22 16.93	+9 ± 4	14 ± 5	Foreground
00 13 41.23	-30 09 26.64	+13 ± 2		
00 13 44.52	-30 21 28.80	+31 ± 1	14 ± 5	Foreground
00 14 35.35	-30 35 00.24	+9 ± 1	4 ± 5	
00 14 39.41	-30 28 21.00	+5 ± 3	9 ± 5	
00 14 40.20	-30 31 40.44	+18 ± 5	6 ± 5	
00 14 42.74	-30 35 15.36	+16 ± 8	2 ± 5	
00 15 06.43	-30 32 05.28	+128 ± 6	7 ± 5	
00 15 32.76	-30 31 46.56	-5 ± 2		
00 16 12.14	-30 15 28.44	-4 ± 5		
00 16 17.62	-30 50 21.84	+10 ± 6		

Table 3.2: RM values derived from RM synthesis on the imaged VLA data of the S-SE field of A2744.

around the polarised sources we drew circles with radii (in ") equal to the RM values in rad m⁻², with opposite colors indicating positive/negative values respectively.

X-ray information is available for very few sources. For two of these, namely the bright lobes of a powerful FR II radio galaxy located at W-NW direction of A2744, we also retrieved redshift information that places the sources in front of A2744 and its related LSSs. The very low statistics unfortunately does not allow to drive any conclusion from a combined analysis of RMs and X-ray data. Part of the discrepancy between the low statistics and our expectations (see Sec. 3.3.2, above) resides in the rms noise held by our deepest observation being about a +50% in addition to the assumed value of 2.5 μJy beam⁻¹.

Another contribution may come from the putative RM signal, that is grounded into the noise of a single channel, but coherently sums up with the signal embedded in all the other channels and thus emerges within the RM-synthesis technique and it is not deconvolved. This case is analogue as to compare the sum of different snapshots of a same source, taken at different times, with the image produced by deconvolution of all the visibilities (at the different times) considered at once. In the latter case in fact the noise

would not just decrease as the square root of the total exposure time, but it would also be de-correlated from the brightest pixels of the source through the PSF deconvolution procedure.

However, by looking in detail at the spectra of the sources, in both total intensity and polarization (not shown), we do not ascribe the poor polarization outcome to the image rms noise level. In fact, in addition to the exceedingly large time needed for imaging, preventing multiple deconvolution runs in case of errors/mistakes, the resulting spectra (and images, not shown here) show that the instrumental polarization was not satisfactorily removed in many channels, which have to be discarded afterwards after user inspection. The reason of the failure of the `awproject` gridded over such channels remained unknown since just recently, when by private communication with the NRAO staff members involved with the development of the `awproject` gridded we were notified of a coding error in the computation of the Stokes U.

This error unfortunately affects the data so that they can be neither trusted nor used.

What lesson can be learned from the outcomes of this experiment so far? Radio astronomy is rapidly moving towards the big-data era, where storage and computational challenges will be part of the everyday concerns. The strategy of SKA precursors such as MeerKAT is being directed towards the delivery of science-ready products to the end user in order to save her/him from the need of indispensable large infrastructures for the data collection and analysis. In this respect polarization studies require a big part of the effort. The risk of neglecting or underestimating the problems that it brings out is to lose a half of the interferometric data products (namely the cross-hand correlations RL and LR). In turn, we will lose the opportunity to explore a lot more of valuable and new physical insights involving polarization. In particular, current studies involving polarization of field (i.e. off-axis) sources at L-band is constrained to the ones holding large polarization fractions (Anderson et al., 2018; Sebokolodi et al., 2020), indeed a rather small class of objects. Development of efficient and accurate algorithms for antenna polarization calibration and imaging is thus capital not just to maximise the science outcomes, but to make them worth at all.

Chapter 4

Fast Radio Bursts

4.1 Fast Radio Bursts as a probe of the IGM

Fast Radio Bursts (FRBs) are a recently discovered class of rapid radio transients and provide the first case of extragalactic rapid radio pulses. In this short introduction on the topic we want to focus on the properties of FRBs that make them suitable probes for, both, the IGM baryonic content and its magnetic field.

FRBs are flashes observed at radio frequencies (\sim GHz) with brightness among the highest known for radio sources in general (1 – 100 Jy). Their brightness, combined with their extremely short duration (\sim 0.1 – 1 ms), requires a coherent non-thermal emission mechanism to produce them (Katz, 2014). Their discovery (Lorimer et al., 2007) curiously followed their actual observation by more than six years as the first FRB was found into archival pulsar observations of the Parkes telescope by searching for unusually large dispersion measures (see Keane and Petroff, 2015, for an outline of the searching method) and was exceptionally bright bringing the receiver to saturation.

Dispersion is indeed one of the most prominent features of this class of transients and first drove their very identification as a new class, and especially as extragalactic objects. It consists in a delay of the time of arrival (TOA) of low frequencies with respect to high ones, producing a characteristic curve $\text{TOA} \propto \nu^{-2}$ in the (ν, TOA) space or dynamic spectrum, as can be seen in Fig. 4.1. The constant of proportionality of the relation, that produces the slope seen in Fig. 4.1, is defined as the dispersion measure (DM) and is physically produced by the column density of free electrons

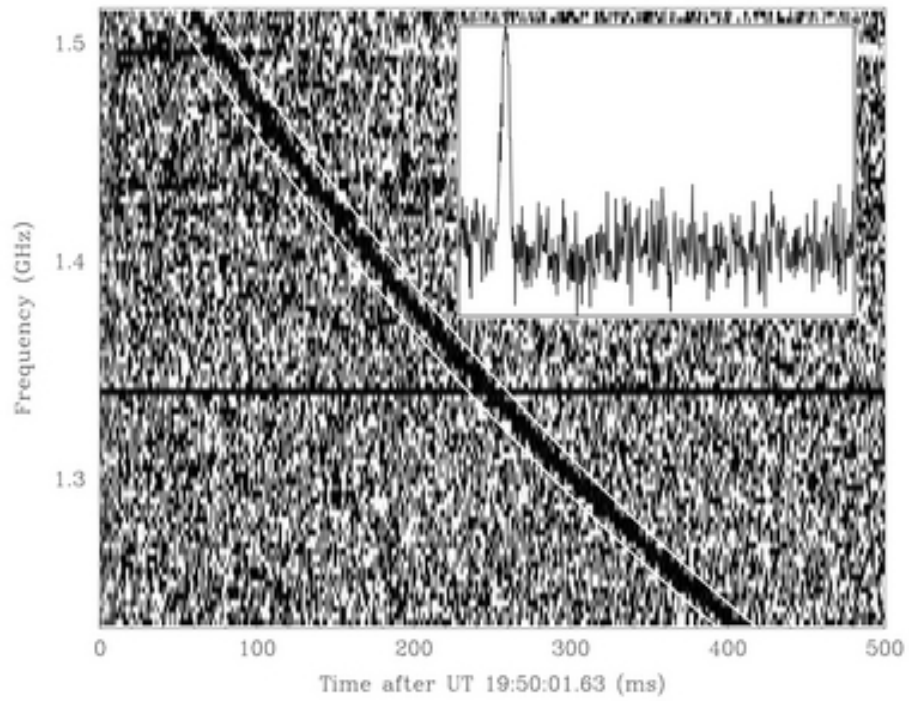


Figure 4.1: [Lorimer et al. \(2007\)](#): Signature in the dynamic spectrum of the first FRB, where the dispersed behaviour $\text{TOA} \propto \nu^{-2}$ is clearly seen. The inset shows the de-dispersed pulse profile integrated over the bandwidth.

along the light travel path from the source to the observer

$$\text{DM} = \int_{\text{src}}^{\text{obs}} n_e dl \quad (4.1)$$

where again we use n_e to indicate the free-electron density. The first indication of the extragalactic nature of FRBs came indeed from the observed value of their DM being way too large to be explained by the Milky Way free electrons alone. A very interesting consequence is that, despite the absence of a redshift measurement, by attributing all or part of the DM excess with respect to the Milky Way to the IGM free-electron content, the residual $\text{DM}_{\text{excess}} = \text{DM}_{\text{obs}} - \text{DM}_{\text{MW}}$ can and have been used as measurement (actually, an upper limit) to the distance of the FRB source. Complementary, the same argument can be recast from an inverse perspective to constrain the IGM baryons along one LoS in the case of localization of the FRB source and its redshift through other methods such as high resolution (interferometric) imaging of the pulse (Bailes et al., 2017; Bannister et al., 2019; Kocz et al., 2019). FRB localization nowadays have been accomplished in several cases (Chatterjee et al., 2017; Michilli et al., 2018; Ravi et al., 2019) and have provided the smoking guns in favor of the FRB extragalactic origin. The redshift information from the small sample of located FRBs have been used to demonstrate that FRBs can be used as powerful cosmological probes and to derive an independent estimate of cosmic baryon density $\Omega_b = 0.051_{-0.025}^{+0.021} h_{70}^{-1}$ with 95% CL (Macquart et al., 2020). A larger sample will not just narrow down the constraints on this parameter, but could also disentangle the fraction of baryons that reside in the IGM f_{IGM} and their distribution around the most massive haloes (McQuinn, 2014) as well as the ionization fractions of hydrogen $X_{\text{e,H}}$ and helium $X_{\text{e,He}}$ (Macquart, 2018).

In addition to dispersion of the signal, similarly also the radio signal is scattered both in time and frequency by n_e variability on short (i.e. \sim comparable to observation) timescales. This effect is called scintillation and currently prevents the determination of the spectral index of FRB emission from \sim GHz observations (Ravi et al., 2016; Macquart et al., 2019). Although to-date FRBs have been individually observed at a range of different radio frequencies from 328 MHz (Pilia et al., 2020) up to 5 GHz (Gajjar et al., 2018), multi-frequency observations have not yet been successful to observe FRBs in multiple bands at once (e.g. Scholz et al., 2016a; Guidorzi et al., 2019; Chang et al., 2019). This fact raises the interesting question whether FRBs are an intrinsically narrow-band phenomenon (Hessels et al., 2018) or their observations is simply too dim or affected by (self-)absorption at higher frequencies.

The proposed models for either the source and emission mechanism(s) that power FRBs are many and different (see [Platts et al., 2019](#), for a review). A breakthrough in the determination of the possible source recently came from observations of a very powerful radio impulse of very short duration comparable with the FRB ones, launched by the known Galactic magnetar SGR 1935+2154 ([Bochenek et al., 2020](#); [The CHIME/FRB Collaboration et al., 2020](#)). Defining this pulse an FRB is ambiguous, since its Galactic nature does not provide it with any DM_{excess} in excess of the Galactic value in the direction of SGR 1935+2154. However, by computing the isotropic luminosity of the burst and placing it to the distance of the closest known FRB, the resulting brightness would be perfectly consistent with that of the other FRBs and the signal would still be detected by the most sensitive single-dishes ([Kirsten et al., 2020](#)). Interestingly, high energy flaring activity was also observed by different probes in coincidence with the radio pulse from the same source ([Ridnaia et al., 2020](#); [Mereghetti et al., 2020](#); [Tavani et al., 2020](#); [Li et al., 2020](#)). This opens up the opportunity to observe a similar correlation also for extragalactic FRBs and to test the hypothesis of the magnetar model for their origin. Before this potential discovery, indirect ways to constrain the source/emission models had to be pursued, and the result they produced can not yet be considered in general as disproven by the bursts from SGR 1935+2154. Within this context, in 2018, we developed and adapted one method to inspect the various source models of stellar-like origins by means of a classical cosmological test used first introduced for Gamma Ray Bursts (GRBs) and known as $\langle V/V_{\text{max}} \rangle$ test. We present this analysis (published in [Locatelli et al., 2019](#)) in Sec. 4.2.

In addition their application to study the baryon content of the IGM, FRBs may come into play also for the inspection of the IGMF. In fact, several FRBs have been observed with a high linear polarization ([Michilli et al., 2018](#); [Day et al., 2020](#); [Cho et al., 2020](#); [Connor et al., 2020](#)). As we have seen in Chapter 3, any polarized signal travelling through the IGM is subject to the Faraday effect if the IGMF is actually present. A great potential advantage of FRBs with respect to the currently used synchrotron radio galaxies as background source RM grid is that polarized FRBs experience both dispersion and polarization-angle rotation. These two effects are both dependent on the free-electron column density along the LoS. The ratio RM/DM and 4.1) is then a proxy of the average magnetic component parallel to the LoS ([Akahori et al., 2016](#)):

$$\frac{RM}{DM} \equiv \frac{\int_{\text{LoS}} n_e B_{\parallel} dl}{\int_{\text{LoS}} n_e dl} = \langle B_{\parallel} \rangle \quad (4.2)$$

4.2. FRBS' COSMOLOGICAL DISTRIBUTION: THE V/V_{MAX} TEST

where B_{\parallel} is the component of B parallel to the LoS direction, positively oriented from the source to the observer.

To properly relate the IGMF intensity to the retrieved value $\langle B_{\parallel} \rangle = \text{RM}/\text{DM}$ a few considerations have to be taken in mind:

- it is an averaged (n_e -weighted) value: for the only IGM the average cancels out at about every coherence length and it is thus dependent on over what scale the B_{\parallel} (vector) sum is dominant; a more instructive value about the IGM magnetisation would need to know in addition B_{rms} , which however it is not probed by this method;
- it is again an average value: if the Milky Way magnetic field or the host galaxy magnetic field, or the near-source environment magnetization dominate the integral of $B_{\parallel}n_e$, then we do not obtain any information on the IGMF. With this respect addressing the FRB source origin, environment and preferred host galaxy type is necessary.

In the favourable case in which RMs from FRBs do include non-negligible information on the IGMF (see [Hackstein et al., 2019](#), for a thorough analysis on the feasibility and limitations), one can ask whether they also provide with a comparable/denser grid than the number of available polarized background radio galaxies per square degree. In order to assess this question the true sky rate over a flux density threshold is the most useful quantity to constrain. The following Sections also aim to assess this quantity by means of either theoretical arguments based on the available FRB population (up to within 2018, Sec. 4.2), or by proposed new instrumental characterization and setup to build an efficient strategy for FRB detection and rate determination (Sec 4.3). We anticipate here that constraining the FRB rate is complementary to address the FRB spectral index, or the correlation (if any) between brightness and observing frequency in the case of intrinsic narrow-band phenomenology of FRBs.

4.2 FRBs' cosmological distribution: the V/V_{max} test ([Locatelli et al., 2019](#))

Abstract We have applied the luminosity–volume test, also known as $\langle V/V_{\text{max}} \rangle$, to fast radio bursts (FRBs). We compare the 23 FRBs, discovered by ASKAP, with 20 of the FRBs found by Parkes. These samples have different flux limits and correspond to different explored volumes. We put constraints on their redshifts with probability distributions (PDFs) and

applied the appropriate cosmological corrections to the spectrum and rate in order to compute the $\langle V/V_{\max} \rangle$ for the ASKAP and Parkes samples. For a radio spectrum of FRBs $\mathcal{F}_\nu \propto \nu^{-1.6}$, we found $\langle V/V_{\max} \rangle = 0.68 \pm 0.05$ for the ASKAP sample, that includes FRBs up to $z = 0.72_{-0.26}^{+0.42}$, and 0.54 ± 0.04 for Parkes, that extends up to $z = 2.1_{-0.38}^{+0.47}$. The ASKAP value suggests that the population of FRB progenitors evolves faster than the star formation rate, while the Parkes value is consistent with it. Even a delayed (as a power law or Gaussian) star formation rate cannot reproduce the $\langle V/V_{\max} \rangle$ of both samples. If FRBs do not evolve in luminosity, the $\langle V/V_{\max} \rangle$ values of ASKAP and Parkes sample are consistent with a population of progenitors whose density strongly evolves with redshift as $\sim z^{2.8}$ up to $z \sim 0.7$.

4.2.1 Context of the experiment

By the end of 2018, a collection of 52 FRBs was made available through a database¹ (described in [Petroff et al., 2016](#)). The large values of the observed dispersion measure DM_{obs} ([Lorimer et al., 2007](#); [Thornton et al., 2013](#)) and the detection of the host galaxy for the repeating FRB 121102 ([Marcote et al., 2017](#)), still seemed to favour their extra-galactic nature, while the Galactic scenario was not yet definitely discarded. The only known host galaxy redshift $z \sim 0.19$ ([Chatterjee et al., 2017](#); [Tendulkar et al., 2017](#)) by the time was also well consistent with the distance estimated from the observed DM. Despite the confirmed extra-galactic origin of this source, the fact that it remains the only repeater holds the possibility that it could be representative of a different class.

The 'debate' on the origin of FRBs reminds much of the similar case of Gamma Ray Bursts (GRBs) (see [Kulkarni, 2018](#)). Indeed, if extragalactic, FRBs have νL_ν luminosities around $10^{43} \text{ erg s}^{-1}$ and energetics of the order of 10^{40} erg (Fig. 4.2).

Such large energies and short duration imply a huge brightness temperature, of the order of $T_B \sim 10^{34} - 10^{37} \text{ K}$. This in turn requires a coherent radiation process possibly originating from masers or compact bunches of emitting particles, as it has been recognised by many authors ([Ghisellini, 2017](#); [Kumar et al., 2017](#); [Yang and Zhang, 2018](#); [Ghisellini and Locatelli, 2018](#); [Katz, 2018](#)).

Many of the proposed progenitor theories of extragalactic FRBs include merging of compact objects such as neutron stars ([Totani, 2013](#)); or white dwarfs ([Kashiyama et al., 2013](#)). FRBs could be flares from magnetars

¹Fast Radio Burst Catalog (FRBCAT) <http://frbcatalog.org/>

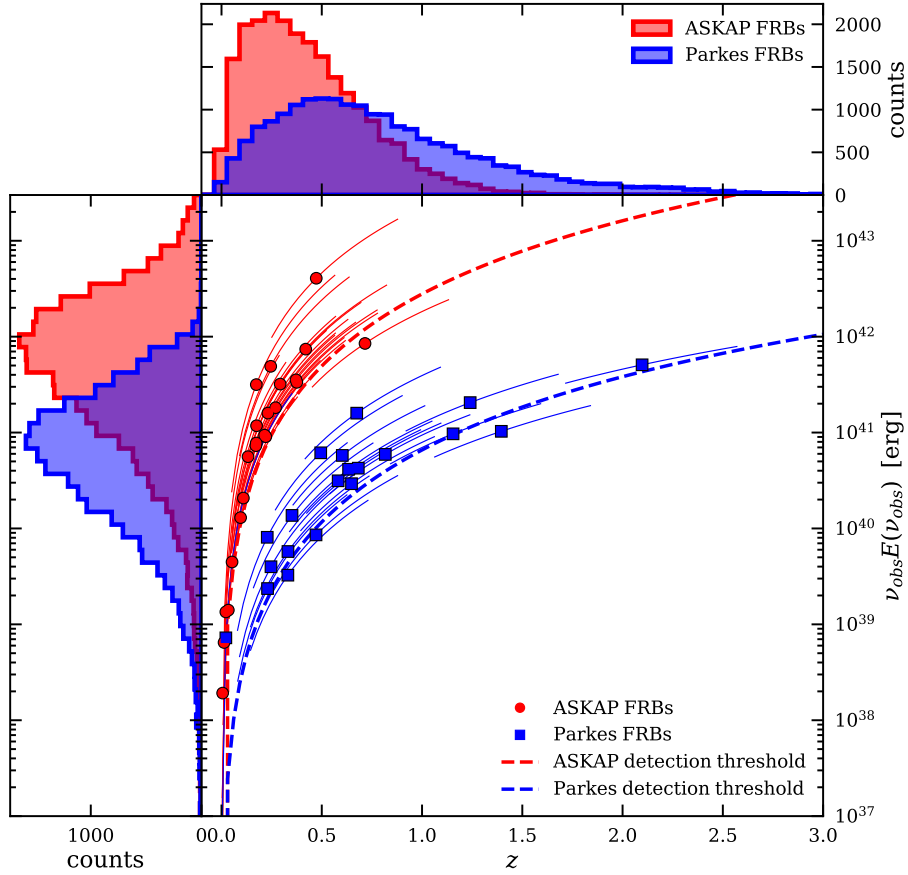


Figure 4.2: Energy (νE_ν) as a function of redshift for FRBs detected by ASKAP (red circles) and Parkes (blue squares). The dashed lines correspond to the fluence limit for ASKAP and Parkes (red and blue respectively) obtained assuming the average FRB duration of the respective samples. The top and right panels show the energy and redshift distributions of the two samples (same colour coding of the central plot). The thin curves represent, for each data point, the 1σ uncertainty on the energy produced by the uncertainty on the redshift.

(Popov and Postnov, 2010; Thornton et al., 2013; Lyubarsky, 2014; Beloborodov, 2017); or giant pulses from pulsars (Cordes and Wasserman, 2016); or they could be associated to the collapse of supra-massive neutron stars (Zhang, 2014; Falcke and Rezzolla, 2014); or dark matter induced collapse of neutron stars (Fuller and Ott, 2015). An updated list of FRB theories can be found in Platts et al. (2019).

A classical way to probe the unknown distance of a population of objects is through the $\langle V/V_{\max} \rangle$ test (also called luminosity–volume test). Firstly proposed by Schmidt (1968), the $\langle V/V_{\max} \rangle$ tests whether the distribution of objects is uniform within the volume of space defined by the observational selection criteria. Among other advantages, it is suitable for samples containing few objects and allows to combine samples of sources obtained with different selection criteria. Historically, it has been employed to study the space distribution of quasars and to assess the cosmic evolution of their population.

For a uniform population of sources with measured fluxes F , V/V_{\max} are the ratios of the volume V within which each source is distributed to the maximum volume V_{\max} within which each source could still be detected (which is individually defined by the sample selection flux limit). In an Euclidean space V/V_{\max} should be uniformly distributed between 0 and 1 with an average value $\langle V/V_{\max} \rangle = 0.5$. Equivalently the cumulative source count distribution is $N(> F) \propto F^{-3/2}$.

The standard Euclidean approach to the luminosity–volume test has been performed on FRBs by different authors: Oppermann et al. (2016) find $N(> F) \propto F^{-n}$ with $0.8 \leq n \leq 1.7$; Caleb et al. (2016), report $n = 0.9 \pm 0.3$ while Li and Zhang (2016) find a much flatter population with $n = 0.14 \pm 0.20$. More recently, James et al. (2019) (hereafter J19) updated these results with 23 new FRBs (Shannon et al., 2018) discovered by the ASKAP array through the CRAFT survey (Macquart et al., 2010). They find $n = 1.52 \pm 0.24$ for the combined ASKAP and Parkes FRB samples. However, for the first time, they compare different surveys with sufficient statistics, claiming a significant difference between the ASKAP CRAFT ($n = 2.20 \pm 0.47$) and Parkes HTRU ($n = 1.18 \pm 0.24$) surveys, respectively.

However, the assumption of a uniform distribution in Euclidean space for the number counts – $\langle V/V_{\max} \rangle$ test does not deal with the transient nature of FRBs. In this work we performed the volume–luminosity test using the redshift estimated through the DM. We accounted for the possible uncertainty on z in terms of a probability density function (PDF) which encodes the uncertainties on i) the Galactic free electron density model; ii) the baryon distribution in the Inter-Galactic Medium (IGM) and iii) the

free electron density model of the FRB host environment. Furthermore, we applied to each FRB the appropriate K-correction and accounted for the proper transformation from the observed to the intrinsic rate.

In §4.2.3 we present the two FRB samples used; in §4.2.4 we describe how to derive their $\langle V/V_{\text{max}} \rangle$ accounting for their cosmological nature. A Monte Carlo approach is adopted to perform the $\langle V/V_{\text{max}} \rangle$ for cosmological rate distributions (4.2.6) and compare with the real samples in §4.2.7. In §4.2.8 we discuss our results, and in §4.2.9 we draw our conclusions. In this Chapter, we adopt a standard cosmology with $\Omega_{\text{max}} = 0.286$, $h = 0.696$ and $\Omega_{\Lambda} = 0.714$.

4.2.2 $\langle V/V_{\text{max}} \rangle$ value estimation

The V/V_{max} computed in this work (Eq. 4.21), which accounts for the cosmological k-correction and proper rate of transient FRBs, is derived as follows. We considered the relation:

$$\mathcal{F}(\nu_{\text{obs}}) = \frac{(1+z)E_{\nu}(\nu_e)}{4\pi D_L^2(z)} \frac{d\nu_e}{d\nu_{\text{obs}}} = \frac{E_{\nu}(\nu_e)}{4\pi D^2(z)}, \quad (4.3)$$

where $\mathcal{F}(\nu) = F(\nu) w_{\text{obs}}$ is the fluence of an event of duration w_{obs} , and we used the relation between luminosity distance and proper distance: $D_L = (1+z)D$; analogously:

$$\mathcal{F}_{\text{lim}}(\nu_{\text{obs}}) = \frac{E_{\nu}(\nu'_e)}{4\pi D_{\text{max}}^2(z_{\text{max}})}, \quad (4.4)$$

where E_{ν} is the intrinsic energy density, $\nu_e = \nu_{\text{obs}}(1+z)$ and $\nu'_e = \nu_{\text{obs}}(1+z_{\text{max}})$ are the emitted frequencies at proper distances $D(z)$ and $D_{\text{max}}(z_{\text{max}})$, respectively.

We assumed that FRBs have a power-law energy spectrum spectral slope α , at least in a frequency range comparable to that probed by the observer frame frequency $\nu_{\text{obs}} \simeq 1.3$ GHz. Therefore, we could write:

$$\begin{aligned} dE &\propto \nu^{-\alpha} d\nu \\ E_{\nu}(\nu_e) &= E_{\nu}(\nu'_e) \cdot \left(\frac{\nu_e}{\nu'_e} \right)^{-\alpha} \\ &= E_{\nu}(\nu'_e) \cdot \left(\frac{\nu_{\text{obs}}(1+z)}{\nu_{\text{obs}}(1+z_{\text{max}})} \right)^{-\alpha} \\ &= E_{\nu}(\nu'_e) \cdot \left(\frac{1+z}{1+z_{\text{max}}} \right)^{-\alpha} \end{aligned} \quad (4.5)$$

Combining eq.4.3, 4.4 and 4.5 we obtained:

$$\frac{D(z)}{D_{\max}(z_{\max})} = \left[\frac{\mathcal{F}_{\lim}(\nu_{\text{obs}})}{\mathcal{F}(\nu_{\text{obs}})} \left(\frac{1+z}{1+z_{\max}} \right)^{-\alpha} \right]^{1/2}. \quad (4.6)$$

From the antenna equation, the signal-to-noise ratio of an event of duration w_{obs} is defined as:

$$S/N = \frac{G F(\nu) \sqrt{N_P \Delta\nu w_{\text{obs}}}}{\eta T_{\text{sys}}}, \quad (4.7)$$

where G is the antenna gain, N_P is the number of polarizations, η is the efficiency and T_{sys} is the antenna temperature. The S/N can also be described in terms of the fluence as:

$$S/N = \frac{\mathcal{F}(\nu)}{\sqrt{w_{\text{obs}}}} \frac{G \sqrt{N_P \Delta\nu}}{\eta T_{\text{sys}}}. \quad (4.8)$$

The limiting threshold over which an FRB is detected can also be described in terms of S/N:

$$S/N_{\lim} = \frac{\mathcal{F}_{\lim}(\nu)}{\sqrt{w'_{\text{obs}}}} \frac{G \sqrt{N_P \Delta\nu}}{\eta T_{\text{sys}}}. \quad (4.9)$$

where $w'_{\text{obs}} = w_{\text{rest}}(1+z_{\max})$; all the parameters related to the observing conditions/setup (G , N_P , $\Delta\nu$, η and T_{sys}) are the same when we want to look for the maximum distance at which the FRB could be observed. However, the observed duration of the transient event changes with redshift. We thus related the ratios of observed and threshold values with a function of their redshifts:

$$\frac{\mathcal{F}(\nu)}{\mathcal{F}_{\lim}(\nu)} = \frac{S/N}{S/N_{\lim}} \left(\frac{1+z}{1+z_{\max}} \right)^{1/2}. \quad (4.10)$$

Through Eq. 4.10 we recast Eq. 4.6 in terms of the S/N with respect to S/N_{\lim}

$$\frac{D(z)}{D_{\max}(z_{\max})} = \left[\frac{S/N_{\lim}}{S/N} \left(\frac{1+z}{1+z_{\max}} \right)^{-\frac{1}{2}-\alpha} \right]^{\frac{1}{2}}, \quad (4.11)$$

retrieving Eq. 4.21. Equivalently one can write it as

$$\frac{S/N}{S/N_{\lim}} D^2(z) (1+z)^{\frac{1}{2}+\alpha} = D_{\max}^2(z) (1+z_{\max})^{\frac{1}{2}+\alpha} \equiv \Upsilon(z_{\max}). \quad (4.12)$$

We put in the right-hand side (RHS) of eq. 4.12 all the terms depending on z_{\max} . We defined the function $\Upsilon(z_{\max})$ as the RHS. $\Upsilon(z_{\max})$ can

4.2. FRBS' COSMOLOGICAL DISTRIBUTION: THE V/V_{MAX} TEST 135

be evaluated using the left-hand side (LHS) of the same equation, that is, combining the observed, instrumental and cosmological information. If the functions $D_{\text{max}}(z)$ and $\Upsilon(z)$ are invertible one can in principle solve the above equation for z_{max} . We note that only for $\alpha > -1/2$ this function is monotonic and invertible. Under this assumption

$$z_{\text{max}} = \Upsilon^{-1} \left[\frac{S/N}{S/N_{\text{lim}}} D^2(z) (1+z)^{\frac{1}{2}+\alpha} \right]. \quad (4.13)$$

The function Υ depends on cosmology through the definition of $D(z)$

$$D(z) = \int_0^z \frac{c dz'}{H_0 \sqrt{\Omega_{\text{max}}(1+z')^3 + \Omega_k(1+z')^2 + \Omega_\Lambda}}, \quad (4.14)$$

and from the spectral index α of the intrinsic FRB specific luminosity.

The estimates of the spectral index is given considering the 23 ASKAP burst signals (Shannon et al., 2018) detected in-band (336 MHz) centred at 1.32 GHz showing intense fine-scale features (Macquart and Ekers, 2018). They calculate a mean spectral index $\alpha = 1.6_{-0.2}^{+0.3}$. This represents the current best (and only) estimate of the spectral index for a non-repeating FRB, as far as any broad-band information will be given.

The analytic form of Eq. 4.13 is not straightforward to obtain so we solved it numerically.

In Eq. 4.13 the ratio between a threshold and the corresponding observed quantity are present (instead of just the observed one). This fact removes the dependency of the test from any survey parameter, since they would play the same role in the definition of both terms in the ratio. The independence of the ratio between observed and threshold S/N from the survey area and time coverage, or any other observation parameter, has been previously proven by J19 in a rigorous way. Our derivation can be helpful in giving an intuitive and straightforward proof of the fact.

The $(S/N)/(S/N)_{\text{lim}}$ approach has also the advantage that any other quantity which varies linearly with the fluence $\mathcal{F}(\nu)$ can be used in its place in Eq. 4.13 (Oppermann et al., 2016). The smartest choice is to use the signal-to-noise ratio (S/N), which is the ratio between the amplitude of the time-integrated FRB signal and the standard deviation of the noise in the continuum (Petroff et al., 2016).

We chose to use S/N as S/N_{lim} is the quantity which is actually defined in a survey in order to claim a detection, rather than the flux density F_ν or the fluence \mathcal{F}_ν . Moreover, the way the S/N is defined is in principle independent from the pulse broadening effect whenever a signal is detected.

In fact, highly-broadened signals could not be recognised as FRB candidates by searching pipelines, but a non-detection does not affect the completeness of the sample in a $\langle V/V_{\max} \rangle$ test.

4.2.3 Data samples

The ASKAP array of radio telescopes and the Parkes telescope provided two relatively large and well defined samples of FRBs which allow us to perform statistical analysis. From the online catalogue FRBCAT² (Petroff et al., 2016), we collected all ASKAP and Parkes FRBs that have been confirmed via publication with a known signal to noise ratio (S/N) threshold.

ASKAP We considered the 23 FRBs detected by ASKAP and recently published by Shannon et al. (2018) and Macquart and Ekers (2018). The ASKAP survey has an exposure of $5.1 \times 10^5 \text{ deg}^2 \text{ h}$ covering a sky area of 20 deg^2 . It has a unique S/N threshold of 9.5 which corresponds to a limiting fluence of $23.16 \times (w_{\text{obs}}/1 \text{ ms})^{1/2} \text{ Jy ms}$ (Shannon et al., 2018). Although FRB 171216 has been detected with a $S/N = 8$ in a single beam, it has a $S/N = 10.3$ considering its detection in the two adjacent beams (Shannon et al., 2018) and we then included this event in our sample.

The ASKAP sample is shown in Fig. 4.2 (red circles). To properly compare the energy density of FRBs at different redshifts we evaluated the energies at the observed frequency $\nu_{\text{obs}} = 1.3 \text{ GHz}$ for all the FRBs. We applied the K-correction assuming an energy power law spectrum $E_\nu \propto \nu^{-\alpha}$ with $\alpha = 1.6$ (Macquart and Ekers, 2018). Therefore the K-corrected energy density is given by eq. 4.5. $E_\nu(\nu_{\text{obs}}) = E_\nu(\nu_{\text{rest}})(1+z)^\alpha$. The red dashed line corresponds to the ASKAP limiting fluence assuming the average intrinsic duration of the ASKAP sample $\langle w_{\text{rest}} \rangle = 2.2 \text{ ms}$. The observed pulse duration (which defines the limiting curve - see above) scales as $w_{\text{obs}} = \langle w_{\text{rest}} \rangle (1+z)$. Because of the large field of view and the high fluence threshold, the ASKAP survey is more sensitive to nearer and relatively powerful events. This is evident in the redshift and energy distributions (top and left panels of Fig. 4.2) of the ASKAP sample whose mean values are $\langle z \rangle = 0.25$ and $\langle E \rangle = 4.3 \times 10^{41} \text{ erg}$ respectively.

Parkes Among all Parkes FRBs we found 20 verified events with known S/N threshold. In this case, since FRBs were detected in various surveys with different instrumental setups, the S/N threshold is not equal for all

²available at <http://www.frbcatalog.org>

FRBs and therefore the corresponding fluence limit is not unique. The mean fluence limit of this sample results $0.54 \times (w_{\text{obs}}/1 \text{ ms})^{1/2} \text{ Jy ms}$ and is represented by the dashed blue line in Fig. 4.2. Compared with ASKAP, the Parkes telescope is characterised by a smaller field of view ($\sim 0.01 \text{ deg}^2$) and a lower fluence limit being thus sensitive to more distant and less powerful events on average (cf. the distributions in the top and left panels of Fig. 4.2). The total exposure of the HTRU survey made at Parkes is $1441 \text{ deg}^2 \text{ h}$ (Champion et al., 2016). The mean redshift and energy of the Parkes sample are $\langle z \rangle = 0.67$ and $\langle E \rangle = 7.2 \times 10^{40} \text{ erg}$, respectively.

The total sample includes 43 FRBs. When different data analyses for the same FRB were found, we chose the one computed with the method presented in Petroff et al. (2016) (if available) in order to build a uniform sample and because alternative searches tend to under-estimate the S/N (see Keane and Petroff, 2015).

Table 4.2 lists the galactic longitude and latitude (gl and gb), the observed dispersion measure (DM_{obs}), the signal to noise ratio (S/N), the survey S/N threshold (S/N_{lim}), fluence $\mathcal{F}(\nu_{\text{obs}})$, duration w_{obs} and flux density $F(\nu_{\text{obs}})$ all evaluated at the observed frequency ν_{obs} , the redshift calculated as presented in §3 and the references of the S/N_{lim} for all the 43 FRBs in our sample.

4.2.4 Method

Redshift information is necessary to perform the luminosity-volume test for a cosmological population of sources. In order to estimate z Ioka (2003) and Inoue (2004) proposed a linear relation between the redshift and the dispersion measure due to the IGM (DM_{IGM}):

$$DM_{\text{IGM}} = C \cdot z, \quad (4.15)$$

where $C = 1200 [\text{pc}/\text{cm}^3]$. The redshift of a transient radio source can be estimated from the residual dispersion measure DM_{excess} , that is, once the Milky Way contribution is subtracted out from the observed DM_{obs} measured for the particular source:

$$\begin{aligned} DM_{\text{excess}} &= DM_{\text{obs}} - DM_{\text{MW}} \\ &= \frac{DM_{\text{host}}}{1+z} + DM_{\text{IGM}}, \end{aligned} \quad (4.16)$$

where DM_{host} is the dispersion measure of the host galaxy environment. The Milky Way dispersion measure DM_{MW} is estimated in this work using the

FRR name	gl deg	gb deg	$D_{M_{\text{obs}}}$ pc/cm ³	S/N	S/N _{lim}	Fluence Jy ms	w_{obs} ms	Flux Jy	z †	Ref.
ASKAP										
180525	349.0	50.7	388.1	27.4	9.5	300	3.8	78.9	0.174 ^{+0.391} _{-0.123}	Ma18
180324	245.2	-20.5	431	9.8	9.5	71	4.3	16.51	0.172 ^{+0.392} _{-0.121}	Ma18
180315	13.2	-20.9	479	10.4	9.5	56	2.4	23.34	0.215 ^{+0.356} _{-0.142}	Ma18
180212	338.3	50.0	167.5	18.3	9.5	96	1.81	53.04	0.022 ^{+0.321} _{-0.020}	Sh18
180131	0.6	-50.7	657.7	13.8	9.5	100	4.5	22.22	0.420 ^{+0.403} _{-0.210}	Sh18
180130	5.9	-51.8	343.5	10.2	9.5	95	4.1	23.17	0.132 ^{+0.350} _{-0.089}	Sh18
180128.2	327.8	-48.6	495.9	9.6	9.5	66	2.3	28.7	0.270 ^{+0.399} _{-0.164}	Sh18
180128.0	326.7	52.2	441.4	12.4	9.5	51	2.9	17.6	0.221 ^{+0.397} _{-0.144}	Sh18
180119	199.5	-50.4	402.7	15.9	9.5	110	2.7	40.74	0.175 ^{+0.394} _{-0.123}	Sh18
180110	7.8	-51.9	715.7	35.6	9.5	420	3.2	131.25	0.472 ^{+0.406} _{-0.222}	Sh18
171216	273.9	-48.4	203.1	10.3	9.5	40	1.9	21.06	0.034 ^{+0.345} _{-0.030}	Sh18
171213	200.6	-48.3	158.6	25.1	9.5	133	1.5	88.67	0.013 ^{+0.308} _{-0.012}	Sh18
171116	205.0	-49.8	618.5	11.8	9.5	63	3.2	19.69	0.372 ^{+0.404} _{-0.198}	Sh18
171020	29.3	-51.3	114.1	19.5	9.5	200	3.2	62.5	0.006 ^{+0.282} _{-0.006}	Sh18
171019	52.5	-49.3	460.8	23.4	9.5	219	5.4	40.56	0.245 ^{+0.391} _{-0.155}	Sh18
171004	282.2	48.9	304	10.9	9.5	44	2	22.	0.095 ^{+0.381} _{-0.075}	Sh18
171003	283.4	46.3	463.2	13.8	9.5	81	2	40.5	0.232 ^{+0.398} _{-0.150}	Sh18
170906	34.2	-49.5	390.3	17	9.5	74	2.5	29.6	0.173 ^{+0.395} _{-0.123}	Sh18
170712	329.3	-51.6	312.79	12.7	9.5	53	1.4	37.86	0.109 ^{+0.383} _{-0.084}	Sh18
170707	269.1	-50.5	235.2	9.5	9.5	52	3.5	14.86	0.053 ^{+0.361} _{-0.045}	Sh18
170428	359.2	-49.9	991.7	10.5	9.5	34	4.4	7.73	0.716 ^{+0.416} _{-0.263}	Sh18
170416	337.6	-50	523.2	13	9.5	97	5	14.4	0.293 ^{+0.402} _{-0.173}	Sh18
170107	266.0	51.4	609.5	16	9.5	58	2.4	24.17	0.376 ^{+0.402} _{-0.198}	Ba17

Table 4.1: Observational and instrumental parameters of FRRBs in our sample. †: Redshifts z are calculated from DMs as in §3. In the last column we report the references for the S/N_{lim}: Ma18: Macquart and Ekers (2018); Sh18: Shannon et al. (2018); Ba17: Bannister et al. (2017); Bh18: Bhandari et al. (2018); Ke16: Keane et al. (2016); Pe17: Petroff et al. (2017); Pe15: Petroff et al. (2015); Sh16: Shand et al. (2016); Ch16: Champion et al. (2016); Sc16: Scholz et al. (2016b); Th13: Thornton et al. (2013); Ke12: Keane et al. (2012). Parkes FRRBs parameters are taken from Petroff et al. (2016) when available, or from the reference in the last column.

4.2. FRBS' COSMOLOGICAL DISTRIBUTION: THE V/V_{MAX} TEST139

FRB name	gl deg	gb deg	DM_{obs} pc/cm ³	S/N	S/N _{lim}	Fluence Jy ms	w_{obs} ms	Flux Jy	$z \dagger$	Ref.
Parkes										
160102	18.9	-60.8	2596.1	16	10	1.8	3.4	1.06	2.097 ^{+0.473} _{-0.381}	Bh18
151230	239.0	34.8	960.4	17	10	1.9	4.4	0.86	0.682 ^{+0.412} _{-0.257}	Bh18
151206	32.6	-8.5	1909.8	10	10	0.9	3	0.6	1.395 ^{+0.445} _{-0.332}	Bh18
150610	278.0	16.5	1593.9	18	10	1.3	2	0.53	1.155 ^{+0.437} _{-0.312}	Bh18
150418	232.7	-3.2	776.2	39	10	1.76	0.8	2.2	0.247 ^{+0.405} _{-0.157}	Ke16
150215	24.7	5.3	1105.6	19	10	2.02	2.88	0.7	0.582 ^{+0.411} _{-0.242}	Pe17
140514	50.8	-54.6	562.7	16	10	1.32	2.82	0.47	0.331 ^{+0.404} _{-0.186}	Pe15
131104	260.6	-21.9	779	34	10	2.75	2.37	1.16	0.352 ^{+0.403} _{-0.192}	Sh16
130729	324.8	54.7	861	14	10	3.43	15.61	0.22	0.602 ^{+0.411} _{-0.246}	Ch16
130628	226.0	30.7	469.88	29	10	1.22	0.64	1.91	0.230 ^{+0.396} _{-0.149}	Ch16
130626	7.5	27.4	952.4	21	10	1.47	1.98	0.75	0.648 ^{+0.413} _{-0.253}	Ch16
121002	308.2	-26.3	1629.18	16	10	2.34	5.44	0.43	1.240 ^{+0.439} _{-0.319}	Ch16
120127	49.3	-66.2	553.3	13	9	0.75	1.21	0.62	0.331 ^{+0.399} _{-0.186}	Th13
110703	81.0	-59.0	1103.6	17	9	1.75	4.3	0.41	0.817 ^{+0.422} _{-0.276}	Th13
110626	355.9	-41.8	723	12	9	0.89	1.41	0.63	0.471 ^{+0.407} _{-0.222}	Th13
110220	50.8	-54.8	944.38	54	9	7.31	6.59	1.11	0.674 ^{+0.417} _{-0.257}	Th13
110214	290.7	-66.6	168.9	13	5	51.3	1.9	27.	0.022 ^{+0.329} _{-0.020}	Pe17
090625	226.4	-60.0	899.55	30	10	2.19	1.92	1.14	0.634 ^{+0.415} _{-0.251}	Ch15
010621	25.4	-4.0	745	18	8	4.24	8.	0.53	0.228 ^{+0.399} _{-0.148}	Pe16
010125	356.6	-20.0	790	25	7	5.72	10.6	0.54	0.495 ^{+0.406} _{-0.226}	Ke12

Table 4.2: Same as Tab. 4.1, for the FRB sub-sample detected by the Parkes telescope.

model of (Yao et al., 2017, YMW16 hereafter). The redshift of the source can be estimated using Eq. 4.16.

In principle, a large uncertainty on the redshift estimate is expected due to either the local environment and host galaxy free electron density and inclination (Xu and Han, 2015; Luo et al., 2018), and to the high variance $\sigma_{\text{DM}}^2(z)$ of the unknown baryon halos and sub-structures along the LoS (McQuinn, 2014; Dolag et al., 2015). In order to take into account these two sources of uncertainty – affecting DM_{host} and DM_{IGM} respectively in Eq. 4.16 – we calculated the $\langle V/V_{\text{max}} \rangle$ building appropriate probability functions for the redshifts $\text{PDF}(z)$, rather than a unique value as obtained through Eq. 4.15.

Firstly we needed to model the host galaxy contribution DM_{host} . Xu and Han (2015) estimated DM_{host} for different galaxy morphologies and inclination angles i with respect to the LoS. In particular, for spiral galaxies they fitted skew normal functions $f(\text{DM}, i)$ to the DM_{host} distributions for different values of the inclination angle i . We found the overall DM_{host} PDF ($P(\text{DM}_{\text{host}})$) by averaging the functions $f(\text{DM}, i)$, each weighted with the probability of the inclination angle $\sin i$. We extracted the DM_{host} values from $P(\text{DM}_{\text{host}})$. This allowed us to calculate the redshift z_{peak} , corresponding to the most probable value to be associated to the $\text{DM}_{\text{excess}}$ of the j -th FRB. The DM distribution of the host galaxy and environment has been also estimated by Luo et al. (2018). They obtained in general a smaller contribution of DM_{host} to the $\text{DM}_{\text{excess}}$ than what derived by Xu and Han (2015). This is probably due to the simplistic but more conservative assumption of a MW, M31-like galaxy as a host environment in the latter work, from which we derived the DM_{host} distribution.

The other source of uncertainty is related to the variance of DM_{IGM} . This has been studied for example by McQuinn (2014) and Dolag et al. (2015). We considered the scenario giving the largest $\sigma_{\text{DM}}(z)$ as reported in McQuinn (2014), obtained with a baryon (i.e. n_e) distribution tracing the dark matter halos above a certain mass threshold. Although dedicated simulations show smaller uncertainties (McQuinn, 2014; Dolag et al., 2015) we chose the most conservative $\sigma_{\text{DM}}(z)$ relation, represented by the power-law function:

$$\sigma_{\text{DM}}(z) = \frac{379.2}{C_{1200}} z^{0.313}, \quad (4.17)$$

where C_{1200} is the coefficient C in units of 1200pc cm^{-3} .

We calculated a lower (z_{inf}) and upper value (z_{sup}) for the redshift in the PDF by introducing the left and right standard deviations $\sigma_{\text{DM}}(z)$ re-

spectively in the RHS of Eq. 4.16:

$$DM_{\text{excess}} \equiv C \cdot z_{\text{inf}} + \sigma_{\text{DM}}(z_{\text{inf}}) + \frac{DM_{\text{host}}}{1+z_{\text{inf}}}, \quad (4.18)$$

$$DM_{\text{excess}} \equiv C \cdot z_{\text{sup}} - \sigma_{\text{DM}}(z_{\text{sup}}). \quad (4.19)$$

In the second equation a null DM_{host} contribution gives an upper limit to the redshift distribution. The PDF was then shaped as an asymmetric Gaussian: the peak of the PDF was assigned to the redshift z_{peak} ; the left and right dispersion are $\sigma_{\text{DM}}(z_{\text{inf}}) = z_{\text{peak}} - z_{\text{inf}}$ and $\sigma_{\text{DM}} = z_{\text{sup}} - z_{\text{peak}}$ respectively, where $z_{\text{inf}} < z_{\text{peak}} < z_{\text{sup}}$.

To calculate the Galactic contribution to the DM (DM_{MW}) we considered two n_e models: the NE2001 model (Cordes and Lazio, 2002) and the model of YMW16³. Assuming different models for the MW free electron contribution did not significantly affect the redshift distribution of the FRB sample. The same result has also been found by Luo et al. (2018) who also considered the presence of a free electron dark halo around the Milky Way. Its effect is found to be negligible however. This enabled us to base our analysis assuming one of the DM models without losing generality. We considered the YMW16 as our baseline model.

Up to now we accounted for the stochastic dispersion around the $DM_{\text{IGM}}(z)$ relation. However, an additional source of uncertainty can systematically arise from the choice of the average $DM_{\text{IGM}}(z)$ relation, namely the C coefficient of Eq. 2. In fact simulations (Dolag et al., 2015) show a lower value than the one derived from modelling of the free electron density in the IGM. To account also for this systematic effect we calculated redshift uncertainties assuming different values of C in the range [950, 1200].

In general, large values of C decrease both the redshift z and the maximum observable redshift z_{max} , but by a slightly different amount, making the average $\langle V/V_{\text{max}} \rangle$ to also decrease. However, the relative change of the $\langle V/V_{\text{max}} \rangle$ values, for the C values considered, is limited to less than 3% for all spectral indices. For simplicity, we thus assumed $C = 1200$.

³Online calculators are available respectively at:
<https://www.nrl.navy.mil/rsd/RORF/ne2001/model.cgi>
<http://www.atnf.csiro.au/research/pulsar/ymw16>

4.2.5 $\langle V/V_{\max} \rangle$ of the FRB samples

The cosmological $\langle V/V_{\max} \rangle$ test is defined as the average over the sample of the ratios between the volume of space included within the source distance and the maximum volume in which an event, holding the same intrinsic properties, could have been observed. A large value of $\langle V/V_{\max} \rangle$ indicates sources distributed closer to the boundary of the volume probed by the given survey. Conversely, a low $\langle V/V_{\max} \rangle$ value indicates a population distributed closer to the observer with respect to the total survey–inspected volume.

In terms of comoving distance $D(z)$, we express:

$$\left\langle \frac{V}{V_{\max}} \right\rangle = \frac{1}{N} \sum_{i=0}^N \left[\frac{D^3(z)}{D_{\max}^3(z_{\max})} \right]_i, \quad (4.20)$$

where N is the total number of FRBs in one sample, $D(z)$ and z are, respectively, the comoving distance and redshift of each object. D_{\max} and z_{\max} are the same quantities that would be evaluated if that same source was observed at the limiting threshold of the same survey that found it, that is if its measured fluence \mathcal{F}_ν (or S/N) coincided with the survey detection thresholds, $\mathcal{F}_{\nu,lim}$ (or S/N_{lim}), assuming the same intrinsic properties of the event.

The largest volume which can be probed $\propto D_{\max}^3(z_{\max})$ is uniquely defined by the survey (e.g. instrumental) parameters once a cosmology is assumed. It can be expressed in terms of the maximum possible redshift z_{\max} at which a given source can be observed with the survey considered. In practice, we solved for z_{\max} Eq. 4.11 (see Sec. 4.2.2 for the complete derivation):

$$\frac{D(z)}{D_{\max}(z_{\max})} = \left[\frac{S/N_{lim}}{S/N} \left(\frac{1+z}{1+z_{\max}} \right)^{-\frac{1}{2}-\alpha} \right]^{\frac{1}{2}}, \quad (4.21)$$

for each FRB in our sample. Here α is the observed spectral index of FRBs. Our formulation of the luminosity–volume test has been implemented for transient events embedded in a non-Euclidean cosmological volume and can be used with any user-defined luminosity function, source distribution, source spectral index and cosmology.

Following Shannon et al. (2018), we assumed a power–law spectrum for the whole FRB population, with non–evolving spectral index α . We considered three possible values of the spectral index $\alpha = 0$, $\alpha = 1.6$ (see Macquart and Ekers, 2018) and $\alpha = 3$ in order to test how the spectral slope affects

4.2. FRBS' COSMOLOGICAL DISTRIBUTION: THE V/V_{MAX} TEST 143

α	ASKAP	Parkes	full sample
0	0.634 ± 0.054	0.443 ± 0.048	0.538 ± 0.109
1.6	0.681 ± 0.049	0.538 ± 0.046	0.624 ± 0.086
3	0.711 ± 0.046	0.593 ± 0.045	0.652 ± 0.075
$\langle z \rangle$	0.429 ± 0.063	0.820 ± 0.120	0.624 ± 0.218

Table 4.3: $\langle V/V_{\text{max}} \rangle$ for different values of the spectral index α . Values were obtained for the full sample and for the ASKAP and Parkes sub-samples. We assumed $C = 1200$. The mean redshift $\langle z \rangle$ in each sample is also reported.

$\langle z \rangle$	CSFR (MD14)	SGRBs (G16)	Const.
0.429	0.536	0.519	0.474
0.624	0.544	0.519	0.464
0.820	0.549	0.516	0.457

Table 4.4: $\langle V/V_{\text{max}} \rangle$ obtained at different $\langle z \rangle$ for populations extracted via the Monte Carlo method from the three tested redshift distributions described in the text.

the estimate of $\langle V/V_{\text{max}} \rangle$. Redshift were obtained through a Monte-Carlo extraction, as described at the beginning of this section. By estimating z_{max} for each FRB we can computed $\langle V/V_{\text{max}} \rangle$ for the two samples of ASKAP and Parkes FRBs and for the full combined ASKAP+Parkes sample. We then repeated the test 10^4 times to account for the stochastic uncertainty on redshift. Considering a spectral index of 1.6 as found by (Macquart and Ekers, 2018), we found $\langle V/V_{\text{max}} \rangle = 0.681 \pm 0.049$ and $\langle V/V_{\text{max}} \rangle = 0.538 \pm 0.046$ for ASKAP and Parkes, respectively, and $\langle V/V_{\text{max}} \rangle = 0.624 \pm 0.086$ for the full sample. Values of $\langle V/V_{\text{max}} \rangle$ for different values of the spectral index α are reported in Table 4.3. By looking at Eq. 4.20 and 4.21 we already expect, for a fixed (sub-)sample $\langle V/V_{\text{max}} \rangle$ to increase with increasing α . Instead, It is instructive to compare the above scenarios of the $\langle V/V_{\text{max}} \rangle$ trend with $\langle z \rangle$, with expectation from known distributions of sources that potentially constitute the FRB engines.

4.2.6 Comparison with simulated populations

We compared the values of the $\langle V/V_{\text{max}} \rangle$ obtained for the ASKAP and Parkes samples with the $\langle V/V_{\text{max}} \rangle$ expected for different cosmological population of sources. We tested three different redshift density distributions: i) the cosmic star formation rate (Madau and Dickinson, 2014, hereafter

MD14); ii) the short GRBs redshift distribution (as found by Ghirlanda et al., 2016, hereafter G16); iii) a constant density distribution (i.e. no evolution).

We called 'energy function' (EF) the density of sources (in the comoving volume) as a function of their radiated energy (in analogy with the luminosity function). For simplicity, we here neglected any EF evolution in cosmic time, considering only the density evolution corresponding to three cases above.

Synthetic populations were generated through a Monte Carlo extraction from a PDF proportional to a given $\psi_k(z)$ which represents the source density (i.e. per unit comoving volume) rate (i.e. per unit comoving time). The sub-scripts $k = 1, 2, 3$ refer to the three cases considered above. By accounting for the cosmological time dilation and volume, the sampling probability density function is:

$$\text{pdf}_k(z) dz \propto \psi_k(z) \cdot (1+z)^{-1} \frac{dV}{dz}(z) dz. \quad (4.22)$$

We then used the following procedure: we assumed a value of z_{\max} as the maximum redshift at which a FRB population can be detected and generate a fake FRB sample from $z = 0$ to $z = z_{\max}$. Then we evaluated the average $\langle V/V_{\max} \rangle$ and average $\langle z \rangle$ of the synthetic sample corresponding to that z_{\max} . The $\langle V/V_{\max} \rangle$ calculated from these events was then assigned to the mean redshift $\langle z \rangle$ of the simulated FRBs, and the pair set a point in the $\langle z \rangle$ versus $\langle V/V_{\max} \rangle$ plane in Fig. 4.3. We repeated this procedure for all values of z_{\max} in order to obtain the model curves in Fig. 4.3.

The value of z_{\max} is linked to the value of the intrinsic energy of the FRB through Eq. 4.12, once the dependence of S/N on the energy, intrinsic duration and distance is made explicit (see Appendix A):

$$D_{\max}^2(z_{\max})(1+z_{\max})^{\alpha+\frac{1}{2}} = \frac{E_\nu(\nu_{\text{obs}})}{4\pi A (w_{\text{rest}}/\text{ms})^{1/2}}, \quad (4.23)$$

where $D_{\max}(z_{\max})$ is the proper distance at redshift z_{\max} ; $E_\nu(\nu_{\text{obs}})$ is the energy density of the FRB at the observed frequency $\nu_{\text{obs}} \simeq 1.3$ GHz. The constants $A = 23.16$ Jy ms for ASKAP and $A = 0.54$ Jy ms for Parkes specify the fluence limit of the two instruments:

$$\mathcal{F}_{\text{lim}}(\nu_{\text{obs}}) = A \sqrt{\frac{w'_{\text{obs}}}{\text{ms}}} = A \left(\frac{w_{\text{rest}}}{\text{ms}} \right)^{1/2} (1+z_{\max})^{1/2} [\text{Jy ms}], \quad (4.24)$$

where $w'_{\text{obs}} = w_{\text{rest}}(1+z_{\max})$ is the pulse duration we would observe if the FRB were located at redshift z_{\max} . Therefore fixing z_{\max} for a given

extraction implies choosing the same intrinsic energy density $E_\nu(\nu_{\text{obs}})$ for all FRBs of the fake sample generated according to that z_{max} .

We note that the resulting curve $\langle V/V_{\text{max}} \rangle$ as a function of $\langle z \rangle$ is actually independent of the instrument (i.e. of the A parameter). In fact, if the A parameter is changed (namely, for different flux limits of the survey), at a given z_{max} the corresponding value of $E_\nu(\nu_{\text{obs}})$ changes, but the curve remains the same.

4.2.7 Results

The $\langle V/V_{\text{max}} \rangle$ test that we performed here includes the cosmological terms (K-correction and time dilation) arising from considering FRBs at cosmological distances as derived from their large observed dispersion measures. The $\langle V/V_{\text{max}} \rangle$ for the FRB sample (ASKAP+Parkes) and individually for the two sub-samples (ASKAP and Parkes) are shown in Table 4.3 for different assumed spectral index α of the FRB intrinsic spectrum.

Fig. 4.3 shows the $\langle V/V_{\text{max}} \rangle$ values distributions, obtained from the Monte-Carlo extraction, as a function of the average redshift for the two samples for ASKAP and Parkes. Values obtained assuming different α are shown in Fig. 4.4. Solid contours show 1-, 2- and 3- σ level of confidence estimated via a bootstrap re-sampling of the FRB population's redshift.

The different curves show the expected $\langle V/V_{\text{max}} \rangle$ as a function of mean redshift for the assumed density distributions (see § 4.2.6). The extension of the curves before their respective turnover is due to the different redshift where the assumed density distributions peak (see also Fig.4.5, bottom panel).

We find the values calculated for the sub-samples differing of $\Delta \langle V/V_{\text{max}} \rangle \simeq 0.12$. We note that they probe different volumes. The Parkes $\langle V/V_{\text{max}} \rangle$ is fully consistent with a cosmic stellar population (CSFR – cyan solid line in Fig. 4.3) or its delayed version (dot-dashed green line in Fig. 4.3). The ASKAP sample instead deviates from the CSFR scenario. An evidence for the difference between the ASKAP and Parkes FRB populations has also been reported by J19, who find different slopes of the source count distribution for the two sub-samples. They also report the difference to be inconsistent with the one which is expected to be due to the different volumes probed by the two surveys.

The larger $\langle V/V_{\text{max}} \rangle$ obtained for the ASKAP sample suggests a faster evolution with respect to the CSFR up to the distances currently explored by the ASKAP survey. This large value can not be explained even considering a delayed-CSFR (green dot-dashed line in Fig. 4.3) or a different spectral

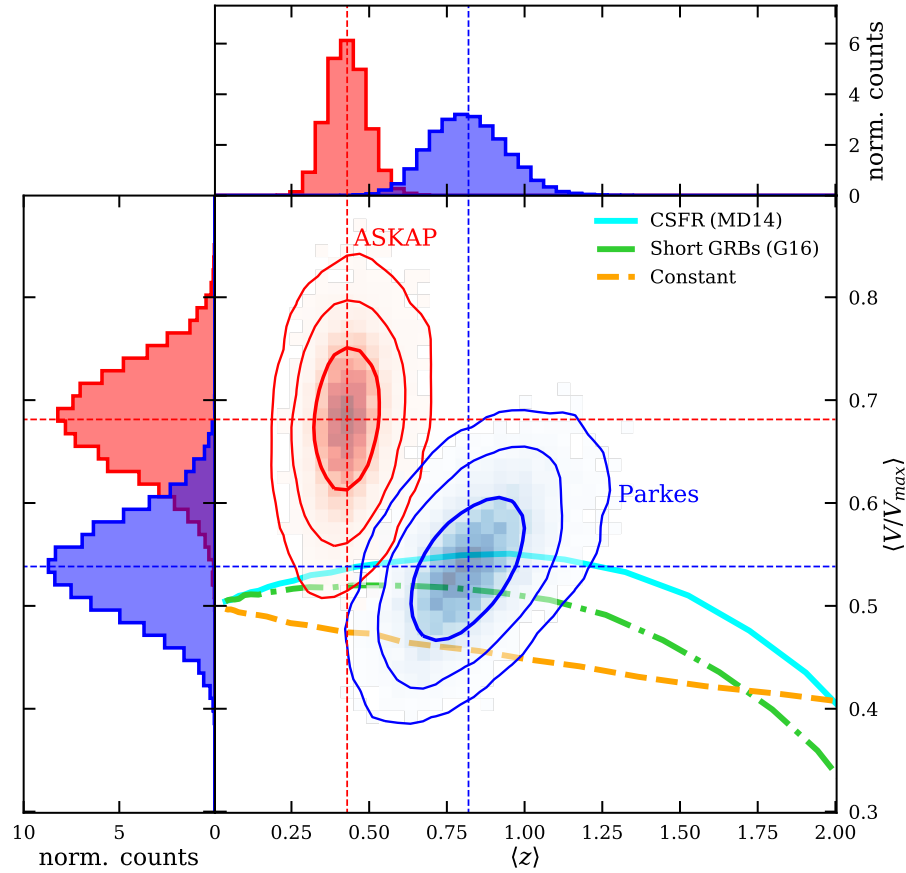


Figure 4.3: $\langle V/V_{\max} \rangle$ of the ASKAP and Parkes FRB samples (red and blue squares, respectively) computed accounting for the cosmological terms (K-correction and rate) and the redshifts dispersion. Contours represent the 1-, 2- and 3- σ uncertainties on $\langle V/V_{\max} \rangle$. A spectral index $\alpha = 1.6$ is assumed in this figure. Similar plots obtained with other possible values of the spectral index are shown in Fig. 4.4. The lines show the trends of $\langle V/V_{\max} \rangle$ as a function of increasing average redshift (i.e. survey depth). The different colours (styles) thick lines show the results of the evolution of $\langle V/V_{\max} \rangle$ obtained assuming different star formation rates (as labelled, see also §4.2.8).

4.2. FRBS' COSMOLOGICAL DISTRIBUTION: THE V/V_{MAX} TEST 147

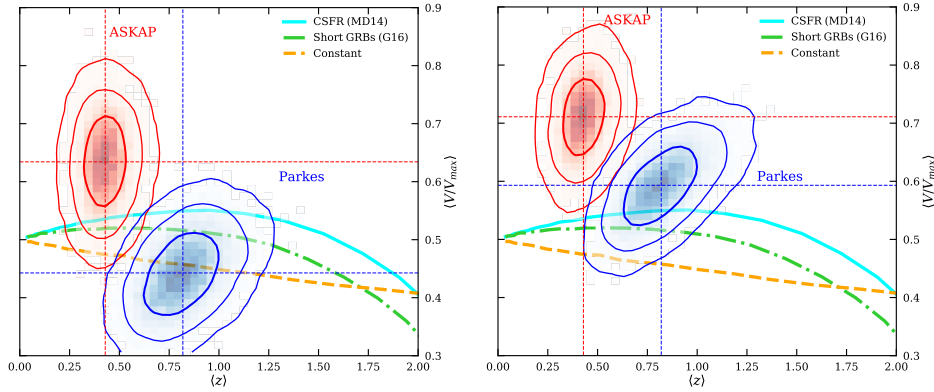


Figure 4.4: Same as Fig. 4.3 where we assumed different FRB spectral index α . Left panel: $\alpha = 0$; right panel: $\alpha = 3$

index for the FRB spectrum, nor a different $\text{DM}_{\text{IGM}}(z)$ relation. Overall, the ASKAP FRBs hint to a population of sources with a redshift density distribution different from those considered above (i.e. CSFR, delayed-CSFR as derived for short GRBs or constant formation rate).

4.2.8 Discussion

We have found that none of the population distributions adopted can account for the observed $\langle V/V_{\text{max}} \rangle$. We demonstrate here that this result is independent of the particular shape of the energy function, as long as it does not evolve in cosmic time. In the procedure we have adopted, each point of the curves in Fig. 4.3 corresponds to a population of sources having the same energy, calculated in such a way that its fluence corresponds to the limiting fluence once the source is at its z_{max} . Smaller $\langle z \rangle$ correspond to less energetic sources.

In reality we have a distribution of energies, each corresponding to a different $\langle V/V_{\text{max}} \rangle$, and $\langle z \rangle$. However all these pairs of values still belong to the plotted curves. As an example, consider a specific EF, say a power law in energy $N(E) \propto E^{-\Gamma}$, with Γ positive. There will be many points at low energies, corresponding to smaller $\langle z \rangle$ for the curve in Fig. 4.3. Many sources at lower $\langle z \rangle$ means that the corresponding $\langle V/V_{\text{max}} \rangle$ will dominate in the computation of the final $\langle V/V_{\text{max}} \rangle$. Still, the final value is constrained to be within the minimum and maximum values of the curve. As can be seen in Fig. 4.3 no curve can account for the $\langle V/V_{\text{max}} \rangle$ of the ASKAP sample.

Cosmic star formation rate Motivated by the strong hints on compact objects as sources of FRBs we considered a population with a rate density distribution described by the cosmic star formation:

$$\psi(z) = a_0 \frac{(1+z)^{a_1}}{1 + \left(\frac{1+z}{1+z_p}\right)^{a_2}}. \quad (4.25)$$

We adopted the parameters as reported by [Madau and Dickinson \(2014\)](#), $a_0 = 0.015$, $a_1 = 2.7$, $a_2 = 5.7$, and $z_p = 1.9$. For $a_1 > 0$ and $a_2 > 1$ the formation rate peaks at z_p with an increasing rate, for $z < z_p$, with slope a_1 . The $\langle V/V_{\max} \rangle$ as a function of $\langle z \rangle$ obtained with this function is shown in Fig. 4.3 (solid cyan line). The comparison with the ASKAP and Parkes values shows that a density evolution of FRBs following the star formation rate (Eq. 4.25) is consistent with the the Parkes $\langle V/V_{\max} \rangle$ value, but is largely below the ASKAP point (which is $\sim 2 - 3\sigma$ above the expectation for a population distributed as Eq. 4.25).

Phenomenological "FRB formation rate" The increase with redshift ($\propto (1+z)^{p_1}$ at low z) of the CSFR as represented by Eq.4.25 is too shallow to account for the ASKAP point. In order to account for the values of $\langle V/V_{\max} \rangle$ of both the ASKAP and Parkes sub-samples we used the form:

$$\text{FRBFR}(z) = p_0 \frac{z^{p_1}}{1 + (z/z_p)^{p_2}}. \quad (4.26)$$

The large $\langle V/V_{\max} \rangle$ of ASKAP is found at an average redshift significantly smaller than the redshift where the CSFR peaks (see the bottom panel of Fig. 4.5). We have verified that we can reproduce both the ASKAP and the Parkes $\langle V/V_{\max} \rangle$ values using, for instance, $p_0 = 1$, $p_1 = 3.7$, $p_2 = 4.8$ and $z_p = 0.6$. In this purely empirical model, p_0 is the density rate measured today ($z = 0$), p_1 is the slope of the density rate before it reaches its peak z_p while at $z \gg z_p$ the function has slope p_1/p_2 . We stress that numerical values provided for the parameters do not correspond to a formal fit and other possible functional forms could well be consistent with the two points. Proper model selection and parameter fitting is out of the scope of the current work. Here we wanted to find an empirical density distribution which we can a-posteriori compared with the cosmic star formation rate.

The model described above is shown by the solid red line in Fig. 4.5 (top panel). For comparison, also the model curve obtained from the CSFR described in the previous section is shown (dotted cyan line).

4.2. FRBS' COSMOLOGICAL DISTRIBUTION: THE V/V_{MAX} TEST 149

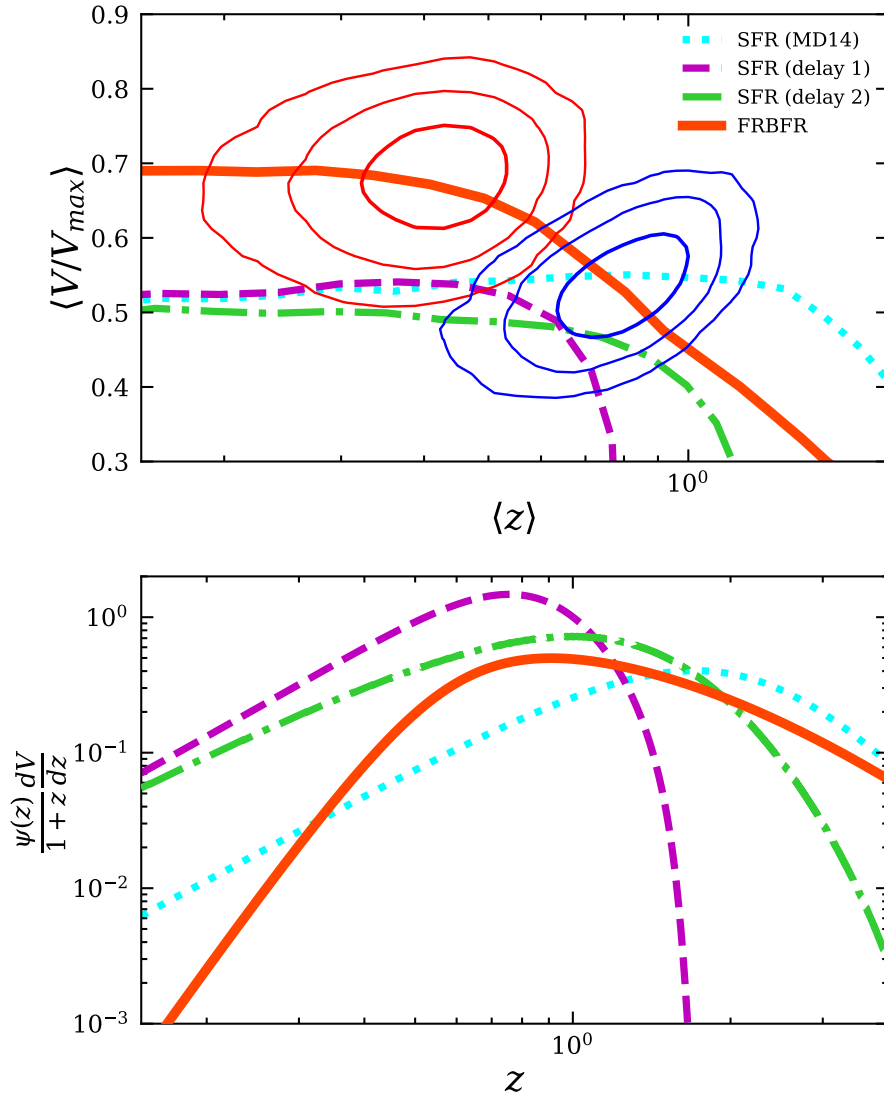


Figure 4.5: Simulated populations obtained from different redshift density distributions $\psi_k(z)$. Upper panel: $\langle V/V_{\text{max}} \rangle$ as function of the average observable redshift. Contours show the ASKAP and Parkes confidence levels assuming $\alpha = 1.6$ (see Fig. 4.3). Bottom panel: normalised source rate as function of redshift. Distributions are normalised to their integral.

Delayed cosmic star formation rate One possibility (e.g. motivated by the similar case of short GRBs) is that the progenitors of FRBs produce the radio flashes at some advanced stage of their evolution. This would introduce a delayed density distribution which in the simplest case can be modelled starting from the CSFR as (see G16)

$$\Psi(z) = \int_z^\infty \psi(z')P(t(z) - t(z'))\frac{dt}{dz'}dz' \quad (4.27)$$

. For the delay function we considered (1) a normal PDF centred on 4 Gyr with a dispersion $\sigma = 0.1$ Gyr, and (2) a power-law with slope $\propto \tau^{-1}$ with a minimum delay equal to 1 Gyr. The latter is what is expected for the merging of compact objects (Greggio, 2005; Belczynski et al., 2006; Mennekens et al., 2010; Ruiter et al., 2011; Mennekens and Vanbeveren, 2016; Cao et al., 2018). The $\langle V/V_{\max} \rangle$ curves obtained with these two models are shown in Fig. 4.5 (top panel) by the dashed (magenta) and dot-dashed (green) lines, respectively. The resulting source rate are plotted in Fig. 4.5 (bottom panel) in purple and green colour respectively. Although they peak at later times by construction, none of the delay models look to be consistent with the ASKAP data. In fact the effect of the delay is just to move the maximum value attainable for the $\langle V/V_{\max} \rangle$ to later times (i.e. smaller redshifts), but does not increase enough to become consistent with the ASKAP value (cfr Fig 4.5, upper panel).

4.2.9 Section summary

We have performed the $\langle V/V_{\max} \rangle$ test for two different FRB samples, assuming that their distances are cosmological. Having characterised each sample through its average redshift, we have verified that the value of $\langle V/V_{\max} \rangle$ for the Parkes sample is similar to the one derived assuming that FRBs follow the star formation rate. This would indicate that FRBs can be associated to compact stellar objects, such as neutron stars. Instead, for the ASKAP sample, sampling a closer volume but slightly more energetic FRBs, the value of $\langle V/V_{\max} \rangle$ is larger than the one derived with a population following the star formation rate. This result depends negligibly on the assumed FRB spectral index and has been determined accounting for the different sources of uncertainty on the estimate of the redshift of FRBs taking on a conservative approach.

At face value, this suggests that the progenitors of FRBs evolve in cosmic time faster than the star formation, and reach their maximum at redshift between the average redshift of the ASKAP and Parkes samples. Such fast

evolution at relatively low redshifts can be due to a density evolution faster than the star formation rate, or to a luminosity (and energy) evolution superposed to a standard star formation rate. This is intriguing, because it would suggest a very peculiar population for the FRB progenitors, but at this stage we are not able to disentangle between these possibilities. A possibility is that, similarly to short Gamma Ray Bursts, there is a delay between the formation of the stars producing the FRB phenomenon and the FRB event. However, we verified that this cannot produce the steep rise (as a function of redshift) of event rate up to $z \sim 0.3 - 0.4$ needed to account for the observed ASKAP $\langle V/V_{\max} \rangle$. The phenomenological 'FRB formation rate' we have found, that can fit both the ASKAP and Parkes $\langle V/V_{\max} \rangle$ cannot be interpreted in a simple way on the basis of known population of sources. While the investigations of possibilities is demanded to a future work, we stress the need of having surveys exploring the same (large) sky area of ASKAP, but with a fluence limit comparable to Parkes. This will show how the FRB population evolves in time in the interesting 0.3–2 redshift range.

4.3 The Northern Cross FRB project at 408 MHz ([Locatelli et al., 2020a](#))

Abstract Fast radio bursts remain one of the most enigmatic astrophysical sources. Observations have significantly progressed over the last few years, thanks to the capabilities of new radio telescopes and the refurbishment of existing ones. Here we describe the upgrade of the Northern Cross radio telescope with the ultimate goal of turning the array into a dedicated instrument to survey the sky for fast radio bursts. We present test observations of the pulsar B0329+54 to characterize the system performance and forecast detectability. Observations with the system currently in place are still limited by modest sky coverage ($\sim 5.9 \text{ deg}^2$) and biased by smearing of high dispersion measure events within each frequency channels. In its final, upgraded configuration, however, the telescope (N-S arm) will be able to carry out unbiased fast radio burst surveys over a $\sim 350 \text{ deg}^2$ instantaneous field of view up to $z \sim 5$, with a (nearly constant) $\sim 760 (\tau/\text{ms})^{-0.5} \text{ mJy}$ rms sensitivity.

4.3.1 Context of the experiment

The FRB excess of dispersion measure with respect to the Galactic contribution is nowadays accepted as a convincing evidence of their extragalactic

origin, but, beyond this, little is still known about their nature and physics (for a review on the topic, see [Petroff et al., 2019](#); [Cordes and Chatterjee, 2019](#)). Almost one hundred FRBs have been observed to date and only a handful of them appear to repeat ([Spitler et al., 2016](#); [CHIME/FRB Collaboration et al., 2019a,b](#); [Kumar et al., 2019](#)). A few FRBs have been localized, confirming their extragalactic origin, and their host environments have been found fairly different ([Chatterjee et al., 2017](#); [Michilli et al., 2018](#); [Ravi et al., 2019](#)). This scenario seem to indicate that FRBs may not be a single class of events and a significant effort is nowadays undertaken to localize more bursts ([Bailes et al., 2017](#); [Bannister et al., 2019](#); [Kocz et al., 2019](#)).

Beyond localization, the detection of a larger number of FRBs is crucial to discriminate among possible different populations ([Caleb et al., 2016](#); [Niino et al., 2018](#); [Macquart and Ekers, 2018](#); [Keane, 2018](#); [James et al., 2019](#); [Locatelli et al., 2019](#)), their emission mechanism ([Lyutikov, 2017](#); [Ghisellini, 2017](#); [Ghisellini and Locatelli, 2018](#)) and their astrophysical environment (see [Platts et al. 2019](#) for an updated review). Moreover, a larger statistic is necessary in order to use FRBs as effective cosmological probes ([McQuinn, 2014](#); [Macquart, 2018](#); [Akhori et al., 2018](#); [Vazza et al., 2018a](#); [Hackstein et al., 2019](#); [Ravi, 2019](#)).

Initially, FRBs were detected at GHz frequencies ([Lorimer et al., 2007](#); [Thornton et al., 2013](#); [Spitler et al., 2014](#); [Burke-Spolaor and Bannister, 2014](#); [Petroff et al., 2015](#); [Bhandari et al., 2018](#); [Patel et al., 2018](#); [Shannon et al., 2018](#)), but recent observations in the 400 – 800 MHz range have enormously increased the FRB statistics (e.g., [Caleb et al., 2016](#); [CHIME/FRB Collaboration et al., 2019a,b](#)) and placed increasingly better upper limits on their event rate ([Sokolowski et al., 2018](#); [Sanidas et al., 2019](#); [ter Veen et al., 2019](#)), showing the advantage of the large field of view (FoV) intrinsic to low frequency observations.

In this work we describe the ongoing effort to turn the Northern Cross (NC) radio telescope into a dedicated FRB survey machine observing at 408 MHz. We describe the current status of the instrumentation and related observations, and the forecast for upcoming surveys.

The Section is organized as follows: in § 4.3.2 we describe the current instrument status and recent upgrade, in § 4.3.3 we present test observations that characterize the system, in § 4.3.4 we forecast the FRB detection with the NC and we conclude in § 4.3.5.

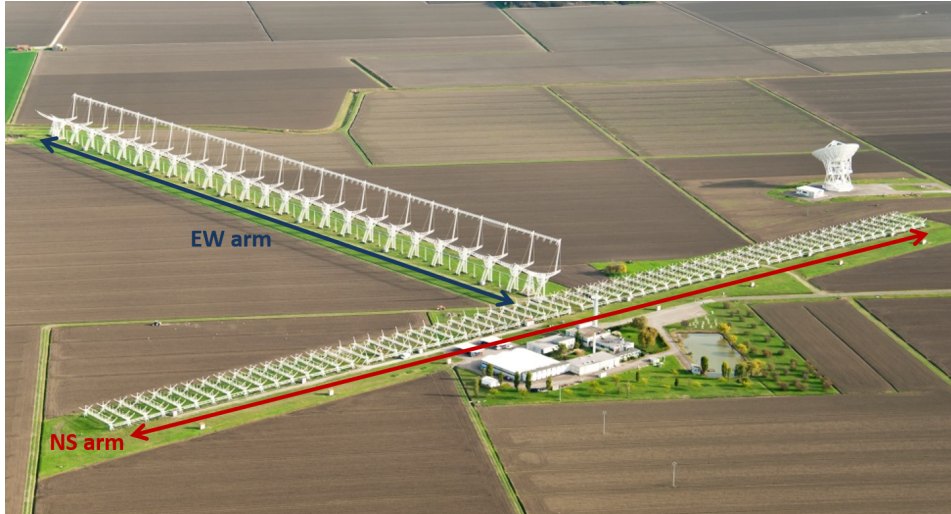


Figure 4.6: Aerial view of the Medicina Radio Astronomical Station. In the foreground, the Northern Cross with its two orthogonal arms.

4.3.2 Instrument description

The NC is a T-shaped radio interferometer operating at 408 MHz, located at the Medicina Radio Astronomical Station (Bologna, Italy). Its orthogonal arms are aligned along the North-South (NS) and East-West directions respectively (Figure 4.6). Historically, the NC was used to survey the sky, producing several catalogues of extragalactic radio sources (e.g., [Colla et al., 1970](#); [Ficarra et al., 1997](#); [Pedani and Grueff, 1999](#)).

The NS arm has 64 reflective cylinders, 7.5×23.5 m each, for a total collecting area $A_{\text{NS}} = 11280 \text{ m}^2$. However, as the antenna efficiency is ~ 0.71 ([Bolli et al., 2008](#)), the effective area is reduced to $A_{\text{NS,eff}} \simeq 8000 \text{ m}^2$. Each cylinder focuses the incoming radiation on 64 dipoles with single polarization, placed on the focal line; cylinders are spaced 10 m apart, leading to a total arm length of 640 m. The East-West arm was not used in this work.

The NS arm underwent an upgrade of six of the antenna and receiving system (see [Montebugnoli et al., 2009](#), for details) which is currently being extended to all antennas in the N-S arm. The focal line of sixteen cylinders has been modified in order to group the signals of sixteen dipoles together, providing four analogue signals per cylinder, i.e. 64 receiving inputs for the refurbished sector (Figure 4.7). The analogue receivers and digital backend

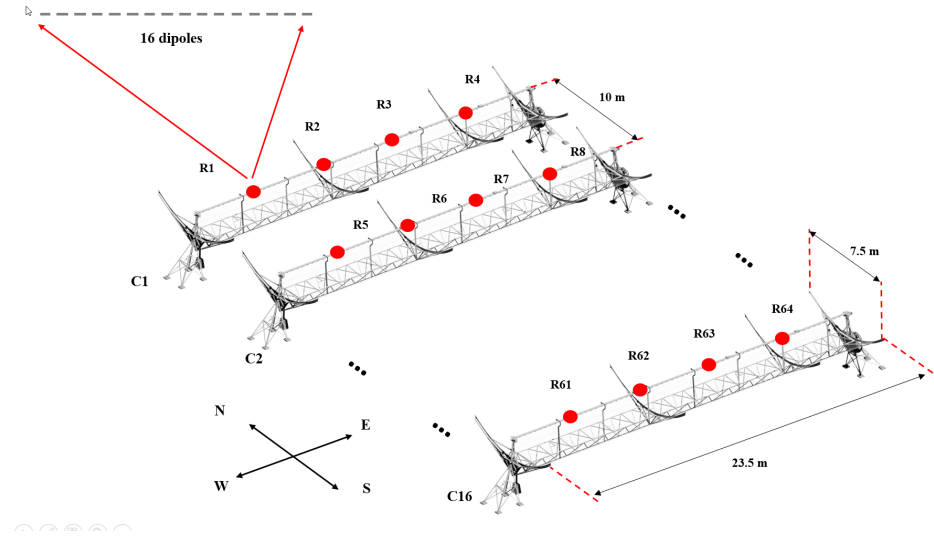


Figure 4.7: Scheme showing the refurbished section of the NS arm. The red circles indicate the position of the four receivers located on the focal line of each cylinder.

systems, as well as the firmware design, are accurately described in [Perini \(2009b,a\)](#); [Perini et al. \(2009\)](#); [Comoretto et al. \(2017\)](#); [Magro et al. \(2017, 2019\)](#) respectively. We refer the reader to these works for more technical details.

For what concerns our analysis, we briefly mention that the final channelized data streams are stored to disk using a simple binary format and are then correlated to generate calibration coefficients (see § 4.3.3). The frequency channels of interest from the fully sampled beam are saved to disk using a modified version of the SIGPROC Filterbank file format ([Lorimer, 2011](#)), where the complex voltages, rather than the power, are stored. This modification reduces the processing requirements (i.e. eliminates per-sample processing), resulting in the system being capable of writing data to disk in real time, and allows for custom offline software to convert the file to different file types such that no signal information is lost. For the tests described in this work, custom filterbank files are converted to filterbank compatible files.

The system (front end and back end) described in the references above is already a major upgrade over the pulsar back end used in the late '90s

Table 4.5: Characteristics of the current acquisition system.

N. of frequency channels	1024
Channel width	781.25 kHz
Time resolution	1.08 μ s
Multibeam beamformer	
N. bits	16 complex
N. channels	384
N. beams	4
Max. time resolution	69.12 μ s
Max. throughput	355.56 Mb/s
Single beam beamformer	
N. bits	16 complex
N. channels	21
Throughput	311.11 Mb/s

for pulsar searches and timing (D’Amico et al., 1996), however, we have already started to further optimize the system for FRB observations. The beamformer will be re-designed in order to produce up to twenty independent beams, placed anywhere inside the single element FoV. We outlined the most useful information characterizing the instrument in Table 4.5.

4.3.3 Test observations

We performed test observations in order to validate the system for FRB studies. As described in § 4.3.2, the digital beamformer requires that the receiver signals are corrected for the corrupting effects that enter along the RF path. This calibration procedure is done through standard interferometric techniques where the channelized complex voltages v from each receiver pair (i, j) are recorded and cross correlated to form visibilities V_{ij} :

$$V_{ij}^o = \langle v_i(t) v_j^*(t) \rangle_{\Delta t}, \quad (4.28)$$

where $\langle \rangle_{\Delta t}$ indicates the average over the integration time Δt and $*$ is the complex conjugate. A software correlator is used to evaluate the right hand side (RHS) of equation 4.28 by integrating the cross products over $\Delta t = 1.13$ s, that is a trade-off between S/N and fringe smearing.

The instrumental corruptions can be described by complex receiver gains g :

$$V_{ij}^o(t, \nu) = g_i(t, \nu) g_j^*(t, \nu) V_{ij}(t, \nu), \quad (4.29)$$

where V° are the observed visibilities, i.e., the visibilities that are corrupted by the instrumental response. The calibration procedure involves determining the instrumental gains g that can be solved for if the visibilities V_{ij} are known, i.e., through the observation of a calibration source. We observed Cas A, a standard calibrator for which we assumed a 4467 Jy flux density at 408 MHz (Perley and Butler, 2017). Observations were carried out for ~ 2 hours in the single beam mode (details are reported in Table 4.6). Six cylinders are formed by a total of 24 receivers, leading to 276 independent baselines, most of which are redundant due to the regular configuration grid (see Figure 4.7 for a reference scheme of the array used).

Table 4.6: Specifications of the NC test observations.

Central observing frequency	408 MHz
Analogue bandwidth	16 MHz
Total number of cylinders	6
Total number of receivers	24
Longest baseline (NS)	50 m
Receiver FoV	$\sim 38 \text{ deg}^2$
Receiver FoV FWHM North–South	5.9°
Receiver FoV FWHM East–West	6.4°

Visibility data were edited and flagged, and calibration equations solved using two different minimization methods (Boonstra and van der Veen, 2003), obtaining consistent solutions. Examples of visibilities compensated for the delay corresponding to the position of Cas A at the local meridian are shown in Figure 4.8. The bottom panel clearly shows that, after calibration, the real part of the visibilities has maxima aligned in the desired direction, at hour angle $\omega = 0^\circ$.

We used the derived antenna gains, combined with the geometric delay compensation coefficients, to beamform the six cylinder array towards the pulsar PSR B0329+54 (Cole and Pilkington, 1968). PSR B0329+54 has a 714 ms period (Hobbs et al., 2004), a $S_{400} = 1500 \text{ mJy}$ flux density at 400 MHz (Lorimer et al., 1995) and a $\text{DM} = 26.7641 \text{ pc cm}^{-3}$ dispersion measure (Hassall et al., 2012). It was observed for ~ 20 minute around transit.

We considered 20 s-long observations that were de-dispersed and over which the pulsar profile was folded. The pulsar is visible in each 20 s observation, and we used data taken closest to transit to estimate a $\text{S/N} \sim 422$ (Figure 4.9), which, in turn, implies an rms noise $\sigma_6 = \frac{S_{400}}{\text{S/N}} \sim 3.6 \text{ mJy}$ -

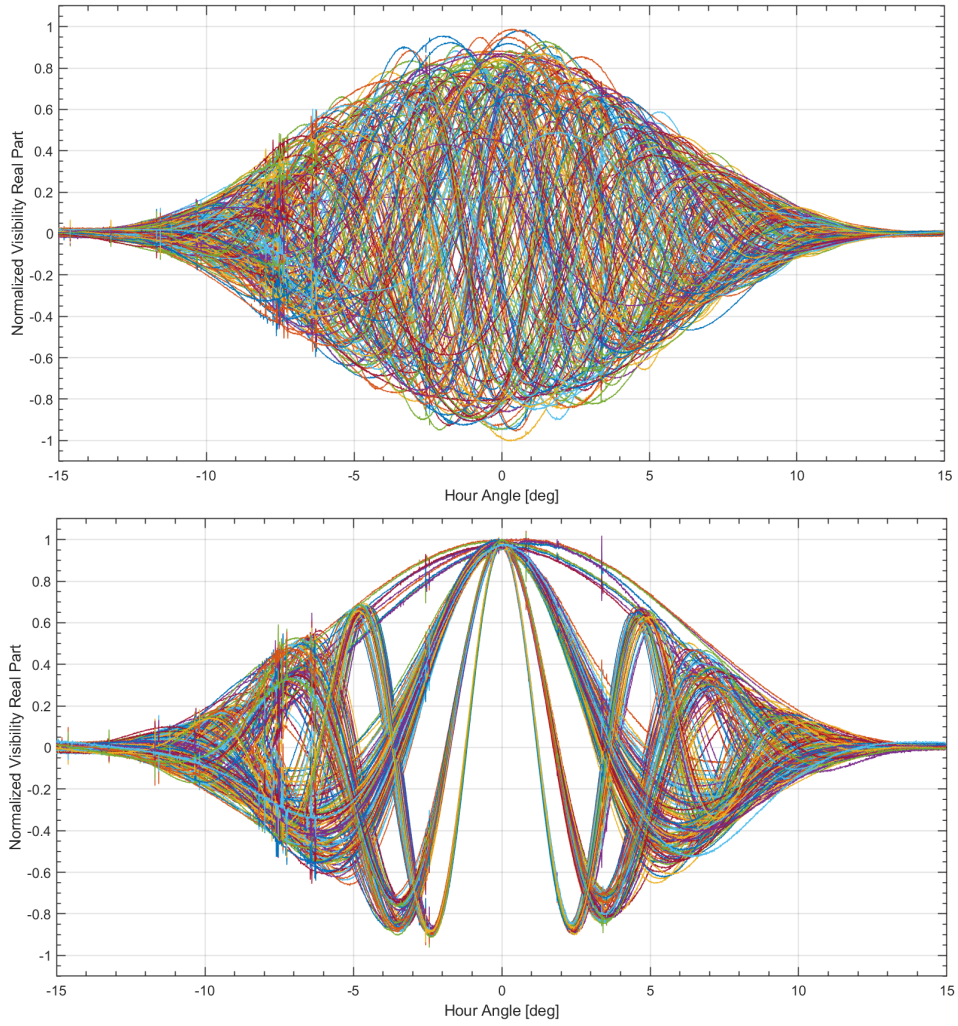


Figure 4.8: Real part of the complex visibilities corresponding to the transit of Cas A before (top panel) and after (bottom panel) calibration. Only the central channel at 407.6875 MHz is shown. Fringes show the main peak at transit ($\omega = 0^\circ$) where they are phased, i.e. where the geometrical delay is compensated. Each colour corresponds to one of the 276 independent baselines. Fringe spacing is proportional to baseline lengths, therefore redundant visibilities appear grouped in subsets that have similar fringe frequencies.

where σ_6 indicates the sensitivity of the six cylinder array.

The derived sensitivity can be used to determine the System Equivalent Flux Density (SEFD) of a single receiver, which is the quantity that we ultimately want to characterize. The receiver sensitivity σ is given by:

$$\sigma = A \sigma_6 \quad (4.30)$$

where $A = 24$ is the ratio between the area corresponding to six cylinders and one receiver respectively. The receiver SEFD is then given by the radiometer equation (for a similar approach, see [Amiri et al., 2017](#)):

$$\text{SEFD} = \sigma \sqrt{N_P B t} = A \sigma_6 \sqrt{N_P B t}, \quad (4.31)$$

where N_P is the number of polarizations measured, B the bandwidth and t the observing time. In our case we have $N_P = 1$, $B = 16$ MHz, $t = 20$ s, obtaining $\text{SEFD} \sim 1530$ Jy.

4.3.4 FRB survey design

The system characterization allows us to forecast the FRB detectability with the NC. The telescope can already be used to observe known - i.e. repeating - FRBs, but, given its large FoV, it is best suited to carry out blind surveys to detect new FRBs.

The NC cylinders can be synchronously steered in declination by a common driveshaft that can be disabled, allowing each cylinder to be moved independently. The elevation range that can be observed without shadowing spans 45° from zenith, therefore $0 < \delta < 90^\circ$ is the maximum observable declination range. Recalling that the receiver FoV is $\sim 6^\circ$ (full width at half of maximum, FWHM), 15 pointings are needed to cover the 90° declination interval. We therefore envisaged three different modes to observe FRBs with the NC:

- I A pilot blind survey: the hardware and software upgrade described in § 4.3.2 has been completed for eight cylinders which can, in turn, be split in two groups of four cylinders, each pointing 6° apart. With the current beamformer, each pointing can be tiled with four beams, each $1^\circ \times 1.6^\circ$ wide, placed along the right ascension direction. Such survey will cover $A_{\text{FoV}} \sim 5.9 \text{ deg}^2$ instantaneously with a sensitivity σ_I :

$$\sigma_I = \frac{\text{SEFD}}{A_{16} \sqrt{B}} \sim 760 (\tau/\text{ms})^{-0.5} \text{ mJy} \quad (4.32)$$

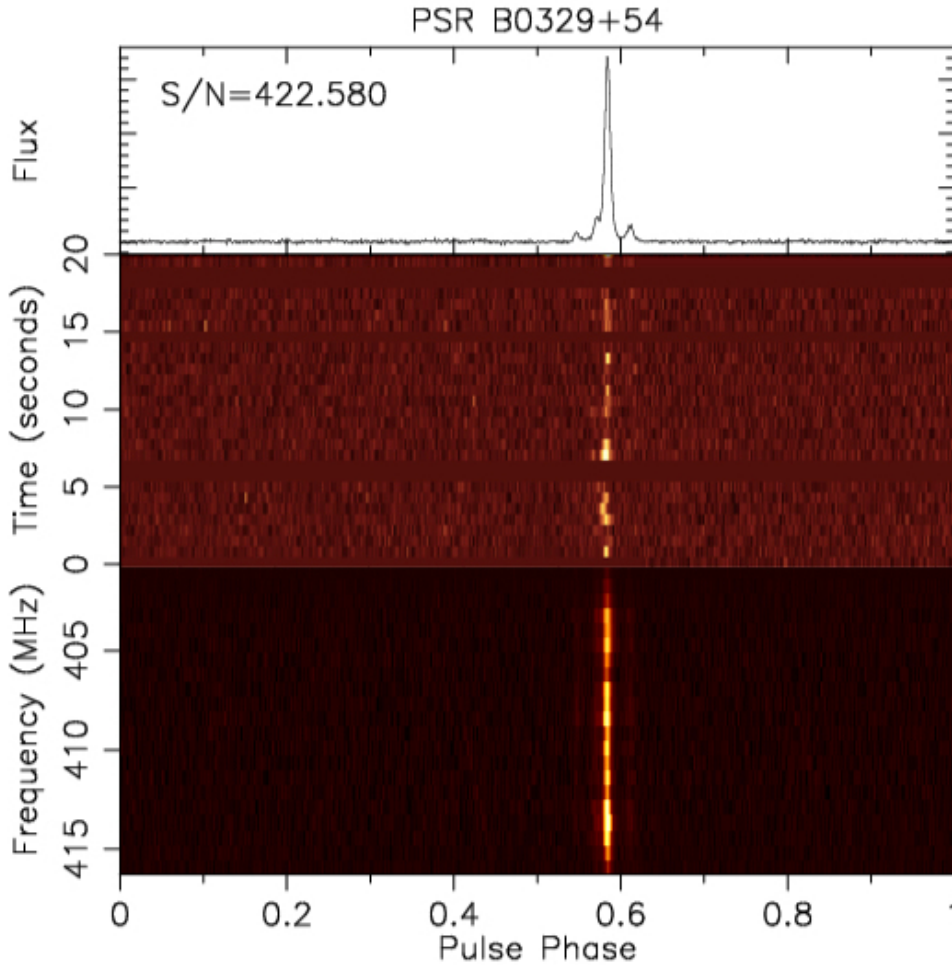


Figure 4.9: Observed profile of B0329+54. Bottom panel: intensity profile as a function of rotational phase and channel width, integrated over 20 s. We note a slight decrease at the band edges due to the sensitivity loss. Central panel: same as the bottom plot but as a function of a single-pulse time (~ 700 ms) over the 16 MHz bandwidth. The blanked horizontal bands represent time affected by RFI and, therefore, discarded. We note that no further flagging was needed. Top panel: pulse profile integrated over frequency and 20 s.

where $A_{16} = 16$, i.e. the number of receivers corresponding to four cylinders and τ is the observed time expressed in milliseconds (see also equation 4.33 below);

II A blind survey that covers the widest possible area: once the whole NS arm is upgraded, the layout of the pilot blind survey can be extended to observe the whole declination range that can be accessed instantaneously, i.e. $0 < \delta < 90^\circ$, covered by fifteen pointings spaced 6° apart. Each pointing is observed with four cylinders, i.e. leading to the same sensitivity as per the survey I. The current system cannot take full advantage of the increased sky coverage as the four independent beams only cover $\sim 10\%$ of the receiver FoV. For this survey we therefore considered that the improved multibeam and channelization capabilities anticipated in § 4.3.2 are already deployed on all the sixty cylinders. If twenty independent beams are independently placed within the receiver FoV, the instantaneous sky coverage improves dramatically to $A_{\text{FoV}} \sim 350 \text{ deg}^2$. We will use this layout as our best case for FRB observations;

- Follow up of known (repeating) FRBs. Known sources can be followed for ~ 30 minutes as they transit through the receiver FoV. If sixty cylinders are beamformed together in a $4.5' \times 1.6^\circ$ beam, a $\sigma_{60} \sim 50 (\tau/\text{ms})^{-0.5}$ mJy sensitivity can be achieved.

A limitation of the current acquisition system is the relatively coarse frequency resolution that can lead to time smearing of high DM events (see Fig. 1.3, where the signal is both broadened over the observing band and its S/N is reduced by the dispersion). For a transient event of intrinsic duration t_i , equal or shorter than the time sampling width Δt_b , the observed time τ is defined as (e.g., Amiri et al., 2017):

$$\tau = \sqrt{\Delta t_b^2 + t_s^2 + t_i^2}, \quad (4.33)$$

where t_s is the scattering time and t_i is the intrinsic time duration of the event. If the signal propagates through an ionized plasma, it experiences an additional dispersion delay t_{DM} so that:

$$\tilde{\tau} = \sqrt{\Delta t_b^2 + t_s^2 + t_i^2 + t_{\text{DM}}^2}, \quad (4.34)$$

where the dispersion time is (e.g., Burke-Spolaor and Bannister, 2014):

$$t_{\text{DM}} = 8.3 \frac{\text{DM}}{\left[\frac{\text{pc}}{\text{cm}^{-3}}\right]} \frac{\Delta\nu_{\text{ch}}}{[\text{MHz}]} \left(\frac{\nu}{[\text{GHz}]}\right)^{-3} \mu\text{s}, \quad (4.35)$$

where $\Delta\nu_{\text{ch}}$ is the channel width and ν is the observing frequency. With the current system, an FRB with a $\text{DM} = 665 \text{ pc cm}^{-3}$ (the mean of the known FRB population, [Bhandari et al., 2018](#)) would experience an intra-channel dispersion (smearing) $\tilde{\tau}$:

$$\tilde{\tau} \simeq t_{\text{DM}} \sim 64 \text{ ms}, \quad (4.36)$$

that becomes 248 ms for the highest DM observed to date, 2596 pc cm^{-3} ([Bhandari et al., 2018](#)). A smaller channel width reduces the intra-channel smearing, normally implying an increase of the sampling time that, however, needs to remain sufficiently small to properly sample the burst duration. We quantified the impact of the intra-channel smearing for the surveys I and II by estimating the FRB event rate following [Connor \(2019\)](#). Table 4.7 summarizes the main specifications of both surveys, where, like we defined above, survey II already employs the finer channelization anticipated in § 4.3.2.

Event rate estimates require the knowledge of the FRB cosmological distribution, their spectral index, their distribution in duration and their intrinsic luminosity. In particular, we adopted the following assumptions:

- a linear relation between the FRB dispersion measure and its redshift, i.e. $\text{DM} = 1000 z \text{ pc cm}^{-3}$ ([Inoue and Ioka, 2012](#); [Dolag et al., 2015](#));
- a log-normal distribution for the FRB luminosity function at 1.4 GHz L_{GHz} , peaking at $10^{33} \text{ erg s}^{-1}$ and full-width at half maximum of 1.5;
- a constant spectral index $\beta = 1.5$ for each event⁴, consistent with the average spectral index of known FRBs ([Macquart et al., 2019](#)). Although this assumption is likely incorrect, it only affects the rates observed at different frequencies and not the rates observed by the two surveys.

We assumed that the FRB cosmic evolution either follows the cosmic star formation rate (CSFR, [Madau and Dickinson, 2014](#)), or a phenomenological formation rate (FRBFR, [Locatelli et al., 2019](#)). In their work, [Locatelli et al. \(2019\)](#) model the FRB cosmological evolution following the observed distribution of the events with $\text{DM} \lesssim 1000 \text{ pc cm}^{-3}$ ([Shannon et al., 2018](#); [Macquart, 2018](#)). In this model, the evolution is faster than the CSFR model and peaks at earlier redshifts. The cumulative event rate $\mathcal{R}_{\mathcal{S}}$ above a given flux density threshold is shown in Figure 4.10 (Figure 4.11) for the CSFR (FRBFR) model. We also calculated the bias parameter b :

⁴ $S_{\nu} \propto \nu^{-\beta}$, where S_{ν} is the flux density at the frequency ν .

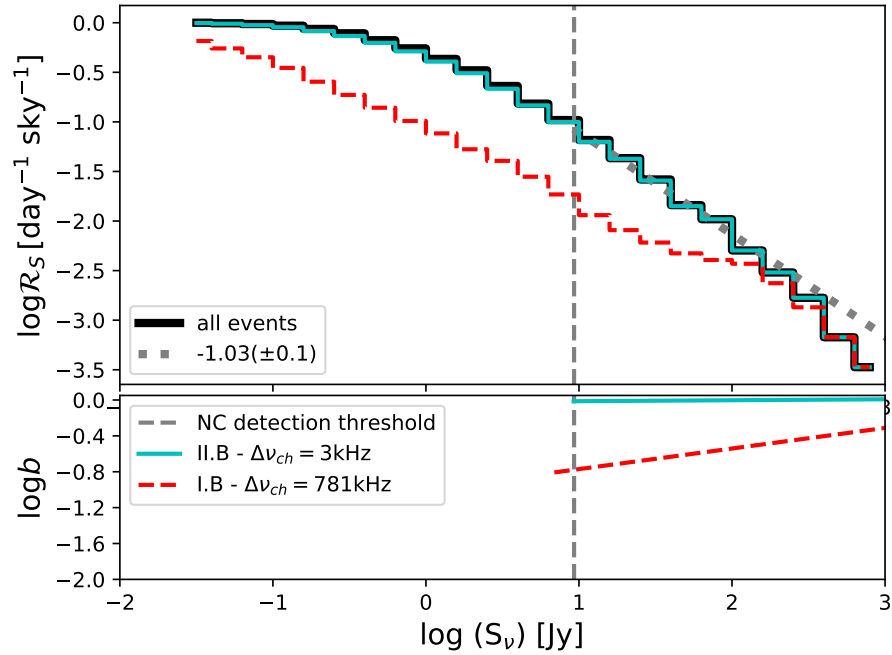


Figure 4.10: *Upper panel:* cumulative event rates \mathcal{R}_S normalized to their relative peaks. The black solid line represents the theoretical prediction for the ideal case with no intra-channel smearing. The curve was fitted by a power law above the detection threshold. The best-fit power law is plotted as a grey dotted line and its slope is reported in legend. The dashed red line and the solid cyan line show case I and II from Table 4.7 respectively. The cyan and black lines are virtually overlapping. The vertical dashed line represent the $10\sigma_I$ detection threshold - which is the same for both surveys. *Lower panel:* bias parameter b as a function of flux density (see text for details).

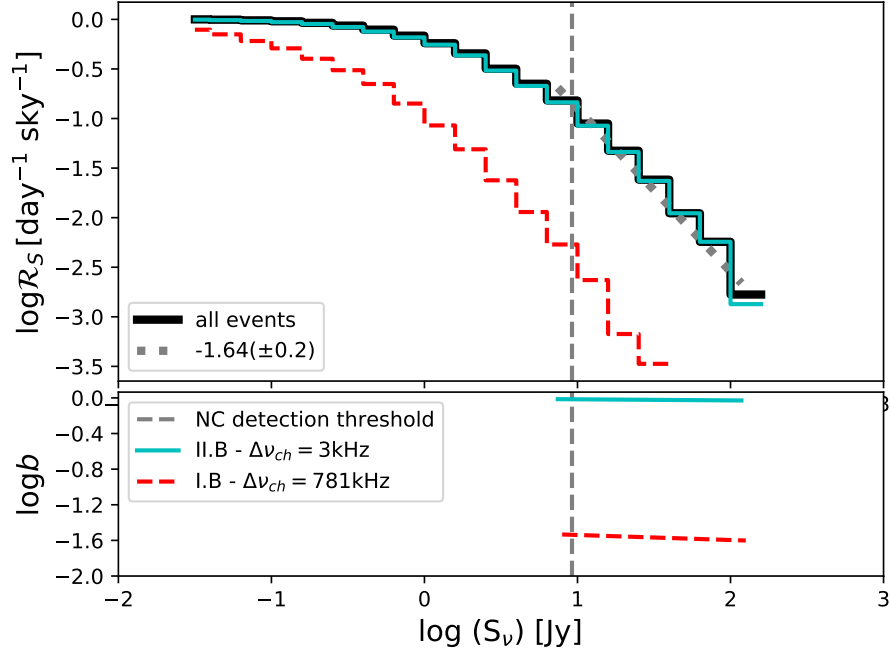


Figure 4.11: Same as Figure 4.10, for the FRBFR model.

Survey type	Δt_b μs	$\Delta \nu_{ch}$ kHz	A_{FoV} \square	σ mJy $(\tau/ms)^{-0.5}$
I	70	781	5.9	760
II	276	3	350	760

Table 4.7: NC parameters for the two proposed surveys (see text for details): survey type; sampling time; channel width; instantaneous sky coverage; expected noise level (per millisecond).

$$b \equiv \frac{\mathcal{R}_S(\Delta\nu_{ch})}{\mathcal{R}_S(\Delta\nu_{ch} \rightarrow 0)}, \quad (4.37)$$

i.e. the ratio between a given rate and the ideal rate - i.e., the rate unaffected by intra-channel smearing.

There is a significant loss of events due to intra-channel smearing for the survey I, with a magnitude that depends upon the chosen FRB model. In the CSFR case, there is essentially no event loss at the bright end of the cumulative event rate, whereas the completeness decreases to 17% at the detection threshold. For the FRBFR case, the loss is already significant for bright events. The reason for this difference is due to the fact that low-redshift events have a higher DM in the FRBFR model than the CSFR one, leading to a higher intra-channel smearing.

Survey II has, conversely, essentially no incompleteness (i.e., $b = 1$), regardless of the evolutionary model. This implies that the channelization adopted for survey II leads to an unbiased estimate of the true event rates.

The bias introduced by intra-channel smearing is redshift dependent as more distant events generally entail larger dispersion measures. Figure 4.12 displays two DM maps obtained from a cosmological simulation of the intergalactic medium (see Vazza et al., 2017, for the simulation details) that clearly show that larger DM values corresponds to larger cosmological volumes and, therefore, higher redshift events. The lower panel of Figure 4.12 quantifies this effect using the linear DM-z relationship. For the survey I case, the dispersion of high redshift FRBs leads to a S/N decrease of about one order of magnitude at $z \sim 1$, that is, only the brightest events are observable at high redshift. For survey II, conversely, the S/N only changes by $\sim 40\%$ up to $z = 5$. We finally assessed how much survey I and II constrain the FRB statistical properties. We assumed that the probability density function \mathcal{P} of observing M events follows a Poissonian distribution (Vedantham et al., 2016; Amiri et al., 2017):

$$\mathcal{P}(M | N(\alpha)) = C \frac{N(\alpha)^M e^{-N(\alpha)}}{M!}, \quad (4.38)$$

where N is the number of expected events and C is a normalization factor, chosen so that $\int \mathcal{P}(\alpha) d\alpha = 1$. We assumed a power law shape for the event rates N :

$$N(\alpha) = 300 \left(\frac{S_\nu}{1 \text{ Jy}} \right)^{-\alpha} \times \text{FoV} \times N_{\text{day}} \text{ sky}^{-1} \text{ day}^{-1}, \quad (4.39)$$

where we used the event rate from CHIME/FRB Collaboration et al. (2019a)

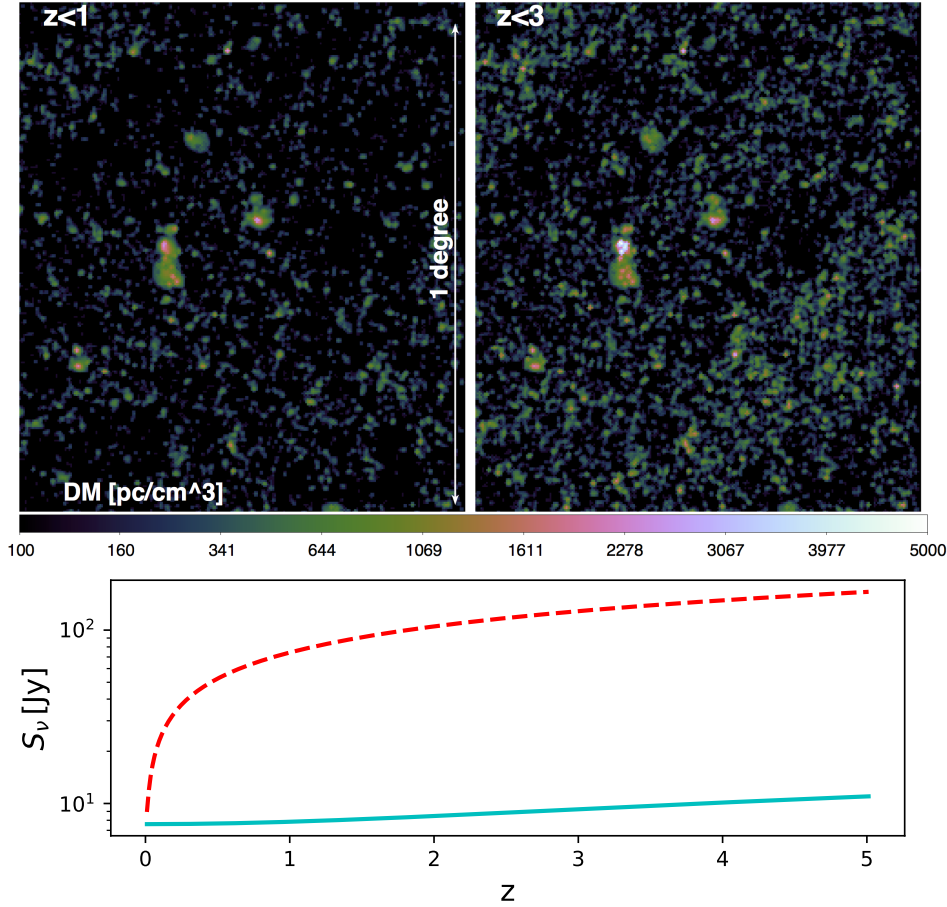


Figure 4.12: Upper panel: Simulated dispersion measure map from a cosmological simulation, for a full lightcone with $\approx 1^\circ$ aperture including the cosmic web up to $z = 1$ (left) or $z = 3$ (right). Lower panel: detection threshold as a function of the burst redshift, assuming a $z - \text{DM}$ linear relation and a 1 ms burst duration, for survey I (dashed-red line) and II (solid cyan line) respectively.

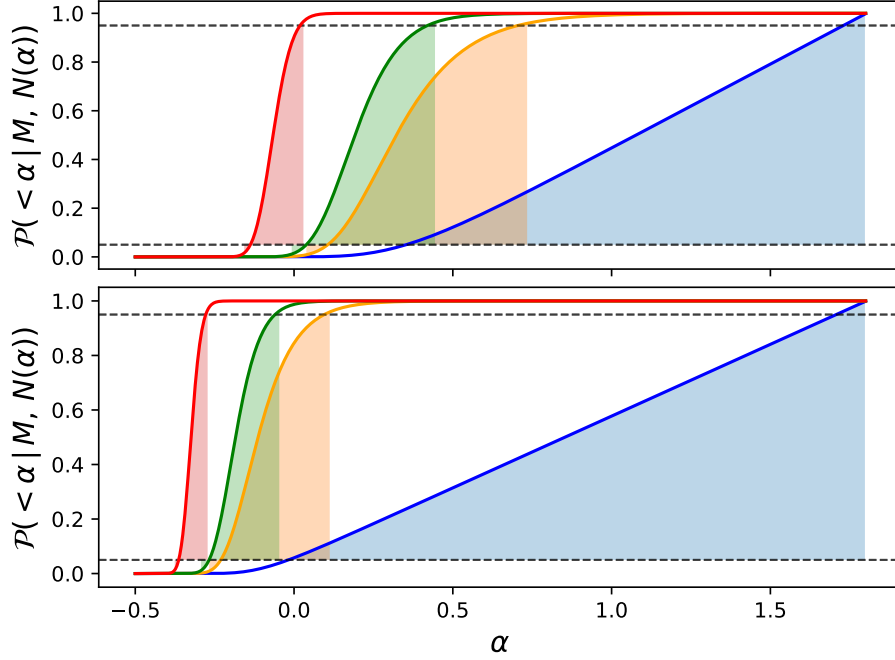


Figure 4.13: Constraints on the slope of the event rates for the survey II (top) and I (bottom panel) respectively. The probability is plotted as a function of 0 (blue), 1 (orange), 2 (green), 10 (red) observed events over $N(\alpha)$ expected events for 30 observing days (720 hours). Horizontal dashed lines show the 5% and 95% confidence levels respectively.

as our pivotal value, that is, 300 events brighter than 1 Jy observed in the 400 – 600 MHz range.

The probability to find a slope smaller than α is thus given by the integral:

$$P(< \alpha) = \int_{-\infty}^{\alpha} \mathcal{P}(M | N(\alpha')) d\alpha', \quad (4.40)$$

while the probability of finding a slope greater than α is $1 - P(< \alpha)$. Constraints on the slope of the event rates are shown in Figure 4.13 for survey I and II assuming a fiducial duration of 30 days. Due to its larger FoV, survey II will place better constraints on the event rate slope than survey I. A non detection, in particular, will be able to rule out flat slopes, constraining $\alpha > 0.35$ at the 95% confidence level.

Assuming $\alpha = 1$ (consistent with estimates at GHz frequencies; [Vedantham et al., 2016](#); [Amiri et al., 2017](#)), we expect $\sim 40 \text{ sky}^{-1} \text{ day}^{-1}$ events above the survey detection threshold, leading to one detection every three days for survey II. For survey I we expect to detect one burst in $\sim 112 \text{ b}^{-1}$ days (continuous), where the bias term incorporates the dependence upon the FRB evolutionary model due to DM smearing.

The amount of data collected by the different survey modes (I and II) can be estimated from the test observation described above (Sec. 4.3.3). The output has been quantified in 2 bytes (for a 16-bit complex number) for each frequency channel, time bin and synthesized beam. The total output thus depend on the observing mode. Considering the values given in Tab. 4.7, survey type I will produce ~ 400 GB per 24h observation. The full N-S arm in used for survey type II will produce about ~ 800 TB every 24h of observation. Currently the telescope is equipped with a 100 TB storage capacity, which will be increased to cover the estimated data output. Buffering and on-line search strategies, which may help reducing the required total capacity have not been considered in this work.

4.3.5 Section summary

In this Section we have described how the Northern Cross radio telescope is currently being equipped to carry out FRB surveys at 408 MHz. The current system uses a 16 MHz bandwidth divided in 21, 781 kHz wide channels and consists of eight cylinders whose inputs can be combined into either a single beam or four independent ones with a sub-ms time sampling. Tests of the digital and software back-end were carried out with six cylinders by observing the pulsar PSR B0329+54 from which the receiver SEFD = 1530 Jy was derived. Based on the derived SEFD, we presented forecasts for FRB searches using two different models of their cosmological evolution for two cases, one which uses the current system with eight cylinders (survey I) and an advanced one that uses sixty cylinders (survey II), for which we assumed the back-end upgrades in terms of multi beam capabilities and finer channelization that are currently under development. For both cases the rms sensitivity is $\sigma_I = 760 (\tau/\text{ms})^{-0.5} \text{ mJy}$, with an instantaneous sky coverage of 5.9 deg^2 and 350 deg^2 respectively.

We found that the survey I is expected to detect one FRB every ~ 112 days, although this rate suffers from smearing of high DM events and, therefore, depends upon the underlying FRB evolutionary model. Survey II is, conversely, immune from intra-channel smearing and is expected to yield

one detection every three days, independently of the FRB model. Due to its large FoV, it is expected to probe FRBs up to $z \sim 5$ with an almost constant detection threshold. Based on the current low frequency event rates (CHIME/FRB Collaboration et al., 2019a), survey II will be able to constrain the slope α of the event rate. In particular, in the case of no detections, a 720 h campaign will yield $\alpha > 0.35$ at the 95% confidence level. Assuming a fiducial slope $\alpha = 1$, we expect $\sim 40 \text{ sky}^{-1} \text{ day}^{-1}$ events above a $10\sigma_I$ detection threshold, that is, one detection every three days.

While the upgrade to carry out survey II is ongoing, the current system is being used to monitor repeating FRBs and improved localization capabilities are being considered by deploying receiving systems at 408 MHz at the other Italian radio astronomical stations.

Chapter 5

Conclusions

The driving mechanism for the amplification of the magnetic fields and particle acceleration in collisionless plasma, in regimes where small scale dynamo is small or negligible, is the compression of the magnetic field lines together with the plasma. The role of mild ($\mathcal{M} \sim 2-4$) and strong ($\mathcal{M} \geq 5$) shocks is paramount for the compression and heating of the plasma over Mpc scales. So, in Sec 2.2, within this scenario and by means of total energy minimization arguments, we have been able to test the magnetic field strength in the outskirts of the cluster A2249. We constrained it to $0.4 \mu\text{G} < B_{\text{Mpc}} < 10 \mu\text{G}$ and we derived for the first time constraints also on the electron acceleration efficiency in radio relics of $5 \times 10^{-5} < \xi_e < 10^{-2}$. These values have been derived thanks to the serendipitous discovery with LOFAR of a new and very faint radio relic. The magnetic field is well line with the estimates in other radio relics, of the order of a few μG (van Weeren et al., 2019). For instance, IC emission places lower limit to $B > 1.6 \mu\text{G}$ in the Toothbrush relic (Itahana et al., 2015), $B > 0.7 \mu\text{G}$ in RXC J1053.7+5453 (Itahana et al., 2017) and $B > 3 \mu\text{G}$ in A3667 (Finoguenov et al., 2010) relics. Equipartition arguments also place $B \sim \mu\text{G}$ in radio relics (e.g. Stuardi et al., 2019), while DSA modeling usually constrains a wider range ($1 \mu\text{G} < B < 20 \mu\text{G}$), but has the advantage of providing also the electron acceleration efficiency ξ_e (Vazza et al., 2015a; Botteon et al., 2020a). With this respect, we found that for the "Cornetto" relic $\xi_e < 10^{-2}$ relaxes the tension (which holds for brighter relics instead, $\xi_e \geq 10^{-2}$, Botteon et al. 2020a) between the proposed model for particle acceleration, namely DSA, and the cluster plasma thermodynamics. This finding, obtained within this PhD thesis, has strengthened the expectation that stronger formation shocks may indeed illuminate also filaments of the cosmic web. Furthermore, this new relic may represent a first

evidence for a sub-class of low frequency faint radio relics, yet unexplored due to selection biases now breached by the LOFAR unprecedented sensitivity.

Further out and deeper into the cosmic web also, we have been able to constrain $B_{\text{Mpc}} < 0.25 - 0.75 \mu\text{G}$ from low frequency observations of pairs of galaxy clusters (Sec. 2.3). In a primordial seeding scenario, this can be translated into constraints on the primordial field strength of $B_0 < 10 - 30 \text{ nG}$. This limit on B_0 is somewhat looser than the ones derived from other independent probes (see Fig. 2.22 and references therein) that place B_{Mpc} to a few nG. We recall that our estimate constitutes a first case for the magnetization strength in the environment proper of (massive) cosmological filament between galaxy clusters, where the magnetic field has strengthen thanks to the larger density of the environment with respect of the volume-filling sheets and voids. We also showed how increasing the modest sky coverage used so far (only a few deg^2), over other massive cluster pair candidates, will rapidly narrow down the window of B_0 even in the case of systematic non-detection of diffuse emission.

In Sec 3.2, we showed that similar field estimates could be tested at the same depth ($\sim 0.1 \mu\text{G}$), to date, by exploiting grids of polarized background sources. In fact a $B_{\text{Mpc}} \sim 0.1 \mu\text{G}$ would result in a $\sim 8 \text{ rad m}^{-2}$ contribute to the rotation of the polarization plane in $\sim \text{Mpc}$ -deep filaments (where $n_e \sim 10^{-4} \text{ cm}^{-3}$). This number is about the sensitivity of the current large radio telescope arrays (JVLA). We provided tools for estimating the requirements to be met by future polarization surveys (e.g. MeerKAT, ASKAP, SKA-Mid) by means of number of sources, RM sensitivity and noise level (i.e. exposure time), in order to break the limits down. We also investigated sources of systematic errors and quantified their effect on the probability of detecting a statistical difference of RM contributed by Faraday rotation from the cosmic web, with respect to a control field.

Unfortunately, the ultimate experiment set to provide the observational support to this forecasts (Sec. 3.3) has met new, unexpected and unsolved challenges. We could not test the magnetisation of the LSS around the massive galaxy cluster A2744, yet we built a very useful dataset that will be crucial to explore the methods, currently under development, to extract the very faint polarization information across the full primary beam of radio telescopes, cleared from instrumental leakage.

Finally, on a separate yet complementary thread, we investigated the population properties of FRBs. By recalling that they have already been proposed as powerful probes of both the IGM and IGMF models, in Sec. 4.2 we focused on their distribution in space to constrain the class of progeni-

tors and their cosmological evolution, finding hints for a star-like origin, as supported by the most recent and rapid developments of the field, and the presence of either an evolution at low redshift of their luminosity function or un-diagnosed selection effects biasing the available samples. With the aim of further exploring this issue, together with the goal of providing the global FRB community with a wide-area survey, down to 408 MHz, in Sec. 4.3 we studied, proposed and (most surprisingly) are actually implementing a refurbished very powerful survey instrument for FRB detection: the Northern Cross in Medicina, which already started pilot activity with know repeating FRB monitoring. The goal is to come to the full exploitation of the N-S arm, which would provide the largest effective area ($A_{\text{NS,eff}} \simeq 8000 \text{ m}^2$) dedicated to FRB search to date, and to increase the current instrument sensitivity to FRBs. We demonstrated that this can be accomplished by optimising the channel width to 1-10 kHz to prevent dispersion smearing. While the system update will require some time (\sim months), on shortest timescales the eight first available antennas are being probed and used in single- and multi-beam mode to observe know repeating FRBs (CHIME/FRB Collaboration et al., 2019b) and the galactic magnetar SGR 1935+2154 (Bochenek et al., 2020) both individually and in collaboration with the network of Italian VLBI antennae for localizing FRBs (Pilia et al., 2020). We hope to make this old yet new instrument very soon again available to the Bologna, Italian and in future possibly international communities.

As a final remark, we notice that the PhD project has been run in coincidence with the beginning of a fortunate era of radioastronomy, in which several large and powerful instruments have been made available (JVLA, uGMRT, LOFAR, MeerKAT). We tried our best to exploit their different features such as high and low resolution, wide bandwidth, different frequency ranges and deep observations, in order to nail down the strength of magnetic fields outside galaxy clusters. Our feeling is that, despite the difficulties met both in the data analysis and the following non-trivial interpretation, this PhD thesis has advanced both the knowledge of targets (fast radio bursts, inter-galactic magnetic fields, acceleration mechanisms) as well as it has refined the understanding of the methods involved (interpretation of diffuse emission, Faraday effect, population statistics and instrumental development). The next years look very promising for obtaining deeper insight in the same directions taken in this work, also thanks to the additional deployment of other paramount projects such as the Square Kilometer Array for the radio and the *eROSITA* and *Athena* Observatories for the X-ray domain.

Chapter 6

Bibliography

Ackermann, M., Ajello, M., Albert, A., Atwood, W. B., Baldini, L., Ballet, J., Barbiellini, G., Bastieri, D., Bechtol, K., Bellazzini, R., Bissaldi, E., Blandford, R. D., Bloom, E. D., Bonino, R., Bottacini, E., Bregeon, J., Bruel, P., Buehler, R., Caliandro, G. A., Cameron, R. A., Caragiulo, M., Caraveo, P. A., Casandjian, J. M., Cavazzuti, E., Cecchi, C., Charles, E., Chekhtman, A., Chiaro, G., Ciprini, S., Cohen-Tanugi, J., Conrad, J., Cutini, S., D'Ammando, F., de Angelis, A., de Palma, F., Desiante, R., Digel, S. W., Di Venere, L., Drell, P. S., Favuzzi, C., Fegan, S. J., Fukazawa, Y., Funk, S., Fusco, P., Gargano, F., Gasparrini, D., Giglietto, N., Giordano, F., Giroletti, M., Godfrey, G., Green, D., Grenier, I. A., Guiriec, S., Hays, E., Hewitt, J. W., Horan, D., Jóhannesson, G., Kuss, M., Larsson, S., Latronico, L., Li, J., Li, L., Longo, F., Loparco, F., Lovellette, M. N., Lubrano, P., Madejski, G. M., Maldera, S., Manfreda, A., Mayer, M., Mazziotta, M. N., Michelson, P. F., Mitthumsiri, W., Mizuno, T., Monzani, M. E., Morselli, A., Moskalenko, I. V., Murgia, S., Nuss, E., Ohsugi, T., Orienti, M., Orlando, E., Ormes, J. F., Paneque, D., Pesce-Rollins, M., Petrosian, V., Piron, F., Pivato, G., Porter, T. A., Rainò, S., Rando, R., Razzano, M., Reimer, A., Reimer, O., Sánchez-Conde, M., Sgrò, C., Siskind, E. J., Spada, F., Spandre, G., Spinelli, P., Tajima, H., Takahashi, H., Thayer, J. B., Tibaldo, L., Torres, D. F., Tosti, G., Troja, E., Vianello, G., Wood, K. S., Zimmer, S., Fermi-LAT Collaboration, and Rephaeli, Y. (2016). Search for Gamma-Ray Emission from the Coma Cluster with Six Years of Fermi-LAT Data. *ApJ*, 819(2):149.

Aghanim, N., Douspis, M., Hurier, G., Crichton, D., Diego, J. M., Hassefield, M., Macias-Perez, J., Marriage, T. A., Pointecouteau, E., Re-

- mazeilles, M., and Soubrié, E. (2019). PACT. I. Combining ACT and Planck data for improved extraction of tSZ signal. *A&A*, 632:A47.
- Aharonian, F., Akhperjanian, A. G., Barres de Almeida, U., Bazer-Bachi, A. R., Behera, B., Beilicke, M., Benbow, W., Bernlöhr, K., Boisson, C., Bolz, O., Borrel, V., Braun, I., Brion, E., Brown, A. M., Bühler, R., Bulik, T., Büsching, I., Boutelier, T., Carrigan, S., Chadwick, P. M., Chounet, L. M., Clapson, A. C., Coignet, G., Cornils, R., Costamante, L., Dalton, M., Degrange, B., Dickinson, H. J., Djannati-Ataï, A., Domainko, W., O’C. Drury, L., Dubois, F., Dubus, G., Dyks, J., Egberts, K., Emmanoulopoulos, D., Espigat, P., Farnier, C., Feinstein, F., Fiasson, A., Förster, A., Fontaine, G., Funk, S., Füßling, M., Gallant, Y. A., Giebels, B., Glicenstein, J. F., Glück, B., Goret, P., Hadjichristidis, C., Hauser, D., Hauser, M., Heinzlmann, G., Henri, G., Hermann, G., Hinton, J. A., Hoffmann, A., Hofmann, W., Holleran, M., Hoppe, S., Horns, D., Jacholkowska, A., de Jager, O. C., Jung, I., Katarzyński, K., Kendziorra, E., Kerschhaggl, M., Khélifi, B., Keogh, D., Komin, N., Kosack, K., Lamanna, G., Latham, I. J., Lemièrre, A., Lemoine-Goumard, M., Lenain, J. P., Lohse, T., Martin, J. M., Martineau-Huynh, O., Marcowith, A., Masterson, C., Maurin, D., Maurin, G., McComb, T. J. L., Moderski, R., Moulin, E., de Naurois, M., Nedbal, D., Nolan, S. J., Ohm, S., Olive, J. P., de Oña Wilhelmi, E., Orford, K. J., Osborne, J. L., Ostrowski, M., Panter, M., Pedalletti, G., Pelletier, G., Petrucci, P. O., Pita, S., Pühlhofer, G., Punch, M., Ranchon, S., Raubenheimer, B. C., Raue, M., Rayner, S. M., Renaud, M., Ripken, J., Rob, L., Rolland, L., Rosier-Lees, S., Rowell, G., Rudak, B., Ruppel, J., Sahakian, V., Santangelo, A., Schlickeiser, R., Schöck, F., Schröder, R., Schwanke, U., Schwarzburg, S., Schwemmer, S., Shalchi, A., Sol, H., Spangler, D., Stawarz, Ł., Steenkamp, R., Stegmann, C., Superina, G., Tam, P. H., Tavernet, J. P., Terrier, R., van Eldik, C., Vasileiadis, G., Venter, C., Vialle, J. P., Vincent, P., Vivier, M., Völk, H. J., Volpe, F., Wagner, S. J., Ward, M., Zdziarski, A. A., and Zech, A. (2007). New constraints on the mid-IR EBL from the HESS discovery of VHE γ -rays from 1ES 0229+200. *A&A*, 475(2):L9–L13.
- Akahori, T. (2018). Strategy to Explore Magnetized Cosmic Web with Forthcoming Large Surveys of Rotation Measure. *Galaxies*, 6(4):118.
- Akahori, T., Gaensler, B. M., and Ryu, D. (2014). Statistical Techniques for Detecting the Intergalactic Magnetic Field from Large Samples of Extragalactic Faraday Rotation Data. *ApJ*, 790(2):123.

- Akahori, T., Ideguchi, S., Aoki, T., Takefuji, K., Ujihara, H., and Takahashi, K. (2018). Optimum frequency of Faraday tomography to explore the intergalactic magnetic field in filaments of galaxies. *Publications of the Astronomical Society of Japan*, 70(6):115.
- Akahori, T. and Ryu, D. (2015). RM due to magnetic fields in the cosmic web and SKA observations. *Highlights of Astronomy*, 16:407–407.
- Akahori, T., Ryu, D., and Gaensler, B. M. (2016). Fast Radio Bursts as Probes of Magnetic Fields in the Intergalactic Medium. *ApJ*, 824:105.
- Akamatsu, H., Fujita, Y., Akahori, T., Ishisaki, Y., Hayashida, K., Hoshino, A., Mernier, F., Yoshikawa, K., Sato, K., and Kaastra, J. S. (2017). Properties of the cosmological filament between two clusters: A possible detection of a large-scale accretion shock by Suzaku. *A&A*, 606:A1.
- Akamatsu, H. and Kawahara, H. (2013). Systematic X-Ray Analysis of Radio Relic Clusters with Suzaku. *Publications of the Astronomical Society of Japan*, 65:16.
- Amiri, M., Bandura, K., Berger, P., Bond, J. R., Cliche, J. F., Connor, L., Deng, M., Denman, N., Dobbs, M., Domagalski, R. S., Fandino, M., Gilbert, A. J., Good, D. C., Halpern, M., Hanna, D., Hincks, A. D., Hinshaw, G., Höfer, C., Hsyu, G., Klages, P., Landecker, T. L., Masui, K., Mena-Parra, J., Newburgh, L. B., Oppermann, N., Pen, U. L., Peterson, J. B., Pinsonneault-Marotte, T., Renard, A., Shaw, J. R., Siegel, S. R., Sigurdson, K., Smith, K., Storer, E., Tretyakov, I., Vanderlinde, K., Wiebe, D. V., and Scientific Collaboration20, C. (2017). Limits on the Ultra-bright Fast Radio Burst Population from the CHIME Pathfinder. *ApJ*, 844(2):161.
- Anderson, C., Heald, G., Riseley, C., and Possum Askap Survey Science Team (2020). Early science from the POSSUM survey: Shocks, turbulence, and a massive extended reservoir of baryons in the Fornax cluster. In Kapinska, A. D., editor, *The 35th Annual New Mexico Symposium*, page 7.
- Anderson, C. S., Gaensler, B. M., Feain, I. J., and Franzen, T. M. O. (2015). Broadband Radio Polarimetry and Faraday Rotation of 563 Extragalactic Radio Sources. *ApJ*, 815(1):49.
- Anderson, C. S., Gaensler, B. M., Heald, G. H., O’Sullivan, S. P., Kaczmarek, J. F., and Feain, I. J. (2018). Broadband Radio Polarimetry of

- Fornax A. I. Depolarized Patches Generated by Advected Thermal Material from NGC 1316. *ApJ*, 855(1):41.
- Astropy Collaboration, Robitaille, T. P., Tollerud, E. J., Greenfield, P., Droettboom, M., Bray, E., Aldcroft, T., Davis, M., Ginsburg, A., Price-Whelan, A. M., Kerzendorf, W. E., Conley, A., Crighton, N., Barbary, K., Muna, D., Ferguson, H., Grollier, F., Parikh, M. M., Nair, P. H., Unther, H. M., Deil, C., Woillez, J., Conseil, S., Kramer, R., Turner, J. E. H., Singer, L., Fox, R., Weaver, B. A., Zabalza, V., Edwards, Z. I., Azalee Bostroem, K., Burke, D. J., Casey, A. R., Crawford, S. M., Dencheva, N., Ely, J., Jenness, T., Labrie, K., Lim, P. L., Pierfederici, F., Pontzen, A., Ptak, A., Refsdal, B., Servillat, M., and Streicher, O. (2013). Astropy: A community Python package for astronomy. *A&A*, 558:A33.
- Athreya, R. M., Kapahi, V. K., McCarthy, P. J., and van Breugel, W. (1998). Large rotation measures in radio galaxies at $Z \gtrsim 2$. *A&A*, 329:809–820.
- Bagchi, J., Durret, F., Neto, G. B. L., and Paul, S. (2006). Giant Ringlike Radio Structures Around Galaxy Cluster Abell 3376. *Science*, 314(5800):791–794.
- Bailes, M., Jameson, A., Flynn, C., Bateman, T., Barr, E. D., Bhandari, S., Bunton, J. D., Caleb, M., Campbell-Wilson, D., Farah, W., Gaensler, B., Green, A. J., Hunstead, R. W., Jankowski, F., Keane, E. F., Krishnan, V. V., Murphy, T., O’Neill, M., Osłowski, S., Parthasarathy, A., Ravi, V., Rosado, P., and Temby, D. (2017). The UTMOST: A Hybrid Digital Signal Processor Transforms the Molonglo Observatory Synthesis Telescope. *Publications of the Astronomical Society of Australia*, 34:e045.
- Banfi, S., Vazza, F., and Wittor, D. (2020). Shock waves in the magnetized cosmic web: the role of obliquity and cosmic ray acceleration. *MNRAS*, 496(3):3648–3667.
- Banfield, J. K., Schnitzeler, D. H. F. M., George, S. J., Norris, R. P., Jarrett, T. H., Taylor, A. R., and Stil, J. M. (2014). Radio galaxies and their magnetic fields out to $z \leq 3$. *MNRAS*, 444(1):700–710.
- Bannister, K. W., Deller, A. T., Phillips, C., Macquart, J. P., Prochaska, J. X., Tejos, N., Ryder, S. D., Sadler, E. M., Shannon, R. M., Simha, S., Day, C. K., McQuinn, M., North-Hickey, F. O., Bhandari, S., Arcus, W. R., Bennert, V. N., Burchett, J., Bouwhuis, M., Dodson, R., Ekers,

- R. D., Farah, W., Flynn, C., James, C. W., Kerr, M., Lenc, E., Mahony, E. K., O'Meara, J., Osłowski, S., Qiu, H., Treu, T., U, V., Bateman, T. J., Bock, D. C. J., Bolton, R. J., Brown, A., Bunton, J. D., Chippendale, A. P., Cooray, F. R., Cornwell, T., Gupta, N., Hayman, D. B., Kesteven, M., Koribalski, B. S., MacLeod, A., McClure-Griffiths, N. M., Neuhold, S., Norris, R. P., Pilawa, M. A., Qiao, R. Y., Reynolds, J., Roxby, D. N., Shimwell, T. W., Voronkov, M. A., and Wilson, C. D. (2019). A single fast radio burst localized to a massive galaxy at cosmological distance. *Science*, 365(6453):565–570.
- Bannister, K. W., Shannon, R. M., Macquart, J. P., Flynn, C., Edwards, P. G., O'Neill, M., Osłowski, S., Bailes, M., Zackay, B., Clarke, N., D'Addario, L. R., Dodson, R., Hall, P. J., Jameson, A., Jones, D., Navarro, R., Trinh, J. T., Allison, J., Anderson, C. S., Bell, M., Chippendale, A. P., Collier, J. D., Heald, G., Heywood, I., Hotan, A. W., Lee-Waddell, K., Madrid, J. P., Marvil, J., McConnell, D., Popping, A., Voronkov, M. A., Whiting, M. T., Allen, G. R., Bock, D. C. J., Brodrick, D. P., Cooray, F., DeBoer, D. R., Diamond, P. J., Ekers, R., Gough, R. G., Hampson, G. A., Harvey-Smith, L., Hay, S. G., Hayman, D. B., Jackson, C. A., Johnston, S., Koribalski, B. S., McClure-Griffiths, N. M., Mirschin, P., Ng, A., Norris, R. P., Pearce, S. E., Phillips, C. J., Roxby, D. N., Troup, E. R., and Westmeier, T. (2017). The Detection of an Extremely Bright Fast Radio Burst in a Phased Array Feed Survey. *ApJ Letters*, 841(1):L12.
- Beck, A. M., Hanasz, M., Lesch, H., Remus, R. S., and Stasyszyn, F. A. (2013). On the magnetic fields in voids. *MNRAS*, 429:L60–L64.
- Beck, R. (2007). Galactic magnetic fields. *Scholarpedia*, 2(8):2411.
- Beck, R. (2012). Magnetic Fields in Galaxies. *Science & Space Review*, 166(1-4):215–230.
- Beck, R. and Krause, M. (2005). Revised equipartition and minimum energy formula for magnetic field strength estimates from radio synchrotron observations. *Astronomische Nachrichten*, 326(6):414–427.
- Beck, R. and Wiełebinski, R. (2013). *Magnetic Fields in Galaxies*, volume 5, page 641.
- Becker, R. H., White, R. L., and Helfand, D. J. (1995). The FIRST Survey: Faint Images of the Radio Sky at Twenty Centimeters. *ApJ*, 450:559.

- Belczynski, K., Perna, R., Bulik, T., Kalogera, V., Ivanova, N., and Lamb, D. Q. (2006). A Study of Compact Object Mergers as Short Gamma-Ray Burst Progenitors. *ApJ*, 648(2):1110–1116.
- Bell, A. R. (1978a). The acceleration of cosmic rays in shock fronts - I. *MNRAS*, 182:147–156.
- Bell, A. R. (1978b). The acceleration of cosmic rays in shock fronts - II. *MNRAS*, 182:443–455.
- Beloborodov, A. M. (2017). A Flaring Magnetar in FRB 121102? *ApJ Letters*, 843(2):L26.
- Beresnyak, A. and Miniati, F. (2016). Turbulent Amplification and Structure of the Intracluster Magnetic Field. *ApJ*, 817(2):127.
- Bhandari, S., Keane, E. F., Barr, E. D., Jameson, A., Petroff, E., Johnston, S., Bailes, M., Bhat, N. D. R., Burgay, M., Burke-Spolaor, S., Caleb, M., Eatough, R. P., Flynn, C., Green, J. A., Jankowski, F., Kramer, M., Krishnan, V. V., Morello, V., Possenti, A., Stappers, B., Tiburzi, C., van Straten, W., Andreoni, I., Butterley, T., Chand ra, P., Cooke, J., Corongiu, A., Coward, D. M., Dhillon, V. S., Dodson, R., Hardy, L. K., Howell, E. J., Jaroenjittichai, P., Klotz, A., Littlefair, S. P., Marsh, T. R., Mickaliger, M., Muxlow, T., Perrodin, D., Pritchard, T., Sawangwit, U., Terai, T., Tominaga, N., Torne, P., Totani, T., Trois, A., Turpin, D., Niino, Y., Wilson, R. W., Albert, A., André, M., Anghinolfi, M., Anton, G., Ardid, M., Aubert, J. J., Avgitas, T., Baret, B., Barrios-Martí, J., Basa, S., Belhorma, B., Bertin, V., Biagi, S., Bormuth, R., Bourret, S., Bouwhuis, M. C., Brânzaș, H., Bruijn, R., Brunner, J., Busto, J., Capone, A., Caramete, L., Carr, J., Celli, S., Moursli, R. C. E., Chiarusi, T., Circella, M., Coelho, J. A. B., Coleiro, A., Coniglione, R., Costantini, H., Coyle, P., Creusot, A., Díaz, A. F., Deschamps, A., De Bonis, G., Distefano, C., Palma, I. D., Domi, A., Donzaud, C., Dornic, D., Drouhin, D., Eberl, T., Bojaddaini, I. E., Khayati, N. E., Elsässer, D., Enzenhöfer, A., Ettahiri, A., Fassi, F., Felis, I., Fusco, L. A., Gay, P., Giordano, V., Glotin, H., Gregoire, T., Gracia-Ruiz, R., Graf, K., Hallmann, S., van Haren, H., Heijboer, A. J., Hello, Y., Hernández-Rey, J. J., Hößl, J., Hofestädt, J., Hugon, C., Illuminati, G., James, C. W., de Jong, M., Jongen, M., Kadler, M., Kalekin, O., Katz, U., Kießling, D., Kouchner, A., Kreter, M., Kreykenbohm, I., Kulikovskiy, V., Lachaud, C., Lahmann, R., Lefèvre, D., Leonora, E., Loucatos, S., Marcelin, M., Margiotta, A., Marinelli, A., Martínez-Mora, J. A., Mele, R., Melis, K., Michael, T.,

- Migliozzi, P., Moussa, A., Navas, S., Nezri, E., Organokov, M., Pāvālaš, G. E., Pellegrino, C., Perrina, C., Piattelli, P., Popa, V., Pradier, T., Quinn, L., Racca, C., Riccobene, G., Sánchez-Losa, A., Saldaña, M., Salvadori, I., Samtleben, D. F. E., Sanguineti, M., Sapienza, P., Schüssler, F., Sieger, C., Spurio, M., Stolarczyk, T., Taiuti, M., Tayalati, Y., Trovato, A., Turpin, D., Tönnis, C., Vallage, B., Van Elewyck, V., Versari, F., Vivolo, D., Vizzocca, A., Wilms, J., Zornoza, J. D., and Zúñiga, J. (2018). The SURvey for Pulsars and Extragalactic Radio Bursts - II. New FRB discoveries and their follow-up. *MNRAS*, 475(2):1427–1446.
- Bhatnagar, S., Cornwell, T. J., Golap, K., and Uson, J. M. (2008). Correcting direction-dependent gains in the deconvolution of radio interferometric images. *A&A*, 487(1):419–429.
- Blandford, R. D. and Ostriker, J. P. (1978). Particle acceleration by astrophysical shocks. *ApJ Letters*, 221:L29–L32.
- Blasi, P., Burles, S., and Olinto, A. V. (1999). Cosmological Magnetic Field Limits in an Inhomogeneous Universe. *ApJ Letters*, 514(2):L79–L82.
- Bochenek, C. D., Ravi, V., Belov, K. V., Hallinan, G., Kocz, J., Kulkarni, S. R., and McKenna, D. L. (2020). A fast radio burst associated with a Galactic magnetar. *Nature*, 587(7832):59–62.
- Böhringer, H., Chon, G., and Kronberg, P. P. (2016). The Cosmic Large-Scale Structure in X-rays (CLASSIX) Cluster Survey. I. Probing galaxy cluster magnetic fields with line of sight rotation measures. *A&A*, 596:A22.
- Bolli, P., Perini, F., Montebugnoli, S., Pelosi, G., and Poppi, S. (2008). Basic Element for Square Kilometer Array Training (BEST): Evaluation of the Antenna Noise Temperature. *IEEE Antennas and Propagation Magazine*, 50(2):58–65.
- Bonafede, A. (2010). *Magnetic fields in galaxy clusters: Faraday rotation and non thermal emission*. PhD thesis, Università degli Studi di Bologna.
- Bonafede, A., Intema, H. T., Brügger, M., Girardi, M., Nonino, M., Kantharia, N., van Weeren, R. J., and Röttgering, H. J. A. (2014). Evidence for Particle Re-acceleration in the Radio Relic in the Galaxy Cluster PLCKG287.0+32.9. *ApJ*, 785(1):1.
- Bonafede, A., Vazza, F., Brügger, M., Akahori, T., Carretti, E., Colafrancesco, S., Feretti, L., Ferrari, C., Giovannini, G., Govoni, F.,

- Johnston-Hollitt, M., Murgia, M., Scaife, A., Vacca, V., Govoni, F., Rudnick, L., and Scaife, A. (2015). Unravelling the origin of large-scale magnetic fields in galaxy clusters and beyond through Faraday Rotation Measures with the SKA. In *Advancing Astrophysics with the Square Kilometre Array (AASKA14)*, page 95.
- Bonafede, A., Vazza, F., Brügger, M., Murgia, M., Govoni, F., Feretti, L., Giovannini, G., and Ogrean, G. (2013). Measurements and simulation of Faraday rotation across the Coma radio relic. *MNRAS*, 433(4):3208–3226.
- Bond, J. R., Kofman, L., and Pogosyan, D. (1996). How filaments of galaxies are woven into the cosmic web. *Nature*, 380(6575):603–606.
- Bonjean, V., Aghanim, N., Salomé, P., Douspis, M., and Beelen, A. (2018). Gas and galaxies in filaments between clusters of galaxies. The study of A399-A401. *A&A*, 609:A49.
- Boonstra, A. and van der Veen, A. (2003). Gain calibration methods for radio telescope arrays. *IEEE Transactions on Signal Processing*, 51(1):25–38.
- Botteon, A., Brunetti, G., Ryu, D., and Roh, S. (2020a). Shock acceleration efficiency in radio relics. *A&A*, 634:A64.
- Botteon, A., Gastaldello, F., and Brunetti, G. (2018). Shocks and cold fronts in merging and massive galaxy clusters: new detections with Chandra. *MNRAS*, 476(4):5591–5620.
- Botteon, A., van Weeren, R. J., Brunetti, G., de Gasperin, F., Intema, H. T., Osinga, E., Di Gennaro, G., Shimwell, T. W., Bonafede, A., Brügger, M., Cassano, R., Cuciti, V., Dallacasa, D., Gastaldello, F., Mandal, S., Rossetti, M., and Röttgering, H. J. A. (2020b). A giant radio bridge connecting two galaxy clusters in Abell 1758. *MNRAS*, 499(1):L11–L15.
- Braglia, F. G., Pierini, D., Biviano, A., and Böhringer, H. (2009). Multi-wavelength study of X-ray luminous clusters at $z \sim 0.3$. I. Star-formation activity of cluster galaxies. *A&A*, 500(3):947–963.
- Brentjens, M. A. and de Bruyn, A. G. (2005). Faraday rotation measure synthesis. *A&A*, 441:1217–1228.
- Briggs, D. S. (1995). High Fidelity Interferometric Imaging: Robust Weighting and NNLS Deconvolution. In *American Astronomical Society Meet-*

ing Abstracts, volume 187 of *American Astronomical Society Meeting Abstracts*, page 112.02.

- Brown, J. C., Taylor, A. R., and Jackel, B. J. (2003). Rotation Measures of Compact Sources in the Canadian Galactic Plane Survey. *ApJS*, 145(2):213–223.
- Brown, S. and Rudnick, L. (2011). Diffuse radio emission in/around the Coma cluster: beyond simple accretion. *MNRAS*, 412(1):2–12.
- Brown, S., Vernstrom, T., Carretti, E., Dolag, K., Gaensler, B. M., Staveley-Smith, L., Bernardi, G., Haverkorn, M., Kesteven, M., and Poppi, S. (2017). Limiting magnetic fields in the cosmic web with diffuse radio emission. *MNRAS*, 468(4):4246–4253.
- Brown, S. D. (2011). Synchrotron Emission on the Largest Scales: Radio Detection of the Cosmic-Web. *Journal of Astrophysics and Astronomy*, 32:577–584.
- Brüggen, M., Ruszkowski, M., Simionescu, A., Hoeft, M., and Dalla Vecchia, C. (2005). Simulations of Magnetic Fields in Filaments. *ApJ Letters*, 631(1):L21–L24.
- Brunetti, G., Setti, G., and Comastri, A. (1997). Inverse Compton X-rays from strong FR II radio-galaxies. *A&A*, 325:898–910.
- Brunetti, G. and Vazza, F. (2020). Second-order Fermi Reacceleration Mechanisms and Large-Scale Synchrotron Radio Emission in Intracluster Bridges. *Physical Review Letters*, 124(5):051101.
- Bryan, G. L., Norman, M. L., O’Shea, B. W., Abel, T., Wise, J. H., Turk, M. J., Reynolds, D. R., Collins, D. C., Wang, P., Skillman, S. W., Smith, B., Harkness, R. P., Bordner, J., Kim, J.-h., Kuhlen, M., Xu, H., Goldbaum, N., Hummels, C., Kritsuk, A. G., Tasker, E., Skory, S., Simpson, C. M., Hahn, O., Oishi, J. S., So, G. C., Zhao, F., Cen, R., Li, Y., and Enzo Collaboration (2014). ENZO: An Adaptive Mesh Refinement Code for Astrophysics. *ApJS*, 211(2):19.
- Bulbul, E., Markevitch, M., Foster, A., Miller, E., Bautz, M., Loewenstein, M., Randall, S. W., and Smith, R. K. (2016). Searching for the 3.5 keV Line in the Stacked Suzaku Observations of Galaxy Clusters. *ApJ*, 831(1):55.

- Burke-Spolaor, S. and Bannister, K. W. (2014). The Galactic Position Dependence of Fast Radio Bursts and the Discovery of FRB011025. *ApJ*, 792(1):19.
- Burles, S. and Tytler, D. (1998a). The Deuterium Abundance toward Q1937-1009. *ApJ*, 499(2):699–712.
- Burles, S. and Tytler, D. (1998b). The Deuterium Abundance toward QSO 1009+2956. *ApJ*, 507(2):732–744.
- Bykov, A. M., Petrov, A. E., Krassilchtchikov, A. M., Levenfish, K. P., Osipov, S. M., and Pavlov, G. G. (2019a). GeV-TeV Cosmic-Ray Leptons in the Solar System from the Bow Shock Wind Nebula of the Nearest Millisecond Pulsar J0437-4715. *ApJ Letters*, 876(1):L8.
- Bykov, A. M., Vazza, F., Kropotina, J. A., Levenfish, K. P., and Paerels, F. B. S. (2019b). Shocks and Non-thermal Particles in Clusters of Galaxies. *Science & Space Review*, 215(1):14.
- Caleb, M., Flynn, C., Bailes, M., Barr, E. D., Hunstead, R. W., Keane, E. F., Ravi, V., and van Straten, W. (2016). Are the distributions of fast radio burst properties consistent with a cosmological population? *MNRAS*, 458(1):708–717.
- Campanelli, L. (2009). Helical Magnetic Fields from Inflation. *International Journal of Modern Physics D*, 18(9):1395–1411.
- Cao, X.-F., Yu, Y.-W., and Zhou, X. (2018). Compact Binary Mergers and the Event Rate of Fast Radio Bursts. *ApJ*, 858(2):89.
- Carilli, C. L. and Taylor, G. B. (2002). Cluster Magnetic Fields. *Annual Review of Astronomy and Astrophysics*, 40:319–348.
- Cassano, R., Bernardi, G., Brunetti, G., Brügger, M., Clarke, T., Dallacasa, D., Dolag, K., Ettori, S., Giacintucci, S., Giocoli, C., Gitti, M., Johnston-Hollitt, M., Kale, R., Markevich, M., Norris, R., Pommier, M. P., Pratt, G., Rottgering, H. J. A., and Venturi, T. (2015). Cluster Radio Halos at the crossroads between astrophysics and cosmology in the SKA era. In *Advancing Astrophysics with the Square Kilometre Array (AASKA14)*, page 73.
- Cen, R., Miralda-Escudé, J., Ostriker, J. P., and Rauch, M. (1994). Gravitational Collapse of Small-Scale Structure as the Origin of the Lyman-Alpha Forest. *ApJ Letters*, 437:L9.

- Cen, R. and Ostriker, J. P. (1999). Where Are the Baryons? *ApJ*, 514(1):1–6.
- Champion, D. J., Petroff, E., Kramer, M., Keith, M. J., Bailes, M., Barr, E. D., Bates, S. D., Bhat, N. D. R., Burgay, M., Burke-Spolaor, S., Flynn, C. M. L., Jameson, A., Johnston, S., Ng, C., Levin, L., Possenti, A., Stappers, B. W., van Straten, W., Thornton, D., Tiburzi, C., and Lyne, A. G. (2016). Five new fast radio bursts from the HTRU high-latitude survey at Parkes: first evidence for two-component bursts. *MNRAS*, 460(1):L30–L34.
- Chang, S.-W., Wolf, C., Onken, C. A., Luvaul, L., Gupta, V., and Flynn, C. (2019). SkyMapper Follow-up observations of FRB 190806. *The Astronomer’s Telegram*, 13008:1.
- Chatterjee, S., Law, C. J., Wharton, R. S., Burke-Spolaor, S., Hessels, J. W. T., Bower, G. C., Cordes, J. M., Tendulkar, S. P., Bassa, C. G., Demorest, P., Butler, B. J., Seymour, A., Scholz, P., Abruzzo, M. W., Bogdanov, S., Kaspi, V. M., Keimpema, A., Lazio, T. J. W., Marcote, B., McLaughlin, M. A., Paragi, Z., Ransom, S. M., Rupen, M., Spitler, L. G., and van Langevelde, H. J. (2017). A direct localization of a fast radio burst and its host. *Nature*, 541(7635):58–61.
- Chernin, A. D. (1967). A Cosmological Model with a Disordered Magnetic Field. *Soviet Astronomy*, 10:634.
- CHIME/FRB Collaboration, Amiri, M., Bandura, K., Bhardwaj, M., Boubel, P., Boyce, M. M., Boyle, P. J., Brar, C., Burhanpurkar, M., Cassanelli, T., Chawla, P., Cliche, J. F., Cubranic, D., Deng, M., Denman, N., Dobbs, M., Fandino, M., Fonseca, E., Gaensler, B. M., Gilbert, A. J., Gill, A., Giri, U., Good, D. C., Halpern, M., Hanna, D. S., Hill, A. S., Hinshaw, G., Höfer, C., Josephy, A., Kaspi, V. M., Landecker, T. L., Lang, D. A., Lin, H. H., Masui, K. W., Mckinven, R., Mena-Parra, J., Merryfield, M., Michilli, D., Milutinovic, N., Moatti, C., Naidu, A., Newburgh, L. B., Ng, C., Patel, C., Pen, U., Pinsonneault-Marotte, T., Pleunis, Z., Rafiei-Ravandi, M., Rahman, M., Ransom, S. M., Renard, A., Scholz, P., Shaw, J. R., Siegel, S. R., Smith, K. M., Stairs, I. H., Tendulkar, S. P., Tretyakov, I., Vanderlinde, K., and Yadav, P. (2019a). A second source of repeating fast radio bursts. *Nature*, 566(7743):235–238.
- CHIME/FRB Collaboration, Andersen, B. C., Bandura, K., Bhardwaj, M., Boubel, P., Boyce, M. M., Boyle, P. J., Brar, C., Cassanelli, T.,

- Chawla, P., Cubranic, D., Deng, M., Dobbs, M., Fandino, M., Fonseca, E., Gaensler, B. M., Gilbert, A. J., Giri, U., Good, D. C., Halpern, M., Hill, A. S., Hinshaw, G., Höfer, C., Josephy, A., Kaspi, V. M., Kothes, R., Landecker, T. L., Lang, D. A., Li, D. Z., Lin, H. H., Masui, K. W., Mena-Parra, J., Merryfield, M., Mckinven, R., Michilli, D., Milutinovic, N., Naidu, A., Newburgh, L. B., Ng, C., Patel, C., Pen, U., Pinsonneault-Marotte, T., Pleunis, Z., Rafiei-Ravandi, M., Rahman, M., Ransom, S. M., Renard, A., Scholz, P., Siegel, S. R., Singh, S., Smith, K. M., Stairs, I. H., Tendulkar, S. P., Tretyakov, I., Vanderlinde, K., Yadav, P., and Zwaniga, A. V. (2019b). CHIME/FRB Discovery of Eight New Repeating Fast Radio Burst Sources. *ApJ Letters*, 885(1):L24.
- Cho, H., Macquart, J.-P., Shannon, R. M., Deller, A. T., Morrison, I. S., Ekers, R. D., Bannister, K. W., Farah, W., Qiu, H., Sammons, M. W., Bailes, M., Bhandari, S., Day, C. K., James, C. W., Phillips, C. J., Prochaska, J. X., and Tuthill, J. (2020). Spectropolarimetric Analysis of FRB 181112 at Microsecond Resolution: Implications for Fast Radio Burst Emission Mechanism. *ApJ Letters*, 891(2):L38.
- Cho, J. and Ryu, D. (2009). Characteristic Lengths of Magnetic Field in Magnetohydrodynamic Turbulence. *ApJ Letters*, 705:L90–L94.
- Colberg, J. M., Krughoff, K. S., and Connolly, A. J. (2005). Intercluster filaments in a Λ CDM Universe. *MNRAS*, 359:272–282.
- Cole, T. W. and Pilkington, J. D. H. (1968). Search for Pulsating Radio Sources in the Declination Range $+44^{\circ} \leq \delta \leq +90^{\circ}$. *Nature*, 219(5154):574–576.
- Colla, G., Fanti, C., Ficarra, A., Formiggini, L., Gandolfi, E., Grueff, G., Lari, C., Padrielli, L., Roffi, G., Tomasi, P., and Vigotti, M. (1970). A catalogue of 3235 radio sources at 408 MHz. *A&AS*, 1(3):281.
- Colless, M., Dalton, G., Maddox, S., Sutherland, W., Norberg, P., Cole, S., Bland-Hawthorn, J., Bridges, T., Cannon, R., Collins, C., Couch, W., Cross, N., Deeley, K., De Propris, R., Driver, S. P., Efstathiou, G., Ellis, R. S., Frenk, C. S., Glazebrook, K., Jackson, C., Lahav, O., Lewis, I., Lumsden, S., Madgwick, D., Peacock, J. A., Peterson, B. A., Price, I., Seaborne, M., and Taylor, K. (2001). The 2dF Galaxy Redshift Survey: spectra and redshifts. *MNRAS*, 328(4):1039–1063.
- Comoretto, G., Chiello, R., Roberts, M., Halsall, R., Adami, K. Z., Alderighi, M., Aminaei, A., Baker, J., Belli, C., Chiarucci, S., D’Angelo,

- S., De Marco, A., Mura, G. D., Magro, A., Mattana, A., Monari, J., Naldi, G., Pastore, S., Perini, F., Poloni, M., Pupillo, G., Rusticelli, S., Schiaffino, M., Schillirò, F., and Zaccaro, E. (2017). The Signal Processing Firmware for the Low Frequency Aperture Array. *Journal of Astronomical Instrumentation*, 6(1):1641015.
- Condon, J. J., Cotton, W. D., Greisen, E. W., Yin, Q. F., Perley, R. A., Taylor, G. B., and Broderick, J. J. (1998). The NRAO VLA Sky Survey. *ApJ*, 115(5):1693–1716.
- Connor, L. (2019). Interpreting the distributions of FRB observables. *MNRAS*, 487(4):5753–5763.
- Connor, L., van Leeuwen, J., Oostrum, L. C., Petroff, E., Maan, Y., Adams, E. A. K., Attema, J. J., Bast, J. E., Boersma, O. M., Dénes, H., Gardenier, D. W., Hargreaves, J. E., Kooistra, E., Pastor-Marazuela, I., Schulz, R., Sclocco, A., Smits, R., Straal, S. M., van der Schuur, D., Vohl, D., Adebahr, B., de Blok, W. J. G., van Cappellen, W. A., Coolen, A. H. W. M., Damstra, S., van Diepen, G. N. J., Frank, B. S., Hess, K. M., Hut, B., Kutkin, A., Loose, G. M., Lucero, D. M., Mika, Á., Moss, V. A., Mulder, H., Oosterloo, T. A., Ruiter, M., Vedantham, H., Vermaas, N. J., Wijnholds, S. J., and Ziemke, J. (2020). A bright, high rotation-measure FRB that skewers the M33 halo. *MNRAS*.
- Connor, T., Kelson, D. D., Mulchaey, J., Vikhlinin, A., Patel, S. G., Balogh, M. L., Joshi, G., Kraft, R., Nagai, D., and Starikova, S. (2018). Wide-field Optical Spectroscopy of Abell 133: A Search for Filaments Reported in X-Ray Observations. *ApJ*, 867(1):25.
- Cordes, J. M. and Chatterjee, S. (2019). Fast Radio Bursts: An Extragalactic Enigma. *Annual Review of Astronomy and Astrophysics*, 57:417–465.
- Cordes, J. M. and Lazio, T. J. W. (2002). NE2001.I. A New Model for the Galactic Distribution of Free Electrons and its Fluctuations. *arXiv e-prints*, pages astro-ph/0207156.
- Cordes, J. M. and Wasserman, I. (2016). Supergiant pulses from extragalactic neutron stars. *MNRAS*, 457(1):232–257.
- Cova, F., Gastaldello, F., Wik, D. R., Boschini, W., Botteon, A., Brunetti, G., Buote, D. A., De Grandi, S., Eckert, D., Etti, S., Feretti, L., Gaspari, M., Ghizzardi, S., Giovannini, G., Girardi, M., Govoni, F., Molendi, S., Murgia, M., Rossetti, M., and Vacca, V. (2019). A joint

- XMM-NuSTAR observation of the galaxy cluster Abell 523: Constraints on inverse Compton emission. *A&A*, 628:A83.
- Cyburt, R. H., Fields, B. D., Olive, K. A., and Yeh, T.-H. (2016). Big bang nucleosynthesis: Present status. *Reviews of Modern Physics*, 88(1):015004.
- D’Amico, N., GruEFF, G., Montebugnoli, S., Maccaferri, A., Cattani, A., Bertolotti, C., Nicastro, L., Fauci, F., Tomassetti, G., Roma, M., Ambrosini, R., and Rodriguez, E. (1996). The New Northern Cross Pulsar System: Four Years of Pulsar Timing Observations. *ApJS*, 106:611.
- Davé, R., Cen, R., Ostriker, J. P., Bryan, G. L., Hernquist, L., Katz, N., Weinberg, D. H., Norman, M. L., and O’Shea, B. (2001). Baryons in the Warm-Hot Intergalactic Medium. *ApJ*, 552(2):473–483.
- Day, C. K., Deller, A. T., Shannon, R. M., Qiu, H., Bannister, K. W., Bhandari, S., Ekers, R., Flynn, C., James, C. W., Macquart, J.-P., Mahony, E. K., Phillips, C. J., and Xavier Prochaska, J. (2020). High time resolution and polarization properties of ASKAP-localized fast radio bursts. *MNRAS*, 497(3):3335–3350.
- de Gasperin, F., Dijkema, T. J., Drabent, A., Mevius, M., Rafferty, D., van Weeren, R., Brüggen, M., Callingham, J. R., Emig, K. L., Heald, G., Intema, H. T., Morabito, L. K., Offringa, A. R., Oonk, R., Orrù, E., Röttgering, H., Sabater, J., Shimwell, T., Shulevski, A., and Williams, W. (2019). Systematic effects in LOFAR data: A unified calibration strategy. *A&A*, 622:A5.
- de Graaff, A., Cai, Y.-C., Heymans, C., and Peacock, J. A. (2019). Probing the missing baryons with the Sunyaev-Zel’dovich effect from filaments. *A&A*, 624:A48.
- de Vaucouleurs, G. (1976). Is the local supercluster a random clumping accident? *ApJ*, 203:33–38.
- Dedner, A., Kemm, F., Kröner, D., Munz, C. D., Schnitzer, T., and Wesenberg, M. (2002). Hyperbolic Divergence Cleaning for the MHD Equations. *Journal of Computational Physics*, 175(2):645–673.
- Dolag, K., Bartelmann, M., and Lesch, H. (1999). SPH simulations of magnetic fields in galaxy clusters. *A&A*, 348:351–363.

- Dolag, K., Gaensler, B. M., Beck, A. M., and Beck, M. C. (2015). Constraints on the distribution and energetics of fast radio bursts using cosmological hydrodynamic simulations. *MNRAS*, 451(4):4277–4289.
- Dolag, K., Meneghetti, M., Moscardini, L., Rasia, E., and Bonaldi, A. (2006). Simulating the physical properties of dark matter and gas inside the cosmic web. *MNRAS*, 370:656–672.
- Domínguez-Fernández, P., Vazza, F., Brüggén, M., and Brunetti, G. (2019). Dynamical evolution of magnetic fields in the intracluster medium. *MNRAS*, 486(1):623–638.
- Donnert, J., Dolag, K., Lesch, H., and Müller, E. (2009). Cluster magnetic fields from galactic outflows. *MNRAS*, 392(3):1008–1021.
- Donnert, J., Vazza, F., Brüggén, M., and ZuHone, J. (2018). Magnetic Field Amplification in Galaxy Clusters and Its Simulation. *Science & Space Review*, 214(8):122.
- Durrer, R. and Neronov, A. (2013). Cosmological magnetic fields: their generation, evolution and observation. *The Astronomy and Astrophysics Review*, 21:62.
- Eckert, D., Jauzac, M., Shan, H., Kneib, J.-P., Erben, T., Israel, H., Jullo, E., Klein, M., Massey, R., Richard, J., and Tchernin, C. (2015). Warm-hot baryons comprise 5-10 per cent of filaments in the cosmic web. *Nature*, 528(7580):105–107.
- Einasto, J., Jöeveer, M., Kivila, A., and Tago, E. (1975). Superclusters of galaxies. *Astronomicheskij Tsirkulyar*, 895:2–4.
- Einasto, J., Jöeveer, M., and Saar, E. (1980). Structure of superclusters and supercluster formation. *MNRAS*, 193:353–375.
- Ensslin, T. A., Biermann, P. L., Klein, U., and Kohle, S. (1998). Cluster radio relics as a tracer of shock waves of the large-scale structure formation. *A&A*, 332:395–409.
- Falcke, H. and Rezzolla, L. (2014). Fast radio bursts: the last sign of supermassive neutron stars. *A&A*, 562:A137.
- Farnsworth, D., Rudnick, L., Brown, S., and Brunetti, G. (2013). Discovery of Megaparsec-scale, Low Surface Brightness Nonthermal Emission in Merging Galaxy Clusters Using the Green Bank Telescope. *ApJ*, 779(2):189.

- Federrath, C., Schober, J., Bovino, S., and Schleicher, D. R. G. (2014). The Turbulent Dynamo in Highly Compressible Supersonic Plasmas. *ApJ Letters*, 797(2):L19.
- Feretti, L., Giovannini, G., Govoni, F., and Murgia, M. (2012). Clusters of galaxies: observational properties of the diffuse radio emission. *The Astronomy and Astrophysics Review*, 20:54.
- Ficarra, A., Grueff, G., and Tomassetti, G. (1997). VizieR Online Data Catalog: The Third Bologna Survey (B3) (Ficarra+ 1985). *VizieR Online Data Catalog*, page VIII/37.
- Finoguenov, A., Sarazin, C. L., Nakazawa, K., Wik, D. R., and Clarke, T. E. (2010). XMM-Newton Observation of the Northwest Radio Relic Region in A3667. *ApJ*, 715(2):1143–1151.
- Franceschini, A., Rodighiero, G., and Vaccari, M. (2008). Extragalactic optical-infrared background radiation, its time evolution and the cosmic photon-photon opacity. *A&A*, 487(3):837–852.
- Fukugita, M., Hogan, C. J., and Peebles, P. J. E. (1998). The Cosmic Baryon Budget. *ApJ*, 503(2):518–530.
- Fuller, J. and Ott, C. D. (2015). Dark matter-induced collapse of neutron stars: a possible link between fast radio bursts and the missing pulsar problem. *MNRAS*, 450:L71–L75.
- Gajjar, V., Siemion, A. P. V., Price, D. C., Law, C. J., Michilli, D., Hessels, J. W. T., Chatterjee, S., Archibald, A. M., Bower, G. C., Brinkman, C., Burke-Spolaor, S., Cordes, J. M., Croft, S., Enriquez, J. E., Foster, G., Gizani, N., Hellbourg, G., Isaacson, H., Kaspi, V. M., Lazio, T. J. W., Lebofsky, M., Lynch, R. S., MacMahon, D., McLaughlin, M. A., Ransom, S. M., Scholz, P., Seymour, A., Spitler, L. G., Tendulkar, S. P., Werthimer, D., and Zhang, Y. G. (2018). Highest Frequency Detection of FRB 121102 at 4-8 GHz Using the Breakthrough Listen Digital Backend at the Green Bank Telescope. *ApJ*, 863(1):2.
- Gheller, C., Vazza, F., and Bonafede, A. (2018). Deep learning based detection of cosmological diffuse radio sources. *MNRAS*, 480(3):3749–3761.
- Gheller, C., Vazza, F., Brüggén, M., Alpaslan, M., Holwerda, B. W., Hopkins, A. M., and Liske, J. (2016). Evolution of cosmic filaments and of their galaxy population from MHD cosmological simulations. *MNRAS*, 462(1):448–463.

- Gheller, C., Vazza, F., Favre, J., and Brüggén, M. (2015). Properties of cosmological filaments extracted from Eulerian simulations. *MNRAS*, 453(2):1164–1185.
- Ghirardini, V., Eckert, D., Ettori, S., Pointecouteau, E., Molendi, S., Gaspari, M., Rossetti, M., De Grandi, S., Roncarelli, M., Bourdin, H., Mazzotta, P., Rasia, E., and Vazza, F. (2019). Universal thermodynamic properties of the intracluster medium over two decades in radius in the X-COP sample. *A&A*, 621:A41.
- Ghirlanda, G., Salafia, O. S., Pescalli, A., Ghisellini, G., Salvaterra, R., Chassande-Mottin, E., Colpi, M., Nappo, F., D’Avanzo, P., Melandri, A., Bernardini, M. G., Branchesi, M., Campana, S., Ciolfi, R., Covino, S., Götz, D., Vergani, S. D., Zennaro, M., and Tagliaferri, G. (2016). Short gamma-ray bursts at the dawn of the gravitational wave era. *A&A*, 594:A84.
- Ghisellini, G. (2017). Synchrotron masers and fast radio bursts. *MNRAS*, 465(1):L30–L33.
- Ghisellini, G. and Locatelli, N. (2018). Coherent curvature radiation and fast radio bursts. *A&A*, 613:A61.
- Giacintucci, S., Venturi, T., Brunetti, G., Dallacasa, D., Mazzotta, P., Casano, R., Bardelli, S., and Zucca, E. (2009). Testing the radio halo-cluster merger scenario. The case of RXC J2003.5-2323. *A&A*, 505(1):45–53.
- Giovannini, G., Bonafede, A., Feretti, L., Govoni, F., and Murgia, M. (2010). The diffuse radio filament in the merging system ZwCl 2341.1+0000. *A&A*, 511:L5.
- Govoni, F., Dolag, K., Murgia, M., Feretti, L., Schindler, S., Giovannini, G., Boschin, W., Vacca, V., and Bonafede, A. (2010). Rotation measures of radio sources in hot galaxy clusters. *A&A*, 522:A105.
- Govoni, F. and Feretti, L. (2004). Magnetic Fields in Clusters of Galaxies. *International Journal of Modern Physics D*, 13(8):1549–1594.
- Govoni, F., Murgia, M., Feretti, L., Giovannini, G., Dolag, K., and Taylor, G. B. (2006). The intracluster magnetic field power spectrum in Abell 2255. *A&A*, 460(2):425–438.

- Govoni, F., Murgia, M., Vacca, V., Loi, F., Girardi, M., Gastaldello, F., Giovannini, G., Feretti, L., Paladino, R., Carretti, E., Concu, R., Melis, A., Poppi, S., Valente, G., Bernardi, G., Bonafede, A., Boschin, W., Brienza, M., Clarke, T. E., Colafrancesco, S., de Gasperin, F., Eckert, D., Enßlin, T. A., Ferrari, C., Gregorini, L., Johnston-Hollitt, M., Junklewitz, H., Orrù, E., Parma, P., Perley, R., Rossetti, M., B Taylor, G., and Vazza, F. (2017). Sardinia Radio Telescope observations of Abell 194. The intra-cluster magnetic field power spectrum. *A&A*, 603:A122.
- Govoni, F., Murgia, M., Xu, H., Li, H., Norman, M., Feretti, L., Giovannini, G., Vacca, V., Bernardi, G., Bonafede, A., Brunetti, G., Carretti, E., Colafrancesco, S., Donnert, J., Ferrari, C., Gitti, M., Iapichino, L., Johnston-Hollitt, M., Pizzo, R., and Rudnick, L. (2015). Cluster magnetic fields through the study of polarized radio halos in the SKA era. *Advancing Astrophysics with the Square Kilometre Array (AASKA14)*, page 105.
- Govoni, F., Murgia, M., Xu, H., Li, H., Norman, M. L., Feretti, L., Giovannini, G., and Vacca, V. (2013). Polarization of cluster radio halos with upcoming radio interferometers. *A&A*, 554:A102.
- Govoni, F., Orrù, E., Bonafede, A., Iacobelli, M., Paladino, R., Vazza, F., Murgia, M., Vacca, V., Giovannini, G., Feretti, L., Loi, F., Bernardi, G., Ferrari, C., Pizzo, R. F., Gheller, C., Manti, S., Brügger, M., Brunetti, G., Cassano, R., de Gasperin, F., Enßlin, T. A., Hoeft, M., Horellou, C., Junklewitz, H., Röttgering, H. J. A., Scaife, A. M. M., Shimwell, T. W., van Weeren, R. J., and Wise, M. (2019). A radio ridge connecting two galaxy clusters in a filament of the cosmic web. *Science*, 364(6444):981–984.
- Greggio, L. (2005). The rates of type Ia supernovae. I. Analytical formulations. *A&A*, 441(3):1055–1078.
- Guidorzi, C., Marongiu, M., Martone, R., Amati, L., Frontera, F., Nicastro, L., Orlandini, M., Margutti, R., and Virgili, E. (2019). A Search for Gamma-Ray Prompt Emission Associated with the Lorimer Burst FRB 010724. *ApJ*, 882(2):100.
- Hackstein, S., Brügger, M., Vazza, F., Gaensler, B. M., and Heesen, V. (2019). Fast radio burst dispersion measures and rotation measures and the origin of intergalactic magnetic fields. *MNRAS*, 488(3):4220–4238.

- Hackstein, S., Vazza, F., Brügger, M., Sigl, G., and Dundovic, A. (2016). Propagation of ultrahigh energy cosmic rays in extragalactic magnetic fields: a view from cosmological simulations. *MNRAS*, 462(4):3660–3671.
- Hardcastle, M. J., Gürkan, G., van Weeren, R. J., Williams, W. L., Best, P. N., de Gasperin, F., Rafferty, D. A., Read, S. C., Sabater, J., Shimwell, T. W., Smith, D. J. B., Tasse, C., Bourne, N., Brienza, M., Brügger, M., Brunetti, G., Chyży, K. T., Conway, J., Dunne, L., Eales, S. A., Maddox, S. J., Jarvis, M. J., Mahony, E. K., Morganti, R., Prandoni, I., Röttgering, H. J. A., Valiante, E., and White, G. J. (2016). LOFAR/H-ATLAS: a deep low-frequency survey of the Herschel-ATLAS North Galactic Pole field. *MNRAS*, 462(2):1910–1936.
- Harrison, E. R. (1973). Magnetic fields in the early Universe. *MNRAS*, 165:185.
- Hassall, T. E., Stappers, B. W., Hessels, J. W. T., Kramer, M., Alexov, A., Anderson, K., Coenen, T., Karastergiou, A., Keane, E. F., Kondratiev, V. I., Lazaridis, K., van Leeuwen, J., Noutsos, A., Serylak, M., Sobey, C., Verbiest, J. P. W., Weltevrede, P., Zagkouris, K., Fender, R., Wijers, R. A. M. J., Bähren, L., Bell, M. E., Broderick, J. W., Corbel, S., Daw, E. J., Dhillon, V. S., Eislöffel, J., Falcke, H., Grießmeier, J. M., Jonker, P., Law, C., Markoff, S., Miller-Jones, J. C. A., Osten, R., Rol, E., Scaife, A. M. M., Scheers, B., Schellart, P., Spreeuw, H., Swinbank, J., ter Veen, S., Wise, M. W., Wijnands, R., Wucknitz, O., Zarka, P., Asgekar, A., Bell, M. R., Bentum, M. J., Bernardi, G., Best, P., Bonafede, A., Boonstra, A. J., Brentjens, M., Brouw, W. N., Brügger, M., Butcher, H. R., Ciardi, B., Garrett, M. A., Gerbers, M., Gunst, A. W., van Haarlem, M. P., Heald, G., Hoeft, M., Holties, H., de Jong, A., Koopmans, L. V. E., Kuniyoshi, M., Kuper, G., Loose, G. M., Maat, P., Masters, J., McKean, J. P., Meulman, H., Mevius, M., Munk, H., Noordam, J. E., Orrú, E., Paas, H., Pandey-Pommier, M., Pandey, V. N., Pizzo, R., Polatidis, A., Reich, W., Röttgering, H., Sluman, J., Steinmetz, M., Sterks, C. G. M., Tagger, M., Tang, Y., Tasse, C., Vermeulen, R., van Weeren, R. J., Wijnholds, S. J., and Yatawatta, S. (2012). Wide-band simultaneous observations of pulsars: disentangling dispersion measure and profile variations. *A&A*, 543:A66.
- Haugen, N. E. L. and Brandenburg, A. (2004). Suppression of small scale dynamo action by an imposed magnetic field. *Physical Review E*, 70(3):036408.

- Haverkorn, M., Gaensler, B. M., Brown, J. C., Bizunok, N. S., McClure-Griffiths, N. M., Dickey, J. M., and Green, A. J. (2006). Enhanced Small-Scale Faraday Rotation in the Galactic Spiral Arms. *ApJ Letters*, 637(1):L33–L35.
- Heiles, C. and Crutcher, R. (2005). *Magnetic Fields in Diffuse HI and Molecular Clouds*, volume 664, page 137.
- Hernquist, L., Katz, N., Weinberg, D. H., and Miralda-Escudé, J. (1996). The Lyman-Alpha Forest in the Cold Dark Matter Model. *ApJ Letters*, 457:L51.
- Hessels, J., Seymour, A., Spitler, L., Michilli, D., Lynch, R. S., Gajjar, V., and Gourdji, K. (2018). FRB121102 Bursts Show Detailed Spectrotemporal Structure. In *American Astronomical Society Meeting Abstracts #231*, volume 231 of *American Astronomical Society Meeting Abstracts*, page 243.19.
- Hobbs, G., Lyne, A. G., Kramer, M., Martin, C. E., and Jordan, C. (2004). Long-term timing observations of 374 pulsars. *MNRAS*, 353(4):1311–1344.
- Hoeft, M. and Brüggén, M. (2007). Radio signature of cosmological structure formation shocks. *MNRAS*, 375(1):77–91.
- Inoue, S. (2004). Probing the cosmic reionization history and local environment of gamma-ray bursts through radio dispersion. *MNRAS*, 348(3):999–1008.
- Inoue, Y. and Ioka, K. (2012). Upper limit on the cosmological gamma-ray background. *Physical Review Letters*, 86(2):023003.
- Intema, H. T., Jagannathan, P., Mooley, K. P., and Frail, D. A. (2017). The GMRT 150 MHz all-sky radio survey. First alternative data release TGSS ADR1. *A&A*, 598:A78.
- Ioka, K. (2003). The Cosmic Dispersion Measure from Gamma-Ray Burst Afterglows: Probing the Reionization History and the Burst Environment. *ApJ Letters*, 598(2):L79–L82.
- Itahana, M., Takizawa, M., Akamatsu, H., Ohashi, T., Ishisaki, Y., Kawahara, H., and van Weeren, R. J. (2015). Suzaku observations of the galaxy cluster 1RXS J0603.3+4214: Implications of particle acceleration processes in the “Toothbrush” radio relic. *Publications of the Astronomical Society of Japan*, 67(6):113.

- Itahana, M., Takizawa, M., Akamatsu, H., van Weeren, R. J., Kawahara, H., Fukazawa, Y., Kaastra, J. S., Nakazawa, K., Ohashi, T., Ota, N., Röttgering, H. J. A., Vink, J., and Zandanel, F. (2017). Suzaku and Chandra observations of the galaxy cluster RXC J1053.7+5453 with a radio relic. *Publications of the Astronomical Society of Japan*, 69(6):88.
- Jagannathan, P., Bhatnagar, S., Rau, U., and Taylor, A. R. (2017). Direction-dependent Corrections in Polarimetric Radio Imaging. I. Characterizing the Effects of the Primary Beam on Full-Stokes Imaging. *ApJ*, 154(2):56.
- James, C. W., Ekers, R. D., Macquart, J. P., Bannister, K. W., and Shannon, R. M. (2019). The slope of the source-count distribution for fast radio bursts. *MNRAS*, 483(1):1342–1353.
- Jansson, R. and Farrar, G. R. (2012). The Galactic Magnetic Field. *ApJ Letters*, 761(1):L11.
- Jarrett, T. H., Masci, F., Tsai, C., Petty, S., and Benford, D. (2011). WISE Nearby Galaxy Atlas. In *American Astronomical Society Meeting Abstracts #218*, volume 218 of *American Astronomical Society Meeting Abstracts*, page 328.10.
- Jedamzik, K. and Pogosian, L. (2020). Relieving the Hubble tension with primordial magnetic fields. *arXiv e-prints*, page arXiv:2004.09487.
- Johnston-Hollitt, M., Govoni, F., Beck, R., Dehghan, S., Pratley, L., Akahori, T., Heald, G., Agudo, I., Bonafede, A., Carretti, E., Clarke, T., Colafrancesco, S., Ensslin, T. A., Feretti, L., Gaensler, B., Haverkorn, M., Mao, S. A., Oppermann, N., Rudnick, L., Scaife, A., Schnitzeler, D., Stil, J., Taylor, A. R., and Vacca, V. (2015). Using SKA Rotation Measures to Reveal the Mysteries of the Magnetised Universe. *Advancing Astrophysics with the Square Kilometre Array (AASKA14)*, page 92.
- Jones, F. C. and Ellison, D. C. (1991). The plasma physics of shock acceleration. *Science & Space Review*, 58(1):259–346.
- Joshi, R. and Chand, H. (2013). Dependence of residual rotation measure on intervening Mg II absorbers at cosmic distances. *MNRAS*, 434(4):3566–3571.
- Kahniashvili, T., Brandenburg, A., and Tevzadze, A. e. G. (2016). The evolution of primordial magnetic fields since their generation. *Physica Scripta*, 91(10):104008.

- Kahniashvili, T., Maravin, Y., Natarajan, A., Battaglia, N., and Tevzadze, A. G. (2013). Constraining Primordial Magnetic Fields through Large-scale Structure. *ApJ*, 770(1):47.
- Kahniashvili, T., Tevzadze, A. G., and Ratra, B. (2011). Phase Transition Generated Cosmological Magnetic Field at Large Scales. *ApJ*, 726(2):78.
- Kahniashvili, T., Tevzadze, A. G., Sethi, S. K., Pandey, K., and Ratra, B. (2010). Primordial magnetic field limits from cosmological data. *Physical Review Letters*, 82(8):083005.
- Kalberla, P. M. W., Burton, W. B., Hartmann, D., Arnal, E. M., Bajaja, E., Morras, R., and Pöppel, W. G. L. (2005). The Leiden/Argentine/Bonn (LAB) Survey of Galactic HI. Final data release of the combined LDS and IAR surveys with improved stray-radiation corrections. *A&A*, 440(2):775–782.
- Kale, R., Venturi, T., Giacintucci, S., Dallacasa, D., Cassano, R., Brunetti, G., Cuciti, V., Macario, G., and Athreya, R. (2015). The Extended GMRT Radio Halo Survey. II. Further results and analysis of the full sample. *A&A*, 579:A92.
- Kang, H. and Ryu, D. (2015). Curved Radio Spectra of Weak Cluster Shocks. *ApJ*, 809(2):186.
- Kang, H., Ryu, D., and Jones, T. W. (2012). Diffusive Shock Acceleration Simulations of Radio Relics. *ApJ*, 756(1):97.
- Kardashev, N. S. (1962). Nonstationarity of Spectra of Young Sources of Nonthermal Radio Emission. *Soviet Astronomy*, 6:317.
- Kashiyama, K., Ioka, K., and Mészáros, P. (2013). Cosmological Fast Radio Bursts from Binary White Dwarf Mergers. *ApJ Letters*, 776(2):L39.
- Katz, J. I. (2014). Coherent emission in fast radio bursts. *Physical Review Letters*, 89(10):103009.
- Katz, J. I. (2018). Coherent plasma-curvature radiation in FRB. *MNRAS*, 481(3):2946–2950.
- Keane, E. F. (2018). The future of fast radio burst science. *Nature Astronomy*, 2:865–872.

- Keane, E. F., Johnston, S., Bhandari, S., Barr, E., Bhat, N. D. R., Burgay, M., Caleb, M., Flynn, C., Jameson, A., Kramer, M., Petroff, E., Posenti, A., van Straten, W., Bailes, M., Burke-Spolaor, S., Eatough, R. P., Stappers, B. W., Totani, T., Honma, M., Furusawa, H., Hattori, T., Morokuma, T., Niino, Y., Sugai, H., Terai, T., Tominaga, N., Yamasaki, S., Yasuda, N., Allen, R., Cooke, J., Jencson, J., Kasliwal, M. M., Kaplan, D. L., Tingay, S. J., Williams, A., Wayth, R., Chandra, P., Perrodin, D., Berezina, M., Mickaliger, M., and Bassa, C. (2016). The host galaxy of a fast radio burst. *Nature*, 530(7591):453–456.
- Keane, E. F. and Petroff, E. (2015). Fast radio bursts: search sensitivities and completeness. *MNRAS*, 447(3):2852–2856.
- Keane, E. F., Stappers, B. W., Kramer, M., and Lyne, A. G. (2012). On the origin of a highly dispersed coherent radio burst. *MNRAS*, 425(1):L71–L75.
- Keshet, U., Waxman, E., and Loeb, A. (2004). Searching for intergalactic shocks with the Square Kilometer Array. *New Astronomy Reviews*, 48(11–12):1119–1135.
- Kierdorf, M., Beck, R., Hoeft, M., Klein, U., van Weeren, R. J., Forman, W. R., and Jones, C. (2017). Relics in galaxy clusters at high radio frequencies. *A&A*, 600:A18.
- Kirsten, F., Snelders, M., Jenkins, M., Nimmo, K., van den Eijnden, J., Hessels, J., Gawronski, M., and Yang, J. (2020). Detection of two bright FRB-like radio bursts from magnetar SGR 1935+2154 during a multi-frequency monitoring campaign. *arXiv e-prints*, page arXiv:2007.05101.
- Kivelson, M. G. (2015). Planetary Magnetodiscs: Some Unanswered Questions. *Science & Space Review*, 187(1-4):5–21.
- Kivelson, M. G., Bagenal, F., Kurth, W. S., Neubauer, F. M., Paranicas, C., and Saur, J. (2004). *Magnetospheric interactions with satellites*, volume 1, pages 513–536.
- Kivelson, M. G., Bargatze, L. F., Khurana, K. K., Southwood, D. J., Walker, R. J., and Coleman, P. J. (1993). Magnetic Field Signatures Near Galileo’s Closest Approach to Gaspra. *Science*, 261(5119):331–334.
- Klypin, A. A. and Shandarin, S. F. (1983). Three-dimensional numerical model of the formation of large-scale structure in the Universe. *MNRAS*, 204:891–907.

- Kocz, J., Ravi, V., Catha, M., D’Addario, L., Hallinan, G., Hobbs, R., Kulkarni, S., Shi, J., Vedantham, H., Weinreb, S., and Woody, D. (2019). DSA-10: a prototype array for localizing fast radio bursts. *MNRAS*, 489(1):919–927.
- Kronberg, P. P. (1994). Extragalactic magnetic fields. *Reports on Progress in Physics*, 57(4):325–382.
- Kronberg, P. P., Bernet, M. L., Miniati, F., Lilly, S. J., Short, M. B., and Higdon, D. M. (2008). A Global Probe of Cosmic Magnetic Fields to High Redshifts. *ApJ*, 676(1):70–79.
- Kronberg, P. P., Perry, J. J., and Zukowski, E. L. H. (1992). Discovery of Extended Faraday Rotation Compatible with Spiral Structure in an Intervening Galaxy at $Z = 0.395$: New Observations of PKS 1229-021. *ApJ*, 387:528.
- Kulkarni, S. R. (2018). From gamma-ray bursts to fast radio bursts. *Nature Astronomy*, 2:832–835.
- Kulsrud, R. M., Cen, R., Ostriker, J. P., and Ryu, D. (1997). The Protogalactic Origin for Cosmic Magnetic Fields. *ApJ*, 480(2):481–491.
- Kumar, P., Lu, W., and Bhattacharya, M. (2017). Fast radio burst source properties and curvature radiation model. *MNRAS*, 468(3):2726–2739.
- Kumar, P., Shannon, R. M., Osłowski, S., Qiu, H., Bhandari, S., Farah, W., Flynn, C., Kerr, M., Lorimer, D. R., Macquart, J. P., Ng, C., Phillips, C. J., Price, D. C., and Spiewak, R. (2019). Faint Repetitions from a Bright Fast Radio Burst Source. *ApJ Letters*, 887(2):L30.
- Laganá, T. F., Durret, F., and Lopes, P. A. A. (2019). Physical properties of the X-ray gas as a dynamical diagnosis for galaxy clusters. *MNRAS*, 484(2):2807–2830.
- Lamee, M., Rudnick, L., Farnes, J. S., Carretti, E., Gaensler, B. M., Haverkorn, M., and Poppi, S. (2016). Magnetic Field Disorder and Faraday Effects on the Polarization of Extragalactic Radio Sources. *ApJ*, 829(1):5.
- Langer, M., Aghanim, N., and Puget, J. L. (2005). Magnetic fields from reionisation. *A&A*, 443(2):367–372.

- Li, C. K., Lin, L., Xiong, S. L., Ge, M. Y., Li, X. B., Li, T. P., Lu, F. J., Zhang, S. N., Tuo, Y. L., Nang, Y., Zhang, B., Xiao, S., Chen, Y., Song, L. M., Xu, Y. P., Liu, C. Z., Jia, S. M., Cao, X. L., Zhang, S., Qu, J. L., Liao, J. Y., Zhao, X. F., Tan, Y., Nie, J. Y., Zhao, H. S., Zheng, S. J., Zheng, Y. G., Luo, Q., Cai, C., Li, B., Xue, W. C., Bu, Q. C., Chang, Z., Chen, G., Chen, L., Chen, T. X., Chen, Y. B., Chen, Y. P., Cui, W., Cui, W. W., Deng, J. K., Dong, Y. W., Du, Y. Y., Fu, M. X., Gao, G. H., Gao, H., Gao, M., Gu, Y. D., Guan, J., Guo, C. C., Han, D. W., Huang, Y., Huo, J., Jiang, L. H., Jiang, W. C., Jin, J., Jin, Y. J., Kong, L. D., Li, G., Li, M. S., Li, W., Li, X., Li, X. F., Li, Y. G., Li, Z. W., Liang, X. H., Liu, B. S., Liu, G. Q., Liu, H. W., Liu, X. J., Liu, Y. N., Lu, B., Lu, X. F., Luo, T., Ma, X., Meng, B., Ou, G., Sai, N., Shang, R. C., Song, X. Y., Sun, L., Tao, L., Wang, C., Wang, G. F., Wang, J., Wang, W. S., Wang, Y. S., Wen, X. Y., Wu, B. B., Wu, B. Y., Wu, M., Xiao, G. C., Yang, J. W., Yang, S., Yang, Y. J., Yang, Y.-J., Yi, Q. B., Yin, Q. Q., You, Y., Zhang, A. M., Zhang, C. M., Zhang, F., Zhang, H. M., Zhang, J., Zhang, T., Zhang, W., Zhang, W. C., Zhang, W. Z., Zhang, Y., Zhang, Y., Zhang, Y. F., Zhang, Y. J., Zhang, Z., Zhang, Z., Zhang, Z. L., Zhou, D. K., Zhou, J. F., Zhu, Y., Zhu, Y. X., and Zhuang, R. L. (2020). Identification of a non-thermal X-ray burst with the Galactic magnetar SGR 1935+2154 and a fast radio burst with Insight-HXMT. *arXiv e-prints*, page arXiv:2005.11071.
- Li, Y. and Zhang, B. (2016). Radio transient following FRB 150418: afterglow or coincident AGN flare? *arXiv e-prints*, page arXiv:1603.04825.
- Locatelli, N., Ronchi, M., Ghirlanda, G., and Ghisellini, G. (2019). The luminosity-volume test for cosmological fast radio bursts. *A&A*, 625:A109.
- Locatelli, N., Vazza, F., and Domínguez-Fernández, P. (2018). The Challenge of Detecting Intracluster Filaments with Faraday Rotation. *Galaxies*, 6(4):128.
- Locatelli, N. T., Bernardi, G., Bianchi, G., Chiello, R., Magro, A., Naldi, G., Pilia, M., Pupillo, G., Ridolfi, A., Setti, G., and Vazza, F. (2020a). The Northern Cross fast radio burst project - I. Overview and pilot observations at 408 MHz. *MNRAS*, 494(1):1229–1236.
- Locatelli, N. T., Rajpurohit, K., Vazza, F., Gastaldello, F., Dallacasa, D., Bonafede, A., Rossetti, M., Stuardi, C., Bonassieux, E., Brunetti, G., Brüggén, M., and Shimwell, T. (2020b). Discovering the most elusive radio

- relic in the sky: diffuse shock acceleration caught in the act? *MNRAS*, 496(1):L48–L53.
- Loi, F., Murgia, M., Govoni, F., Vacca, V., Bonafede, A., Ferrari, C., Prandoni, I., Feretti, L., Giovannini, G., and Li, H. (2019a). Rotation measure synthesis applied to synthetic SKA images of galaxy clusters. *MNRAS*, 490(4):4841–4857.
- Loi, F., Murgia, M., Govoni, F., Vacca, V., Feretti, L., Giovannini, G., Carretti, E., Gastaldello, F., Girardi, M., Vazza, F., Concu, R., Melis, A., Paladino, R., Poppi, S., Valente, G., Boschini, W., Clarke, T. E., Colafrancesco, S., Enßlin, T., Ferrari, C., de Gasperin, F., Gregorini, L., Johnston-Hollitt, M., Junklewitz, H., Orrù, E., Parma, P., Perley, R., and Taylor, G. B. (2017). Observations of the galaxy cluster CIZA J2242.8+5301 with the Sardinia Radio Telescope. *MNRAS*, 472(3):3605–3623.
- Loi, F., Murgia, M., Govoni, F., Vacca, V., Prandoni, I., Bonafede, A., and Feretti, L. (2019b). Simulations of the polarized radio sky and predictions on the confusion limit in polarization for future radio surveys. *MNRAS*, 485(4):5285–5293.
- Lopes, P. A. A., Trevisan, M., Laganá, T. F., Durret, F., Ribeiro, A. L. B., and Rembold, S. B. (2018). Optical substructure and BCG offsets of Sunyaev-Zel’dovich and X-ray-selected galaxy clusters. *MNRAS*, 478(4):5473–5490.
- Lorimer, D. R. (2008). Binary and Millisecond Pulsars. *Living Reviews in Relativity*, 11(1):8.
- Lorimer, D. R. (2011). SIGPROC: Pulsar Signal Processing Programs.
- Lorimer, D. R., Bailes, M., McLaughlin, M. A., Narkevic, D. J., and Crawford, F. (2007). A Bright Millisecond Radio Burst of Extragalactic Origin. *Science*, 318(5851):777.
- Lorimer, D. R., Yates, J. A., Lyne, A. G., and Gould, D. M. (1995). Multi-frequency flux density measurements of 280 pulsars. *MNRAS*, 273(2):411–421.
- Luo, R., Lee, K., Lorimer, D. R., and Zhang, B. (2018). On the normalized FRB luminosity function. *MNRAS*, 481(2):2320–2337.

- Lynds, R. (1971). The Absorption-Line Spectrum of 4c 05.34. *ApJ Letters*, 164:L73.
- Lyubarsky, Y. (2014). A model for fast extragalactic radio bursts. *MNRAS*, 442:L9–L13.
- Lyutikov, M. (2017). Fast Radio Bursts’ Emission Mechanism: Implication from Localization. *ApJ Letters*, 838(1):L13.
- Macquart, J.-P. (2018). Probing the Universe’s baryons with fast radio bursts. *Nature Astronomy*, 2:836–838.
- Macquart, J.-P., Bailes, M., Bhat, N. D. R., Bower, G. C., Bunton, J. D., Chatterjee, S., Colegate, T., Cordes, J. M., D’Addario, L., Deller, A., Dodson, R., Fender, R., Haines, K., Hall, P., Harris, C., Hotan, A., Johnston, S., Jones, D. L., Keith, M., Koay, J. Y., Lazio, T. J. W., Majid, W., Murphy, T., Navarro, R., Phillips, C., Quinn, P., Preston, R. A., Stansby, B., Stairs, I., Stappers, B., Staveley-Smith, L., Tingay, S., Thompson, D., van Straten, W., Wagstaff, K., Warren, M., Wayth, R., Wen, L., and CRAFT Collaboration (2010). The Commensal Real-Time ASKAP Fast-Transients (CRAFT) Survey. *Publications of the Astronomical Society of Australia*, 27(3):272–282.
- Macquart, J. P. and Ekers, R. (2018). FRB event rate counts - II. Fluence, redshift, and dispersion measure distributions. *MNRAS*, 480(3):4211–4230.
- Macquart, J. P., Prochaska, J. X., McQuinn, M., Bannister, K. W., Bhandari, S., Day, C. K., Deller, A. T., Ekers, R. D., James, C. W., Marnoch, L., Osłowski, S., Phillips, C., Ryder, S. D., Scott, D. R., Shannon, R. M., and Tejos, N. (2020). A census of baryons in the Universe from localized fast radio bursts. *Nature*, 581(7809):391–395.
- Macquart, J. P., Shannon, R. M., Bannister, K. W., James, C. W., Ekers, R. D., and Bunton, J. D. (2019). The Spectral Properties of the Bright Fast Radio Burst Population. *ApJ Letters*, 872(2):L19.
- Madau, P. and Dickinson, M. (2014). Cosmic Star-Formation History. *Annual Review of Astronomy and Astrophysics*, 52:415–486.
- Magro, A., Bugeja, K., Chiello, R., and DeMarco, A. (2019). A high-performance, flexible data acquisition library for radio instruments. In *2019 IEEE-APS Topical Conference on Antennas and Propagation in Wireless Communications (APWC)*, pages 069–074.

- Magro, A., Chiello, R., Albanese, C., Baker, J., Comoretto, G., DeMarco, A., Gravina, A., Halsall, R., Roberts, M., and Adami, K. Z. (2017). A software infrastructure for firmware-software interaction: The case of tpms. In *2017 International Conference on Signals and Systems (ICSigSys)*, pages 190–196.
- Mao, S. A., Carilli, C., Gaensler, B. M., Wucknitz, O., Keeton, C., Basu, A., Beck, R., Kronberg, P. P., and Zweibel, E. (2017). Detection of micro-gauss coherent magnetic fields in a galaxy five billion years ago. *Nature Astronomy*, 1:621–626.
- Marcote, B., Paragi, Z., Hessels, J. W. T., Keimpema, A., van Langevelde, H. J., Huang, Y., Bassa, C. G., Bogdanov, S., Bower, G. C., Burke-Spolaor, S., Butler, B. J., Campbell, R. M., Chatterjee, S., Cordes, J. M., Demorest, P., Garrett, M. A., Ghosh, T., Kaspi, V. M., Law, C. J., Lazio, T. J. W., McLaughlin, M. A., Ransom, S. M., Salter, C. J., Scholz, P., Seymour, A., Siemion, A., Spitler, L. G., Tendulkar, S. P., and Wharton, R. S. (2017). The Repeating Fast Radio Burst FRB 121102 as Seen on Milliarcsecond Angular Scales. *ApJ Letters*, 834(2):L8.
- Marinacci, F., Vogelsberger, M., Mocz, P., and Pakmor, R. (2015). The large-scale properties of simulated cosmological magnetic fields. *MNRAS*, 453(4):3999–4019.
- Markevitch, M., Govoni, F., Brunetti, G., and Jerius, D. (2005). Bow Shock and Radio Halo in the Merging Cluster A520. *ApJ*, 627(2):733–738.
- Masters, A., Sulaiman, A. H., Stawarz, Ł., Reville, B., Sergis, N., Fujimoto, M., Burgess, D., Coates, A. J., and Dougherty, M. K. (2017). An in situ Comparison of Electron Acceleration at Collisionless Shocks under Differing Upstream Magnetic Field Orientations. *ApJ*, 843(2):147.
- McMullin, J. P., Waters, B., Schiebel, D., Young, W., and Golap, K. (2007). CASA Architecture and Applications. In Shaw, R. A., Hill, F., and Bell, D. J., editors, *Astronomical Data Analysis Software and Systems XVI*, volume 376 of *Astronomical Society of the Pacific Conference Series*, page 127.
- McQuinn, M. (2014). Locating the “Missing” Baryons with Extragalactic Dispersion Measure Estimates. *ApJ Letters*, 780(2):L33.
- Mechev, A., Oonk, J. B. R., Danezi, A., Shimwell, T. W., Schrijvers, C., Intema, H., Plaat, A., and Rottgering, H. J. A. (2017). An Automated

- Scalable Framework for Distributing Radio Astronomy Processing Across Clusters and Clouds. In *Proceedings of the International Symposium on Grids and Clouds (ISGC) 2017*, page 2.
- Medezinski, E., Umetsu, K., Okabe, N., Nonino, M., Molnar, S., Massey, R., Dupke, R., and Merten, J. (2016). Frontier Fields: Subaru Weak-Lensing Analysis of the Merging Galaxy Cluster A2744. *ApJ*, 817(1):24.
- Mennekens, N. and Vanbeveren, D. (2016). The delay time distribution of massive double compact star mergers. *A&A*, 589:A64.
- Mennekens, N., Vanbeveren, D., De Greve, J. P., and De Donder, E. (2010). The delay-time distribution of Type Ia supernovae: a comparison between theory and observation. *A&A*, 515:A89.
- Mereghetti, S., Savchenko, V., Ferrigno, C., Götz, D., Rigoselli, M., Tiengo, A., Bazzano, A., Bozzo, E., Coleiro, A., Courvoisier, T. J. L., Doyle, M., Goldwurm, A., Hanlon, L., Jourdain, E., von Kienlin, A., Lutovinov, A., Martin-Carrillo, A., Molkov, S., Natalucci, L., Onori, F., Panessa, F., Rodi, J., Rodriguez, J., Sánchez-Fernández, C., Sunyaev, R., and Ubertini, P. (2020). INTEGRAL Discovery of a Burst with Associated Radio Emission from the Magnetar SGR 1935+2154. *ApJ Letters*, 898(2):L29.
- Merten, J., Coe, D., Dupke, R., Massey, R., Zitrin, A., Cypriano, E. S., Okabe, N., Frye, B., Braglia, F. G., Jiménez-Teja, Y., Benítez, N., Broadhurst, T., Rhodes, J., Meneghetti, M., Moustakas, L. A., Sodr e, L., J., Krick, J., and Bregman, J. N. (2011). Creation of cosmic structure in the complex galaxy cluster merger Abell 2744. *MNRAS*, 417(1):333–347.
- Michilli, D., Seymour, A., Hessels, J. W. T., Spitler, L. G., Gajjar, V., Archibald, A. M., Bower, G. C., Chatterjee, S., Cordes, J. M., Gourdji, K., Heald, G. H., Kaspi, V. M., Law, C. J., Sobey, C., Adams, E. A. K., Bassa, C. G., Bogdanov, S., Brinkman, C., Demorest, P., Fernandez, F., Hellbourg, G., Lazio, T. J. W., Lynch, R. S., Maddox, N., Marcote, B., McLaughlin, M. A., Paragi, Z., Ransom, S. M., Scholz, P., Siemion, A. P. V., Tendulkar, S. P., van Rooy, P., Wharton, R. S., and Whitlow, D. (2018). An extreme magneto-ionic environment associated with the fast radio burst source FRB 121102. *Nature*, 553(7687):182–185.
- Miniati, F. and Bell, A. R. (2011). Resistive Magnetic Field Generation at Cosmic Dawn. *ApJ*, 729(1):73.

- Miralda-Escudé, J., Cen, R., Ostriker, J. P., and Rauch, M. (1996). The Ly alpha Forest from Gravitational Collapse in the Cold Dark Matter + Lambda Model. *ApJ*, 471:582.
- Mohan, N. and Rafferty, D. (2015). PyBDSF: Python Blob Detection and Source Finder.
- Montebugnoli, S., Bianchi, G., Monari, J., Naldi, G., Perini, F., and Schiaffino, M. (2009). BEST: Basic Element for SKA Training. In *Wide Field Astronomy & Technology for the Square Kilometre Array*, page 58.
- Murgia, M., Govoni, F., Feretti, L., Giovannini, G., Dallacasa, D., Fanti, R., Taylor, G. B., and Dolag, K. (2004). Magnetic fields and Faraday rotation in clusters of galaxies. *A&A*, 424:429–446.
- Natwariya, P. K. (2020). Constraint on Primordial Magnetic Fields In the Light of ARCADE 2 and EDGES Observations. *arXiv e-prints*, page arXiv:2007.09938.
- Neronov, A. and Vovk, I. (2010). Evidence for Strong Extragalactic Magnetic Fields from Fermi Observations of TeV Blazars. *Science*, 328(5974):73.
- Neuhäuser, M. (2011). *Wilcoxon–Mann–Whitney Test*, pages 1656–1658. Springer Berlin Heidelberg, Berlin, Heidelberg.
- Nicastro, F. (2016). A Decade of WHIM search: Where do We Stand and Where do We Go. In *XMM-Newton: The Next Decade*, page 27.
- Nicastro, F., Kaastra, J., Krongold, Y., Borgani, S., Branchini, E., Cen, R., Dadina, M., Danforth, C. W., Elvis, M., Fiore, F., Gupta, A., Mathur, S., Mayya, D., Paerels, F., Piro, L., Rosa-Gonzalez, D., Schaye, J., Shull, J. M., Torres-Zafra, J., Wijers, N., and Zappacosta, L. (2018). Observations of the missing baryons in the warm-hot intergalactic medium. *Nature*, 558(7710):406–409.
- Nicastro, F., Krongold, Y., Mathur, S., and Elvis, M. (2017). A decade of warm hot intergalactic medium searches: Where do we stand and where do we go? *Astronomische Nachrichten*, 338(281):281–286.
- Niino, Y., Tominaga, N., Totani, T., Morokuma, T., Keane, E., Possenti, A., Sugai, H., and Yamasaki, S. (2018). A search for optical transients associated with fast radio burst 150418^{yz}. *Publications of the Astronomical Society of Japan*, 70(5):L7.

- Nuza, S. E., Gelszinnis, J., Hoeft, M., and Yepes, G. (2017). Can cluster merger shocks reproduce the luminosity and shape distribution of radio relics? *MNRAS*, 470(1):240–263.
- Offringa, A. R., McKinley, B., Hurley-Walker, N., Briggs, F. H., Wayth, R. B., Kaplan, D. L., Bell, M. E., Feng, L., Neben, A. R., Hughes, J. D., Rhee, J., Murphy, T., Bhat, N. D. R., Bernardi, G., Bowman, J. D., Cappallo, R. J., Corey, B. E., Deshpande, A. A., Emrich, D., Ewall-Wice, A., Gaensler, B. M., Goeke, R., Greenhill, L. J., Hazelton, B. J., Hindson, L., Johnston-Hollitt, M., Jacobs, D. C., Kasper, J. C., Kratzenberg, E., Lenc, E., Lonsdale, C. J., Lynch, M. J., McWhirter, S. R., Mitchell, D. A., Morales, M. F., Morgan, E., Kudryavtseva, N., Oberoi, D., Ord, S. M., Pindor, B., Procopio, P., Prabu, T., Riding, J., Roshi, D. A., Shankar, N. U., Srivani, K. S., Subrahmanyan, R., Tingay, S. J., Waterson, M., Webster, R. L., Whitney, A. R., Williams, A., and Williams, C. L. (2014). WSCLEAN: an implementation of a fast, generic wide-field imager for radio astronomy. *MNRAS*, 444(1):606–619.
- Oh, S., Kim, K., Lee, J. H., Sheen, Y.-K., Kim, M., Ree, C. H., Ho, L. C., Kyeong, J., Sung, E.-C., Park, B.-G., and Yi, S. K. (2018). KYDISC: Galaxy Morphology, Quenching, and Mergers in the Cluster Environment. *ApJS*, 237(1):14.
- Oppermann, N., Connor, L. D., and Pen, U.-L. (2016). The Euclidean distribution of fast radio bursts. *MNRAS*, 461(1):984–987.
- Oppermann, N., Junklewitz, H., Greiner, M., Enßlin, T. A., Akahori, T., Carretti, E., Gaensler, B. M., Goobar, A., Harvey-Smith, L., Johnston-Hollitt, M., Pratley, L., Schnitzeler, D. H. F. M., Stil, J. M., and Vacca, V. (2015). Estimating extragalactic Faraday rotation. *A&A*, 575:A118.
- Oppermann, N., Junklewitz, H., Robbers, G., Bell, M. R., Enßlin, T. A., Bonafede, A., Braun, R., Brown, J. C., Clarke, T. E., Feain, I. J., Gaensler, B. M., Hammond, A., Harvey-Smith, L., Heald, G., Johnston-Hollitt, M., Klein, U., Kronberg, P. P., Mao, S. A., McClure-Griffiths, N. M., O’Sullivan, S. P., Pratley, L., Robishaw, T., Roy, S., Schnitzeler, D. H. F. M., Sotomayor-Beltran, C., Stevens, J., Stil, J. M., Sunstrum, C., Tanna, A., Taylor, A. R., and Van Eck, C. L. (2012). An improved map of the Galactic Faraday sky. *A&A*, 542:A93.
- O’Sullivan, S. P., Brügggen, M., Vazza, F., Carretti, E., Locatelli, N. T., Stuardi, C., Vacca, V., Vernstrom, T., Heald, G., Horellou, C., Shimwell,

- T. W., Hardcastle, M. J., Tasse, C., and Röttgering, H. (2020). New constraints on the magnetization of the cosmic web using LOFAR Faraday rotation observations. *MNRAS*, 495(3):2607–2619.
- O’Sullivan, S. P., Machalski, J., Van Eck, C. L., Heald, G., Brügger, M., Fynbo, J. P. U., Heintz, K. E., Lara-Lopez, M. A., Vacca, V., Hardcastle, M. J., Shimwell, T. W., Tasse, C., Vazza, F., Andernach, H., Birkinshaw, M., Haverkorn, M., Horellou, C., Williams, W. L., Harwood, J. J., Brunetti, G., Anderson, J. M., Mao, S. A., Nikiel-Wroczyński, B., Takahashi, K., Carretti, E., Vernstrom, T., van Weeren, R. J., Orrú, E., Morabito, L. K., and Callingham, J. R. (2019). The intergalactic magnetic field probed by a giant radio galaxy. *A&A*, 622:A16.
- Owen, F. N., Rudnick, L., Eilek, J., Rau, U., Bhatnagar, S., and Kogan, L. (2014). Wideband Very Large Array Observations of A2256. I. Continuum, Rotation Measure, and Spectral Imaging. *ApJ*, 794(1):24.
- Owers, M. S., Randall, S. W., Nulsen, P. E. J., Couch, W. J., David, L. P., and Kempner, J. C. (2011). The Dissection of Abell 2744: A Rich Cluster Growing Through Major and Minor Mergers. *ApJ*, 728(1):27.
- Pakmor, R., Marinacci, F., and Springel, V. (2014). Magnetic Fields in Cosmological Simulations of Disk Galaxies. *ApJ Letters*, 783(1):L20.
- Paoletti, D. and Finelli, F. (2019). Constraints on primordial magnetic fields from magnetically-induced perturbations: current status and future perspectives with LiteBIRD and future ground based experiments. *Journal of Cosmology and Astroparticle Physics*, 2019(11):028.
- Patel, C., Agarwal, D., Bhardwaj, M., Boyce, M. M., Brazier, A., Chatterjee, S., Chawla, P., Kaspi, V. M., Lorimer, D. R., McLaughlin, M. A., Parent, E., Pleunis, Z., Ransom, S. M., Scholz, P., Wharton, R. S., Zhu, W. W., Alam, M., Caballero Valdez, K., Camilo, F., Cordes, J. M., Crawford, F., Deneva, J. S., Ferdman, R. D., Freire, P. C. C., Hessels, J. W. T., Nguyen, B., Stairs, I., Stovall, K., and van Leeuwen, J. (2018). PALFA Single-pulse Pipeline: New Pulsars, Rotating Radio Transients, and a Candidate Fast Radio Burst. *ApJ*, 869(2):181.
- Peacock, J. A. (1985). The high-redshift evolution of radio galaxies and quasars. *MNRAS*, 217:601–631.
- Pearce, C. J. J., van Weeren, R. J., Andrade-Santos, F., Jones, C., Forman, W. R., Brügger, M., Bulbul, E., Clarke, T. E., Kraft, R. P., Medezinski,

- E., Mroczkowski, T., Nonino, M., Nulsen, P. E. J., Randall, S. W., and Umetsu, K. (2017). VLA Radio Observations of the HST Frontier Fields Cluster Abell 2744: The Discovery of New Radio Relics. *ApJ*, 845(1):81.
- Pedani, M. and Grueff, G. (1999). The 408 MHz B3.2 survey. *A&A*, 350:368–378.
- Perini, F. (2009a). Analogue optical links experiences in the framework of the SKA/BEST activities. In *Wide Field Astronomy & Technology for the Square Kilometre Array*, page 61.
- Perini, F. (2009b). Low noise design experience for the SKADS/BEST demonstrator. In *Wide Field Astronomy & Technology for the Square Kilometre Array*, page 60.
- Perini, F., Bianchi, G., Schiaffino, M., and Monari, J. (2009). BEST receiver experience: general architecture, design and integration. In *Wide Field Astronomy & Technology for the Square Kilometre Array*, page 62.
- Perley, R. A. and Butler, B. J. (2013). Integrated Polarization Properties of 3C48, 3C138, 3C147, and 3C286. *ApJS*, 206(2):16.
- Perley, R. A. and Butler, B. J. (2017). An Accurate Flux Density Scale from 50 MHz to 50 GHz. *ApJS*, 230(1):7.
- Petroff, E., Bailes, M., Barr, E. D., Barsdell, B. R., Bhat, N. D. R., Bian, F., Burke-Spolaor, S., Caleb, M., Champion, D., Chandra, P., Da Costa, G., Delvaux, C., Flynn, C., Gehrels, N., Greiner, J., Jameson, A., Johnston, S., Kasliwal, M. M., Keane, E. F., Keller, S., Kocz, J., Kramer, M., Leloudas, G., Malesani, D., Mulchaey, J. S., Ng, C., Ofek, E. O., Perley, D. A., Possenti, A., Schmidt, B. P., Shen, Y., Stappers, B., Tisserand, P., van Straten, W., and Wolf, C. (2015). A real-time fast radio burst: polarization detection and multiwavelength follow-up. *MNRAS*, 447(1):246–255.
- Petroff, E., Barr, E. D., Jameson, A., Keane, E. F., Bailes, M., Kramer, M., Morello, V., Tabbara, D., and van Straten, W. (2016). FRBCAT: The Fast Radio Burst Catalogue. *Publications of the Astronomical Society of Australia*, 33:e045.
- Petroff, E., Burke-Spolaor, S., Keane, E. F., McLaughlin, M. A., Miller, R., Andreoni, I., Bailes, M., Barr, E. D., Bernard, S. R., Bhandari, S., Bhat, N. D. R., Burgay, M., Caleb, M., Champion, D., Chandra, P., Cooke,

J., Dhillon, V. S., Farnes, J. S., Hardy, L. K., Jaroenjittichai, P., Johnston, S., Kasliwal, M., Kramer, M., Littlefair, S. P., Macquart, J. P., Mickaliger, M., Possenti, A., Pritchard, T., Ravi, V., Rest, A., Rowlinson, A., Sawangwit, U., Stappers, B., Sullivan, M., Tiburzi, C., van Straten, W., ANTARES Collaboration, Albert, A., André, M., Anghinolfi, M., Anton, G., Ardid, M., Aubert, J. J., Avgitas, T., Baret, B., Barrios-Martí, J., Basa, S., Bertin, V., Biagi, S., Bormuth, R., Bourret, S., Bouwhuis, M. C., Bruijn, R., Brunner, J., Busto, J., Capone, A., Caramete, L., Carr, J., Celli, S., Chiarusi, T., Circella, M., Coelho, J. A. B., Coleiro, A., Coniglione, R., Costantini, H., Coyle, P., Creusot, A., Deschamps, A., de Bonis, G., Distefano, C., di Palma, I., Donzaud, C., Dornic, D., Drouhin, D., Eberl, T., El Bojaddaini, I., Elsässer, D., Enzenhöfer, A., Felis, I., Fusco, L. A., Galatà, S., Gay, P., Geißelsöder, S., Geyer, K., Giordano, V., Gleixner, A., Glotin, H., Grégoire, T., Gracia-Ruiz, R., Graf, K., Hallmann, S., van Haren, H., Heijboer, A. J., Hello, Y., Hernández-Rey, J. J., Hößl, J., Hofestädt, J., Hugon, C., Illuminati, G., James, C. W., de Jong, M., Jongen, M., Kadler, M., Kalekin, O., Katz, U., Kießling, D., Kouchner, A., Kreter, M., Kreykenbohm, I., Kulikovskiy, V., Lachaud, C., Lahmann, R., Lefèvre, D., Leonora, E., Lotze, M., Loucatos, S., Marcellin, M., Margiotta, A., Marinelli, A., Martínez-Mora, J. A., Mathieu, A., Mele, R., Melis, K., Michael, T., Migliozi, P., Moussa, A., Mueller, C., Nezri, E., Pāvālaš, G. E., Pellegrino, C., Perrina, C., Piattelli, P., Popa, V., Pradier, T., Quinn, L., Racca, C., Riccobene, G., Roensch, K., Sánchez-Losa, A., Saldaña, M., Salvadori, I., Samtleben, D. F. E., Sanguineti, M., Sapienza, P., Schnabel, J., Seitz, T., Sieger, C., Spurio, M., Stolarczyk, T., Taiuti, M., Tayalati, Y., Trovato, A., Tselengidou, M., Turpin, D., Tönnis, C., Vallage, B., Vallée, C., van Elewyck, V., Vivolo, D., Vizzoca, A., Wagner, S., Wilms, J., Zornoza, J. D., Zúñiga, J., H. E. S. S. Collaboration, Abdalla, H., Abramowski, A., Aharonian, F., Ait Benkhali, F., Akhperjanian, A. G., Andersson, T., Angüner, E. O., Arrieta, M., Aubert, P., Backes, M., Balzer, A., Barnard, M., Becherini, Y., Tjus, J. B., Berge, D., Bernhard, S., Bernlöhr, K., Blackwell, R., Böttcher, M., Boisson, C., Bolmont, J., Bordas, P., Bregeon, J., Brun, F., Brun, P., Bryan, M., Bulik, T., Capasso, M., Casanova, S., Cerruti, M., Chakraborty, N., Chalme-Calvet, R., Chaves, R. C. G., Chen, A., Chevalier, J., Chrétien, M., Colafrancesco, S., Cologna, G., Condon, B., Conrad, J., Cui, Y., Davids, I. D., Decock, J., Degrange, B., Deil, C., Devin, J., Dewilt, P., Dirson, L., Djannati-Ataï, A., Domainko, W., Donath, A., Drury, L. O., Dubus, G., Dutson, K., Dyks, J., Edwards, T., Egberts, K., Eger, P., Ernenwein, J. P., Eschbach, S., Farnier, C., Fegan, S., Fer-

nandes, M. V., Fiasson, A., Fontaine, G., Förster, A., Funk, S., Füßling, M., Gabici, S., Gajdus, M., Gallant, Y. A., Garrigoux, T., Giavitto, G., Giebels, B., Glicenstein, J. F., Gottschall, D., Goyal, A., Grondin, M. H., Hadasch, D., Hahn, J., Haupt, M., Hawkes, J., Heinzelmann, G., Henri, G., Hermann, G., Hervet, O., Hinton, J. A., Hofmann, W., Hoischen, C., Holler, M., Horns, D., Ivascenko, A., Jacholkowska, A., Jamrozy, M., Janiak, M., Jankowsky, D., Jankowsky, F., Jingo, M., Jogler, T., Jouvin, L., Jung-Richardt, I., Kastendieck, M. A., Katarzyński, K., Kerszberg, D., Khélifi, B., Kieffer, M., King, J., Klepser, S., Klochkov, D., Kluźniak, W., Kolitzus, D., Komin, N., Kosack, K., Krakau, S., Kraus, M., Krayzel, F., Krüger, P. P., Laffon, H., Lamanna, G., Lau, J., Lees, J. P., Lefaucheur, J., Lefranc, V., Lemièrre, A., Lemoine-Goumard, M., Lenain, J. P., Leser, E., Lohse, T., Lorentz, M., Liu, R., López-Coto, R., Lypova, I., Marandon, V., Marcowith, A., Mariaud, C., Marx, R., Maurin, G., Maxted, N., Mayer, M., Meintjes, P. J., Meyer, M., Mitchell, A. M. W., Moderski, R., Mohamed, M., Mohrmann, L., Morâ, K., Moulin, E., Murach, T., de Naurois, M., Niederwanger, F., Niemiec, J., Oakes, L., O'Brien, P., Odaka, H., Öttl, S., Ohm, S., Ostrowski, M., Oya, I., Padovani, M., Panter, M., Parsons, R. D., Pekeur, N. W., Pelletier, G., Perennes, C., Petrucci, P. O., Peyaud, B., Piel, Q., Pita, S., Poon, H., Prokhorov, D., Prokoph, H., Pühlhofer, G., Punch, M., Quirrenbach, A., Raab, S., Reimer, A., Reimer, O., Renaud, M., Reyes, R. D. L., Rieger, F., Romoli, C., Rosier-Lees, S., Rowell, G., Rudak, B., Rulten, C. B., Sahakian, V., Salek, D., Sanchez, D. A., Santangelo, A., Sasaki, M., Schlickeiser, R., Schulz, A., Schüssler, F., Schwanke, U., Schwemmer, S., Settimo, M., Seyffert, A. S., Shafi, N., Shilon, I., Simoni, R., Sol, H., Spanier, F., Spengler, G., Spies, F., Stawarz, Ł., Steenkamp, R., Stegmann, C., Stinzing, F., Stycz, K., Sushch, I., Tavernet, J. P., Tavernier, T., Taylor, A. M., Terrier, R., Tibaldo, L., Tiziani, D., Tluczykont, M., Trichard, C., Tuffs, R., Uchiyama, Y., Walt, D. J. V. D., van Eldik, C., van Rensburg, C., van Soelen, B., Vasileiadis, G., Veh, J., Venter, C., Viana, A., Vincent, P., Vink, J., Voisin, F., Völk, H. J., Vuillaume, T., Wadiasingh, Z., Wagner, S. J., Wagner, P., Wagner, R. M., White, R., Wierzcholska, A., Willmann, P., Wörnlein, A., Wouters, D., Yang, R., Zabalza, V., Zaborov, D., Zacharias, M., Zanin, R., Zdziarski, A. A., Zech, A., Zefi, F., Ziegler, A., and Żywucka, N. (2017). A polarized fast radio burst at low Galactic latitude. *MNRAS*, 469(4):4465–4482.

Petroff, E., Hessels, J. W. T., and Lorimer, D. R. (2019). Fast radio bursts. *The Astronomy and Astrophysics Review*, 27(1):4.

- Pfrommer, C., Springel, V., Enßlin, T. A., and Jubelgas, M. (2006). Detecting shock waves in cosmological smoothed particle hydrodynamics simulations. *MNRAS*, 367(1):113–131.
- Piffaretti, R., Arnaud, M., Pratt, G. W., Pointecouteau, E., and Melin, J. B. (2011). The MCXC: a meta-catalogue of x-ray detected clusters of galaxies. *A&A*, 534:A109.
- Pilia, M., Burgay, M., Possenti, A., Ridolfi, A., Gajjar, V., Corongiu, A., Perrodin, D., Bernardi, G., Naldi, G., Pupillo, G., Ambrosino, F., Bianchi, G., Burtovoi, A., Casella, P., Casentini, C., Cecconi, M., Ferrigno, C., Fiori, M., Gendreau, K. C., Ghedina, A., Naletto, G., Nicastro, L., Ochner, P., Palazzi, E., Panessa, F., Papitto, A., Pittori, C., Rea, N., Castillo, G. A. R., Savchenko, V., Setti, G., Tavani, M., Trois, A., Trudu, M., Turatto, M., Ursi, A., Verrecchia, F., and Zampieri, L. (2020). The Lowest-frequency Fast Radio Bursts: Sardinia Radio Telescope Detection of the Periodic FRB 180916 at 328 MHz. *ApJ Letters*, 896(2):L40.
- Pinzke, A., Oh, S. P., and Pfrommer, C. (2013). Giant radio relics in galaxy clusters: reacceleration of fossil relativistic electrons? *MNRAS*, 435(2):1061–1082.
- Planck Collaboration, Ade, P. A. R., Aghanim, N., Arnaud, M., Ashdown, M., Atrio-Barandela, F., Aumont, J., Baccigalupi, C., Balbi, A., Banday, A. J., and et al. (2013). Planck intermediate results. VIII. Filaments between interacting clusters. *A&A*, 550:A134.
- Planck Collaboration, Ade, P. A. R., Aghanim, N., Arnaud, M., Ashdown, M., Aumont, J., Baccigalupi, C., Banday, A. J., Barreiro, R. B., Barrena, R., Bartlett, J. G., Bartolo, N., Battaner, E., Battye, R., Benabed, K., Benoît, A., Benoit-Lévy, A., Bernard, J. P., Bersanelli, M., Bielewicz, P., Bikmaev, I., Böhringer, H., Bonaldi, A., Bonavera, L., Bond, J. R., Borrill, J., Bouchet, F. R., Bucher, M., Burenin, R., Burigana, C., Butler, R. C., Calabrese, E., Cardoso, J. F., Carvalho, P., Catalano, A., Challinor, A., Chamballu, A., Chary, R. R., Chiang, H. C., Chon, G., Christensen, P. R., Clements, D. L., Colombi, S., Colombo, L. P. L., Combet, C., Comis, B., Couchot, F., Coulais, A., Crill, B. P., Curto, A., Cuttaia, F., Dahle, H., Danese, L., Davies, R. D., Davis, R. J., de Bernardis, P., de Rosa, A., de Zotti, G., Delabrouille, J., Désert, F. X., Dickinson, C., Diego, J. M., Dolag, K., Dole, H., Donzelli, S., Doré, O., Douspis, M., Ducout, A., Dupac, X., Efstathiou, G., Eisenhardt, P. R. M., Elsner, F.,

Enßlin, T. A., Eriksen, H. K., Falgarone, E., Fergusson, J., Feroz, F., Ferragamo, A., Finelli, F., Forni, O., Frailis, M., Fraisse, A. A., Franceschi, E., Frejsel, A., Galeotta, S., Galli, S., Ganga, K., Génova-Santos, R. T., Giard, M., Giraud-Héraud, Y., Gjerløw, E., González-Nuevo, J., Górski, K. M., Grainge, K. J. B., Gratton, S., Gregorio, A., Gruppuso, A., Gudmundsson, J. E., Hansen, F. K., Hanson, D., Harrison, D. L., Hempel, A., Henrot-Versillé, S., Hernández-Monteagudo, C., Herranz, D., Hildebrandt, S. R., Hivon, E., Hobson, M., Holmes, W. A., Hornstrup, A., Hovest, W., Huppenberger, K. M., Hurier, G., Jaffe, A. H., Jaffe, T. R., Jin, T., Jones, W. C., Juvela, M., Keihänen, E., Keskitalo, R., Khamitov, I., Kisner, T. S., Kneissl, R., Knoche, J., Kunz, M., Kurki-Suonio, H., Lagache, G., Lamarre, J. M., Lasenby, A., Lattanzi, M., Lawrence, C. R., Leonardi, R., Lesgourgues, J., Levrier, F., Liguori, M., Lilje, P. B., Linden-Vørnle, M., López-Caniego, M., Lubin, P. M., Macías-Pérez, J. F., Maggio, G., Maino, D., Mak, D. S. Y., Mandolesi, N., Mangilli, A., Martin, P. G., Martínez-González, E., Masi, S., Matarrese, S., Mazzotta, P., McGehee, P., Mei, S., Melchiorri, A., Melin, J. B., Mendes, L., Mennella, A., Migliaccio, M., Mitra, S., Miville-Deschênes, M. A., Moneti, A., Montier, L., Morgante, G., Mortlock, D., Moss, A., Munshi, D., Murphy, J. A., Naselsky, P., Nastasi, A., Nati, F., Natoli, P., Netterfield, C. B., Nørgaard-Nielsen, H. U., Noviello, F., Novikov, D., Novikov, I., Olamaie, M., Oxborrow, C. A., Paci, F., Pagano, L., Pajot, F., Paoletti, D., Pasian, F., Patanchon, G., Pearson, T. J., Perdereau, O., Perotto, L., Perrott, Y. C., Perrotta, F., Pettorino, V., Piacentini, F., Piat, M., Pierpaoli, E., Pietrobon, D., Plaszczynski, S., Pointecouteau, E., Polenta, G., Pratt, G. W., Prézeau, G., Prunet, S., Puget, J. L., Rachen, J. P., Reach, W. T., Rebolo, R., Reinecke, M., Remazeilles, M., Renault, C., Renzi, A., Ristorcelli, I., Rocha, G., Rosset, C., Rossetti, M., Roudier, G., Roza, E., Rubiño-Martín, J. A., Rumsey, C., Rusholme, B., Rykoff, E. S., Sandri, M., Santos, D., Saunders, R. D. E., Savelainen, M., Savini, G., Schammel, M. P., Scott, D., Seiffert, M. D., Shellard, E. P. S., Shimwell, T. W., Spencer, L. D., Stanford, S. A., Stern, D., Stolyarov, V., Stompor, R., Streblyanska, A., Sudiwala, R., Sunyaev, R., Sutton, D., Suur-Uski, A. S., Sygnet, J. F., Tauber, J. A., Terenzi, L., Toffolatti, L., Tomasi, M., Tramonte, D., Tristram, M., Tucci, M., Tuovinen, J., Umana, G., Valenziano, L., Valiviita, J., Van Tent, B., Vielva, P., Villa, F., Wade, L. A., Wandelt, B. D., Wehus, I. K., White, S. D. M., Wright, E. L., Yvon, D., Zacchei, A., and Zonca, A. (2016a). Planck 2015 results. XXVII. The second Planck catalogue of Sunyaev-Zeldovich sources. *A&A*, 594:A27.

Planck Collaboration, Ade, P. A. R., Aghanim, N., Arnaud, M., Ashdown, M., Aumont, J., Baccigalupi, C., Banday, A. J., Barreiro, R. B., Bartlett, J. G., Bartolo, N., Battaner, E., Battye, R., Benabed, K., Benoît, A., Benoit-Lévy, A., Bernard, J. P., Bersanelli, M., Bielewicz, P., Bock, J. J., Bonaldi, A., Bonavera, L., Bond, J. R., Borrill, J., Bouchet, F. R., Boulanger, F., Bucher, M., Burigana, C., Butler, R. C., Calabrese, E., Cardoso, J. F., Catalano, A., Challinor, A., Chamballu, A., Chary, R. R., Chiang, H. C., Chluba, J., Christensen, P. R., Church, S., Clements, D. L., Colombi, S., Colombo, L. P. L., Combet, C., Coulais, A., Crill, B. P., Curto, A., Cuttaia, F., Danese, L., Davies, R. D., Davis, R. J., de Bernardis, P., de Rosa, A., de Zotti, G., Delabrouille, J., Désert, F. X., Di Valentino, E., Dickinson, C., Diego, J. M., Dolag, K., Dole, H., Donzelli, S., Doré, O., Douspis, M., Ducout, A., Dunkley, J., Dupac, X., Efstathiou, G., Elsner, F., Enßlin, T. A., Eriksen, H. K., Farhang, M., Fergusson, J., Finelli, F., Forni, O., Frailis, M., Fraisse, A. A., Franceschi, E., Frejsel, A., Galeotta, S., Galli, S., Ganga, K., Gauthier, C., Gerbino, M., Ghosh, T., Giard, M., Giraud-Héraud, Y., Giusarma, E., Gjerløw, E., González-Nuevo, J., Górski, K. M., Gratton, S., Gregorio, A., Gruppuso, A., Gudmundsson, J. E., Hamann, J., Hansen, F. K., Hanson, D., Harrison, D. L., Helou, G., Henrot-Versillé, S., Hernández-Monteagudo, C., Herranz, D., Hildebrandt, S. R., Hivon, E., Hobson, M., Holmes, W. A., Hornstrup, A., Hovest, W., Huang, Z., Huppenberger, K. M., Hurier, G., Jaffe, A. H., Jaffe, T. R., Jones, W. C., Juvela, M., Keihänen, E., Keskitalo, R., Kisner, T. S., Kneissl, R., Knoch, J., Knox, L., Kunz, M., Kurki-Suonio, H., Lagache, G., Lähteenmäki, A., Lamarre, J. M., Lasenby, A., Lattanzi, M., Lawrence, C. R., Leahy, J. P., Leonardi, R., Lesgourgues, J., Levrier, F., Lewis, A., Liguori, M., Lilje, P. B., Linden-Vørnle, M., López-Cañiego, M., Lubin, P. M., Macías-Pérez, J. F., Maggio, G., Maino, D., Mandolesi, N., Mangilli, A., Marchini, A., Maris, M., Martin, P. G., Martinelli, M., Martínez-González, E., Masi, S., Matarrese, S., McGehee, P., Meinhold, P. R., Melchiorri, A., Melin, J. B., Mendes, L., Mennella, A., Migliaccio, M., Millea, M., Mitra, S., Miville-Deschênes, M. A., Moneti, A., Montier, L., Morgante, G., Mortlock, D., Moss, A., Munshi, D., Murphy, J. A., Naselsky, P., Nati, F., Natoli, P., Netterfield, C. B., Nørgaard-Nielsen, H. U., Noviello, F., Novikov, D., Novikov, I., Oxborrow, C. A., Paci, F., Pagano, L., Pajot, F., Paladini, R., Paoletti, D., Partridge, B., Pasian, F., Patanchon, G., Pearson, T. J., Perdereau, O., Perotto, L., Perrotta, F., Pettorino, V., Piacentini, F., Piat, M., Pierpaoli, E., Pietrobon, D., Plaszczynski, S., Pointecouteau, E., Polenta, G., Popa, L., Pratt, G. W., Prézeau, G., Prunet, S., Puget, J. L., Rachen, J. P., Reach, W. T., Rebolo,

- R., Reinecke, M., Remazeilles, M., Renault, C., Renzi, A., Ristorcelli, I., Rocha, G., Rosset, C., Rossetti, M., Roudier, G., Rouillé d'Orfeuil, B., Rowan-Robinson, M., Rubiño-Martín, J. A., Rusholme, B., Said, N., Salvatelli, V., Salvati, L., Sandri, M., Santos, D., Savelainen, M., Savini, G., Scott, D., Seiffert, M. D., Serra, P., Shellard, E. P. S., Spencer, L. D., Spinelli, M., Stolyarov, V., Stompor, R., Sudiwala, R., Sunyaev, R., Sutton, D., Suur-Uski, A. S., Sygnet, J. F., Tauber, J. A., Terenzi, L., Toffolatti, L., Tomasi, M., Tristram, M., Trombetti, T., Tucci, M., Tuovinen, J., Türler, M., Umana, G., Valenziano, L., Valiviita, J., Van Tent, F., Vielva, P., Villa, F., Wade, L. A., Wandelt, B. D., Wehus, I. K., White, M., White, S. D. M., Wilkinson, A., Yvon, D., Zacchei, A., and Zonca, A. (2016b). Planck 2015 results. XIII. Cosmological parameters. *A&A*, 594:A13.
- Planelles, S., Schleicher, D. R. G., and Bykov, A. M. (2016). *Large-Scale Structure Formation: From the First Non-linear Objects to Massive Galaxy Clusters*, volume 51, pages 93–139.
- Platts, E., Weltman, A., Walters, A., Tendulkar, S. P., Gordin, J. E. B., and Kandhai, S. (2019). A living theory catalogue for fast radio bursts. *Physics Reports*, 821:1–27.
- Popov, S. B. and Postnov, K. A. (2010). Hyperflares of SGRs as an engine for millisecond extragalactic radio bursts. In Harutyunian, H. A., Mickaelian, A. M., and Terzian, Y., editors, *Evolution of Cosmic Objects through their Physical Activity*, pages 129–132.
- Pshirkov, M. S., Tinyakov, P. G., and Urban, F. R. (2016). New Limits on Extragalactic Magnetic Fields from Rotation Measures. *Physical Review Letters*, 116(19):191302.
- Purcell, C. R., Van Eck, C. L., West, J., Sun, X. H., and Gaensler, B. M. (2020). RM-Tools: Rotation measure (RM) synthesis and Stokes QU-fitting.
- Rajpurohit, K., Hoeft, M., van Weeren, R. J., Rudnick, L., Röttgering, H. J. A., Forman, W. R., Brüggen, M., Croston, J. H., Andrade-Santos, F., Dawson, W. A., Intema, H. T., Kraft, R. P., Jones, C., and Jee, M. J. (2018). Deep VLA Observations of the Cluster 1RXS J0603.3+4214 in the Frequency Range of 1-2 GHz. *ApJ*, 852(2):65.
- Rauch, M., Miralda-Escudé, J., Sargent, W. L. W., Barlow, T. A., Weinberg, D. H., Hernquist, L., Katz, N., Cen, R., and Ostriker, J. P. (1997).

- The Opacity of the Ly α Forest and Implications for Ω_b and the Ionizing Background. *ApJ*, 489(1):7–20.
- Ravi, V. (2019). Measuring the Circumgalactic and Intergalactic Baryon Contents with Fast Radio Bursts. *ApJ*, 872(1):88.
- Ravi, V., Catha, M., D’Addario, L., Djorgovski, S. G., Hallinan, G., Hobbs, R., Kocz, J., Kulkarni, S. R., Shi, J., Vedantham, H. K., Weinreb, S., and Woody, D. P. (2019). A fast radio burst localized to a massive galaxy. *Nature*, 572(7769):352–354.
- Ravi, V., Shannon, R. M., Bailes, M., Bannister, K., Bhandari, S., Bhat, N. D. R., Burke-Spolaor, S., Caleb, M., Flynn, C., Jameson, A., Johnston, S., Keane, E. F., Kerr, M., Tiburzi, C., Tuntsov, A. V., and Vedantham, H. K. (2016). The magnetic field and turbulence of the cosmic web measured using a brilliant fast radio burst. *Science*, 354(6317):1249–1252.
- Rees, M. J. (2006). Origin of cosmic magnetic fields. *Astronomische Nachrichten*, 327:395.
- Reich, W. (2006). Galactic polarization surveys. *arXiv e-prints*, pages astro-ph/0603465.
- Ridnaia, A., Svinkin, D., Frederiks, D., Bykov, A., Popov, S., Aptekar, R., Golenetskii, S., Lysenko, A., Tsvetkova, A., Ulanov, M., and Cline, T. (2020). A peculiar hard X-ray counterpart of a Galactic fast radio burst. *arXiv e-prints*, page arXiv:2005.11178.
- Rieder, M. and Teyssier, R. (2016). A small-scale dynamo in feedback-dominated galaxies as the origin of cosmic magnetic fields - I. The kinematic phase. *MNRAS*, 457(2):1722–1738.
- Rieder, M. and Teyssier, R. (2017). A small-scale dynamo in feedback-dominated galaxies - III. Cosmological simulations. *MNRAS*, 472(4):4368–4373.
- Riseley, C. J., Galvin, T. J., Sobey, C., Vernstrom, T., White, S. V., Zhang, X., Gaensler, B. M., Heald, G., Anderson, C. S., Franzen, T. M. O., Hancock, P. J., Hurley-Walker, N., Lenc, E., and Van Eck, C. L. (2020). The Polarised GLEAM Survey (POGS) II: Results from an all-sky rotation measure synthesis survey at long wavelengths. *Publications of the Astronomical Society of Australia*, 37:e029.

- Rudnick, L. and Owen, F. N. (2014). The Distribution of Polarized Radio Sources $\geq 15 \mu\text{Jy}$ in GOODS-N. *ApJ*, 785(1):45.
- Ruiter, A. J., Belczynski, K., Sim, S. A., Hillebrandt, W., Fryer, C. L., Fink, M., and Kromer, M. (2011). Delay times and rates for Type Ia supernovae and thermonuclear explosions from double-detonation sub-Chandrasekhar mass models. *MNRAS*, 417(1):408–419.
- Rybicki, G. B. and Lightman, A. P. (1986). *Radiative Processes in Astrophysics*.
- Ryu, D. and Kang, H. (2003). Clusters of Galaxies: Shock Waves and Cosmic Rays. *Journal of Korean Astronomical Society*, 36(3):105–110.
- Ryu, D., Kang, H., Cho, J., and Das, S. (2008). Turbulence and Magnetic Fields in the Large-Scale Structure of the Universe. *Science*, 320(5878):909.
- Sanidas, S., Cooper, S., Bassa, C. G., Hessels, J. W. T., Kondratiev, V. I., Michilli, D., Stappers, B. W., Tan, C. M., van Leeuwen, J., Cerrigone, L., Fallows, R. A., Iacobelli, M., Orrú, E., Pizzo, R. F., Shulevski, A., Toribio, M. C., ter Veen, S., Zucca, P., Bondonneau, L., Griebmeier, J. M., Karastergiou, A., Kramer, M., and Sobey, C. (2019). The LOFAR Tied-Array All-Sky Survey (LOTAAS): Survey overview and initial pulsar discoveries. *A&A*, 626:A104.
- Schlickeiser, R. (2012). Cosmic Magnetization: From Spontaneously Emitted Aperiodic Turbulent to Ordered Equipartition Fields. *Physical Review Letters*, 109(26):261101.
- Schmidt, M. (1968). Space Distribution and Luminosity Functions of Quasi-Stellar Radio Sources. *ApJ*, 151:393.
- Schnitzeler, D. H. F. M. (2010). The latitude dependence of the rotation measures of NVSS sources. *MNRAS*, 409(1):L99–L103.
- Scholz, P., Spitler, L., Hessels, J., Bogdanov, S., Brazier, A., Camilo, F., Chatterjee, S., Cordes, J. M., Crawford, F., Deneva, J. S., Ferdman, R., Freire, P., Kaspi, V. M., Lazarus, P., Lynch, R., Madsen, E., McLaughlin, M., Patel, C., Ransom, S. M., Seymour, A., Stairs, I. H., Stappers, B., van Leeuwen, J., and Zhu, W. (2016a). A Repeating Fast Radio Burst: Radio and X-ray Follow-up Observations of FRB 121102. In *AAS/High Energy Astrophysics Division #15*, AAS/High Energy Astrophysics Division, page 105.03.

- Scholz, P., Spitler, L. G., Hessels, J. W. T., Chatterjee, S., Cordes, J. M., Kaspi, V. M., Wharton, R. S., Bassa, C. G., Bogdanov, S., Camilo, F., Crawford, F., Deneva, J., van Leeuwen, J., Lynch, R., Madsen, E. C., McLaughlin, M. A., Mickaliger, M., Parent, E., Patel, C., Ransom, S. M., Seymour, A., Stairs, I. H., Stappers, B. W., and Tendulkar, S. P. (2016b). The Repeating Fast Radio Burst FRB 121102: Multi-wavelength Observations and Additional Bursts. *ApJ*, 833(2):177.
- Sebokolodi, M. L. L., Perley, R., Eilek, J., Carilli, C., Smirnov, O., Laing, R., Greisen, E. W., and Wise, M. (2020). A Wideband Polarization Study of Cygnus A with the Jansky Very Large Array. I. The Observations and Data. *ApJ*, 903(1):36.
- Segalovitz, A. (1976). High resolution six-cm observations of Messier 51. *A&A*, 52(2):167–174.
- Semikoz, V. B. and Sokoloff, D. D. (2005). Generation of primordial magnetic fields by α -effect driven by collective neutrino-plasma interaction. *Nuclear Physics B Proceedings Supplements*, 143:519–519.
- Seymour, N., Dwelly, T., Moss, D., McHardy, I., Zoghbi, A., Rieke, G., Page, M., Hopkins, A., and Loaring, N. (2008). The star formation history of the Universe as revealed by deep radio observations. *MNRAS*, 386(3):1695–1708.
- Shand, Z., Ouyed, A., Koning, N., and Ouyed, R. (2016). Quark nova model for fast radio bursts. *Research in Astronomy and Astrophysics*, 16(5):80.
- Shannon, R. M., Macquart, J. P., Bannister, K. W., Ekers, R. D., James, C. W., Osłowski, S., Qiu, H., Sammons, M., Hotan, A. W., Voronkov, M. A., Beresford, R. J., Brothers, M., Brown, A. J., Bunton, J. D., Chippendale, A. P., Haskins, C., Leach, M., Marquarding, M., McConnell, D., Pilawa, M. A., Sadler, E. M., Troup, E. R., Tuthill, J., Whiting, M. T., Allison, J. R., Anderson, C. S., Bell, M. E., Collier, J. D., Gürkan, G., Heald, G., and Riseley, C. J. (2018). The dispersion-brightness relation for fast radio bursts from a wide-field survey. *Nature*, 562(7727):386–390.
- Shimwell, T. W., Röttgering, H. J. A., Best, P. N., Williams, W. L., Djikema, T. J., de Gasperin, F., Hardcastle, M. J., Heald, G. H., Hoang, D. N., Horneffer, A., Intema, H., Mahony, E. K., Mandal, S., Mechev, A. P., Morabito, L., Oonk, J. B. R., Rafferty, D., Retana-Montenegro, E., Sabater, J., Tasse, C., van Weeren, R. J., Brüggén, M., Brunetti,

G., Chyży, K. T., Conway, J. E., Haverkorn, M., Jackson, N., Jarvis, M. J., McKean, J. P., Miley, G. K., Morganti, R., White, G. J., Wise, M. W., van Bemmell, I. M., Beck, R., Brienza, M., Bonafede, A., Calistro Rivera, G., Cassano, R., Clarke, A. O., Cseh, D., Deller, A., Drabent, A., van Driel, W., Engels, D., Falcke, H., Ferrari, C., Fröhlich, S., Garrett, M. A., Harwood, J. J., Heesen, V., Hoeft, M., Horellou, C., Israel, F. P., Kapińska, A. D., Kunert-Bajraszewska, M., McKay, D. J., Mohan, N. R., Orrú, E., Pizzo, R. F., Prandoni, I., Schwarz, D. J., Shulevski, A., Sipior, M., Smith, D. J. B., Sridhar, S. S., Steinmetz, M., Stroe, A., Varenus, E., van der Werf, P. P., Zensus, J. A., and Zwart, J. T. L. (2017). The LOFAR Two-metre Sky Survey. I. Survey description and preliminary data release. *A&A*, 598:A104.

Shimwell, T. W., Tasse, C., Hardcastle, M. J., Mechev, A. P., Williams, W. L., Best, P. N., Röttgering, H. J. A., Callingham, J. R., Dijkema, T. J., de Gasperin, F., Hoang, D. N., Hugo, B., Mirmont, M., Oonk, J. B. R., Prandoni, I., Rafferty, D., Sabater, J., Smirnov, O., van Weeren, R. J., White, G. J., Atemkeng, M., Bester, L., Bonnassieux, E., Brüggem, M., Brunetti, G., Chyży, K. T., Cochrane, R., Conway, J. E., Croston, J. H., Danezi, A., Duncan, K., Haverkorn, M., Heald, G. H., Iacobelli, M., Intema, H. T., Jackson, N., Jamrozy, M., Jarvis, M. J., Lakhoo, R., Mevius, M., Miley, G. K., Morabito, L., Morganti, R., Nisbet, D., Orrú, E., Perkins, S., Pizzo, R. F., Schrijvers, C., Smith, D. J. B., Vermeulen, R., Wise, M. W., Alegre, L., Bacon, D. J., van Bemmell, I. M., Beswick, R. J., Bonafede, A., Botteon, A., Bourke, S., Brienza, M., Calistro Rivera, G., Cassano, R., Clarke, A. O., Conselice, C. J., Dettmar, R. J., Drabent, A., Dumba, C., Emig, K. L., Enßlin, T. A., Ferrari, C., Garrett, M. A., Génova-Santos, R. T., Goyal, A., Gürkan, G., Hale, C., Harwood, J. J., Heesen, V., Hoeft, M., Horellou, C., Jackson, C., Kokotanekov, G., Kondapally, R., Kunert-Bajraszewska, M., Mahatma, V., Mahony, E. K., Mandal, S., McKean, J. P., Merloni, A., Mingo, B., Miskolczi, A., Mooney, S., Nikiel-Wroczyński, B., O’Sullivan, S. P., Quinn, J., Reich, W., Roskowiński, C., Rowlinson, A., Savini, F., Saxena, A., Schwarz, D. J., Shulevski, A., Sridhar, S. S., Stacey, H. R., Urquhart, S., van der Wiel, M. H. D., Varenus, E., Webster, B., and Wilber, A. (2019). The LOFAR Two-metre Sky Survey. II. First data release. *A&A*, 622:A1.

Shull, J. M., Smith, B. D., and Danforth, C. W. (2012). The Baryon Census

- in a Multiphase Intergalactic Medium: 30% of the Baryons May Still be Missing. *ApJ*, 759(1):23.
- Smirnov, O. M. and Tasse, C. (2015). Radio interferometric gain calibration as a complex optimization problem. *MNRAS*, 449(3):2668–2684.
- Snowden, S. L., Mushotzky, R. F., Kuntz, K. D., and Davis, D. S. (2008). A catalog of galaxy clusters observed by XMM-Newton. *A&A*, 478(2):615–658.
- Sobey, C., Bilous, A. V., Griebmeier, J. M., Hessels, J. W. T., Karastergiou, A., Keane, E. F., Kondratiev, V. I., Kramer, M., Michilli, D., Noutsos, A., Pilia, M., Polzin, E. J., Stappers, B. W., Tan, C. M., van Leeuwen, J., Verbiest, J. P. W., Weltevrede, P., Heald, G., Alves, M. I. R., Carretti, E., Enßlin, T., Haverkorn, M., Iacobelli, M., Reich, W., and Van Eck, C. (2019). Low-frequency Faraday rotation measures towards pulsars using LOFAR: probing the 3D Galactic halo magnetic field. *MNRAS*, 484(3):3646–3664.
- Sokolowski, M., Bhat, N. D. R., Macquart, J. P., Shannon, R. M., Bannister, K. W., Ekers, R. D., Scott, D. R., Beardsley, A. P., Crosse, B., Emrich, D., Franzen, T. M. O., Gaensler, B. M., Horsley, L., Johnston-Hollitt, M., Kaplan, D. L., Kenney, D., Morales, M. F., Pallot, D., Slep, G., Steele, K., Tingay, S. J., Trott, C. M., Walker, M., Wayth, R. B., Williams, A., and Wu, C. (2018). No Low-frequency Emission from Extremely Bright Fast Radio Bursts. *ApJ Letters*, 867(1):L12.
- Spitler, L. G., Cordes, J. M., Hessels, J. W. T., Lorimer, D. R., McLaughlin, M. A., Chatterjee, S., Crawford, F., Deneva, J. S., Kaspi, V. M., Wharton, R. S., Allen, B., Bogdanov, S., Brazier, A., Camilo, F., Freire, P. C. C., Jenet, F. A., Karako-Argaman, C., Knispel, B., Lazarus, P., Lee, K. J., van Leeuwen, J., Lynch, R., Ransom, S. M., Scholz, P., Siemens, X., Stairs, I. H., Stovall, K., Swiggum, J. K., Venkataraman, A., Zhu, W. W., Aulbert, C., and Fehrmann, H. (2014). Fast Radio Burst Discovered in the Arecibo Pulsar ALFA Survey. *ApJ*, 790(2):101.
- Spitler, L. G., Scholz, P., Hessels, J. W. T., Bogdanov, S., Brazier, A., Camilo, F., Chatterjee, S., Cordes, J. M., Crawford, F., Deneva, J., Ferdman, R. D., Freire, P. C. C., Kaspi, V. M., Lazarus, P., Lynch, R., Madsen, E. C., McLaughlin, M. A., Patel, C., Ransom, S. M., Seymour, A., Stairs, I. H., Stappers, B. W., van Leeuwen, J., and Zhu, W. W. (2016). A repeating fast radio burst. *Nature*, 531(7593):202–205.

- Stuardi, C., Bonafede, A., Wittor, D., Vazza, F., Botteon, A., Locatelli, N., Dallacasa, D., Golovich, N., Hoeft, M., van Weeren, R. J., Brügger, M., and de Gasperin, F. (2019). Particle re-acceleration and Faraday-complex structures in the RXC J1314.4-2515 galaxy cluster. *MNRAS*, 489(3):3905–3926.
- Stuardi, C., O’Sullivan, S. P., Bonafede, A., Brügger, M., Dabhade, P., Horellou, C., Morganti, R., Carretti, E., Heald, G., Iacobelli, M., and Vacca, V. (2020). The LOFAR view of intergalactic magnetic fields with giant radio galaxies. *A&A*, 638:A48.
- Subramanian, K. (2016). The origin, evolution and signatures of primordial magnetic fields. *Reports on Progress in Physics*, 79(7):076901.
- Sun, X. H., Reich, W., Waelkens, A., and Enßlin, T. A. (2008). Radio observational constraints on Galactic 3D-emission models. *A&A*, 477(2):573–592.
- Tasse, C. (2014a). Applying Wirtinger derivatives to the radio interferometry calibration problem. *arXiv e-prints*, page arXiv:1410.8706.
- Tasse, C. (2014b). Nonlinear Kalman filters for calibration in radio interferometry. *A&A*, 566:A127.
- Tasse, C., Hugo, B., Mirmont, M., Smirnov, O., Atemkeng, M., Bester, L., Hardcastle, M. J., Lakhoo, R., Perkins, S., and Shimwell, T. (2018). Faceting for direction-dependent spectral deconvolution. *A&A*, 611:A87.
- Tavani, M., Ursi, A., Verrecchia, F., Casentini, C., Pittori, C., Pilia, M., Cardillo, M., Piano, G., Bulgarelli, A., Fioretti, V., Parmiggiani, N., Lucarelli, F., Donnarumma, I., Vercellone, S., Gianotti, F., Trifoglio, M., Giuliani, A., Mereghetti, S., Caraveo, P., Perotti, F., Chen, A., Argan, A., Costa, E., Del Monte, E., Evangelista, Y., Feroci, M., Lazzarotto, F., Lapshov, I., Pacciani, L., Soffitta, P., Vittorini, V., Di Cocco, G., Fuschino, F., Galli, M., Labanti, C., Marisaldi, M., Pellizzoni, A., Trois, A., Barbiellini, G., Vallazza, E., Longo, F., Morselli, A., Picozza, P., Prest, M., Lipari, P., Zanello, D., Cattaneo, P. W., Rappoldi, A., Ferrari, A., Paoletti, F., Antonelli, A., Giommi, P., Salotti, L., Valentini, G., and D’Amico, F. (2020). AGILE detection of a hard X-ray burst in temporal coincidence with a radio burst from SGR 1935+2154. *The Astronomer’s Telegram*, 13686:1.

- Tavecchio, F., Ghisellini, G., Foschini, L., Bonnoli, G., Ghirlanda, G., and Coppi, P. (2010). The intergalactic magnetic field constrained by Fermi/Large Area Telescope observations of the TeV blazar 1ES0229+200. *MNRAS*, 406(1):L70–L74.
- Taylor, G. B., Govoni, F., Allen, S. W., and Fabian, A. C. (2001). Magnetic fields in the 3C 129 cluster. *MNRAS*, 326(1):2–10.
- Tendulkar, S. P., Bassa, C. G., Cordes, J. M., Bower, G. C., Law, C. J., Chatterjee, S., Adams, E. A. K., Bogdanov, S., Burke-Spolaor, S., Butler, B. J., Demorest, P., Hessels, J. W. T., Kaspi, V. M., Lazio, T. J. W., Maddox, N., Marcote, B., McLaughlin, M. A., Paragi, Z., Ransom, S. M., Scholz, P., Seymour, A., Spitler, L. G., van Langevelde, H. J., and Wharton, R. S. (2017). The Host Galaxy and Redshift of the Repeating Fast Radio Burst FRB 121102. *ApJ Letters*, 834(2):L7.
- ter Veen, S., Enriquez, J. E., Falcke, H., Rachen, J. P., van den Akker, M., Schellart, P., Bonardi, A., Breton, R. P., Broderick, J. W., Corbel, S., Corstanje, A., Eisloffel, J., Griebmeier, J. M., Hörandel, J. R., van der Horst, A. J., Law, C. J., van Leeuwen, J., Nelles, A., Rossetto, L., Rowlinson, A., Winchen, T., and Zarka, P. (2019). The FRATS project: real-time searches for fast radio bursts and other fast transients with LO-FAR at 135 MHz. *A&A*, 621:A57.
- The CHEX-MATE Collaboration, :, Arnaud, M., Etori, S., Pratt, G. W., Rossetti, M., Eckert, D., Gastaldello, F., Gavazzi, R., Kay, S. T., Lovisari, L., Maughan, B. J., Pointecouteau, E., Sereno, M., Bartalucci, I., Bonafede, A., Bourdin, H., Cassano, R., Duffy, R. T., Iqbal, A., Maurogordato, S., Rasia, E., Sayers, J., Andrade-Santos, F., Aussel, H., Barnes, D. J., Barrena, R., Borgani, S., Burkutean, S., Clerc, N., Corasaniti, P. S., Cuillandre, J. C., De Grandi, S., De Petris, M., Dolag, K., Donahue, M., Ferragamo, A., Gaspari, M., Ghizzardi, S., Gitti, M., Haines, C. P., Jauzac, M., Johnston-Hollitt, M., Jones, C., Kéruzoré, F., Le Brun, A. M. C., Mayet, F., Mazzotta, P., Melin, J. B., Molendi, S., Nonino, M., Okabe, N., Paltani, S., Perotto, L., Pires, S., Radovich, M., Rubino-Martin, J. A., Salvati, L., Saro, A., Sartoris, B., Schellenberger, G., Streblyanska, A., Tarrio, P., Tozzi, P., Umetsu, K., van der Burg, R. F. J., Vazza, F., Venturi, T., Yepes, G., and Zarattini, S. (2020). The Cluster HERitage project with XMM-Newton: Mass Assembly and Thermodynamics at the Endpoint of structure formation. I. Programme overview. *arXiv e-prints*, page arXiv:2010.11972.

- The CHIME/FRB Collaboration, :, Andersen, B. C., Bandura, K. M., Bhardwaj, M., Bij, A., Boyce, M. M., Boyle, P. J., Brar, C., Cassanelli, T., Chawla, P., Chen, T., Cliche, J. F., Cook, A., Cubranic, D., Curtin, A. P., Denman, N. T., Dobbs, M., Dong, F. Q., Fandino, M., Fonseca, E., Gaensler, B. M., Giri, U., Good, D. C., Halpern, M., Hill, A. S., Hinshaw, G. F., Höfer, C., Josephy, A., Kania, J. W., Kaspi, V. M., Landecker, T. L., Leung, C., Li, D. Z., Lin, H. H., Masui, K. W., McKinven, R., Mena-Parra, J., Merryfield, M., Meyers, B. W., Michilli, D., Milutinovic, N., Mirhosseini, A., Münchmeyer, M., Naidu, A., Newburgh, L. B., Ng, C., Patel, C., Pen, U. L., Pinsonneault-Marotte, T., Pleunis, Z., Quine, B. M., Rafiei-Ravandi, M., Rahman, M., Ransom, S. M., Renard, A., Sanghavi, P., Scholz, P., Shaw, J. R., Shin, K., Siegel, S. R., Singh, S., Smegal, R. J., Smith, K. M., Stairs, I. H., Tan, C. M., Tendulkar, S. P., Tretyakov, I., Vanderlinde, K., Wang, H., Wulf, D., and Zwaniga, A. V. (2020). A bright millisecond-duration radio burst from a Galactic magnetar. *arXiv e-prints*, page arXiv:2005.10324.
- Thornton, D., Stappers, B., Bailes, M., Barsdell, B., Bates, S., Bhat, N. D. R., Burgay, M., Burke-Spolaor, S., Champion, D. J., Coster, P., D’Amico, N., Jameson, A., Johnston, S., Keith, M., Kramer, M., Levin, L., Milia, S., Ng, C., Possenti, A., and van Straten, W. (2013). A Population of Fast Radio Bursts at Cosmological Distances. *Science*, 341(6141):53–56.
- Tosa, M. and Fujimoto, M. (1978). The Configuration of Magnetic Fields in the Spiral Galaxy M 51. *Publications of the Astronomical Society of Japan*, 30:315–326.
- Totani, T. (2013). Cosmological Fast Radio Bursts from Binary Neutron Star Mergers. *Publications of the Astronomical Society of Japan*, 65:L12.
- Turner, M. S. and Widrow, L. M. (1988). Inflation-produced, large-scale magnetic fields. *Physical Review Letters*, 37(10):2743–2754.
- Uchiyama, Y., Aharonian, F. A., Tanaka, T., Takahashi, T., and Maeda, Y. (2007). Extremely fast acceleration of cosmic rays in a supernova remnant. *Nature*, 449(7162):576–578.
- Vacca, V., Murgia, M., Govoni, F., Loi, F., Vazza, F., Finoguenov, A., Carretti, E., Feretti, L., Giovannini, G., Concu, R., Melis, A., Gheller, C., Paladino, R., Poppi, S., Valente, G., Bernardi, G., Boschini, W., Brienza, M., Clarke, T. E., Colafrancesco, S., Enßlin, T. A., Ferrari, C., de Gasperin,

- F., Gastaldello, F., Girardi, M., Gregorini, L., Johnston-Hollitt, M., Junklewitz, H., Orrù, E., Parma, P., Perley, R., and Taylor, G. B. (2018). Observations of a nearby filament of galaxy clusters with the Sardinia Radio Telescope. *MNRAS*, 479(1):776–806.
- Vacca, V., Oppermann, N., Enßlin, T., Jasche, J., Selig, M., Greiner, M., Junklewitz, H., Reinecke, M., Brüggen, M., Carretti, E., Feretti, L., Ferrari, C., Hales, C. A., Horellou, C., Ideguchi, S., Johnston-Hollitt, M., Pizzo, R. F., Röttgering, H., Shimwell, T. W., and Takahashi, K. (2016). Using rotation measure grids to detect cosmological magnetic fields: A Bayesian approach. *A&A*, 591:A13.
- Vallee, J. P. (1998). Observations of the Magnetic Fields Inside and Outside the Solar System: From Meteorites (~ 10 attoparsecs), Asteroids, Planets, Stars, Pulsars, Masers, to Protostellar Cloudlets ($\ll 1$ parsec). *Fundamentals of Cosmic Physics*, 19:319–422.
- Van Eck, C. L., Brown, J. C., Stil, J. M., Rae, K., Mao, S. A., Gaensler, B. M., Shukurov, A., Taylor, A. R., Haverkorn, M., Kronberg, P. P., and McClure-Griffiths, N. M. (2011). Modeling the Magnetic Field in the Galactic Disk Using New Rotation Measure Observations from the Very Large Array. *ApJ*, 728(2):97.
- van Haarlem, M. P., Wise, M. W., Gunst, A. W., Heald, G., McKean, J. P., Hessels, J. W. T., de Bruyn, A. G., Nijboer, R., Swinbank, J., Fallows, R., Brentjens, M., Nelles, A., Beck, R., Falcke, H., Fender, R., Hörandel, J., Koopmans, L. V. E., Mann, G., Miley, G., Röttgering, H., Stappers, B. W., Wijers, R. A. M. J., Zaroubi, S., van den Akker, M., Alexov, A., Anderson, J., Anderson, K., van Ardenne, A., Arts, M., Asgekar, A., Avruch, I. M., Batejat, F., Bähren, L., Bell, M. E., Bell, M. R., van Bemmel, I., Bennema, P., Bentum, M. J., Bernardi, G., Best, P., Birzan, L., Bonafede, A., Boonstra, A. J., Braun, R., Bregman, J., Breitling, F., van de Brink, R. H., Broderick, J., Broekema, P. C., Brouw, W. N., Brüggen, M., Butcher, H. R., van Cappellen, W., Ciardi, B., Coenen, T., Conway, J., Coolen, A., Corstanje, A., Damstra, S., Davies, O., Deller, A. T., Dettmar, R. J., van Diepen, G., Dijkstra, K., Donker, P., Doorduyn, A., Dromer, J., Drost, M., van Duin, A., Eislöffel, J., van Enst, J., Ferrari, C., Frieswijk, W., Gankema, H., Garrett, M. A., de Gasperin, F., Gebbers, M., de Geus, E., Gießmeier, J. M., Grit, T., Gruppen, P., Hamaker, J. P., Hassall, T., Hoeft, M., Holties, H. A., Horneffer, A., van der Horst, A., van Houwelingen, A., Huijgen, A., Iacobelli, M., Intema, H., Jackson,

- N., Jelic, V., de Jong, A., Juette, E., Kant, D., Karastergiou, A., Koers, A., Kollen, H., Kondratiev, V. I., Kooistra, E., Koopman, Y., Koster, A., Kuniyoshi, M., Kramer, M., Kuper, G., Lambropoulos, P., Law, C., van Leeuwen, J., Lemaitre, J., Loose, M., Maat, P., Macario, G., Markoff, S., Masters, J., McFadden, R. A., McKay-Bukowski, D., Meijering, H., Meulman, H., Mevius, M., Middelberg, E., Millenaar, R., Miller-Jones, J. C. A., Mohan, R. N., Mol, J. D., Morawietz, J., Morganti, R., Mulcahy, D. D., Mulder, E., Munk, H., Nieuwenhuis, L., van Nieuwpoort, R., Noordam, J. E., Norden, M., Noutsos, A., Offringa, A. R., Olofsson, H., Omar, A., Orrú, E., Overeem, R., Paas, H., Pandey-Pommier, M., Pandey, V. N., Pizzo, R., Polatidis, A., Rafferty, D., Rawlings, S., Reich, W., de Reijer, J. P., Reitsma, J., Renting, G. A., Riemers, P., Rol, E., Romein, J. W., Roosjen, J., Ruiter, M., Scaife, A., van der Schaaf, K., Scheers, B., Schellart, P., Schoenmakers, A., Schoonderbeek, G., Serylak, M., Shulevski, A., Sluman, J., Smirnov, O., Sobey, C., Spreeuw, H., Steinmetz, M., Sterks, C. G. M., Stiepel, H. J., Stuurwold, K., Tagger, M., Tang, Y., Tasse, C., Thomas, I., Thoudam, S., Toribio, M. C., van der Tol, B., Usov, O., van Veelen, M., van der Veen, A. J., ter Veen, S., Verbiest, J. P. W., Vermeulen, R., Vermaas, N., Vocks, C., Vogt, C., de Vos, M., van der Wal, E., van Weeren, R., Weggemans, H., Weltevrede, P., White, S., Wijnholds, S. J., Wilhelmsson, T., Wucknitz, O., Yatawatta, S., Zarka, P., Zensus, A., and van Zwieten, J. (2013). LOFAR: The LOw-Frequency ARray. *A&A*, 556:A2.
- van Weeren, R. J., Andrade-Santos, F., Dawson, W. A., Golovich, N., Lal, D. V., Kang, H., Ryu, D., Brügger, M., Ogreaan, G. A., Forman, W. R., Jones, C., Placco, V. M., Santucci, R. M., Wittman, D., Jee, M. J., Kraft, R. P., Sobral, D., Stroe, A., and Fogarty, K. (2017). The case for electron re-acceleration at galaxy cluster shocks. *Nature Astronomy*, 1:0005.
- van Weeren, R. J., de Gasperin, F., Akamatsu, H., Brügger, M., Feretti, L., Kang, H., Stroe, A., and Zandanel, F. (2019). Diffuse Radio Emission from Galaxy Clusters. *Science & Space Review*, 215(1):16.
- van Weeren, R. J., Röttgering, H. J. A., Brügger, M., and Hoeft, M. (2010). Particle Acceleration on Megaparsec Scales in a Merging Galaxy Cluster. *Science*, 330(6002):347.
- van Weeren, R. J., Williams, W. L., Hardcastle, M. J., Shimwell, T. W., Rafferty, D. A., Sabater, J., Heald, G., Sridhar, S. S., Dijkema, T. J., Brunetti, G., Brügger, M., Andrade-Santos, F., Ogreaan, G. A.,

- Röttgering, H. J. A., Dawson, W. A., Forman, W. R., de Gasperin, F., Jones, C., Miley, G. K., Rudnick, L., Sarazin, C. L., Bonafede, A., Best, P. N., Birzan, L., Cassano, R., Chyży, K. T., Croston, J. H., Ensslin, T., Ferrari, C., Hoeft, M., Horellou, C., Jarvis, M. J., Kraft, R. P., Mevius, M., Intema, H. T., Murray, S. S., Orrú, E., Pizzo, R., Simionescu, A., Stroe, A., van der Tol, S., and White, G. J. (2016). LOFAR Facet Calibration. *ApJS*, 223(1):2.
- Vazza, F., Brüggén, M., Gheller, C., Hackstein, S., Wittor, D., and Hinz, P. M. (2017). Simulations of extragalactic magnetic fields and of their observables. *Classical and Quantum Gravity*, 34(23):234001.
- Vazza, F., Brüggén, M., Gheller, C., and Wang, P. (2014). On the amplification of magnetic fields in cosmic filaments and galaxy clusters. *MNRAS*, 445(4):3706–3722.
- Vazza, F., Brüggén, M., Hinz, P. M., Wittor, D., Locatelli, N., and Gheller, C. (2018a). Probing the origin of extragalactic magnetic fields with Fast Radio Bursts. *MNRAS*, 480(3):3907–3915.
- Vazza, F., Brüggén, M., Wittor, D., Gheller, C., Eckert, D., and Stubbe, M. (2016). Constraining the efficiency of cosmic ray acceleration by cluster shocks. *MNRAS*, 459(1):70–83.
- Vazza, F., Brunetti, G., Brüggén, M., and Bonafede, A. (2018b). Resolved magnetic dynamo action in the simulated intracluster medium. *MNRAS*, 474(2):1672–1687.
- Vazza, F., Brunetti, G., Gheller, C., and Brunino, R. (2010). Massive and refined: A sample of large galaxy clusters simulated at high resolution. I: Thermal gas and properties of shock waves. *New Astronomy*, 15(8):695–711.
- Vazza, F., Eckert, D., Brüggén, M., and Huber, B. (2015a). Electron and proton acceleration efficiency by merger shocks in galaxy clusters. *MNRAS*, 451(2):2198–2211.
- Vazza, F., Ettori, S., Roncarelli, M., Angelinelli, M., Brüggén, M., and Gheller, C. (2019). Detecting shocked intergalactic gas with X-ray and radio observations. *A&A*, 627:A5.
- Vazza, F., Ferrari, C., Brüggén, M., Bonafede, A., Gheller, C., and Wang, P. (2015b). Forecasts for the detection of the magnetised cosmic web from cosmological simulations. *A&A*, 580:A119.

- Vedantham, H. K., Ravi, V., Hallinan, G., and Shannon, R. M. (2016). The Fluence and Distance Distributions of Fast Radio Bursts. *ApJ*, 830(2):75.
- Vernstrom, T., Gaensler, B. M., Brown, S., Lenc, E., and Norris, R. P. (2017). Low-frequency radio constraints on the synchrotron cosmic web. *MNRAS*, 467(4):4914–4936.
- Vernstrom, T., Gaensler, B. M., Rudnick, L., and Andernach, H. (2019). Differences in Faraday Rotation between Adjacent Extragalactic Radio Sources as a Probe of Cosmic Magnetic Fields. *ApJ*, 878(2):92.
- Wang, P. and Abel, T. (2009). Magnetohydrodynamic Simulations of Disk Galaxy Formation: The Magnetization of the Cold and Warm Medium. *ApJ*, 696(1):96–109.
- Weinberg, D. H., Davé, R., Katz, N., and Kollmeier, J. A. (2003). The Lyman- α Forest as a Cosmological Tool. In Holt, S. H. and Reynolds, C. S., editors, *The Emergence of Cosmic Structure*, volume 666 of *American Institute of Physics Conference Series*, pages 157–169.
- Weinberg, D. H., Miralda-Escudé, J., Hernquist, L., and Katz, N. (1997). A Lower Bound on the Cosmic Baryon Density. *ApJ*, 490(2):564–570.
- Weiss, B. P., Elkins-Tanton, L. T., Antonietta Barucci, M., Sierks, H., Snodgrass, C., Vincent, J.-B., Marchi, S., Weissman, P. R., Pätzold, M., Richter, I., Fulchignoni, M., Binzel, R. P., and Schulz, R. (2012). Possible evidence for partial differentiation of asteroid Lutetia from Rosetta. *Planetary and Space Science*, 66(1):137–146.
- Widrow, L. M. (2002). Origin of galactic and extragalactic magnetic fields. *Reviews of Modern Physics*, 74(3):775–823.
- Widrow, L. M., Ryu, D., Schleicher, D. R. G., Subramanian, K., Tsagas, C. G., and Treumann, R. A. (2012). The First Magnetic Fields. *Science & Space Review*, 166(1-4):37–70.
- Wielebinski, R. and Beck, R. (2005). *Cosmic Magnetic Fields*, volume 664.
- Williams, W. L., van Weeren, R. J., Röttgering, H. J. A., Best, P., Dijkema, T. J., de Gasperin, F., Hardcastle, M. J., Heald, G., Prandoni, I., Sabater, J., Shimwell, T. W., Tasse, C., van Bemmelen, I. M., Brüggemann, M., Brunetti, G., Conway, J. E., Enßlin, T., Engels, D., Falcke, H., Ferrari, C., Haverkorn, M., Jackson, N., Jarvis, M. J., Kapińska, A. D.,

- Mahony, E. K., Miley, G. K., Morabito, L. K., Morganti, R., Orrú, E., Retana-Montenegro, E., Sridhar, S. S., Toribio, M. C., White, G. J., Wise, M. W., and Zwart, J. T. L. (2016). LOFAR 150-MHz observations of the Boötes field: catalogue and source counts. *MNRAS*, 460(3):2385–2412.
- Willingale, R., Starling, R. L. C., Beardmore, A. P., Tanvir, N. R., and O’Brien, P. T. (2013). Calibration of X-ray absorption in our Galaxy. *MNRAS*, 431(1):394–404.
- Willott, C. J., Rawlings, S., Blundell, K. M., Lacy, M., and Eales, S. A. (2001). The radio luminosity function from the low-frequency 3CRR, 6CE and 7CRS complete samples. *MNRAS*, 322(3):536–552.
- Wittor, D., Vazza, F., and Brüggén, M. (2017). Testing cosmic ray acceleration with radio relics: a high-resolution study using MHD and tracers. *MNRAS*, 464(4):4448–4462.
- Wittor, D., Vazza, F., Ryu, D., and Kang, H. (2020). Limiting the shock acceleration of cosmic ray protons in the ICM. *MNRAS*, 495(1):L112–L117.
- Xu, H., Li, H., Collins, D. C., Li, S., and Norman, M. L. (2009). Turbulence and Dynamo in Galaxy Cluster Medium: Implications on the Origin of Cluster Magnetic Fields. *ApJ Letters*, 698(1):L14–L17.
- Xu, J. and Han, J. L. (2015). Extragalactic dispersion measures of fast radio bursts. *Research in Astronomy and Astrophysics*, 15(10):1629.
- Xu, R., Spitkovsky, A., and Caprioli, D. (2020). Electron Acceleration in One-dimensional Nonrelativistic Quasi-perpendicular Collisionless Shocks. *ApJ Letters*, 897(2):L41.
- Xu, Y., Kronberg, P. P., Habib, S., and Dufton, Q. W. (2006). A Faraday Rotation Search for Magnetic Fields in Large-scale Structure. *ApJ*, 637:19–26.
- Yang, Y.-P. and Zhang, B. (2018). Bunching Coherent Curvature Radiation in Three-dimensional Magnetic Field Geometry: Application to Pulsars and Fast Radio Bursts. *ApJ*, 868(1):31.
- Yao, J. M., Manchester, R. N., and Wang, N. (2017). A New Electron-density Model for Estimation of Pulsar and FRB Distances. *ApJ*, 835(1):29.

- Zel'dovich, Y. B. (1970). The Hypothesis of Cosmological Magnetic Inhomogeneity. *Soviet Astronomy*, 13:608.
- Zhang, B. (2014). A Possible Connection between Fast Radio Bursts and Gamma-Ray Bursts. *ApJ Letters*, 780(2):L21.

Acknowledgments

The author wishes to thank all the referees who provided their valuable comments and remarks to the various works presented in this thesis, in particular Federica Govoni and Hiroki Akamatsu. He also acknowledges financial support from the ERC Starting Grant ‘MAGCOW’, no. 714196. Radio imaging made use of WSCLEAN (Offringa et al., 2014, v2.6), CASA (McMullin et al., 2007, <https://casa.nrao.edu>) and DDF (Tasse et al., 2018). This work is based (in part) on data obtained with the International LOFAR Telescope and analysed using LOFAR-IT infrastructure. LOFAR (van Haarlem et al., 2013) is the Low-Frequency Array designed and constructed by ASTRON and collectively operated by the ILT Foundation. The data in Sec. 2.3 were (partly) processed by the LOFAR Two-Metre Sky Survey (LoTSS) team. This team made use of the LOFAR direction independent calibration pipeline (<https://github.com/lofar-astron/prefactor>) which was deployed by the LOFAR e-infragroup on the Dutch National Grid infrastructure with support of the SURF Co-operative through grants e-infra 160022 and e-infra 160152 (Mechev et al., 2017, PoS ISGC2017002). Part of the simulations were run on the JUWELS cluster at Juelich Supercomputing Centre (JSC), under project account HHH42. The Northern Cross radio telescope is a facility of the University of Bologna operated under agreement by the Institute of Radio Astronomy of Bologna (INAF). The ENZO (enzo-project.org) simulation used for this work was produced on the Marconi-KNL Supercomputer at CINECA, under project no. INA17C4A28 (PI Franco Vazza). We also acknowledge the usage of online storage tools kindly provided by the INAF Astronomical Archive (IA2) initiative (<http://www.ia2.inaf.it>). Part of our research made use of ASTROPY, a community-developed core PYTHON package for Astronomy (Astropy Collaboration et al., 2013).

The author wishes to express his most profound gratitude to Franco Vazza, Annalisa Bonafede and Chiara Stuardi. No words will ever suffice to thank them enough.

The list of collaborators and friends who actually made this work possible is endless, different and serious attempts to quote all of them have failed miserably as the lists manifestly lacked of completeness. However, special mentions go to: the supervising work of Daniele Dallacasa and Gianni Bernardi; the help provided by Kamlesh Rajpurohit; the endless support by the Locatelli, Colombi and Fiaska Vuota families; the daily laughs shared with the IRA PhD students Giovanni Sabatini, Alessandro Ignesti, Beatrice Terni de Gregory, Ilaria Ruffa and Quirino D'Amato; the priceless time spent together with the author, with or without their will, by Matteo Bruno, Eleonora Morosini, Valentina Fanafani and Cristina Nanci.